

Mechanics of the Pediatric Thoracic Spine and its Role in the Kinematics of the Head in
Automotive Frontal Impacts

A dissertation presented to the faculty of the
School of Engineering and Applied Science,
University of Virginia

In partial fulfillment
of the requirements for the degree

Doctor of Philosophy in Mechanical and Aerospace Engineering

by
Francisco J. Lopez-Valdes
May 2013

© Copyright by
Francisco J. Lopez-Valdes
All Rights Reserved
May 2013

This dissertation is submitted in partial fulfillment
of the requirements for the degree of
Doctor of Philosophy in Mechanical and Aerospace Engineering

Francisco J. Lopez Valdes

Author

The dissertation has been read and approved by the examining committee:

Richard Kent

Dissertation Advisor

Jeff Crandall

Chairperson

Kristy Arbogast

Silvia Blemker

Mark Sochor

Accepted for the School of Engineering and Applied Science:

James H. Aylor

Dean, School of Engineering and Applied Science

May 2013

A María y a Blanca.

A mis padres.

Abstract

Road traffic injuries are the second leading cause of death among 5-14 year-olds. Traumatic brain injuries are the most common severe injuries sustained by pediatric occupants and responsible for one third of all pediatric injury deaths. Literature shows that current pediatric Anthropomorphic Test Devices, and more specifically the Hybrid III 6-year-old (6YO), fail to predict the kinematics of the pediatric head and spine. The goal of this dissertation research is to provide corridors for the trajectories of the head and thoracic spine of a 6YO occupant in a 40 km/h frontal impact. The challenge is the absence of experimental data that can guide the development of these corridors at this speed.

To overcome the dearth of pediatric kinematic data in high-speed impacts, four different data sources were combined: pediatric and adult volunteers test at 9 km/h, cadaveric tests at 9 km/h and 40 km/h, animal surrogate tests at 9 km/h and 40 km/h and *in vitro* bending tests of sections of the pediatric and adult thoracic spine. The results from the 9 km/h volunteer tests showed that conventional methods that scale between pediatric and adult subjects underpredicted the forward excursion of the pediatric head by 42% (SAE method) and 49% (mass scaling). Two new methods predicting the displacement of pediatric occupants were developed within this dissertation. The first one assumed conservation of energy and underpredicted the excursion of the head by 29%. The second one was based on the use of a linear time-invariant 2D model of the occupant. The values of the effective stiffness and damping joint parameters were obtained to minimize the error between the model and the observed pediatric displacements at 9 km/h. A quasilinear viscoelastic characterization of the bending behavior of the pediatric thoracic spine was used to relate the stiffness of the upper and middle thoracic spine regions and to reduce the number of unknown joint properties in the model. The model overpredicted the forward displacement of the head (5% error) and T1 (6% error). This model was then used to predict the trajectories of a 6YO in a 40 km/h frontal impact. The assumptions made regarding the time-invariant characteristic of the model as well as the loading environment at 40 km/h were checked against the animal-surrogate and cadaveric tests. The predictions of the sagittal trajectories of the pediatric head, T1 and T8 obtained from the simulation of the model were combined to produce corridors. The limitations of the method are discussed in the dissertation.

Acknowledgments

Grad school has taken me farther and beyond a mere Academic experience. Looking backwards to my last five years, I can see frustration, happiness, mistakes, successes, publications, rejections, unanswered questions, excitement, astonishment, early mornings, late nights... And above all, a good deal of support and friendship.

First, I would like to thank Dr. Arbogast, Dr. Blemker, Dr. Sochor, Dr. Crandall and Dr. Kent, the members of my committee, for all their guidance, encouragement, difficult questions and availability. Working with Rich throughout all these years has been an honor. His approach to solving problems by stripping them from all non-essential layers has been always inspiring. Discussing results with Jeff and listening to his “I don’t get it” and learning that it really meant “you don’t get it and I know it” has been always an enriching opportunity for learning. I treasure all the times in which I was not able to provide a convincing answer: even if I got, and will get, frustrated, they were an opportunity to push myself towards a more honest scientific approach to the problem.

I am also indebted to all the people at the Center for Applied Biomechanics. It has been a pleasure to work with you all. Through long days of testing and long nights of analyzing data I learned many things from all of you. And this is also the fruit of many, many lively discussions (and re-discussions). Dipan, Damien, Joe, Pat, David, Jason, Greg, Matt, Sabrina, Rebecca, Rob, Qi, Jaeho, Dan, Anthony, John, Jason and a long list of past and present colleagues had always the door open to listen carefully and share their ideas. I specially thank those of you that came and opened the door of my office when it was closed and I did not want to talk to anyone. I want also to thank all the people from ECIP: they know very well why.

My gratitude goes also to my siblings. Through all these years being away from you and the family, you have been always very supportive of what I was doing.

My parents are and always will be in a different league. They taught me how to live and trusted me that I would live a Good Life. With capital “G” and “L”.

Finally, I would have never crossed the Ocean without Maria. She told me that seeking the Truth is more important than being convinced of having it. And usually more uncomfortable. But always worth trying.

Table of contents

List of Symbols and Abbreviations		v
List of Figures		ix
List of Tables		xiv
1	INTRODUCTION	1
1.1	Motivation	1
1.2	Background	2
1.2.1	Anatomy of the human spine	2
1.2.2	Thoracic Spine	5
1.2.3	Limitations of the Hybrid III 50 th percentile to describe the kinematics of the human spine in a frontal impact	7
1.2.4	The development of the Hybrid III 6YO	10
1.2.5	Pediatric PMHS sled tests: assessment of the spinal biofidelity of the Hybrid III 6YO	14
1.2.6	Background summary	20
1.3	Objective of this dissertation	21
2	SUMMARY OF THE METHODOLOGICAL APPROACH AND THE DATA SOURCES USED IN THIS DISSERTATION	25
2.1	Assessment of currently used scaling techniques	27
2.2	Development of a scaling methodology assuming conservation of energy during the impact	28
2.3	Development of a methodology to predict the kinematics at 40 km/h using a 2d model of the occupant	29
2.4	Summary of methodological approach	31
3	VOLUNTEER EXPERIMENTS	32
3.1	Introduction	32
3.2	Methods	32
3.2.1	Test setup	32
3.2.2	Test subjects	33
3.2.3	Instrumentation	35
3.2.4	Calculation of the kinematic response of an average subject within each age group and its associated corridor	36
3.3	RESULTS	37
3.3.1	Kinematic comparison between restrained children and adults in a low-speed frontal impact.	37
3.3.2	Kinematics of the average subject within each age group. Corridor development	39
3.4	Discussion	41

3.5	Conclusion.....	42
4	POST MORTEM HUMAN SURROGATES SLED TESTS	44
4.1	Introduction	44
4.2	Methods	45
4.2.1	Test setup	45
4.2.2	Test subjects.....	46
4.2.3	Instrumentation	47
4.2.4	Elongation of the spine during the forward motion of the occupant	50
4.3	Results	50
4.3.1	PMHS kinematics in the sagittal plane (XZ).....	50
4.3.2	PMHS average displacement in the sagittal plane and development of corridors.....	53
4.3.3	PMHS kinematics in the XY plane	56
4.3.4	Elongation	58
4.4	Discussion	60
4.4.1	Influence of muscle activation	60
4.4.2	Influence of the femur fracture observed in PMHS2 in the kinematics of the spine	63
4.5	Conclusion.....	64
5	THORACIC SPINE CHARACTERIZATION.....	65
5.1	Introduction	65
5.2	Review of relevant tests on the characterization of the spine	66
5.2.1	Pediatric cervical spine	66
5.2.2	Thoracic spine	70
5.2.3	Review of scaling between pediatric and adult cervical spinal responses.....	73
5.3	Methods.....	76
5.3.1	Test setup	76
5.3.2	Test specimens	78
5.3.3	Instrumentation	79
5.3.4	Quasi-linear viscoelastic formulation.....	81
5.3.5	Stiffness relationships in the human thoracic spine	82
5.4	Results	83
5.4.1	QLV model of the human thoracic spine	83
5.4.2	Comparison of the instantaneous elastic response of two thoracic FSU	85
5.4.3	Change of the instantaneous elastic response of the same thoracic FSU with age.....	86
5.5	Discussion	87
5.6	Conclusion.....	88
6	SCALING ADULT DATA TO PREDICT PEDIATRIC KINEMATICS	89
6.1	Introduction	89
6.2	Methodology	89
6.2.1	Mass scaling method.....	89

6.2.2	SAE scaling method.....	90
6.2.3	Development of an energy-based scaling method.....	91
6.3	Results	93
6.3.1	Assessment of conventional scaling methods	93
6.3.2	Assessment of energy-based scaling method. Comparison with historic scaling methods	95
6.4	Discussion.....	97
6.4.1	Assessment of historic scaling methodologies: SAE and mass scaling	97
6.4.2	Assessment of energy-based scaling method	98
6.4.3	Developmental changes in the human spine	102
6.4.4	Aspects to be considered in the prediction of pediatric trajectories	105
6.5	Conclusion.....	107
7	USING A 2D MULTIBODY MODEL TO PREDICT PEDIATRIC KINEMATICS	109
7.1	Introduction.....	109
7.2	Overview of the development of the linear time-invariant 2d model of the occupant.....	109
7.3	Using a linear time-invariant model to describe the kinematics of a restrained pediatric occupant.....	112
7.4	Using optimization to solve for unknown parameters in the system matrices.....	114
7.4.1	Optimization.....	114
7.4.2	Assessment criteria for the acceptance of a model.....	115
7.5	Hypothesis 1: A linear, time-invariant multibody model can predict the sagittal displacement of a restrained occupant at different impact speeds.....	116
7.5.1	Mass of the body regions	117
7.5.2	Length of the body regions	117
7.5.3	Moment of inertia of the body regions.....	118
7.5.4	Joint stiffness.....	119
7.5.5	Joint damping.....	123
7.5.6	Generalized forces.....	124
7.5.7	Constraints	127
7.5.8	Model predictions of the forward displacements of the head and the thoracic spine ...	127
7.5.9	Discussion	128
7.6	Hypothesis 2: a linear time-invariant multibody model can predict the sagittal displacement of a restrained 6yo in a frontal 9 km/h impact.....	129
7.6.1	Mass.....	129
7.6.2	Length.....	131
7.6.3	Moment of inertia.....	131
7.6.4	External forces.....	131
7.6.5	Position of vertebra L2 in the pediatric group.....	132
7.6.6	Joint stiffness and damping	132
7.6.7	Refinement of the model.....	134

7.6.8	Model predictions	136
7.6.9	Discussion	138
7.7	Hypothesis 3: joint parameters estimated at 9 km/h can predict the sagittal trajectories of the head and thoracic spine at 40 km/h.	140
7.7.1	Discussion	142
7.8	Hypothesis 4: forces acting on a pediatric subject at 40 km/h can be estimated if the forces acting at 9 km/h are known	145
7.8.1	Development of the method. Volunteer test at 9 km/h.	145
7.8.2	Assessment of the method using a different set of data.	149
7.8.3	Prediction of the forces acting on a restrained 6YO occupant at 40 km/h	150
7.8.4	Discussion	153
7.9	Kinematic corridors of pediatric occupants at 40 km/h	153
7.10	Discussion	155
7.10.1	Model assessment criteria	155
7.10.2	Assumptions made in the development of the pediatric model and in its application to predict the kinematics at 40 km/h	156
7.10.3	Pelvis position and pelvic rotation	160
8	PROPOSED RESPONSE TARGETS FOR THE DISPLACEMENT OF THE 6YO HEAD AND THORACIC SPINE	167
8.1	Proposed targets for the displacement of the head and first thoracic vertebra of a human 6yo in a 40 km/h frontal impact	167
8.2	Comparison between the different methods predicting the kinematics of pediatric occupants in frontal impacts	169
8.3	Implications. Use of the multibody model to predict the pediatric response in high speed impacts 170	
8.3.1	Pediatric head injuries due to direct contact against the interior of the car	170
8.3.2	Specificity of the results to a particular loading environment	171
8.3.3	Specificity of the 2D model to the experimental subjects. Extrapolation to other sizes within the same age group	172
8.3.4	How is this model to be used in the field. Applicability of the results of this dissertation	173
9	CONCLUSIONS AND CONTRIBUTIONS	174
	REFERENCES	179
A1-Appendix:	Calculation of bending moment and shear force at the ends of the fsu	186
A2-Appendix:	Derivation of equations of motion of a linear, time-invariant 2d model of the occupant	203
A3-Appendix:	Generalized coordinates time history plots	216
A4-Appendix:	Proportional damping approximation	228
A5-Appendix:	Kangaroo sled tests	232

List of Symbols and Abbreviations

Chapter 1 Introduction

C1	first cervical vertebra
C7	seventh cervical vertebra
T1	first thoracic vertebra
T12	twelfth thoracic vertebra
L1	first lumbar vertebra
L5	fifth lumbar vertebra
T3	third thoracic vertebra
T4	fourth thoracic vertebra
T9	ninth thoracic vertebra
T8	eight thoracic vertebra
ATD	Anthropomorphic Test Device
PMHS	Post Mortem Human Surrogate
6YO	6-year-old
F _x	shear force at the occipital junction
F _z	axial force at the occipital junction
M _y	flexion moment at the occipital junction
N _{TF}	neck criterion (tension-flexion)
g	acceleration of gravity (g= 9.8 ms ⁻²)
HIC	Head Injury Criterion
N _{ij}	neck criterion
km	kilometer
h	hour
yrs	years
kg	kilogram
cm	centimeter
AIS	abbreviated injury scale
3-pt-belt	three point belt
IARV	Injury Assessment Reference Value
PT+FL	pretensioned, force-limited belt
ST	standard belt

Chapter 2 Summary of the methodological approach and the data sources used in this dissertation

SAE	Society of Automotive Engineers
$\underline{\underline{M}}$	mass matrix
$\underline{\underline{C}}$	damping matrix
$\underline{\underline{K}}$	stiffness matrix
$\underline{\underline{\dot{q}}}$	generalized accelerations
$\underline{\dot{q}}$	generalized velocities
\underline{q}	generalized coordinates
\underline{Q}	generalized forces
m	mass
I	moment of inertia
k	torsional stiffness
c	torsional damping
2D	two dimensional
MC	motion capture
f ₁	function

f_2 function

Chapter 3 Volunteer experiments

BMI body mass index
 3D three dimensional
 PED pediatric subject
 M male
 NA Not applicable
 EAM External Auditory Meatus
 AD adult
 p p value
 mm millimeter

Chapter 4 Post Mortem Human Surrogates sled tests

ms millisecond
 DOF degrees of freedom
 T_M^B transformation matrix between bone coordinate system and array of markers
 T_G^M transformation matrix between array of markers and global coordinate system
 T_G^B transformation matrix between bone coordinate system and global coordinate system
 CT computerized tomography
 $L(t)$ distance between two consecutive spinal segments at time t
 L_0 distance between two consecutive spinal segments at time t_0
 t_0 initiation of deceleration
 t_{\max} time of maximum forward head excursion
 BCS buck coordinate system
 t time
 LCS local coordinate system

Chapter 5 Thoracic spine characterization

N Newton
 Nm Newton-meter
 FSU functional spinal unit
 IHA instantaneous helical axis
 K_F tensile stiffness
 K_B bending stiffness
 Hz hertz
 CGS global coordinate system
 QLV quasi linear viscoelastic
 D1, ..., D5 growing amplitudes in QLV tests
 deg degrees
 $\theta_{superior}$ angle rotated at the superior end
 $\theta_{inferior}$ angle rotated at the inferior end
 α angle rotated by specimen
 CFC channel frequency class
 $M[t]$ moment generated at the specimen
 $G[t]$ generalized relaxation function
 β_i time constants
 G_i associated weights to decreasing exponentials
 G_∞ steady state response
 $M_e[\alpha]$ instantaneous elastic response
 IER instantaneous elastic response

$1/\tau_1$ relationship between the IER of the upper and the middle thoracic section in the FSU experiments

Chapter 6 Scaling adult data to predict pediatric kinematics

λ_L	length scaling factor
λ_x	length scaling factor in the x direction
λ_y	length scaling factor in the y direction
λ_z	length scaling factor in the z direction
λ_ρ	mass density scaling factor
λ_E	Young's modulus scaling factor
λ_m	mass scaling factor
λ_t	time scaling factor
V_F	final speed at position max_s
V_0	initial speed at position 0
s	path followed by the point mass
F	forces acting on the point mass
m_{ped}	mass of pediatric occupant
m_{ad}	mass of adult occupant
F_{ped}	external force acting on pediatric occupant
F_{ad}	external force acting on adult occupant
φ	trajectory angle to apportion the path into x and z components

Chapter 7 Using a 2D multibody model to predict pediatric kinematics

FUSB	upper shoulder belt force (T1)
FMSB	middle shoulder belt force (T8)
FLSB	lower shoulder belt force (L2)
FLapB	lap belt force (pelvis)
FS	seat reaction force
FKB	knee bolster reaction force
δr_i	virtual displacements associated to the generalized coordinates
l_i	length of i-th body region
SSE	sum of square error
CH	head and cervical body region
UT	upper torso body region
LT	lower torso body region
L	lumbar body region
UL	upper leg body region
LL	lower leg body region
a	minor axis of an ellipse
b	major axis of an ellipse
k_{T8}	model stiffness at T8 joint
k_{T1}	model stiffness at T1 joint
k_{L2}	model stiffness at L2 joint
f_{T5-T8}	quasi-static flexibility coefficient of T5-T8 FSU
$f_{T11-T12}$	quasi-static flexibility coefficient of T11-T12 FSU
k_{T5-T8}	quasi-static stiffness coefficient of T5-T8 FSU
$k_{T11-T12}$	quasi-static stiffness coefficient of T11-T12 FSU
τ_2	relationship between model stiffness at L2 and model stiffness at T8
LPangle	lab belt angle with respect to the horizontal
USangle	upper shoulder belt angle with respect to the horizontal
LSangle	lower shoulder belt angle with respect to the horizontal

R_i	ratio of model stiffness coefficients at the i-th joint between 9 km/h and 40 km/h
S_i	ratio of model damping coefficients at the i-th joint between 9 km/h and 40 km/h
m'	average mass of the two body regions connected by a joint
γ	unknown dimensional constant that relates mass to damping
δ	unknown dimensional constant that relates stiffness to damping
m_e	effective mass of the link
R_{cs}	radius of the cross-sectional area of the corresponding body region
α	unknown dimensional magnitude relating stiffness to effective mass, length and cross sectional area
β	unknown dimensional magnitude relating stiffness to effective mass, length and cross sectional area
E	Young's Modulus of a simple beam in flexion
M'	pure bending moment applied to a beam
$\left(\frac{dy}{dx}\right)$	angle rotated by a beam section in flexion
I	moment of inertia of the beam section
R_{cs}	radio of the cross sectional area of the beam
MPa	mega Pascal
γ_1	constant relating age to Young's modulus of soft tissue (ligament)
BMD	bone mineral density
ϑ	constant relating BMD to Young's modulus of bone tissue
γ_2	constant relating age to Young's modulus of both soft and bone tissue
α_1	effective elasticity modulus for the spine
α_2	constant relating the effective elasticity modulus of the spine to the effective elasticity modulus of the pelvis
α_3	constant relating the effective elasticity modulus of the spine to the effective elasticity modulus of the knee and ankle
Var_{PED}	variability observed in the magnitude of external forces acting on subject PED
PSIS	posterior superior iliac spine

Chapter 8 Proposed response targets for the displacement of the 6yo head and thoracic spine

Chapter 9 Conclusions and contributions

List of Figures

Figure 1.1 Lateral view of the spine (adapted from Gray (1918)).	3
Figure 1.2 Geometry of a typical lumbar vertebra. Upper: superior view. Lower: lateral view, mid-sagittal section (adapted from Gray (1918)).	3
Figure 1.3 Lateral view of a mid-sagittal plane cross-section of the vertebral column showing the intervertebral discs and the spinal ligaments (adapted from Gray (1918)).	5
Figure 1.4 Lateral view of a section of the spine illustrating the articulation of adjacent vertebrae at the facet joints (adapted from Gray (1918)).	6
Figure 1.5 Schematic of the parts of the Hybrid III 50th and detail of the construction of the rigid thoracic spine.	8
Figure 1.6 Comparison of the sagittal trajectories of the head, spine and pelvis between the Hybrid III 50th and a PMHS in a 40km/h frontal impact (Lopez-Valdes et al., 2010b).	9
Figure 1.7 Comparison of peak neck loads (axial and shear force, flexion moment) between the Hybrid III 50th and a PMHS in a 9 km/h (left) and in a 40km/h (right) frontal impact (Lopez-Valdes et al., 2010b).	10
Figure 1.8 Left: Test rig used in the FMVSS 213 (source: www.iihs.com). Right: detail of the construction of the Hybrid III 6YO thoracic spine with the thoracic box outlined in yellow.	12
Figure 1.9 Overall view of pediatric PMHS test setup (Kallieris et al., 1976).	14
Figure 1.10 Spinal contours of the pediatric PMHS (left) and Hybrid III 10 YO (right). The solid black line corresponds to the approximate trajectory of T1 in both plots. Adapted from Ash et al. (2009).	16
Figure 1.11 Overall view of test setup (left). Comparison between head and spine positions at 80 ms between the pediatric cadaver and the dummy. Adapted from Wismans et al. (1979).	17
Figure 1.12 XZ trajectories of the Hybrid III 6YO and the scaled small adult PMHS in a 48 km/h frontal impact (PT+FL belt).	19
Figure 1.13 Comparison between the spinal deformation of the Hybrid III 6YO and the small adult PMHS at 140 ms in a 48 km/h impact (ST belt).	19
Figure 2.1 Experimental data combined in this dissertation research.	25
Figure 2.2 Schematic showing the data sources and processes involved in the assessment of currently used scaling techniques (aim 1).	28
Figure 2.3 Schematic showing the data sources and steps (validation and prediction) involved in the development and use of the scaling method based on conservation of energy (aim 2).	29
Figure 3.1 Low-speed acceleration sled. Pneumatic system and sled buck.	33
Figure 3.2 Phases of the acceleration pulse used in the volunteer tests.	33
Figure 3.3 Frontal and oblique view of a volunteer showing the position of the reflective markers on the subject.	36
Figure 3.4 Normalized anterior excursion (relative to initial position) for the head by age group.	37
Figure 3.5 Normalized anterior excursion (relative to initial position) for the spine by age group.	37
Figure 3.6 Normalized vertical excursion (relative to initial position) for the head by age group.	38
Figure 3.7 Normalized vertical excursion (relative to initial position) for the spine by age group.	38
Figure 3.8 Comparison of the XZ trajectory of the head-top marker between pediatric volunteers (dashed line) and adult volunteers (solid line).	38

Figure 3.9 Time history of the angle between a segment connecting C4 and T1 and a segment connecting T1 and T4 by age.	39
Figure 3.10 Time history of the angle between a segment connecting C4 and T1 and a segment connecting T1 and T4 by age.	39
Figure 3.11 Comparison of the normalized average displacements (solid lines) and displacement corridors (blue shaded areas) in the sagittal plane between the pediatric (right) and adult (left) volunteers, 9 km/h.	40
Figure 4.1 Comparison between the volunteer pulse (orange corridor) and the low-speed pulses of the PMHS tests.	45
Figure 4.2 PMHS pulse at high-speed.	45
Figure 4.3 Frontal and side view of a PMHS showing the position of the reflective markers on the subject. Note that the absence of knee bolster at low-speed (left).	47
Figure 4.4 Schematic showing the transformations between coordinate systems to report the position with respect to the buck coordinate system (BCS).	48
Figure 4.5 Definition of the local coordinate systems (LCS) attached to each considered bony structure.	49
Figure 4.6 Trajectories (solid red lines) of the head, T1, T8, L2 and pelvis at 9 km/h (left) and 40 km/h (right) in the XZ sagittal plane with respect to the BCS. Dashed blue lines connect the position of the anatomical structures every 50 ms.	52
Figure 4.7 Normalized average displacements (solid blue line) and displacement corridors (shaded area) of the PMHS head T1, T8 and pelvis at 9 km/h. Dots indicate the position of the relevant structure every 50 ms and at the maximum head excursion.	54
Figure 4.8 Normalized average displacements (solid blue line) and displacement corridors (shaded area) of the PMHS head, T1, T8 and pelvis at 40 km/h. Dots indicate the position of the relevant structure every 50 ms and at the maximum head excursion.	55
Figure 4.9 Trajectories of the PMHS head, spine and pelvis in the XY plane of the BCS at 40 km/h (* indicates the final position of the structure).	57
Figure 4.10. Elongation of spinal segments (head to T1, T1 to T8, T8 to L2 and L2 to pelvis) at 9 km/h (left column) and 40 km/h (right column)	59
Figure 4.11 From top to bottom, comparison of the head, T1, T8 and pelvis sagittal trajectories between adult volunteers and PMHS at 9 km/h.	61
Figure 5.1 Local coordinate system in Panjabi et al. (1976)	70
Figure 5.2 Schematic showing the test setup, instrumentation and positioning of the specimen	77
Figure 5.3 CT images showing the position of the marker on the FSU (specimen M320-T1T5).	79
Figure 5.4 Schematic of the FSU showing the calculation of the relative angle between the two distal vertebrae.	80
Figure 5.5 Comparison between the moment predicted (Mest, red) and the calculated average moment (Mave, blue) of the upper thoracic section of pediatric specimen F470.	83
Figure 5.6 Comparison between the moment predicted (Mest, red) and the calculated average moment (Mave, blue) of the middle thoracic section of pediatric specimen F470.	84
Figure 5.7 Comparison between the instantaneous elastic response between the T2T4 (red) and T7T9 (blue) thoracic sections for specimens F470 (7YO, top) and M485 (15YO, bottom).	85
Figure 5.8 Prediction of the upper thoracic IER given by the calculated proportionality factor applied to the middle thoracic IER.	86

Figure 5.9 Comparison between the instantaneous elastic responses of the middle thoracic section across subjects	86
Figure 6.1 Schematic showing the parameters needed to apportion the length of the path at each time step (ds) between the X and Z axes if the preceding point and the angle formed by the tangent to the arc and the horizontal is known. See Equation 6.6	93
Figure 6.2 Comparison between the measured pediatric average displacements (solid red line) and corridors (blue shaded area) and the predicted pediatric response given by the SAE (green dotted line) and the mass scaling methods (green crossed line) at 9 km/h. From top to bottom: head, T1, T8 and pelvis.	94
Figure 6.3 Comparison between the measured pediatric average displacements (solid red line) and corridors (blue shaded area), the conventional scaling methods (SAE and mass scaling) and the energy-based scaling method (blue solid line). Buck coordinate system. From top to bottom: head, T1, T8 and pelvis.	96
Figure 6.4 Comparison of the trajectories of T1 and T8 between pediatric and adult volunteers in the sagittal plane at 9 km/h. Reproduced from Figure 3.11.	101
Figure 6.5 Torso anatomy of a newborn (left) and an adult (right). Note the changes in organ volume and the associated changes in mass distribution of the trunk between the two subjects (Kent et al., 2009).	106
Figure 6.6 Relationship between percent of body weight and percent of body height in a 50th percentile adult and in a 6YO. Applicable only to the torso and head of the subjects.	106
Figure 7.1 Definition of the generalized coordinates and points of application of external forces.	112
Figure 7.2 Schematic of a beam subjected to bending.	119
Figure 7.3 Correlation between age and elastic modulus of ligaments as provided by Iida et al. (2002).	120
Figure 7.4 Linear relationship between the elasticity modulus and the bone mineral density of bone tissue as given by Diamant et al. (2005).	121
Figure 7.5 Mean total body BMD of adults aged 20 years and older by age, sex. Non-hispanic white people. Adapted from (Looker et al. (2009).	122
Figure 7.6 Relationship between the lower and upper shoulder belt forces obtained from the combination of data from 8 PMHS tests in a similar test setup.	125
Figure 7.7 Predicted pediatric trajectory (blue solid line) and corridor (purple shaded area) as given by modified model B2.2 and comparison with observed experimental data from pediatric volunteers at 9 km/h (red solid line: average 6YO response; blue shaded area: corridor). (Top: head; Center: T1; Bottom: T8).	137
Figure 7.8 Kangaroo sagittal displacements. Comparison between the XZ trajectory predicted by the model (red) and the actual trajectory measured (blue) at 9 km/h (left) and at 40 km/h (right). Top: head; Center: T1; Bottom: T8. Note the change of scale in the axes between the two speeds.	141
Figure 7.9 Displacement of the pelvis of the kangaroo in the sagittal plane at 40 km/h.	145
Figure 7.10 Shoulder belt forces per group age as reported by (Arbogast et al., 2009).	146
Figure 7.11 Seat normal forces per group age as reported by (Arbogast et al., 2009).	146
Figure 7.12 Volunteer shoulder belt forces. Comparison between the scaled adult average force (dashed dark green line) and the pediatric average force (solid light green line). Solid red lines are the adult individual belt forces and solid blue lines are the pediatric individual belt forces. Solid dark green line is the average adult belt force.	147
Figure 7.13 Comparison between predicted pediatric shoulder belt forces (green) and measured pediatric forces (red). Upper shoulder belt force (left), lower shoulder belt force (right).	148

Figure 7.14 Comparison between predicted pediatric lap belt force (green) and measured force (red).	148
Figure 7.15 Upper shoulder force measured at 29 km/h (right) and at 48 km/h (left). H3 50th percentile (red) and AF 5th percentile (blue). Data taken from Forman et al. (2008).	150
Figure 7.16 Comparison between the scaled upper shoulder force of the Hybrid III 50th (dashed-red line) and the upper shoulder belt force of the AM 5th (solid blue line).	150
Figure 7.17 Prediction of pediatric upper shoulder belt force at 40 km/h: FUSBx (left) and FUSBY (right).	151
Figure 7.18 Prediction of pediatric middle shoulder belt force at 40 km/h: FMSBx (left) and FMSBY (right).	151
Figure 7.19 Prediction of pediatric lower shoulder belt force at 40 km/h: FLSBx (left) and FLSBY (right).	151
Figure 7.20 Prediction of pediatric lap belt force at 40 km/h: FLBx (left) and FLBY (right).	152
Figure 7.21 Prediction of pediatric seat force at 40 km/h: FSeatx (left) and FSeaty (right).	152
Figure 7.22 Prediction of pediatric knee bolster force at 40 km/h: FKBU (left) and FKBV (right).	152
Figure 7.23 Prediction of the average sagittal trajectories (blue solid line) and corridors (purple shaded area) of the pediatric head, T1 and T8 at 40 km/h. Top to bottom: head, T1 and T8.	154
Figure 7.24 Schematic showing the typical seating position of a pediatric occupant and selected pelvic anatomical landmarks. Adapted from (Reed et al. (2006).	160
Figure 7.25 Comparison between the sagittal trajectory of the PSIS of the PMHS test (blue solid line) and its associated corridor with the one of the ilioacromion of the adult volunteers (green solid line) and its associated corridor.	161
Figure 7.26 Comparison between the average sagittal trajectory (blue solid line) (and associated corridor, purple-shaded area) of the head of the 6YO at 9 km/h, when the pelvis is assumed to move 30%, 60% and 100% of the adult pelvic range of motion (top to bottom).	163
Figure 7.27 Comparison between the average sagittal trajectory (blue solid line) (and associated corridor, purple-shaded area) of the T1 vertebra of the 6YO at 9 km/h, when the pelvis is assumed to move 30%, 60% and 100% of the adult pelvic range of motion (top to bottom).	164
Figure 7.28 Comparison between the average sagittal trajectory (blue solid line) (and associated corridor, purple-shaded area) of the T8 of the 6YO at 9 km/h, when the pelvis is assumed to move 30%, 60% and 100% of the adult pelvic range of motion (top to bottom).	165
Figure 8.1 Proposed XZ average displacement (blue solid line) and associated corridors (blue-shaded area) for the head (top) and T1 vertebra (bottom) of a human 6YO in a 40 km/h frontal impact.	168
Figure A1.1 Angle vs. Time response comparison between one pediatric and one adult specimen showing the similar angular rate applied.	186
Figure A1.2 Preconditioning of pediatric specimen (F470 T7-T9).	187
Figure A1.3 Preconditioning of adult specimen (M320 T7-T9).	187
Figure A1.4 Free body diagram of the fixture with the specimen.	189
Figure A1.5 Free body diagram of the fixture with the specimen.	190
Figure A1.6 Schematic showing the bending moments MO_i at the center of the vertebrae and the parameters involved in the calculations.	191
Figure A1.7 Comparison between the moment predicted (M_{est} , red) and the calculated average moment (M_{ave} , blue) of the upper thoracic section of pediatric specimen F470.	194
Figure A1.8 Comparison between the moment predicted (M_{est} , red) and the calculated average moment (M_{ave} , blue) of the middle thoracic section of pediatric specimen F470.	194

Figure A1.9 Comparison between the moment predicted (Mest, red) and the calculated average moment (Mave, blue) of the upper thoracic section of pediatric specimen M485.	195
Figure A1.10 Comparison between the moment predicted (Mest, red) and the calculated average moment (Mave, blue) of the middle thoracic section of pediatric specimen M485.	196
Figure A1.11 Time-history plot of the calculated average moment (Mave) of the upper thoracic section of adult specimen M319.	197
Figure A1.12 Comparison between the moment predicted by the QLV model and the calculated average moment (Mave) of the middle thoracic section of adult specimen M319.	198
Figure A1.13 Time history of forces F_y measured during the preconditioning of M320-T2T4.	199
Figure A1.14 Detail of preconditioning forces F_y during the first 10 s. Specimen M320-T2T4.	199
Figure A1.15 Comparison between the moment predicted by the QLV model and the calculated average moment (Mave) of the middle thoracic section of adult specimen M320.	200
Figure A1.16 Schematic showing the dimensions measured at the distal and proximal vertebra of each specimen.	201
Figure A3.1 PED2 time history of generalized coordinates.	216
Figure A3.2 PED2 time history of generalized velocities.	217
Figure A3.3 PED2 time history of generalized accelerations.	218
Figure A3.4 PED2 time history of generalized forces.	219
Figure A3.5 Time history of generalized coordinates calculated for a PMHS at low speed.	220
Figure A3.6 Time history of generalized velocities calculated for a PMHS at low speed.	221
Figure A3.7 Time history of generalized accelerations calculated for a PMHS at low speed.	222
Figure A3.8 Time history of generalized coordinates calculated for a PMHS at low speed.	223
Figure A3.9 Time history of generalized coordinates calculated for a PMHS at high speed.	224
Figure A3.10 Time history of generalized velocities calculated for a PMHS at high speed.	225
Figure A3.11 Time history of generalized accelerations calculated for a PMHS at high speed.	226
Figure A3.12 Time history of generalized forces calculated for a PMHS at high speed.	227
Figure A4.1 Generalized Maxwell model proposed by (Semblat, 1997) and attenuation curve.	229
Figure A4.2 Comparison between the Rayleigh damping model (circles) and the generalized Maxwell model (solid line) in a one-dimensional wave propagation model for different values of the damping coefficient ((a) $\xi=5\%$; (b) $\xi=13\%$; (c) $\xi=26\%$; (d) $\xi=52\%$).	231
Figure A5.1 Kangaroo deceleration at low speed.	233
Figure A5.2 Kangaroo deceleration at high speed.	233
Figure A5.3 General setup of the kangaroo sled tests.	235
Figure A5.4 Marker plates along the spine and the pelvis of the kangaroo.	235
Figure A5.5 Displacements of the kangaroo at 9 km/h.	236
Figure A5.6 Displacements of the kangaroo at 40 km/h.	237
Figure A5.7 Comparison between PMHS and kangaroo at the 9km/s impact.	238
Figure A5.8 Comparison between PMHS and kangaroo at the start, intermediate position and final position of the 40 km/s impact.	238

List of Tables

Table 1.1 Maximum values of injury criteria as specified in FMVSS 213.	13
Table 1.2 Summary of pediatric PMHS sled tests in the literature adapted from Kent et al. (2009).....	15
Table 1.3 Summary of biofidelity parameters in the comparison between pediatric PMHS and pediatric ATD in the literature. (✓: data included in the paper; X: data not available in the paper).....	20
Table 3.1 Anthropometry of volunteers and reference value for a 50th percentile 6-year-old and for a 50th percentile adult male (Arbogast et al., 2009).....	34
Table 3.2 Maximum change in volunteer head angle (in degrees).	39
Table 4.1 PMHS anthropometry and characteristics.	46
Table 4.2 Peak forward displacement of PMHS head, vertebrae and pelvis. 9 km/h. X(mm), time (ms).	50
Table 4.3 Peak forward displacement of PMHS head, vertebrae and pelvis. 40 km/h. X(mm), time (ms).	51
Table 4.4 Peak lateral displacement of PMHS head, vertebrae and pelvis. 9 km/h. Y(mm), time (ms). 56	
Table 4.5 Peak lateral displacement of PMHS head, vertebrae and pelvis. 40 km/h. Y(mm), time (ms).	56
Table 5.1 Summary of studies on the biomechanics of the pediatric cervical spine	67
Table 5.2 Summary of studies on the biomechanics of the immature cervical spine using animal models.	68
Table 5.3 Summary of studies on the biomechanics of the adult thoracic spine	71
Table 5.4 Comparison of average intervertebral joint flexibility coefficients (inverse of stiffness coefficients) for several thoracic segments (deg/Nm).	73
Table 5.5 Summary of scaling factors for the response of the cervical spine in tension.	74
Table 5.6 Summary of scaling factors for the response of the cervical spine in compression.	75
Table 5.7 Summary of scaling factors for the response of the cervical spine in flexion/extension.	76
Table 5.8 Test matrix.....	77
Table 5.9 General characteristics of the PMHS.....	78
Table 5.10 Coefficient values of the QLV model of the human thoracic spine.	84
Table 5.11 Relationships between the instantaneous elastic responses of the tested FSU.	85
Table 6.1 Scaling factors between a 50th percentile adult and a 50th percentile 6YO.....	90
Table 6.2 Summary of the forward peak displacement in the buck coordinate system (X) of the pediatric subjects and the predicted scaled displacements.	95
Table 6.3 Summary of the forward peak displacement in the buck coordinate system (X) of the pediatric subjects and the predicted scaled displacements (mm).....	97
Table 6.4 Comparison between the ratios of the lengths of the path of the selected anatomical structures.	100
Table 6.5 Comparison between the ratios of the lengths of the path of the selected anatomical structures.	101
Table 7.1 Parameters included in the 2D model.....	116

Table 7.2 Equivalence between the body regions used in the NASA study and the model body regions.	117
Table 7.3 Body region mass of PMHS (kg).	117
Table 7.4 Body region length of PMHS1 (m).	118
Table 7.5 Body region moment of inertia of PMHS (kg m ²).	118
Table 7.6 Estimated BMD for the PMHS considered in this dissertation.	122
Table 7.7 Relationships between the stiffness of different vertebral levels found in the literature.	123
Table 7.8 Summary of the external forces applied to the occupant.	124
Table 7.9 Comparison between the maximum X displacement measured in the tests and the predictions given by Model B2.1. Low speed tests. Results shown as: absolute displacement (relative error).....	127
Table 7.10 Comparison between the maximum X displacement measured in the tests and the predictions given by Model B2.1. High-speed tests. Results shown as: absolute displacement (relative error).....	128
Table 7.11 Comparison between the average error in the prediction of the peak forward excursions of the head, T1 and T8.	128
Table 7.12 Body region mass of a 6YO as reported by (Irwin and Mertz, 1997) and distribution of mass for the 6YO model (kg).....	130
Table 7.13 Body region mass of pediatric volunteers (kg).	130
Table 7.14 Body region length of pediatric occupants (m).	131
Table 7.15 Body region moment of inertia of pediatric occupants (kg m ²).	131
Table 7.16 Summary of available sensor data within different subject groups.	132
Table 7.17 Stiffness and damping coefficients of the joints of pediatric occupants in model B2.2.	133
Table 7.18 Stiffness and damping coefficients of the joints of pediatric occupants in model B2.2.	135
Table 7.19 Mass of the body regions considered unknown in the modified model B2.2.	136
Table 7.20 Comparison between the maximum X displacement measured in the tests and the predictions given by model B2.2. Results shown as: absolute displacement (relative error).....	136
Table 7.21 Comparison of the optimized stiffness value of the T8 joint between PMHS (adult) and pediatric occupants.	139
Table 7.22 Estimation of joint parameters for the kangaroo model.	140
Table 7.23 Comparison of experimental-observed and model-estimated kangaroo peak forward displacements (X) at 9 km/h and at 40 km/h.	142
Table 7.24 Scaling factors obtained at low speed. Subject variability for each of the forces applied to the occupant.....	149
Table 7.25 Predicted peak excursions of a 6YO occupant at 40 km/h.	155
Table 8.1 Error in the prediction of the peak forward excursion of an average 6-year-old child's head and thoracic spine in a 9-km/h frontal impact using the four methods analyzed in this dissertation.....	169
Table A1.1 Bounds used in the optimization.	192
Table A1.2 Coefficient values of the QLV model of the human thoracic spine.....	193
Table A1.3 Dimensions (mm) of the proximal vertebra of each T7-T9 specimen as defined in Figure A1.16.....	201
Table A1.4 Dimensions (mm) of the distal vertebra of each T7-T9 specimen as defined in Figure A1.16.....	201

Table A5.1 Kangaroo test matrix.	233
Table A5.2 Kangaroo characteristics.	234
Table A5.3 Body region mass of kangaroo (kg).....	239
Table A5.4 Body region length of kangaroo (m).	239
Table A5.5 Body region moment of inertia of kangaroo (kg m ²).	239

1 INTRODUCTION

1.1 MOTIVATION

In 2004, road traffic injuries accounted for approximately 262,000 deaths among children aged 0-19 years, according to the World Health Organization (WHO). This figure represents almost 30% of all injury related pediatric deaths and 2% of all pediatric deaths. In middle-income and high-income countries, it is estimated that, while 33% of all child deaths are pedestrians, 65% are distributed between car occupants and motorcycle or bicycle riders. Globally, road traffic injuries are the leading cause of death among 15-19 year olds and the second leading cause among 5-14 year-olds (Peden et al., 2008).

An accurate estimation of the burden of pediatric road traffic related morbidity is currently not possible, especially in low and middle-income countries. WHO estimates about 10 million children injured or disabled each year as a result of road traffic crashes worldwide. A number of studies have tried to describe the frequency, type and severity of pediatric injuries. Globally, head and limbs are the most common injured body regions among children (Peden et al., 2008). A study combining hospital discharge data from 10 European countries showed that traumatic brain injuries and fractures to the limbs, followed by injuries to the abdominal and thoracic organs, were the most frequent types of injuries sustained by children younger than 12 years old (Sethi et al., 2008; Lopez-Valdes et al., 2008). In the United States, traumatic brain and skull injuries are the most common severe injuries sustained by pediatric occupants in road traffic crashes, regardless of age, crash direction and restraint type (Arbogast et al., 2002). Head injuries are responsible for one third of all pediatric injury deaths (Adekoya et al., 2002; Thompson and Irby, 2003).

Two mechanisms can lead to a head injury: a direct contact of the head with any of the hard surfaces of the interior of the vehicle or the relative motion of the brain within the skull causing shear, tensile and compressive strain within the head (Gennarelli, 1993). Regardless of the actual injury mechanism, the prevention and mitigation of head injuries requires an accurate knowledge of the position and attitude of the head, which is dictated by the motion of the spine. The kinematics of the spine also determines the interaction between the seatbelt and the torso of the occupant (Alem et al., 1978). Thus, it is not possible to

predict the kinematics of the head neither to assess the performance of a pediatric restraint systems that can contribute to mitigate head injury risk without a correct understanding of the spinal motion.

1.2 BACKGROUND

1.2.1 Anatomy of the human spine

The spine is the main vertical load-bearing structure of the neck, thorax, and abdomen. It provides protection for the spinal cord and provides a framework where-by other components of the musculo-skeletal system are connected. The spine is comprised of 24 individual vertebra and nine fused vertebrae (Figure 1.1). These vertebrae are connected to each other by intervertebral discs, spinal ligaments, and muscles. The spine is divided into five distinct regions. The cervical spine is located at the superior end of the spine, and is comprised of seven vertebrae (beginning superiorly with the 1st cervical vertebra, C1, and ending with the 7th cervical vertebra, C7). The thoracic region is just inferior to the cervical spine, is comprised of twelve vertebrae (T1-T12), and articulates bilaterally with the ribcage. The lumbar region is inferior to the thoracic spine and is composed of five vertebrae (L1-L5). Finally, the sacrum and coccyx are inferior to the lumbar spine, and form the posterior border of the pelvic bowl. These are composed of nine fused vertebrae, 5 in the sacrum and 4 small vertebrae in the coccyx.

Although the characteristics of one spinal region are distinct from the others, some common elements are shared by all regions. This section first describes the general anatomy of the vertebrae, discs, and ligaments, and then discusses the characteristics that are specific to the thoracic region which is the main focus of this dissertation.

1.2.1.1 Vertebrae

The vertebrae are irregular bones consisting of an anterior body and a posterior arch (Figure 1.2). The anterior body is a rough cylinder composed primarily of trabecular bone, surrounded by a thin layer of cortical bone. The posterior arch is composed of two pedicles connected to the postero-lateral surface of the vertebral body. The arch is then completed by the lamina, connecting the posterior termini of the pedicles. The hole bounded by the anterior surface of the vertebral arch and the posterior surface of the vertebral

body is called the vertebral foramen, commonly referred to as the spinal canal. Several processes branch off of the posterior vertebral arch. First, the spinous process extends posteriorly off of the laminae in the mid-sagittal plane. These serve as attachment points for several ligaments and muscles of the spine. Second, transverse processes extend laterally off of the junctions between the laminae and the pedicles. These also provide locations for ligamentous and muscular attachment, and in the thoracic spine they provide the location for the articular joints that connect the spine to the ribs.

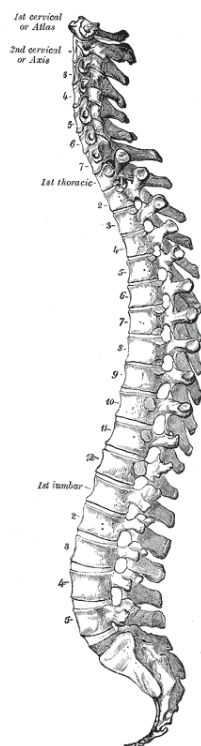


Figure 1.1 Lateral view of the spine (adapted from Gray (1918)).

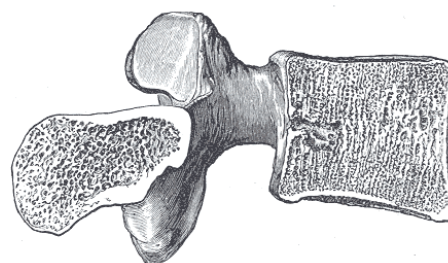
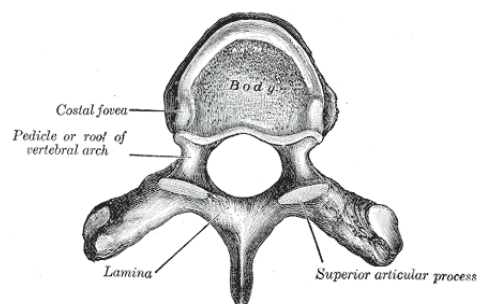


Figure 1.2 Geometry of a typical lumbar vertebra. Upper: superior view. Lower: lateral view, mid-sagittal section (adapted from Gray (1918)).

Lastly, articular processes extend superiorly and inferiorly from the vertebral arches, approximately at the junctions between the laminae and the pedicles. These processes provide locations for the articular facets that form joints with the adjacent vertebrae (Figure 1.2). The superior articular facets are located on the superior articular processes; the inferior articular facets are located on the inferior articular processes. In general, the superior articular facets face postero-superiorly and the inferior articular facets face antero-inferiorly, although the exact orientations of these facets change between spinal regions. Between each

adjacent vertebra pair (except between the first and second cervical vertebrae) synovial joints encapsulated by capsular ligaments connect the inferior articular facets of the superior vertebra to the superior articular facets of the inferior vertebra. The orientation of the facet joints is biomechanically important since they share the load-bearing function of the spine with the vertebral bodies. There exist gaps between the articular processes and bodies of adjacent vertebrae form the intervertebral foramens, providing conduits for nerve roots and blood vessels extending into the spinal canal.

1.2.1.2 Discs

With the exception of the junction between the first and second vertebrae, the bodies of adjacent vertebrae are joined by inter-vertebral discs. These discs consist of an inner gelatinous material (the nucleus pulposus) surrounded by concentric lamellae of fibrocartilage (the annulus fibrosus). The nucleus pulposus is located in the center of the disc in the cervical and thoracic regions, and at the union between the posterior third and the anterior two-thirds of the disc in the lumbar spine. The annulus fibrosus is formed by successive layers of interlaced fibrous tissue fixed to the platforms of the vertebral bodies. In general, the height of the discs increases moving inferiorly down the spine. These discs join adjacent vertebrae, bear a portion of the compressive loads transmitted down the spinal column and together with the capsular ligaments provide the necessary compliance for the motion of the spine.

1.2.1.3 Ligaments

Ligaments connect nearly every exterior face of adjacent vertebrae, providing stability to the vertebral column. Some of these ligaments solely connect adjacent vertebrae, but others extend throughout portions or the entire length of the vertebral column. The anterior longitudinal and posterior longitudinal ligaments both extend along the length of the column, running along the anterior surfaces and posterior surfaces of the vertebral bodies (Figure 1.3). Similarly, the ligamentum flavum runs along the posterior surface of the vertebral arch, connecting adjacent laminae. The supraspinous ligament also extends along the length of the column, connecting the posterior surfaces of the spinous processes. The interspinous ligaments connect adjacent vertebrae between the superior and inferior surfaces of the spinous processes. Similarly, the intertransverse ligaments connect adjacent transverse processes. Finally, capsular ligaments connect adjacent articular processes, forming the capsules of the intervertebral facet joints.

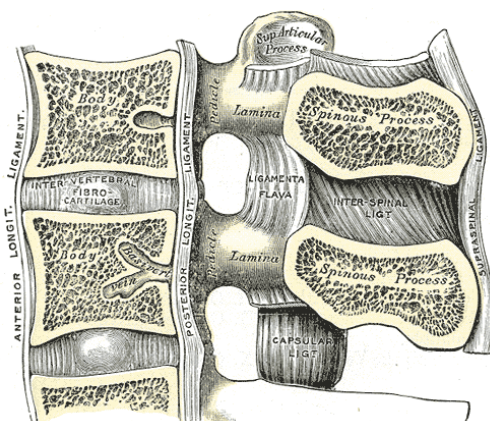


Figure 1.3 Lateral view of a mid-sagittal plane cross-section of the vertebral column showing the intervertebral discs and the spinal ligaments (adapted from Gray (1918)).

1.2.1.4 Spinal Cord

In addition to providing stability to the body, one of the major functions of the spine is to provide a conduit for the passage and protection of the spinal cord. The spinal cord is the primary neural pathway through which the brain communicates with the rest of the body. The spinal cord begins as an extension of the medulla oblongata (the caudal portion of the brainstem), and extends down the spine through the spinal canal. It is protected by the bones and ligaments of the spine, and also by the layers of the spinal meninges (the pia, arachnoid, and dura maters). The cord is roughly of the shape of an elliptical cylinder, and is composed of both white and gray matter. The cord itself extends only to the superior-inferior location of the second lumbar vertebra. The cord communicates with inferior portions of the body via a nerve-root bundle termed the cauda equine (named for its resemblance to a horse's tail).

1.2.2 Thoracic Spine

The thoracic spine is located posteriorly in the chest and consists of 12 vertebrae. Because the thoracic spine provides posterior support to the rib cage, these vertebrae exhibit lateral facets that articulate with the ribs. The thoracic spine exhibits a kyphotic curvature (convexity in the antero-posterior direction) (Figure 1.4). The anteroposterior diameter of the vertebral bodies increases gradually from T1 to T12, whereas the transverse width decreases from T1 to T3 and then increases progressively down to T12. Anterior vertebral body height is slightly smaller than posterior height, which contributes partially to thoracic kyphosis.

The T1-T4 vertebrae share some features of the cervical vertebrae. T1 has a long horizontal spinous process typical of a cervical vertebra. The T9-T12 vertebrae, on the other hand, share features of the lumbar vertebrae. Most of the transition between the thoracic and lumbar spine, however, happens just at T12.

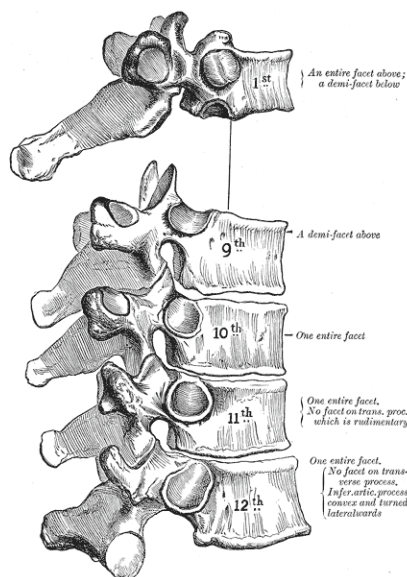


Figure 1.4 Lateral view of a section of the spine illustrating the articulation of adjacent vertebrae at the facet joints (adapted from Gray (1918)).

In the thoracic spine, laminae are broad and heavily overlapped. The size of the spinal canal varies along the thoracic spine, but its narrowest segment happens to be in this section of the vertebral column.

There is a change in the angle of the articulation at the facet joints between the upper thoracic vertebrae (they are oriented 15 to 20 degrees to the vertical plane facing posterolaterally) and the inferior ones (oriented almost vertically and facing anterolaterally). The shape of the articular processes of the thoracic vertebrae permits rotation and lateral flexion of the vertebral column in this region.

The articulation with the rib cage and the overlapping spinous processes limits flexion and extension in the thoracic spine. Each rib articulates with the vertebrae at two sites and the orientation of the joints also changes along the thoracic spine (Figure 1.4). The rib heads articulate with the vertebrae at the disc (costovertebral joint), and the rib tubercles articulate with the transverse process of the vertebrae at the costotransverse articulation (el-Khoury and Whitten, 1993). This two-point articulation limits both the motion of the rib head and the relative motion of adjacent vertebrae.

Despite these constraints, the thoracic spine constitutes a multi-segment structure able to rotate somewhat in the sagittal, coronal and transverse anatomical planes. Moreover, the range of motion varies over the length of the thoracic spine. Physiological ranges-of-motion in the sagittal and coronal plane are increased in a cephalocaudal direction while axial rotation is higher in the mid thoracic region. Occasionally, these motions are coupled. Though flexion and extension can be relatively pure plane motions (accompanied by slight axial rotation), lateral flexion is always coupled to axial rotation (up to a proportion of 1-to-1 at the T4–T8 location) (Willems et al., 1996).

1.2.3 Limitations of the Hybrid III 50th percentile to describe the kinematics of the human spine in a frontal impact.

As illustrated in the previous section, the human spine is a flexible, multi-segmented structure that can adopt complex three-dimensional (3D) configurations during an impact (Begeman et al., 1973; Alem et al., 1978; Lessley et al., 2010; Lopez-Valdes et al., 2010b). In the particular case of frontal impacts, there has been a substantial effort to assess the biofidelity of the spine of the Hybrid III midsize adult male dummy (Hybrid III 50th), the Anthropomorphic Test Device (ATD) most commonly used in frontal impacts as human surrogate.

In 1974, General Motors initiated an internal project to modify a previous ATD developed in 1972 resulting in the current Hybrid III adult male dummy. In 1983, General Motors Corporation petitioned the National Highway Traffic Safety Administration (NHTSA) to allow the use of the Hybrid III 50th as an alternative test device for FMVSS 208 compliance test, given the good repeatability, reproducibility, durability and measurement capabilities of the ATD, as well as the improved biofidelity based on a large number of Post Mortem Human Surrogate (PMHS) test. Along with the petition, General Motors published a set of thresholds to be used as injury indicators with the Hybrid III 50th. These values were called Injury Assessment Reference Values (IARV). Soon, the Hybrid III 50th became the most widely used dummy in vehicle and restraint development programs worldwide. Backaitis and Mertz (1994) offers a compilation of published papers documenting the bases of its development.

That the Hybrid III 50th ATD has played a critical role in the continuous improvement of restraint systems is out of question, and yet, there is a growing body of literature pointing to substantial differences in spinal kinematics between humans and that ATD. The analysis of the biofidelity of the Hybrid III 50th percentile neck and the associated injury criteria originated in the late 1960s and early 1970s based on volunteer (Foster et al., 1977) and cadaveric studies (Mertz H.J. and Patrick, 1971; Culver et al., 1994). Subsequent studies have identified a lack of biofidelity in a range of loading environments (Seeman et al., 1986; Yoganandan et al., 1989; Lopez-Valdes et al., 2010b) some of which can be attributed to the design of the ATD spine. While the human spine is a multi-segmented system, the Hybrid III 50th thoracic spine is of welded steel construction and essentially rigid (Foster et al., 1977). The design of the lumbar spine in the ATD allows primarily flexion and extension motions in the sagittal plane (Foster et al., 1977).

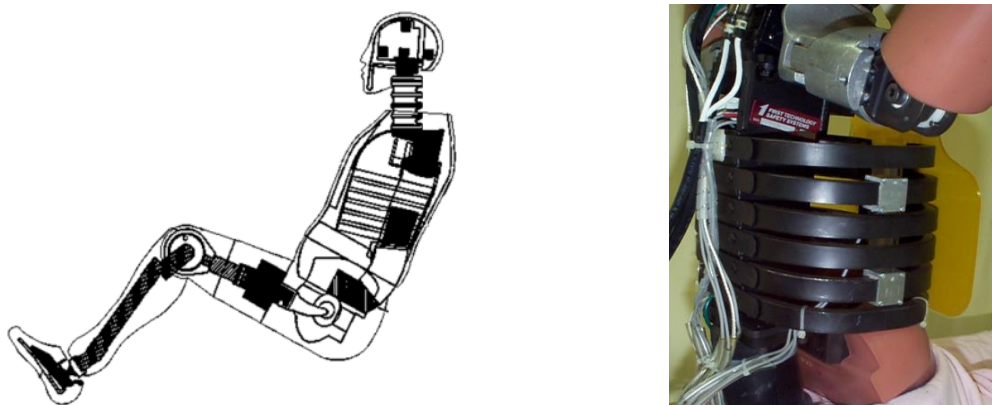


Figure 1.5 Schematic of the parts of the Hybrid III 50th and detail of the construction of the rigid thoracic spine.

In a comparison between the Hybrid III 50th, THOR (a different ATD used also in frontal impacts that incorporates an extra joint in the thoracic spine and a more biofidelic neck) and four PMHS, Shaw et al. (2000) showed that the spinal motion of THOR was more biofidelic in 48 km/h frontal sled tests. THOR lap belt loads, upper spine (T1) movement, head acceleration and movement of the anterior chest wall were more similar to those observed in the matching PMHS tests than were those of the Hybrid III. The biofidelic improvements of the THOR dummy over the Hybrid III were partially attributed to THOR's extra spinal joint. Despite this extra joint, both THOR and the Hybrid III 50th underestimated the magnitude of the forward excursion of the head and overestimated the forward excursion of the upper spine (T1).

In a different study, Shaw et al. (2001) compared the magnitude of acceleration measured at different levels on the spine of a PMHS to that recorded by the Hybrid III 50th in 48 km/h frontal sled impacts. A multibody MADYMO model was used to further explore the differences observed during the physical tests, showing that the flexibility of the human torso was the cause of the substantial differences observed in the kinematics.

Lopez-Valdes et al., (2010b) identified marked different spine trajectories in a comparison between the Hybrid III 50th and three adult PMHS at two different speeds (9 km/h and 40 km/h). The highly coupled structure of the dummy manifested in a synchronous motion of the head, spine and pelvis of the ATD. On the contrary, the multi-segmented structure of the human spine decoupled the motion of the different anatomical structures. These results are consistent with those reported by Shaw et al. (2000) in that the Hybrid III 50th underestimated the forward excursion of the head (Figure 1.6). In the loading environment analyzed by Lopez-Valdes et al. (2010), the comparison of the trajectories showed that while the pelvis of the dummy acted as fulcrum for the rotation of the ATD upper torso and head, the PMHS pelvis moved anteriorly and superiorly, with all the spinal levels and head moving almost rectilinearly until the time of peak shoulder belt force in which the head and T1 started to describe a flexion trajectory.

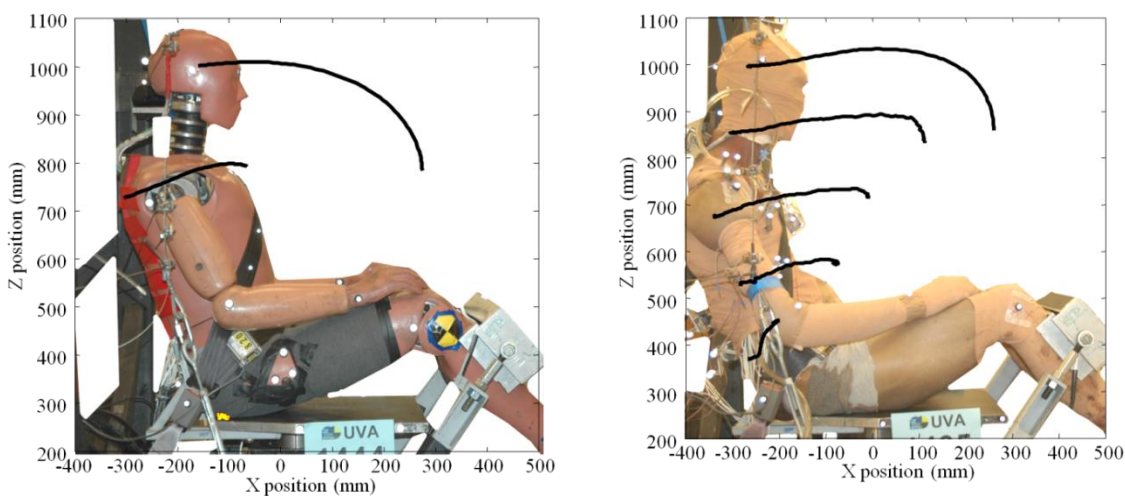


Figure 1.6 Comparison of the sagittal trajectories of the head, spine and pelvis between the Hybrid III 50th and a PMHS in a 40km/h frontal impact (Lopez-Valdes et al., 2010b).

Lopez-Valdes et al. (2010b) also explored the influence of the differences in spinal compliance on the values of the upper neck loads. Regardless of the speed, the estimated neck loads (axial and shear force, flexion moment) at the atlanto-occipital joint of the PMHS were larger than those measured by the upper neck ATD load cell. The main difference was found in the ATD estimation of the peak value of the shear force (F_z) as shown in Figure 1.7. At 40 km/h, the average shear force measured by the Hybrid III 50th was $F_z=1534$ N, while the estimated forces in the three PMHS were $F_z=2696$ N, $F_z=3909$ and $F_z=4170$ N. The study also found that even if the values for the combined tension-flexion ATD neck injury mechanism ($N_{TF}=0.06$ at 9 km/h and $N_{TF}=0.28$ at 40 km/h) were far from being close to the IARV ($N_{TF}=1$) for the upper neck, one of the PMHS sustained ligamentous and osseous injuries.

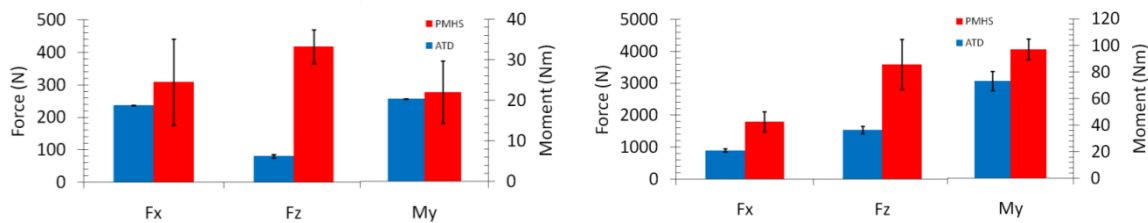


Figure 1.7 Comparison of peak neck loads (axial and shear force, flexion moment) between the Hybrid III 50th and a PMHS in a 9 km/h (left) and in a 40km/h (right) frontal impact (Lopez-Valdes et al., 2010b).

In summary, recent investigations have shown that there are important differences in the trajectories of the spine between the Hybrid III 50th and PMHS. These differences caused the ATD to underestimate the peak forward excursion of the PMHS head, but also to exhibit a different head trajectory. Another important dissimilarity between the two surrogates was the ATD underestimation of upper neck loads. All these differences have been attributed to the lack of compliance of the Hybrid III 50th spine as discussed in Shaw et al., (2001).

1.2.4 The development of the Hybrid III 6YO

The Hybrid III 50th was the first of a series of frontal ATD that were scaled to represent different occupant sizes (including pediatric subjects) while keeping the basic characteristics and measurement capabilities of the midsize adult male dummy (Irwin and Mertz, 1997; Mertz et al., 2003; Mertz et al., 1989). The Hybrid III 6YO is the member of the ATD family designed to represent the behavior of a human 6YO in a frontal

crash and it is currently in use in regulation FMVSS 213 (Child Restraint Systems), which is the standard specifying requirements for child restraint systems in motor vehicles.

1.2.4.1 Scaling

Although the characteristic dimensions and segment weights of the new child dummy were defined based on anthropometric data from the American pediatric population, the corresponding IARV of the Hybrid III 6YO were obtained through the application of a set of multiplying factors (the so-called scaling factors) to the response of the Hybrid III 50th.

The technique used to develop these scaling factors was dimensional analysis, which permits obtaining the response of a prototype based on the experimental results of a scaled model (Binder, 1949). Dimensional analysis allows finding intrinsic relationships between physical magnitudes that are dimensionally consistent, since physical laws do not depend on the unit system chosen to express them. Prototype and scaled model must satisfy two requirements so that dimensional analysis can be applied: there must be geometrical and dynamic similarity between them (Robertson and Crowe, 1980). The first requirement, geometrical similarity, establishes that the model is a replica of the prototype and, therefore, the relative angles between faces and edges must remain constant and the length parameters are proportional to each other with the same proportionality constant. Dynamic similarity requires that the system of forces must act on homologous points of both model and prototype and that the magnitude of the forces must be proportional.

Neither of these two requirements is satisfied by the pediatric ATD within the Hybrid III family, however, using dimensional analysis was considered to be a reasonable approach to the problem of finding the IARV in the absence of experimental data to be used in the development of specific IARV for other dummy sizes. The derivation of the scaling factors to be used in the scaling of the IARV from the Hybrid III 50th percentile to other ATD sizes is detailed in Irwin and Mertz (1997) and Nahum and Melvin (2002). Some of the scaling factors were updated later and the new values were published in Mertz et al. (2003).

The lack of available experimental data on the mechanical response of pediatric subjects motivated that local relationships that were obtained for specific parts of the body were used in the scaling of other body

regions or even in the response of the whole subject. For instance, the scaling factor for the elastic bending modulus originally used in all IARV scaling relationships (regardless of body region) was obtained as the ratio between the elastic bending modulus of the parietal adult bone and that of a 6 year-old. Another remark is that the data came from studies that used different methods to test the samples and therefore, the results were not directly comparable (Hubbard, 1971; McPherson and Kriewall, 1979).

1.2.4.2 FMVSS 213 Child Restraint Systems

As mentioned above, the standard FMVSS 213 specifies requirements for child restraint systems with the purpose of reducing the number of fatal and injured children in motor vehicle crashes. In case of the child restraints designed to protect 6YO occupants, FMVSS 213 requires the use of the Hybrid III 6YO and establishes a set of performance limits that the response of the dummy must not exceed when the standard-specified test rig (including the child restraint) is accelerated according to a trapezoidal corridor with maximum plateau acceleration of 25 g and minimum plateau acceleration of 19 g.

Figure 1.8 (left) shows the test setup required by the standard, while the performance limit values for the Hybrid III 6YO are shown in Table 1.1. The excursions of the knee and the head are measured with respect to a reference (point Z) defined on the test rig by the standard.

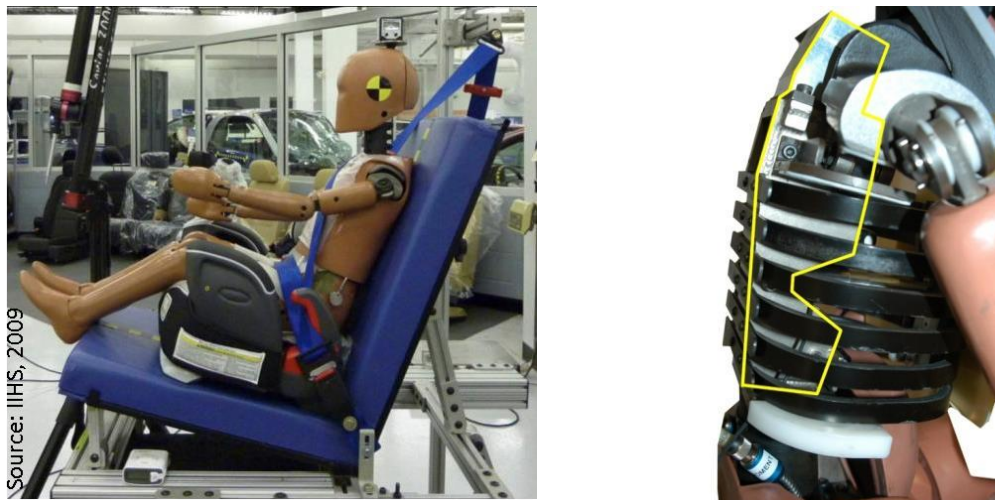


Figure 1.8 Left: Test rig used in the FMVSS 213 (source: www.iihs.com). Right: detail of the construction of the Hybrid III 6YO thoracic spine with the thoracic box outlined in yellow.

Table 1.1 Maximum values of injury criteria as specified in FMVSS 213.

FMVSS 213-Injury Criteria	Hybrid III 6 YO
Head Injury Criterion (HIC15 ms)	700
Neck Criterion (Nij)	1
Critical Neck Values	
F_z : Tension (N)	3096
F_z : Compression (N)	2800
M_y : Flexion (Nm)	93
M_y : Extension (Nm)	42
Head Excursion	
With Tether (mm)	720
Without Tether (mm)	813
Knee Excursion (mm)	915

Note: F_z : axial neck force; M_y : flexion/extension neck moment

Interestingly, several of the required limits used in the assessment of child restraints relate to head acceleration (HIC) and head excursion as well as to neck loads. Given that the response of the Hybrid III 6YO was obtained through the scaling of the performance of the Hybrid III 50th, the biofidelity issues showed for the kinematics and neck loads of the adult male dummy are potentially present in the pediatric one (the thoracic spine of the 6YO is also rigid, as shown in Figure 1.8).

As mentioned above, scaling was needed due to the lack of enough experimental data from pediatric subjects to be used in the design of pediatric ATD. The following subsection presents the few available studies reporting on the whole body kinematics of pediatric cadaveric subjects exposed to frontal decelerations. A handful of these studies compared the response of the pediatric cadavers to that of pediatric ATD, highlighting the differences between the two types of surrogates. Subsection 1.2.5 also discusses why the available experimental pediatric data were not suitable to be used in the assessment of current pediatric ATD due to the existing technical limitations at the time in which these experiments were performed.

1.2.5 Pediatric PMHS sled tests: assessment of the spinal biofidelity of the Hybrid III 6YO.

Kent et al. (2009) reviewed the literature identifying a total of 15 full-scale sled test performed with 11 pediatric PMHS (Brun-Casan et al., 1993; Dejeammes et al., 1984; Kallieris et al., 1976; Kallieris et al., 1978; Mattern et al., 2002; Wismans et al., 1979) and three-full scale sled tests with an adult PMHS having the approximate size of a 10 year-old (Lopez-Valdes et al., 2010a). The restraint conditions of these tests included lap belt and shield, 4-point and 5-point harness and 3-point seatbelt systems. Table 1.2 is adapted from the Kent study and provides a summary of these tests.

Kallieris et al. (1976) compared the kinematic response of four pediatric PMHS (ranging from 2.5 years old to 11 years old) to the response of two 6YO dummies. Test subjects were restrained by a combination of lap belt and a polystyrene deformable lap table. The study reported similar forward excursions of the head, shoulder and torso of the cadavers and the dummies. However, the authors observed substantial differences in the flexion of the spine between both surrogates. Although the cadavers were heavier than the dummy, ATD measured belt forces were greater than the corresponding cadaveric ones. The authors suggested two factors to explain this result: the difference in spinal compliance and the interaction of the cadavers with the foot rest (see Figure 1.9). Although the study reports the trajectories of several markers, the differences in the anthropometry of cadavers and dummies make difficult the comparison between the surrogates.

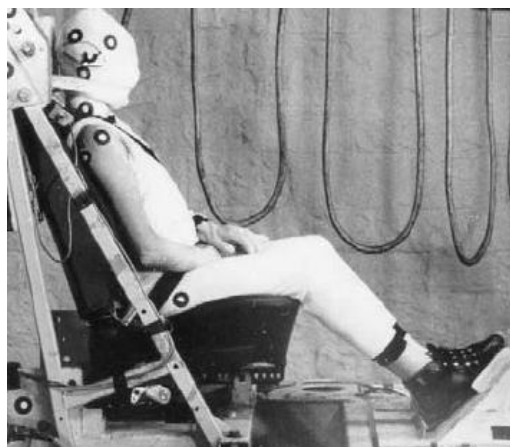


Figure 1.9 Overall view of pediatric PMHS test setup (Kallieris et al., 1976).

Table 1.2 Summary of pediatric PMHS sled tests in the literature adapted from Kent et al. (2009).

Test *	Speed (km/h)	Avg. sled decel. (g)	Restraint	Age (yrs)	Gender	Mass (kg)	Stature (cm)	Ref.†	Injury summary	Notes
HD 36-75	31	18	Lap belt with shield	2.5	M	16	97	1	AIS 1 hemorrhages in spine.	Originally reported in ref. 1.
HD 38-75	40	20	Lap belt with shield	6	F	27	125	1	None	Originally reported in ref. 1.
HD 39-75	40	21	Lap belt with shield	6	M	30	124	1	AIS 1 hemorrhages in spine	Originally reported in ref. 1.
HD 41-75	40	21	Lap belt with shield	11	M	31	139	1	AIS 2 hemorrhages in spine	Originally reported in ref. 1. #77 in ref. 3. Stature is reported inconsistently between ref.3, 4, and (Mattern et al., 2002). Heidelberg test number is 77/01.
HD 5	46	15	4-pt harness	10	M	39	139-150	3	AIS 2 spine injuries	This subject was tested 5 times (see also APR 2). These 4 tests are #'s 78, 79, 80, 82 in ref. 3.
APR 1	48	13	Shield (Int. 2)	2	F	13	87	3	None	Shoulder abrasion. Liver contusion of unknown severity
	50	13							None	
	50	13							None	
	50	13							None	
HSRI	50	20	5-pt harness child restraint	6	M	17	109	2	Liver contusion of unknown severity	Originally reported in ref. 2.
HD 8	49	15	6-kN load-limited 3-pt belt	13	M	39	162	3	None	#71 in ref. 3. Ref. 4 cites ref. 1 for methods. Submarining #73 in ref. 3. Ref. 4 cites ref. 1 for methods. Belt force is the only measurement. Submarining.
HD 9	49	25	3-pt belt	12	F	52	144	3	AIS 1 in thoracic spine	Same subject as APR 1 tests. #84 in ref. 3.
APR 2	50	13	Shield (tot guard)	2	F	13	87	3	C1 fx w/ AO disloc.	
HD 89-12	49	18	Shield with shell (Romer Peggy)	2.5	F	17	91	4	AIS 3 hemorrhages in spine, ligamentum flavum lac., dens fx.	Ref. 4 cites ref. 1 for methods.
76/41	50	20	3-pt belt (17% elongation)	12	M	41	147	1	AIS 1 skin abrasions over L shoulder and both hips	Limited results published by (Kallieris et al., 1978), and (Ash et al., 2009). Detail in (Mattern et al., 2002)

*Numbering used in (Brun-Casan et al., 1993) except test 76/41, which was not discussed in that study. Different authors used different numbering schemes (see notes).

†1(Kallieris et al., 1976; Kallieris et al., 1978); 2-(Wismans et al., 1979); 3-(Dejeammes et al., 1984); 4-(Brun-Casan et al., 1993). The reference given is the first reference in which the test was reported, but unique results from some of these tests are reported in more than one of these six references and others.

Ash et al. (2009) compared an unpublished 12-year-old cadaver sled test done by Kallieris et al. in 1976 to the Hybrid III 10YO in matching conditions. Results were scaled anthropometrically to make possible the comparison. The authors found a good correlation of the head peak forward excursion as reported in the original Kallieris' study. Point tracking of several points along the spine showed the lack of compliance of the thoracic spine of the ATD (Figure 1.10).

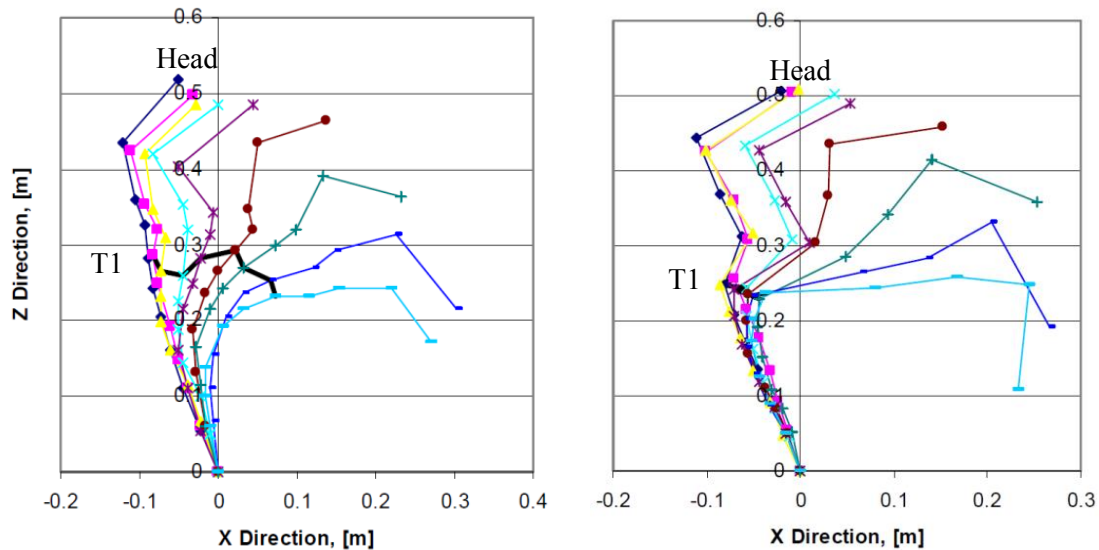


Figure 1.10 Spinal contours of the pediatric PMHS (left) and Hybrid III 10 YO (right). The solid black line corresponds to the approximate trajectory of T1 in both plots. Adapted from Ash et al. (2009).

Kallieris et al. (1978) reports results from 127 frontal sled tests conducted on a total of 61 subjects with ages varying between 13 and 74 years. However, the results are aggregated and it is not possible to compare the behavior between the children and the adults.

Wismans et al. (1979) compared the kinematics of a 6-year-old cadaver (though with an anthropometry closer to a 4-year-old) and a 3-year-old dummy in a nominally 50 km/h frontal impact. Both surrogates were restrained by a child restraint system attached to a bench seat by a car lap belt and a special top tether strap. The child restraint system incorporated a 5-point harness. No injuries other than abrasions on the shoulder and a contusion on the liver were reported in the necropsy of the cadaver. Particularly, no injuries to the spine were noted although excessive looseness was reported at the capsules about the C1/C2 lateral articulations and the atlantoaxial membrane. The study reported a complicated cadaver head-neck-torso

motion that resulted in a larger spine deformation than the observed dummy one. Figure 1.11 illustrates the differences found between the two surrogates as well as the child restraint used in the tests. Instrumentation values indicated also differences between cadaver and dummy kinematics. Forward acceleration of the cadaver head was lower (22 g versus 40 g for the ATD) while inferior head acceleration was slightly higher (40 g versus 35 g for the ATD). The shape of the anterior chest acceleration time history was also different, with the dummy showing a trapezoidal shape with a 30 g plateau and the cadaver exhibiting an early peak of 40g followed by a lower plateau at 20 g.

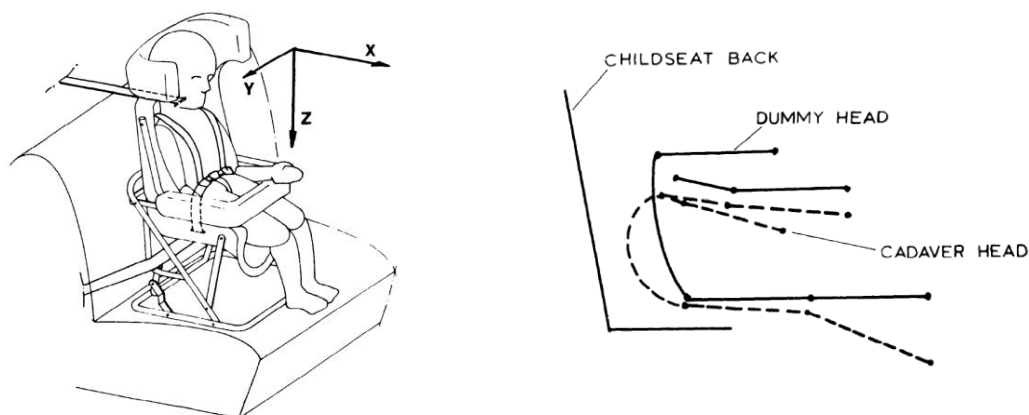


Figure 1.11 Overall view of test setup (left). Comparison between head and spine positions at 80 ms between the pediatric cadaver and the dummy. Adapted from Wismans et al. (1979).

The test data produced by Kallieris et al. (1976) and Wismans et al. (1979), were augmented in Dejeammes et al. (1984) providing data on four additional pediatric subjects (HD5, HD8, HD9 and APR1/2 in Table 1.2). The study compared the injuries found in the cadavers depending on the type of restraint used (note that cadaver APR1/2 was subjected to five impacts in two different restraints). Although some information about the kinematics of the tests subjects is provided, it is difficult to draw any conclusion on the kinematics of the pediatric spine due to the variety of restraints and speeds used. As an additional complexity, the data available from these tests were very limited in some of the studies (i.e. in HD9, shoulder belt force was the only available measurement).

The study by Brun-Casan et al. (1993) is particularly interesting since it compares child dummies and the existing pediatric cadaver data in identical experimental conditions. Brun-Casan et al. compiled the information from the previous cited studies and added data from a tenth pediatric subject (2.5 years old)

described as HD 89-12 in Table 1.2. Due to the variety of test conditions and restraints used in the pediatric tests, the authors selected only two of the pediatric tests to be compared to two dummies: the CRABI 3YO and the TNO-P3. The pediatric tests selected for the comparison were H 89-12 and H 36-75, using two different types of restraints (a child restraint system called Romer Peggy (Britax) and a shield type system Romer Vario Shield). The study failed to provide a comparison between the pediatric cadavers and the dummies, but rather compared the performance of the two dummies. The only assessment of the biofidelity of either dummy stated that neither dummy reproduced exactly the head and thorax kinematics of the cadavers.

Mattern et al. (2002) only provides additional data (mainly anthropometry) on case HD5 (77/01) and presents a new pediatric subject (76/41), providing head acceleration and a detailed description of the geometry of the test and subject anthropometry. This report does not present any analysis of the data.

Sherwood et al. (2003) evaluated the Hybrid III 6YO in the context of the standard FMVSS 213, with special focus on the assessment of neck loads as injury indicator to the cervical spine. The study found a severe hyperflexion of the dummy neck causing the chin to impact the chest and producing unrealistically high neck loads. All dummy tests exceeded the IARV for the neck ($N_{ij}=1$) regardless of the restraint system used (high back booster seat, low back booster seat, three-point belt without booster seat). This study hypothesized that the rigid ATD thoracic spine was the cause of the extreme cervical loads.

Although the test subject in the study by Lopez-Valdes et al. (2009) was not a pediatric PMHS, the anthropometry of the subject was very close to a 10 YO. Therefore, the study compared the frontal response of a booster-seated adult PMHS to that of the Hybrid III 6YO. The comparison was done at two different speeds (29 km/h and 48 km/h) and using two different restraints (standard belt (ST) and pretensioning force-limiting belt (PT+FL)). The scaled displacements of selected landmarks in the dummy predicted correctly the PMHS displacements (Figure 1.12), although the ATD could not replicate correctly the whole kinematic behavior of the PMHS (head and spinal accelerations) (Figure 1.13). Also the ATD failed to capture some of the features observed in the PMHS test using the two different types of belt.

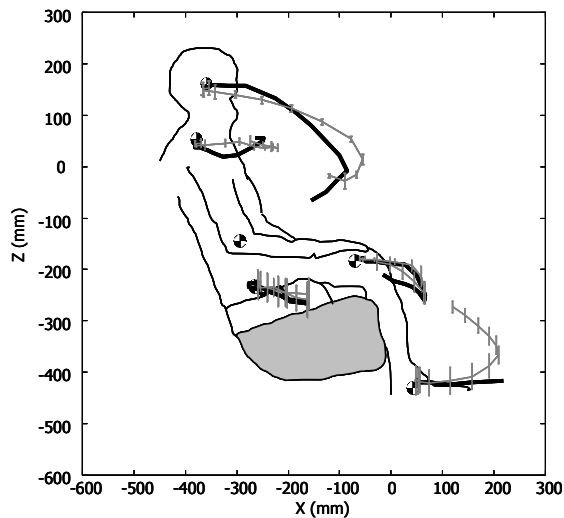


Figure 1.12 XZ trajectories of the Hybrid III 6YO and the scaled small adult PMHS in a 48 km/h frontal impact (PT+FL belt).



Figure 1.13 Comparison between the spinal deformation of the Hybrid III 6YO and the small adult PMHS at 140 ms in a 48 km/h impact (ST belt).

Apart from these full sled tests with pediatric PMHS, juvenile animals have been used in sled testing as pediatric human surrogates. Backaitis et al. (1975) compared the frontal response of juvenile baboons and a pediatric ATD in matching impact conditions. In this case, despite the ATD was heavier than any of the animal models, belt forces were greater for the animal surrogates. Dejeammes et al. (1984) also reported results from the comparison of two animal data sets to pediatric ATD. The first one used a juvenile baboon restrained in 4 and 5-point harnesses (the same surrogate was exposed to 10 successive tests without sustaining injury). The baboon surrogate showed higher head acceleration than those measured in pediatric PMHS in comparable restraint and impact conditions. The animal model also exhibited spinal and head trajectories more similar to those of the pediatric PMHS than those of the pediatric ATD. The second set of data corresponded to two juvenile chimpanzees that were restrained in a bucket seat and a 5-point harness and exposed to 32, 40 and 50 km/h impacts. No injuries were found, but these tests did not collect any physical magnitude and therefore no comparison to either pediatric PMHS or ATD can be established. Although in some instances animal models have been used successfully to approximate the pediatric impact response (Kent et al., 2008), the utility of the animal research discussed here is limited since no assessment

was provided of how closely the animal model represents the pediatric human occupant in a full scale sled tests.

The preceding paragraphs described how disperse and limited is the knowledge on the kinematics and dynamics of children in frontal impacts. Table 1.3 summarizes the results from the comparison between pediatric PMHS and pediatric ATD from those of the previous studies with available information. The reader is reminded that with the exception of Sherwood et al. (2003), Ash et al. (2009) and Lopez-Valdes et al. (2009) the ATD used in the comparison were not part of the Hybrid III family.

Table 1.3 Summary of biofidelity parameters in the comparison between pediatric PMHS and pediatric ATD in the literature. (✓: data included in the paper; X: data not available in the paper)

	Head excursion	Head acceleration	Spine trajectory	Spine acceleration	Belt force	Neck loads
Kallieris et al. (1976)	✓	NA	X	X	X	NA
Wismans et al. (1979)	X	X	X	X	X	NA
Dejeammes et al. (1984)	NA	NA	NA	NA	NA	NA
Brun-Casan et al. (1993)*	X	X	X	X	NA	NA
Sherwood et al. (2003)	✓	NA	X	X	NA	X
Ash et al. (2009)	✓	✓	X	NA	✓	NA
Lopez-Valdes et al. (2009)	✓	✓	X	✓	✓	NA

* considering only the new cases that had not been published before.

NA: data measured in the tests, but not included in the paper.

In conclusion, the available comparisons between pediatric PMHS and pediatric ATD show that the ATD fail to predict head acceleration, spine trajectory and acceleration, belt loads and neck loads. Most of the previously mentioned studies have attributed all these biofidelity issues to the difference in compliance between the thoracic spine of the ATD and the cadavers.

1.2.6 Background summary

In summary, the following statements provide the background upon which this dissertation research is based:

1. The human spine is a multi-segmented flexible structure which motion determines the kinematics of the head. It also influences the interaction between the occupant and the vehicle restraints.

2. Although current adult ATD have demonstrated a successful contribution to the understanding of the kinematics of the occupants and consequently to the development of restraints, there are aspects of the kinematics of the spine that are not adequately described by these models. Previous research has suggested the rigid thoracic spine of the dummy as one potential cause for this lack of biofidelity.
3. There is a paucity of pediatric PMHS experimental data that can be used to propose specifications for the development of either physical or computational models of pediatric subjects. Moreover, the loading environment (i.e. restraint systems) used in the existing available tests is not representative of current solutions and the limitations of the instrumentation hinders the amount of information that can be drawn from these experiments.
4. Thus, the Hybrid III 6 YO dummy and its associated IARV were developed as a scaled model of the Hybrid III 50th percentile without considering any developmental changes that might violate the conditions required by dimensional analysis to be applicable.
5. Several of the assessment values used in the current standard FMVSS 213 depend on the biofidelity of the spine of the Hybrid III 6YO, that has been shown to be limited.

In light of the previous facts and considering the high incidence of pediatric head injuries in the field, there is need for an improved understanding of the kinematics of the head and thoracic spine of a human 6YO in dynamic conditions. This research focuses on frontal impacts, reviewing and assessing current methodologies used to approximate the kinematics of pediatric occupants during those events and developing other methods intended to improve the prediction of the head and thoracic spinal motion of a 6YO. The objective of this dissertation research is detailed in the next section.

1.3 OBJECTIVE OF THIS DISSERTATION

The main objective of this dissertation research is to provide corridors for the sagittal trajectories of the head and thoracic spine of a 6YO occupant in a 40 km/h frontal impact that can be used to benchmark

future physical or computational models of a 6YO. The completion of this objective is challenged by the paucity of pediatric experimental data available to develop these corridors.

As discussed above, the lack of experimental data on the response of pediatric subjects motivated the use of dimensional analysis techniques to design pediatric ATD and to propose their associated mechanical response. Thus, this research started with an assessment of the prediction of the pediatric kinematics given by these historical scaling methods. The poor estimations obtained with these methods prompted to develop a new scaling paradigm based on energy conservation. The new method assumed conservation of energy during the deceleration of the occupant and used the ratio between the peak belt forces and the masses of the subjects to scale between different sizes of occupants. Although the prediction of the pediatric kinematics improved substantially the results obtained previously, the method still ignored some fundamental aspects of the mechanical behavior of children. The assessment of these scaling methodologies was done using experimental data from pediatric and adult volunteers that were exposed to a 9 km/h non-injurious impact.

As an alternative to the limitations imposed by scaling, a new method based on using a multibody model of the occupant was used to predict the kinematics of children in frontal impacts. The method assumed that the motion of the occupant in the sagittal plane during the deceleration can be approximated using a linear time-invariant 2D model. The effective stiffness and damping coefficients of the model idealized joints were obtained minimizing the error between measured experimental displacements and the ones predicted by the simulation of the model. This method improved the results obtained with the scaling ones. Additional information required in the use of the method was obtained from sled tests performed with PMHS at 9 km/h and 40 km/h, sled tests using juvenile animal surrogates (kangaroos) at 9 and 40 km/h and *in vitro* dynamic bending tests on two sections of the human thoracic spine.

In summary, this dissertation research combines experimental data from different types of subjects and specimens (pediatric and adult volunteers, adult PMHS, juvenile kangaroos and sections of the human thoracic spine) exposed to different loading environments (frontal impacts at 9 km/h and 40 km/h, *in vitro* dynamic bending tests) with the goal of predicting the sagittal motion of a human 6YO in a 40 km/h frontal impact.

2 SUMMARY OF THE METHODOLOGICAL APPROACH AND THE DATA SOURCES USED IN THIS DISSERTATION

The best way to achieve the objective of this dissertation would be to combine into displacement corridors data measured in frontal sled tests of restrained pediatric occupants at 40 km/h. The absence of these data led the research towards analyzing the kinematics of the head and thoracic spine of different types of restrained occupants and at different speeds with the objective of getting a better understanding of the motion of these structures during a frontal deceleration.

Figure 2.1 summarizes the different types of full sled tests that were analyzed within this dissertation research. All these experiments shared a common methodology to allow comparing the responses of one particular type of subject with the others.

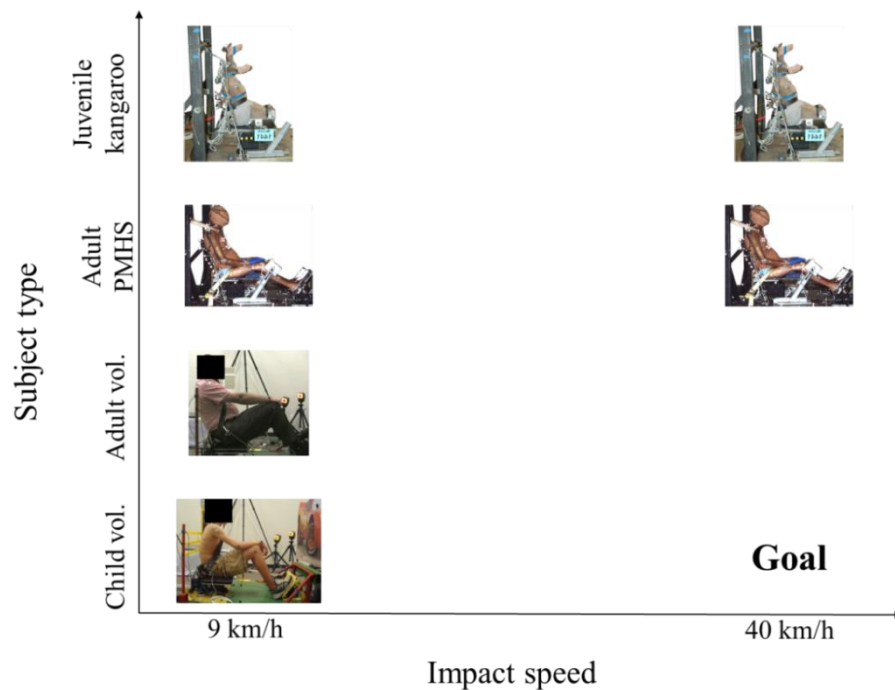


Figure 2.1 Experimental data combined in this dissertation research.

In addition to these sled tests, experimental data characterizing the *in vitro* behavior of sections of the human thoracic spine were also considered. Data from the sled tests and the *in vitro* thoracic spine tests

were combined in multiple ways, always with the ultimate objective of approximating the pediatric behavior during high-speed frontal impacts. This chapter provides an overview of how the experimental data were combined. More detailed explanations of the methodology are given in subsequent chapters, but given the complex structure of data sources used in this research, they are introduced here.

First, pediatric and adult volunteer data were used to assess the utility of historic scaling methods to predict the trajectories of pediatric occupants from adult data in frontal impacts. Although the limitations of these methods were mentioned in Chapter 1, the question of whether dimensional analysis can approximate the sagittal trajectories of the 6YO human head and spine using experimental data from adults remained unanswered. The assessment of these scaling methods constituted the first aim of the dissertation research.

The second aim of the dissertation took a more empirical approach to the problem and developed a new scaling method between adult and pediatric subjects. The new method improved the predictions of the magnitude of the pediatric displacements over the historical scaling methods, and yet, the method neglected some of the observed characteristics exhibited by the pediatric volunteers.

After discussing the inherent limitations of applying any scaling technique between pediatric and adult subjects, the third dissertation aim consisted of developing a model that instead of scaling between different occupant types (pediatric vs. adult) related the response of the occupant at high speed to the response of the occupant at low speed, while addressing some of the limitations exhibited by scaling methods.

In summary, this dissertation research committed to achieve the following three aims with the goal of finding a methodology able to provide a biofidelic approximation to the kinematics of a pediatric occupant in a frontal impact:

- 1) To assess the prediction of the kinematics of a 6YO from adult data in a frontal impact given by historic scaling methodologies, with focus on the head and thoracic spine.
- 2) To develop a new scaling methodology that improved the previous prediction of the displacement of the head, thoracic spine and pelvis of a restrained 6YO occupant in a frontal impact.

- 3) To develop a method that allowed predicting the kinematics of the head and thoracic spine of a restrained occupant at 40 km/h if the kinematics at 9 km/h were known, by developing a linear time-invariant 2D model of the occupant.

After discussing the limitations of each method, this dissertation research used the one developed within aim 3 to provide an approximation to the kinematic response of a 6YO occupant in a high-speed frontal impact, which was the main objective of the research.

Chapter 3, chapter 4 and chapter 5 focus on introducing the data sets used in the dissertation. Then, chapter 6 shows the results of the assessment of the scaling methods and chapter 7, the results obtained using the linear time-invariant model of the occupant. Finally, chapter 8 provides the estimation of the kinematic frontal response of a 6YO at 40 km/h in the sagittal plane, which constitutes the goal of this dissertation research.

The following sections provide more information about the data used in the achievement of each of the aforementioned three aims.

2.1 ASSESSMENT OF CURRENTLY USED SCALING TECHNIQUES

Whether dimensional analysis provides a reasonable approximation of the displacements of pediatric anatomical landmarks based on those of adult subjects had never been assessed before. Thus, the first aim of this dissertation addressed this question using data from the low-speed experiments that were performed with children and adult volunteers, as indicated in the shaded area in Figure 2.2.

In particular, two historic scaling methodologies (mass scaling and SAE scaling) were assessed. Strictly speaking, although only the first technique is based on dimensional analysis, the second one partially borrows the methods from dimensional analysis to calculate a set of scaling factors relating the two different sizes of occupants.

As expected, both techniques failed to provide a satisfactory prediction of the pediatric displacement. The direct application of the scaling methodologies made use of pure geometrical relationships between pediatric and adult occupants disregarding completely the action of the external forces to arrest the forward motion of the occupant. The joint consideration of the displacement of the occupant and the external forces arresting its motion was at the core of the development of a new scaling method, as detailed in the following section.

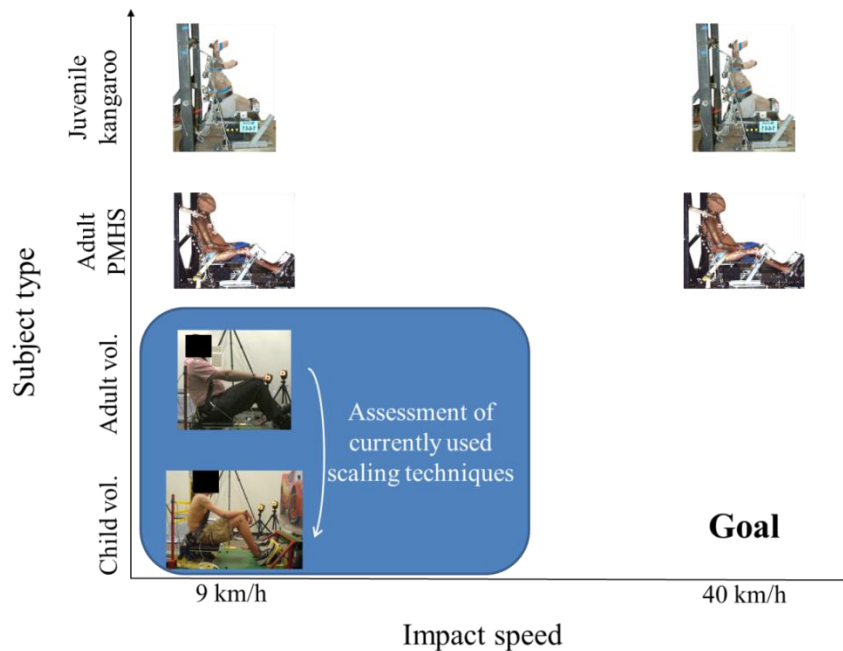


Figure 2.2 Schematic showing the data sources and processes involved in the assessment of currently used scaling techniques (aim 1).

2.2 DEVELOPMENT OF A SCALING METHODOLOGY ASSUMING CONSERVATION OF ENERGY DURING THE IMPACT

Displacement and force can be combined into the physical magnitude of work and therefore, the second aim of this dissertation consisted of finding a scaling method based on the energy needed to arrest the forward motion of the occupant. The development of this scaling method is the focus of chapter 6 (Scaling adult data to predict pediatric kinematics).

The experimental data from the low-speed volunteer tests were used again to assess the method (blue-shaded area in Figure 2.3). As aforementioned, the method improved the prediction given by the SAE and mass scaling methods at 9 km/h, yet its assessment showed that specific aspects of the kinematic pediatric behavior were missing. Giving the inherent limitations of using scaling to approximate the kinematics of pediatric subjects, aim 3 of this dissertation consisted of developing a method that considered aspects associated to the development of children and the interaction between the restraint system and the occupant in a more detailed manner.

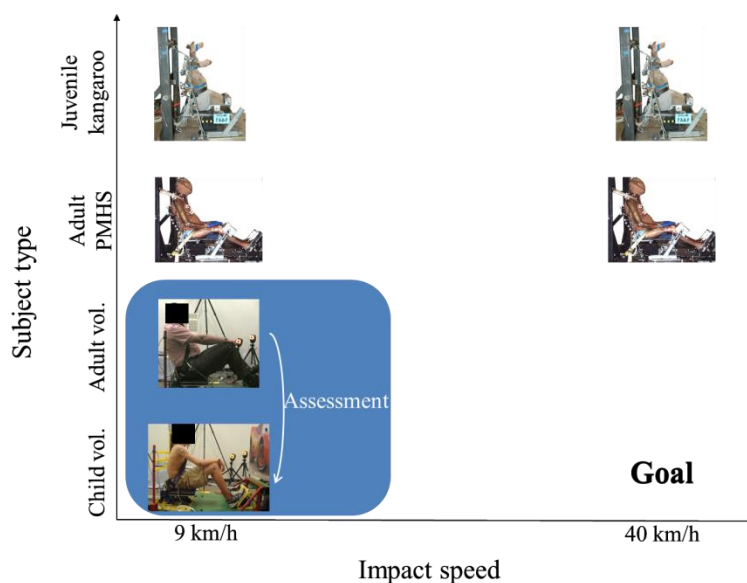


Figure 2.3 Schematic showing the data sources and steps (validation and prediction) involved in the development and use of the scaling method based on conservation of energy (aim 2).

2.3 DEVELOPMENT OF A METHODOLOGY TO PREDICT THE KINEMATICS AT 40 KM/H USING A 2D MODEL OF THE OCCUPANT

Even if considering the action of the external forces on the magnitude of the displacement of the occupant had improved the prediction of pediatric trajectories, scaling based on the conservation of energy during the impact exhibited severe limitations that will be discussed later. Thus, the third aim of this dissertation consisted of developing and using a model that could address some of the limitations shown by the previously discussed scaling methods. In particular, a linear time-invariant 2D multibody model of the occupant was developed to predict the trajectories of children at 40 km/h.

The purpose of the model was to predict the trajectory of the head and of selected vertebrae of the thoracic spine of pediatric occupants in a high-speed frontal impact without attempting to describe the exact mechanics of the phenomenon.

The dynamic equations governing the motion of a mechanical system under the action of external loads can be reduced to a form such as:

$$\underline{\underline{M}} \cdot \ddot{\underline{q}} + \underline{\underline{C}} \cdot \dot{\underline{q}} + \underline{\underline{K}} \cdot \underline{q} = \underline{Q} \quad \text{Equation 2.1}$$

where $\underline{\underline{M}}$ is the mass matrix of the system, $\underline{\underline{C}}$ is the damping matrix and $\underline{\underline{K}}$ is the stiffness matrix. The vector $\ddot{\underline{q}}$ is formed by the generalized accelerations, $\dot{\underline{q}}$ contains the generalized velocities and the elements in \underline{q} are the generalized coordinates. The generalized forces are the elements of vector \underline{Q} , which is given by a combination of the external forces and moments applied to the system and the generalized coordinates.

The elements within the $\underline{\underline{M}}$, $\underline{\underline{K}}$ and $\underline{\underline{C}}$ matrices are given by relationships between the mass (m), moments of inertia (I) and geometry of the system, and the torsional stiffness (k) and damping (c) of the joints. The generalized accelerations and velocities are the second and first time derivatives of the generalized coordinates that are known if the position of the each rigid body is known.

It was important to limit the number of unknowns in Equations 2.1. To that end, additional tests were run to obtain a mechanical model of the human thoracic spine in flexion. These tests' goal was finding a relationship between the flexion stiffness of different sections of the thoracic spine that could be incorporated into the 2D model. Chapter 5 is devoted to explain the results obtained from *in vitro* tests of the thoracic spine. Although these tests were motivated by the need of reducing the number of unknowns in the occupant model, the results obtained show the first mathematical model of the bending behavior of the human thoracic spine, which can be considered a contribution to the existing knowledge on its own.

The model was also required to recognize inter-subject variability in the parameters characterizing the behavior of the joints. Therefore, it was sought to express the stiffness and damping of the joints as

functions of characteristics of the body regions such as their length (l), moment of inertia (J), and mass (m), among others.

Once the $\underline{\underline{M}}$, $\underline{\underline{K}}$ and $\underline{\underline{C}}$ matrices are known for a specific system (i.e. restrained occupant), Equation 2.1 can be used to predict the response (displacements) of the system for a particular set of external forces acting on it.

2.4 SUMMARY OF METHODOLOGICAL APPROACH

In summary, the following three chapters present the main sources of data that are used within this dissertation: the low-speed volunteer sled tests, the adult PMHS sled tests and the *in-vitro* bending tests to obtain a mechanical model of the human thoracic spine in flexion.

Chapter 6 integrates some of the different sources of experimental data presented in the previous three chapters to assess the approximation to the pediatric kinematics given by three different scaling methods (two historical ones and the one based on energy conservation, developed in this dissertation). Chapter 7 formulates a new methodology to predict the kinematics of the head and thoracic spine of pediatric occupants during a frontal impact using a linear time-invariant multibody model. The next chapter shows the proposed corridors for the sagittal displacement of the head and thoracic spine of a 6YO in a frontal impact at 40 km/h, which was the objective of this dissertation research. Chapter 8 also discusses the assumptions and limitations of the methodology. Finally, chapter 9 summarizes the contributions of the dissertation and suggests future research.

3 VOLUNTEER EXPERIMENTS

3.1 INTRODUCTION

Non-injurious pediatric and adult volunteer frontal impact tests were performed at The Children's Hospital of Philadelphia with the goal of quantifying the kinematic responses of the restrained child's head and spine in low-speed frontal collision-like events and of comparing the pediatric response to that of the adult group. The following sections describe the methods and main results obtained in these tests. When appropriate, it is indicated which results correspond to analysis done by the researchers at The Children's Hospital of Philadelphia and which are original contribution of this research. In particular, the development of kinematic corridors for the anatomical landmarks of the volunteers constitutes newly obtained results as fruit of the reanalysis of the experimental data. Selected results of these volunteer experiments have been reported by Arbogast et al. (2009) and Seacrist et al. (2010).

3.2 METHODS

Pediatric and adult volunteers were exposed to the same deceleration in an analogous impact environment. The study protocol was reviewed and approved by the Institutional Review Board at The Children's Hospital of Philadelphia (Philadelphia, PA) and Rowan University (Glassboro, NJ).

3.2.1 Test setup

A pneumatically actuated, hydraulically controlled low-speed acceleration sled was designed and built to provide a realistic occupant environment while providing enough clearance to be used in conjunction with a motion capture system (Figure 3.1). The crash pulse, impact conditions and buck setup were chosen after a pilot study to ensure that the volunteers were exposed to a safety environment at all times (Figure 3.2). The sled buck incorporated a real automotive seatbelt equipped with a retractor. The lap belt anchors were fixed throughout the test series and the lap belt buckle angle to the horizontal was set at 70 degrees at initial position for all the subjects. The height of the shoulder belt was adjusted to provide similar fit across the

subjects (fixing at 70 degrees the angle of the shoulder portion of the belt at the D-ring). Supplementary restraint to the occupants was provided by a foot rest. Additional details on the construction and safety design of the experiments can be found in Arbogast et al. (2009).

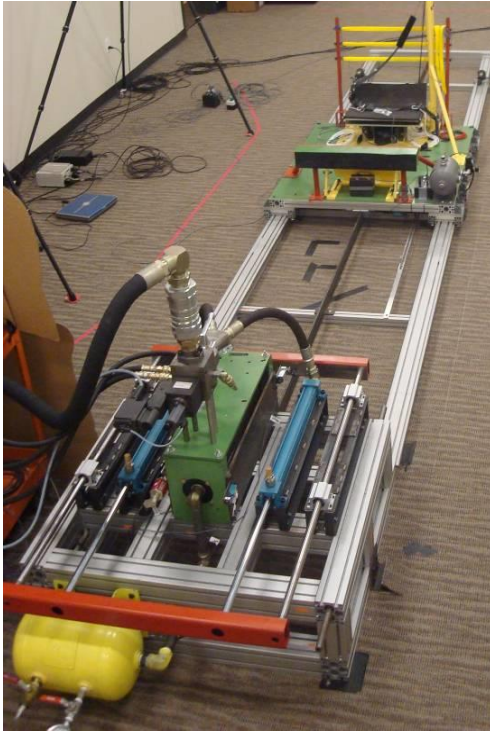


Figure 3.1 Low-speed acceleration sled. Pneumatic system and sled buck.

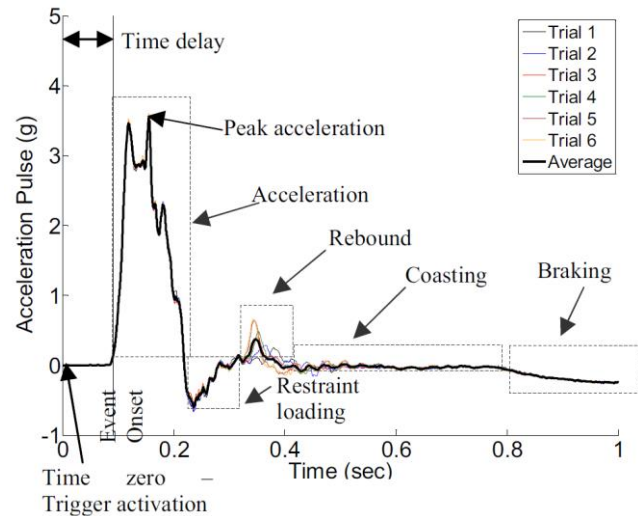


Figure 3.2 Phases of the acceleration pulse used in the volunteer tests.

The experimental procedure consisted of six trials per volunteer. Participants were informed that they could withdraw from the study at any time. Before each test, the occupant was asked to relax his muscles to minimize the musculature effect on the kinematics. There was a waiting time of approximately 10 minutes between subsequent tests.

3.2.2 Test subjects

Male subjects aged between 6 and 40 years whose height, weight and BMI were within 5th and 95th percentile for the subject's age were recruited for the study. Other inclusion criteria were that subjects did not present any neurologic, orthopedic, genetic and neuromuscular conditions, nor any previous injury or

pathology affecting the head, neck or spine. The original study involved a total of 20 children (aged between 6 and 14 years) and 10 adults (aged between 18 and 30 years). For the purpose of this research, only the pediatric volunteers within the 6-year-old (6YO) group and the adults that were closer to the anthropometry of an adult male 50th percentile were considered. Table 3.1 provides basic anthropometric information from the subjects that were considered in this dissertation research.

Table 3.1 Anthropometry of volunteers and reference value for a 50th percentile 6-year-old and for a 50th percentile adult male (Arbogast et al., 2009).

	Age (years)	Gender	Weight (kg)	Height (cm)	Seated height (cm) ⁺
PED1	6	M	24	122	69
PED2	8	M	35	140	73
PED3	7	M	28	133	70
PED4	8	M	29	130	71
AD1	24	M	68	165	84
AD2	22	M	107	180	97
AD3	24	M	74	169	91
AD4	30	M	81	180	93
AD5	20	M	82	178	93
6 YO*	6	NA	20.86	116.8	63.5
Adult 50 th *	40	M	78.20	175.1	90.7

⁺ Measured from seat to top of the head * (Mertz et al., 2001)

The occupant's initial torso angle with respect to the horizontal and knee angle were set at 110 degrees by adjusting the position of the nylon back support and the fore-aft position of the footrest to mimic the position of a rear seated occupant in an automobile. Initial torso angle was defined as the angle made by the line joining the right iliac crest and the right acromion to the horizontal. Initial knee angle was defined as the angle made between the line joining the right iliac crest and right femoral epicondyle and the line joining the right femoral epicondyle and the right lateral malleolus. In order to minimize the differences in head initial position, the subjects were asked to position their head by focusing on a point placed directly in front of them at the level of their nasion.

3.2.3 Instrumentation

3.2.3.1 *Optical instrumentation.*

Spherical reflective markers were placed on the head, neck, torso and upper and lower extremities. Markers were tracked at 100 Hz using a 3D motion analysis system (Model Eagle 4, Motion Analysis Corporation, Santa Rosa, CA). The system records the 3D position of the markers within a calibrated 3D volume. In the body regions of interest for this study, the markers were attached to the following anatomical landmarks:

- Head: on a tight-fitting elastic cap (left and right temple, top and front of head in two places along the mid-sagittal plane, and on the occiput posteriorly), nasion and anterior to the left and right external auditory meatus (EAM).
- Spine: spinous process of C4, T1, T4, T8 and T12.
- Pelvis: left iliac crest (most superior point on the iliac crest).

Spherical markers were also placed at various locations of the sled buck. Figure 3.3 shows the location of the reflective markers on a volunteer.

3.2.3.2 *Other (non-optical) instrumentation.*

An angular rate sensor (ARS-300, DTS Inc, Seal Beach, CA) was mounted via a custom fixture to a subject-specific mouth guard to measure the head rotational speed. A piezoresistive accelerometer (Model 7264-200, Endevco, San Juan, CA) was mounted to the moving platform frame. Lightweight belt webbing load cells (Model 6200FL-41-30, Denton ATD Inc, Rochester Hills, MI) were attached at a fix distance of five inches from the D-ring on the shoulder belt and bilaterally on the lap belt. Two six-axis load cells were placed under the seat pan (Model IF-217, FTSS, Plymouth, MI) and under the footrest (Model IF-234, FTSS, Plymouth, MI) to measure the reaction forces on these contact surfaces.



Figure 3.3 Frontal and oblique view of a volunteer showing the position of the reflective markers on the subject.

3.2.4 Calculation of the kinematic response of an average subject within each age group and its associated corridor

To facilitate the comparison between children and adults, the responses of the subjects within each age group (PED1-PED4 in the 6YO group; AD1-AD5 in the adult group) were combined to produce corridors for the displacement of the head, T1, T8 and pelvis of an average 6YO and of an adult 50th percentile. The development of these corridors followed the methodology proposed by Lessley et al. (2004) that preserves the characteristic shape of the response in the process of averaging the individual contributions. This method also provides the calculation of the standard deviation of the responses in both the X and Z axis.

As a first step, the method requires the normalization of the response of the subjects within each age group using the mass-scaling method proposed by Eppinger et al. (1984). The anthropometrical values needed in this process were obtained from Mertz et al. (2001). Additional details on the process used to obtain these corridors were reported in Lopez-Valdes et al. (2012).

Results are shown as displacement in the sagittal plane (normalized to the initial position of each anatomical structure) and reported with respect to a coordinate system fixed to the test buck. The X axis pointed forward and the Z axis pointed upwards with respect to the buck. The Y axis was chosen to

complete a right-handed orthogonal coordinate system. The analysis was done up to the instant of maximum forward head excursion (maximum X displacement).

3.3 RESULTS

3.3.1 Kinematic comparison between restrained children and adults in a low-speed frontal impact.

These tests provided the unique opportunity of comparing the kinematics between adults and children in a similar loading environment and that was the goal of the work published in Arbogast et al. (2009) that is summarized below.

First, the comparison between the normalized forward displacements (displacement was normalized by subject's seated height) in the sagittal plane showed that for all markers on the head and the spine, the normalized change in excursion in the anterior direction significantly decreased with age ($p < 0.001$). Second, the normalized superior excursion of the spinal markers also decreased significantly with age ($p < 0.01$).

Figure 3.4 through Figure 3.7 show the comparison of the X and Z normalized excursions of all the head and spinal markers by group age. Figure 3.8 compares the normalized trajectories of the head-top marker in the sagittal plane between the pediatric (dashed lines) and the adult group (solid lines), showing the greater normalized excursion in both axes for the pediatric occupants.

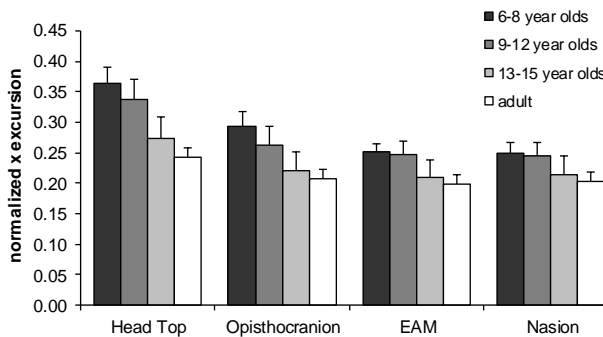


Figure 3.4 Normalized anterior excursion (relative to initial position) for the head by age group

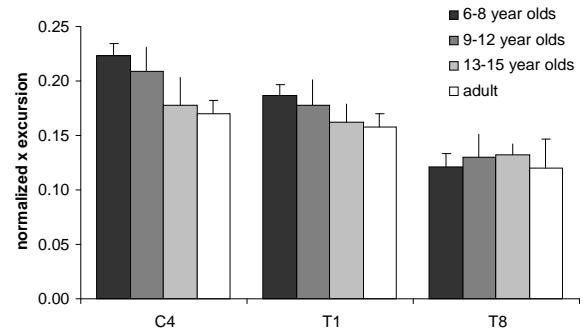


Figure 3.5 Normalized anterior excursion (relative to initial position) for the spine by age group

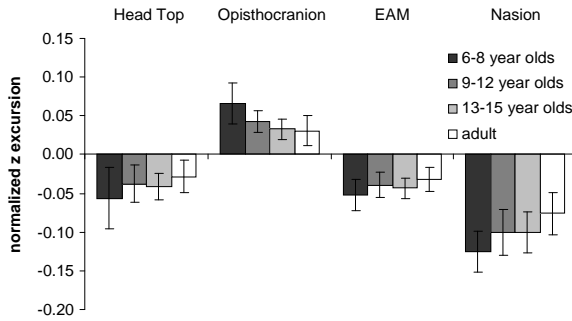


Figure 3.6 Normalized vertical excursion (relative to initial position) for the head by age group

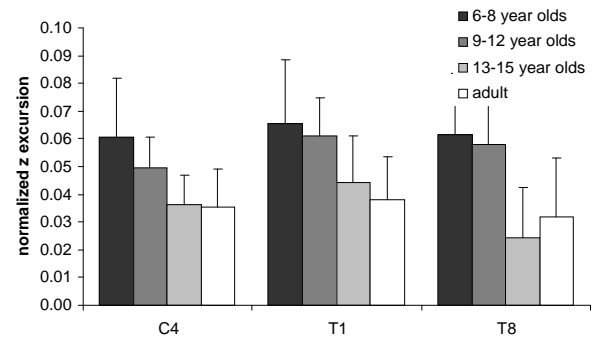


Figure 3.7 Normalized vertical excursion (relative to initial position) for the spine by age group

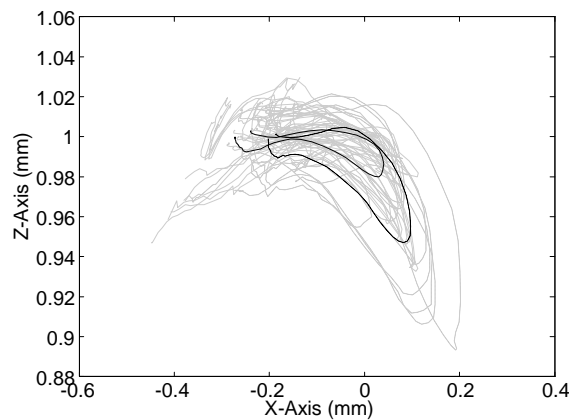


Figure 3.8 Comparison of the XZ trajectory of the head-top marker between pediatric volunteers (dashed line) and adult volunteers (solid line)

Arbogast et al. (2009) also calculated the time history of the angle formed by two consecutive rigid links joining the head and the tracked vertebrae along the spine. Figure 3.9 and Figure 3.10 show how the change of the angle between the C4-T1 and the T1-T4 links of the younger group was substantially greater than in the adult group. Flexion of the spine occurred mostly at these two spinal levels. Flexion continued to occur also in the lower thoracic spine although the magnitude appeared similar across the groups. These differences in relative spine rotation led to statistically significant differences in average maximum head rotation towards the occupant’s chest that were age-dependent as shown in Table 3.2

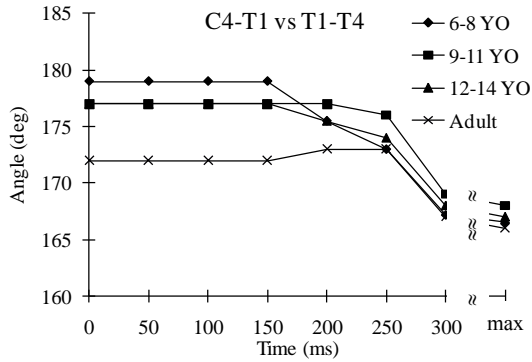


Figure 3.9 Time history of the angle between a segment connecting C4 and T1 and a segment connecting T1 and T4 by age.

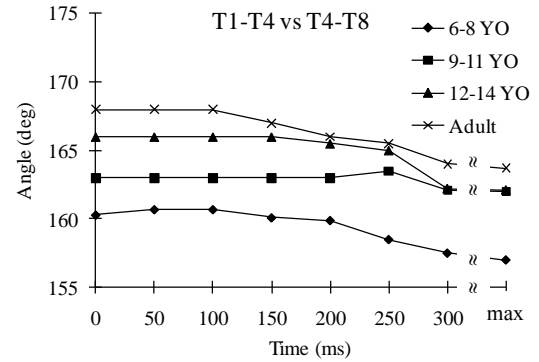


Figure 3.10 Time history of the angle between a segment connecting C4 and T1 and a segment connecting T1 and T4 by age.

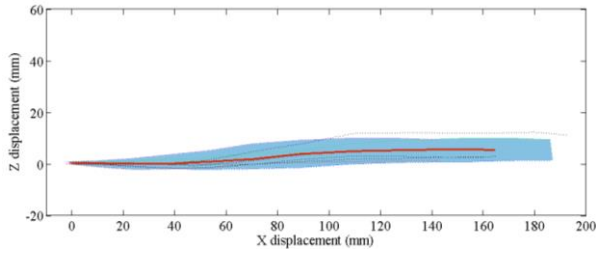
Table 3.2 Maximum change in volunteer head angle (in degrees).

Age group	Relative to sled coordinate system	Relative to segment joining T1-T4
6-8 years	42.9±6.4	12.4±6.5
Adults (21-37 years)	22.8±8.1	5.3±5.2

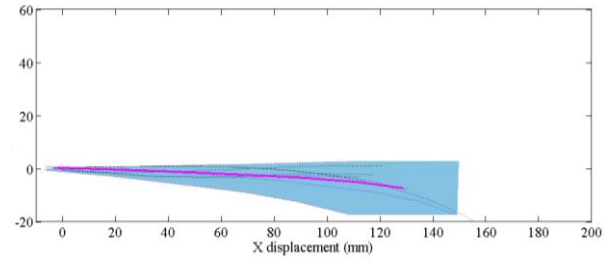
3.3.2 Kinematics of the average subject within each age group. Corridor development

Arbogast et al. (2009) compared the normalized kinematics of the head and the thoracic spine across different age groups, highlighting the differences observed between adult and pediatric subjects that constitute the rationale for this dissertation. The current subsection compares the displacement without normalizing by seated height. As described in the methods section, the sagittal displacements of the subjects within each group were combined to produce the characteristic average response and the associated corridor.

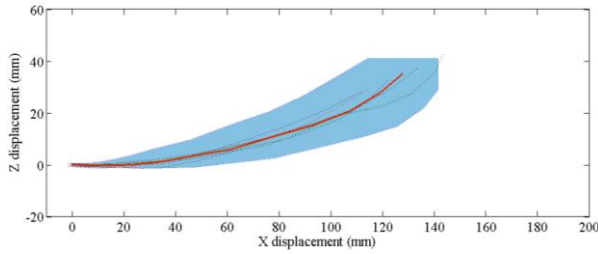
The plots in Figure 3.11 compare the displacement in the sagittal plane (XZ plane) of the head, two thoracic vertebrae and the pelvis of an average 6YO and an average adult volunteer. The comparison between these corridors was done in Lopez-Valdes et al. (2012).



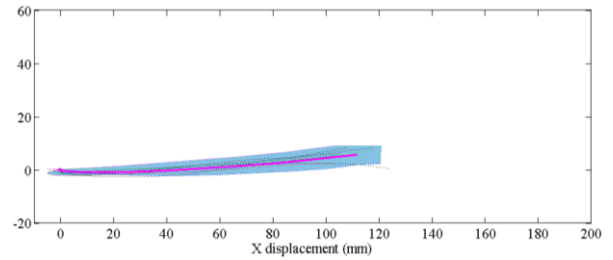
Displacement corridor of the pediatric head.



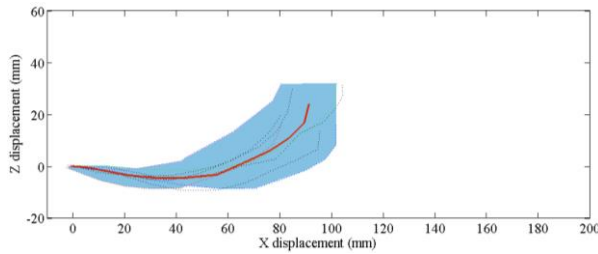
Displacement corridor of the adult head.



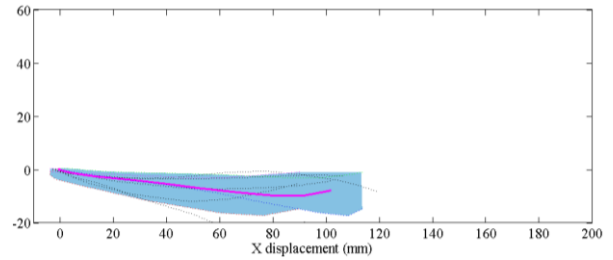
Displacement corridor of the pediatric T1.



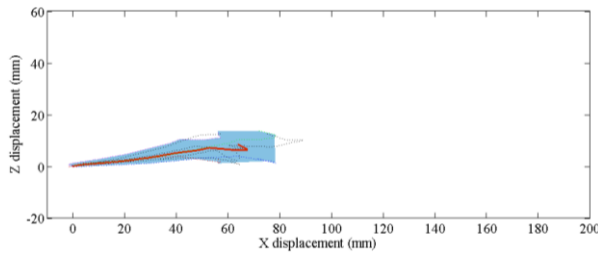
Displacement corridor of the adult T1.



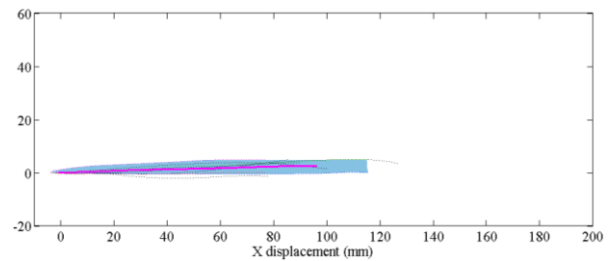
Displacement corridor of the pediatric T8.



Displacement corridor of the adult T8.



Displacement corridor of the pediatric pelvis.



Displacement corridor of the adult pelvis.

Figure 3.11 Comparison of the normalized average displacements (solid lines) and displacement corridors (blue shaded areas) in the sagittal plane between the pediatric (right) and adult (left) volunteers, 9 km/h.

The two main conclusions that are relevant to the objectives of this dissertation research were:

- That the head and T1 absolute forward displacements (X axis) of the average pediatric volunteer (head: 164.6 mm; T1: 128.0 mm) was found to be greater than that of the average adult (head: 128.8 mm; T1: 112.7 mm).
- That the displacement of the pediatric thoracic vertebrae (T1 and T8) exhibited a concave curvilinear trajectory while the corresponding adult displacements remained almost parallel to the X axis.

As it had been already shown by Arbogast et al. (2009), the differences between the two types of occupants are not limited merely to the magnitude of the displacement but also to the nature of the displacement itself. Up to the time of the maximum forward excursion of the head, the pediatric thoracic spine exhibited a curvilinear trajectory that was not seen in the case of the adult subjects.

3.4 DISCUSSION

The comparison of the head, spinal and pelvic trajectories between children and adult occupants in a low-speed frontal impact showed that there were significant differences between these two occupant types.

Arbogast et al. (2009) normalized the displacements of the anatomical structures by subject's seated height to focus on the effect of age on the kinematics of the subjects. This study showed that there were substantial differences in the X and Z normalized displacements of the head, C4 and T1. There were also statistically significant differences in the head-to-chest rotation magnitude depending on the age of the test subject. By normalizing the displacements by seated height, Arbogast et al. focused on the differences between the two types of subjects that could be attributed to age (as a proxy to subject's development) if the size effect could be taken out of the problem. And the study found that age effectively influenced the response of the volunteers. In particular, Arbogast et al. concluded that:

- The normalized forward excursion of the head and spinal markers significantly decreased with age.

- All spinal markers moved upward, but the magnitude of this motion decreased with increasing subject's age.
- The majority of the spine flexion occurred at the base of the neck and not in the upper cervical spine.
- The magnitude of spinal flexion was greater for the younger subjects.
- Additional flexion to that observed at the lower cervical spine occurred in the thoracic spine.
- The primary factor governing the differences in normalized head and spinal trajectories between the age groups was decreasing head-to-neck girth ratio with increasing age.

The analysis done here for an average subject within each group showed that even when the data was not normalized by size, the pediatric head and T1 vertebra exhibited a greater forward displacement than those of the adult subjects. In this case, subjects' data within each group were consolidated to obtain the response of an average subject and the corresponding corridor (consisting on the area surrounded by the average response plus/minus one standard deviation) and the comparison was done between the response of the average 6YO and adult subjects.

3.5 CONCLUSION

Chapter 3 used the experimental data from the volunteer test to compare the kinematic response between pediatric and adult restrained occupants in a 9 km/h frontal impact. It was found that there were substantial differences that can be related to the differences in size and age (and age-associated changes in the morphology of the head and spine) between the two groups.

Both the normalized and absolute forward displacements of the head in the pediatric group were greater than those in the adult group. The same situation was observed in the case of T1. The differences between the two types of subjects were not limited to the magnitude of the displacement: also the nature of the displacement of the thoracic vertebrae was found to be different between them. The plots in Figure 3.11

showed the curvilinear trajectory exhibited by the T1 and T8 vertebrae of an average 6YO that was not observed in the average adult subject.

The trajectory plots for an average subject within each group shown in Figure 3.11 will be used later in this dissertation in the assessment of scaling methods that is the focus of Chapter 6.

4 POST MORTEM HUMAN SURROGATES SLED TESTS

4.1 INTRODUCTION

A series of frontal full-scale sled tests using PMHS was performed at the Center for Applied Biomechanics of the University of Virginia. As introduced in Chapter 2, the experimental data from these tests were fundamental in the development, assessment and application of the methodologies developed within this dissertation to provide a prediction of the kinematics of restrained children in high-speed frontal impacts.

This chapter focuses on describing the main results observed in the tests without discussing how the results were organized to be used in the execution of aim three, and ultimately, of the objective of the dissertation. The chapter first presents the displacements of selected anatomical locations of the PMHS at 9 km/h and at 40 km/h with respect to the test buck. These displacements were required in the assessment of the methodology that used a 2D model to predict the kinematics of the occupants. Then, the results from individual subjects were combined according to the method proposed in Lessley et al. (2004) to produce the displacement response in the sagittal plane of an average subject together with the corresponding corridor at 9 km/h and 40 km/h. These results paralleled the ones showed in the previous chapter for the adult volunteers and were used to illustrate the differences observed between volunteers and PMHS in a similar loading environment.

The chapter also shows the absolute subject's displacements in a plane parallel to the subject's transversal plane and the change in length of spinal segments during the forward motion of the occupant. These results were important to understand some of the limitations present in the 2D model that was used to predict the kinematics of children.

4.2 METHODS

The design of the experimental setup was made to match that of the volunteer tests. The handling, preparation and testing of the cadavers was done in accordance with the guidelines included in the Protocol for the Handling of Biological Material (Center for Applied Biomechanics, 2006) and approved by the Oversight Committee of the Center for Applied Biomechanics, University of Virginia.

4.2.1 Test setup

The test fixture was designed to provide a reasonable approximation of frontal impact kinematics of a restrained occupant in a vehicle, while providing repeatable and reproducible conditions and line-of-sight for the motion capture system (Shaw et al., 2009). Each subject was exposed to two simulated frontal impacts at two different speeds. The first impact was designed to mimic that of the volunteers (Figure 4.1), resulting on a nominal change of speed of 9 km/h. Subsequently, each subject was exposed to a second test at a higher speed. The chosen deceleration pulse was trapezoidal in shape with a plateau at approximately 14g and a total duration of 125 ms (Figure 4.2). This second deceleration pulse resulted in a nominal change of speed of 40 km/h.

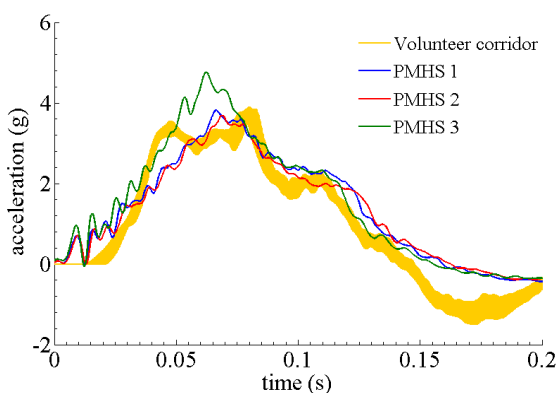


Figure 4.1 Comparison between the volunteer pulse (orange corridor) and the low-speed pulses of the PMHS tests.

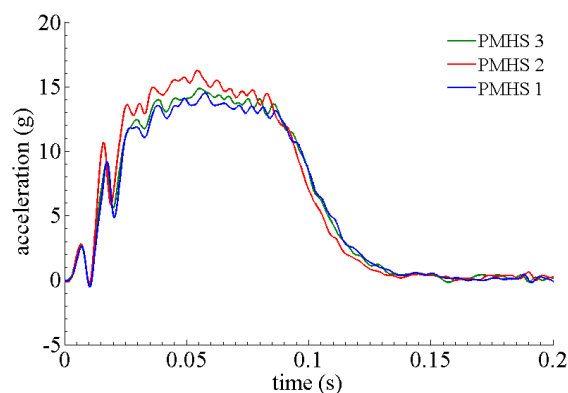


Figure 4.2 PMHS pulse at high-speed.

Occupants were restrained by a conventional 3-point belt equipped with a retractor. The anchor points of the seatbelt with respect to the seat matched the position of the belt used in the volunteer tests. The belt

was replaced after each test. Test subjects were positioned on a flat rigid seat with the torso and head being supported by a set of cables that were adjustable in height and tension. Additional restraint was provided by a foot rest and a knee bolster (the latter, only in the case of the high-speed test).

4.2.2 Test subjects

The three PMHS included in this study were screened before testing and confirmed free of blood infectious diseases (HIV, Hepatitis B and C). Absence of any other pathology that could influence injury occurrence was also confirmed via high-resolution computed tomography (CT) scans. Anthropometric characteristics of the PMHS can be found in Table 4.1. PMHS were chosen to be nominally a 50th percentile male.

Initial positioning of the subjects and belt geometry were chosen to match those used in the volunteer study (Arbogast et al., 2009). Torso angle (as measured between the spinous process of T1, the position of the greater trochanter and the horizontal) was set (nominally) to 110 degrees in the cadavers. The angle between the femur and the tibia at the knee joint was also set (nominally) to 110 degrees. Initial head angle in the sagittal plane was set at zero degrees. Figure 4.3 shows the initial position of one of the test subjects.

Table 4.1 PMHS anthropometry and characteristics.

	PMHS 1	PMHS 2	PMHS 3
Test number	1397, 1398	1401, 1402	1404, 1405
Age (years)	59	69	60
Gender	Female	Male	Male
Cause of death	Renal failure	Renal failure	Renal failure
Stature (cm)	167	178	191
Weight (kg)	80	84	81
Seated height (cm)	93	92	93

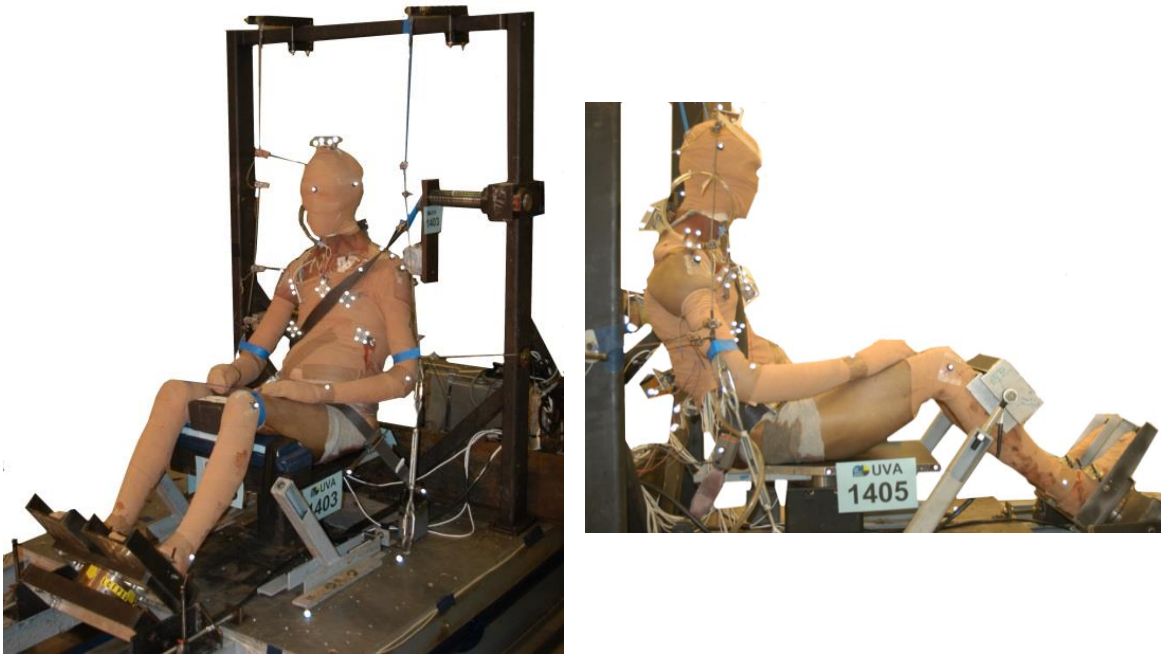


Figure 4.3 Frontal and side view of a PMHS showing the position of the reflective markers on the subject. Note that the absence of knee bolster at low-speed (left).

4.2.3 Instrumentation

Optical instrumentation.

Orthogonal arrays of four markers were attached to the superior aspect of the skull, right acromion, T1, T8, L2, L4, pelvis, 4th and 8th ribs bilaterally and sternum. These arrays allow the 6 DOF reconstruction of the motion of each bony structure. The method first obtains the transformation matrix between the coordinate system defined by the array of markers and the local coordinate system of the bone (T_M^B). Then, this matrix can be combined with the transformation matrix between the coordinate system of the array of markers and any other coordinate system defined within the VICON volume (T_G^M). The combination of these two matrices makes possible obtaining the position and orientation of a local coordinate system with

respect a different coordinate system according to Equation 4.1 (Kinzel et al., 1972). This process is schematized in Figure 4.4.

$$T_G^B = T_M^B \cdot T_G^M \quad \text{Equation 4.1}$$

A coordinate system attached to the test fixture (BCS), with the X axis pointing forward, the Z axis pointing upwards and the Y axis chosen to complete a right-handed orthogonal coordinate system was selected. The creation of each bony local coordinate system (LCS) as well as detailed information on the processing of the data is described in Shaw et al. (2009) and the position and orientation of these local coordinate systems are shown in Figure 4.5. In addition to the marker clusters, individual markers were used to determine the position of selected anatomical landmarks.

Kinematic data were obtained using a 16-camera Vicon MX™ motion capture system operating at 1000 Hz. The cameras tracked the motion of spherical retroreflective targets within the cameras' collective viewing volume. A calibration procedure, performed prior to testing each subject, estimated the optical characteristics of each camera and established its position and orientation in a reference coordinate system. With this information a photogrammetric algorithm within the Vicon Nexus software package reconstructed the 3D position of each target for each video sample increment from the multiple 2D camera images.

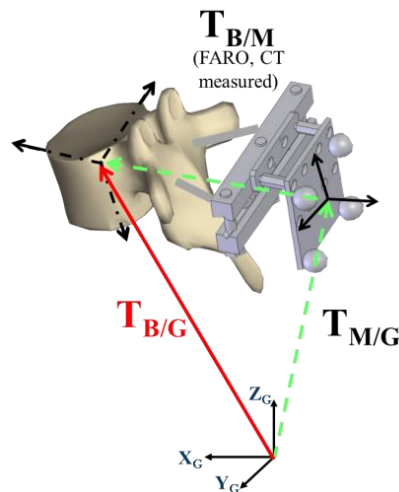


Figure 4.4 Schematic showing the transformations between coordinate systems to report the position with respect to the buck coordinate system (BCS).

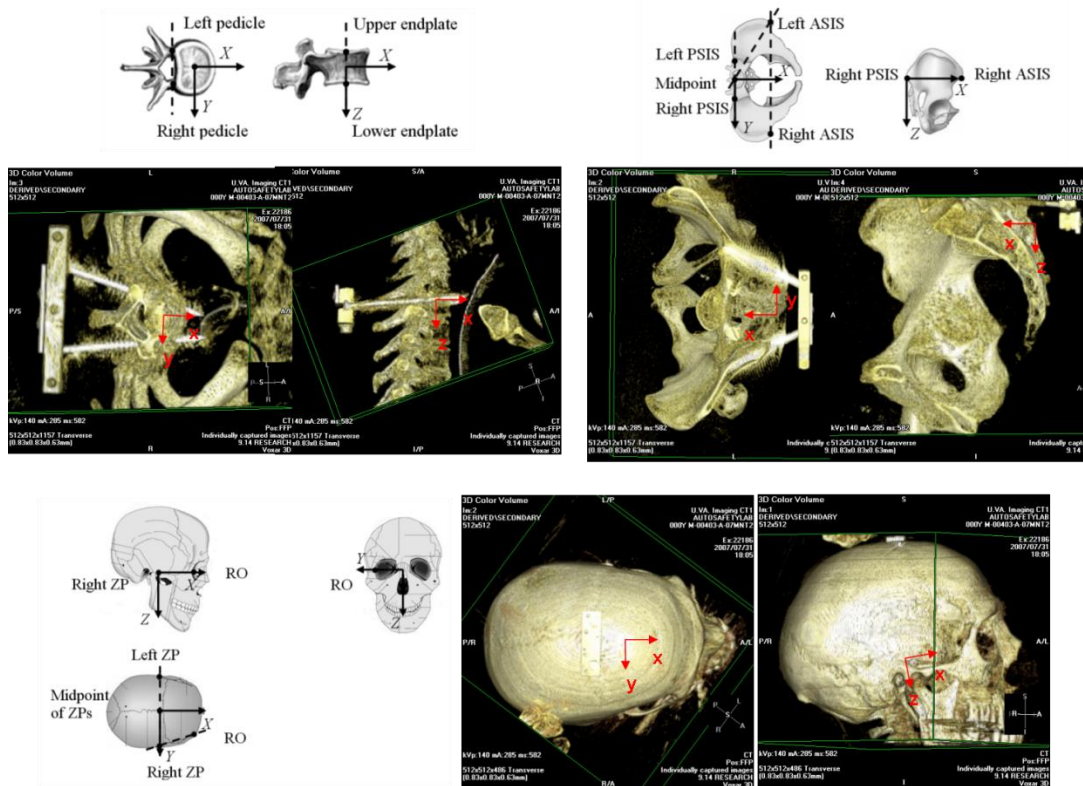


Figure 4.5 Definition of the local coordinate systems (LCS) attached to each considered bony structure.

Other (non-optical) instrumentation. Tri-axial accelerometers (Endevco model 7264B) were mounted on the head, T1, T8, L2 vertebrae and the pelvis. Tri-axial angular rate sensors (DTS model ARS-12k) were also used on the head and T1. All these instruments were rigidly attached to the corresponding anatomical structure through mounting plates screwed into the bones. The relative position and orientation of these sensors with respect to the center of gravity of the bone was obtained using CT images, allowing for transformation between the local instrument coordinate system and the corresponding local anatomical system. A comprehensive description of cadaver preparation and sensor installation can be found in Shaw et al. (2009). Tension belt gages (Model 419-3.5 K, Eaton Lebow) were attached to three locations on the seatbelt (upper shoulder, inner lap and outer lap portions). Load cells measuring the reaction forces and moments were used under the seat, in the knee bolster and under the feet support. Instrument data were collected using an onboard TDAS data acquisition system at 10000 Hz.

4.2.4 Elongation of the spine during the forward motion of the occupant

The elongation of four spinal sections (head-T1, T1-T8, T8-L2 and L2-pelvis) was calculated as the change in distance between the center of the corresponding LCS origin of each of the anatomical structures. The calculation was performed at every millisecond between the beginning of the deceleration (t_0) and the time of maximum forward head excursion (t_{max}). The elongation at each time t was defined according to Equation 4.2:

$$Elongation = \frac{L(t) - L_0}{L_0} \quad \text{Equation 4.2}$$

where $L(t)$ is the actual distance between the considered rigid bodies at time t and L_0 is the distance at t_0 .

4.3 RESULTS

All analyses were done up to the time of maximum forward head excursion (t_{max}) and reported with respect to the buck coordinate system (BCS), unless otherwise noted.

4.3.1 PMHS kinematics in the sagittal plane (XZ)

The analysis of the kinematics of the cadavers in the sagittal plane was published in Lopez-Valdes et al. (2010b). Table 4.2 and Table 4.3 show the maximum forward excursion and timing of the head, spine and pelvis each PMHS at 9 km/h and at 40 km/h.

Table 4.2 Peak forward displacement of PMHS head, vertebrae and pelvis. 9 km/h. X(mm), time (ms).

	PMHS1		PMHS2		PMHS3	
	X	t	X	t	X	t
Head	283.8	233 (t_{max})	291.6	239 (t_{max})	319.7	291 (t_{max})
T1	211.0	223	203.7	200	217.3	207
T8	161.4	190	129.7	180	157.7	167
L2	95.78	162	80.40	154	108.4	148
Pelvis	51.96	149	58.5	141	67.5	131

Table 4.3 Peak forward displacement of PMHS head, vertebrae and pelvis. 40 km/h. X(mm), time (ms).

	PMHS1		PMHS2		PMHS3	
	X	t	X	t	X	t
Head	493.8	126 (t_{\max})	572.2	125 (t_{\max})	525.4	130 (t_{\max})
T1	428.2	133	457.2	133	418.7	134
T8	385.7	132	346.4	117	327.7	128
L2	242.2	124	208.5	106	208.9	116
Pelvis	104.4	120	67.51	117	64.85	113

The trajectories of the selected anatomical locations in the XZ sagittal plane are shown in Figure 4.6, comparing the kinematics observed at 9 km/h and those at 40 km/h for the same subject. Blue dashed lines connect the position of the head, the spinal segments and the pelvis every 50 ms and until the time of maximum head forward excursion (t_{\max}).

At 9 km/h, the forward displacement (X) of the upper segments of the spine and the head lagged the lower segments. The values in Table 4.2 and the low-speed plots in Figure 4.6 show that the head and upper spinal segments reached their peak forward excursion only after the pelvis and lower spine were already rebounding and moving in the negative X direction. All the body segments described almost a parallel trajectory moving in the positive X and Z directions up to the moment in which the head started to describe a curvilinear trajectory in flexion at around $t=150$ ms.

At 40 km/h, the motions of the head, spinal segments and pelvis were more synchronous, reaching their peak forward excursion at about the same time as shown in Table 4.3. Despite of using a knee bolster at this speed, there was considerable forward motion of the pelvis, made possible by a simultaneous vertical displacement. The pelvis of the subjects underwent a rotation about the knee bolster that acted as fulcrum. The curvilinear translation of the pelvis was not transmitted to the contiguous segments of the spine. The vertebrae exhibited mostly a translation in the X direction with increasing amplitude along the spine from the lumbar to the cervical portion. The trajectory of the head remained parallel to that of the vertebrae until shortly before 100 ms, instant in which the head started to describe a curvilinear trajectory in flexion.

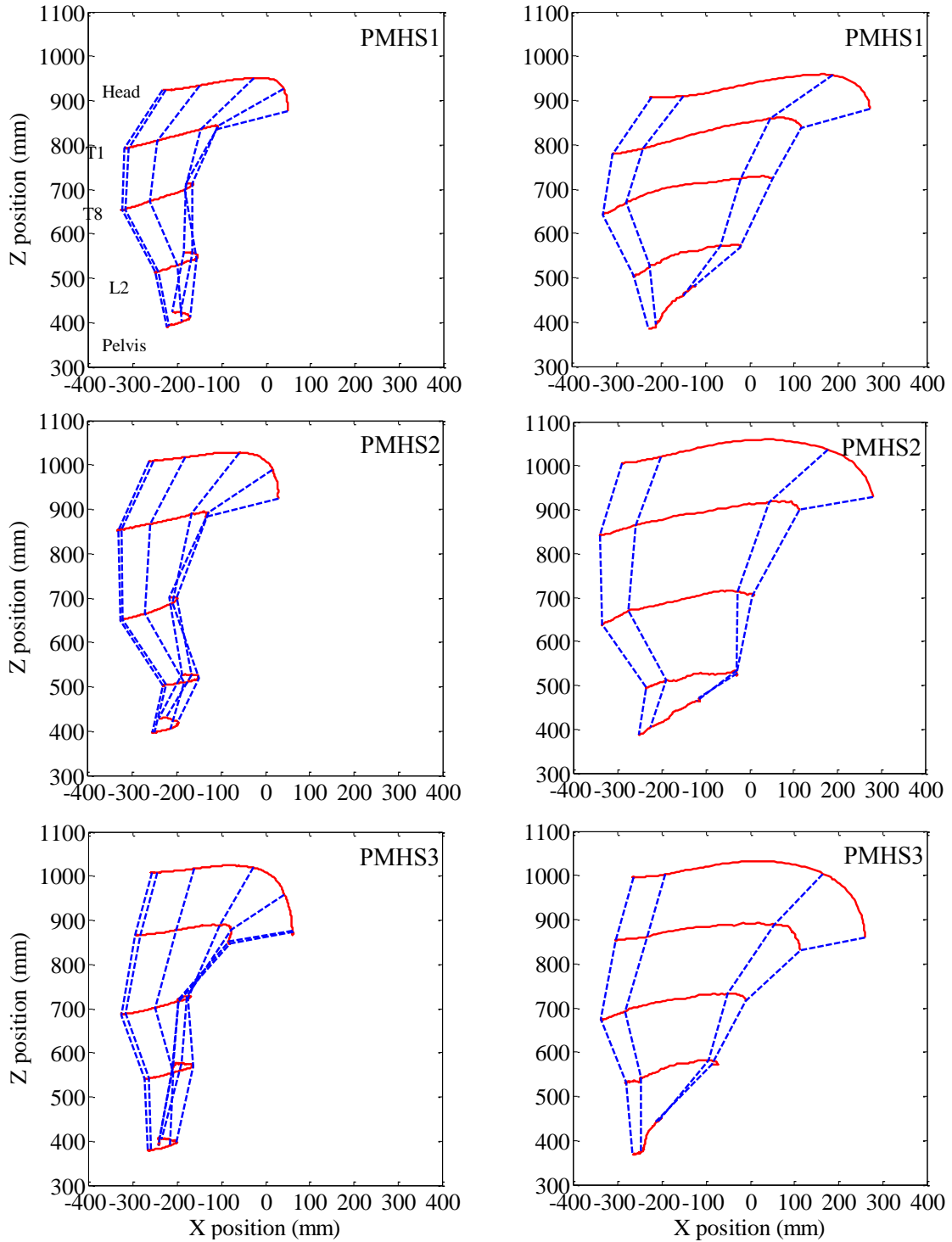


Figure 4.6 Trajectories (solid red lines) of the head, T1, T8, L2 and pelvis at 9 km/h (left) and 40 km/h (right) in the XZ sagittal plane with respect to the BCS. Dashed blue lines connect the position of the anatomical structures every 50 ms.

4.3.2 PMHS average displacement in the sagittal plane and development of corridors

Lopez-Valdes et al. (2012) reanalyzed the data from the cadaveric experiments, calculating the displacement response of the average 50th percentile PMHS and the associated displacement corridor. Similarly to what had been done previously with the reanalysis of the volunteers, the methodology proposed in Lessley et al. (2004) was used to estimate the response of the average subject within the 50th percentile group and the associated kinematic corridor. The subjects were mass-scaled to a 50th percentile size (Eppinger, 1984) before combining their individual responses. The reanalysis focused on the head, thoracic spine and pelvis with the purpose of comparing the observed PMHS kinematics with those of the volunteers and to be used in the methodologies to predict the kinematics of a 6YO that are the subject of subsequent chapters in this dissertation.

Figure 4.7 and in Figure 4.8 show the corresponding average sagittal trajectory and associated corridor of the low-speed and high-speed tests. Blue solid lines correspond to the average response of the 50th percentile size and the blue shaded area is the associated corridor. The thin dotted lines are the individual responses of the three subjects before combining them. Finally, the solid blue dots mark the position of each anatomical structures at $t=0$, every 50 ms and then at $t=t_{max}$.

Obviously, the results obtained in the reanalysis of the data do not differ substantially from those presented in the previous subsection although this treatment allows describing the displacement response of an average PMHS subject during a 9km/h and 40 km/h frontal impact in the specific loading conditions of the test setup described earlier.

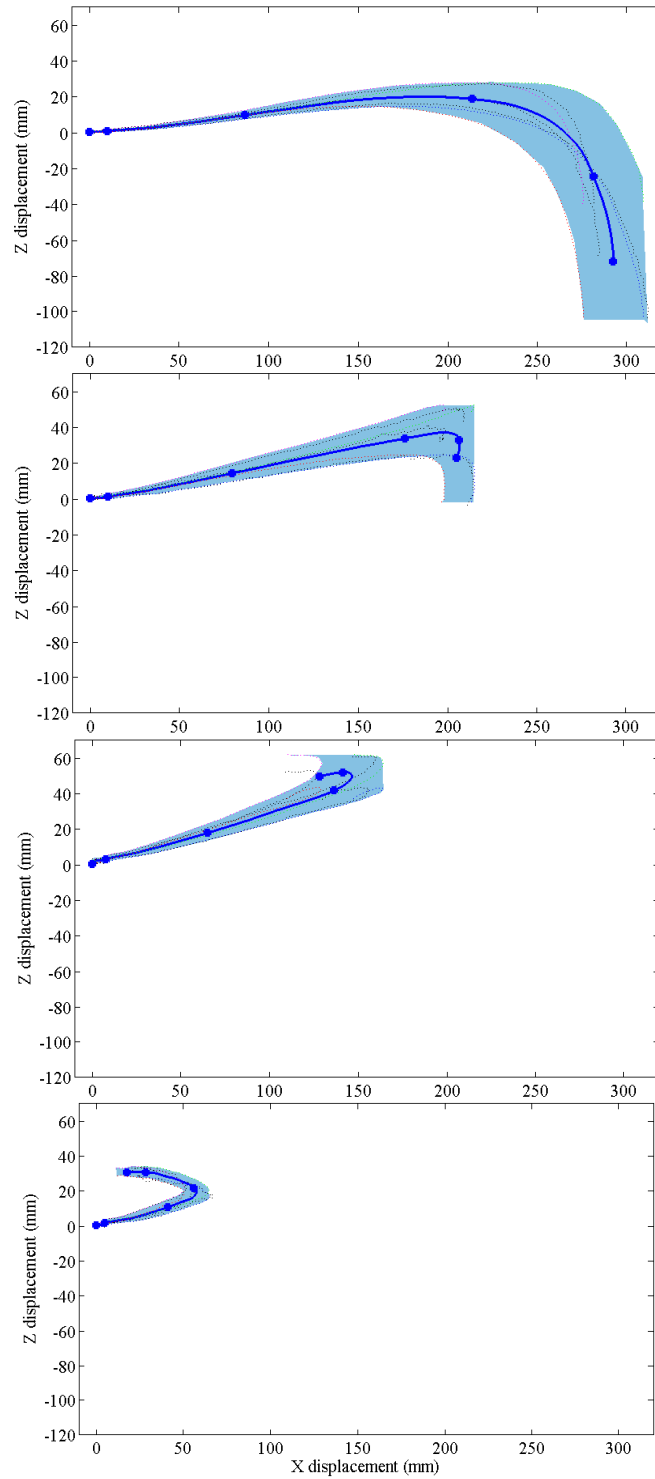


Figure 4.7 Normalized average displacements (solid blue line) and displacement corridors (shaded area) of the PMHS head T1, T8 and pelvis at 9 km/h.. Dots indicate the position of the relevant structure every 50 ms and at the maximum head excursion.

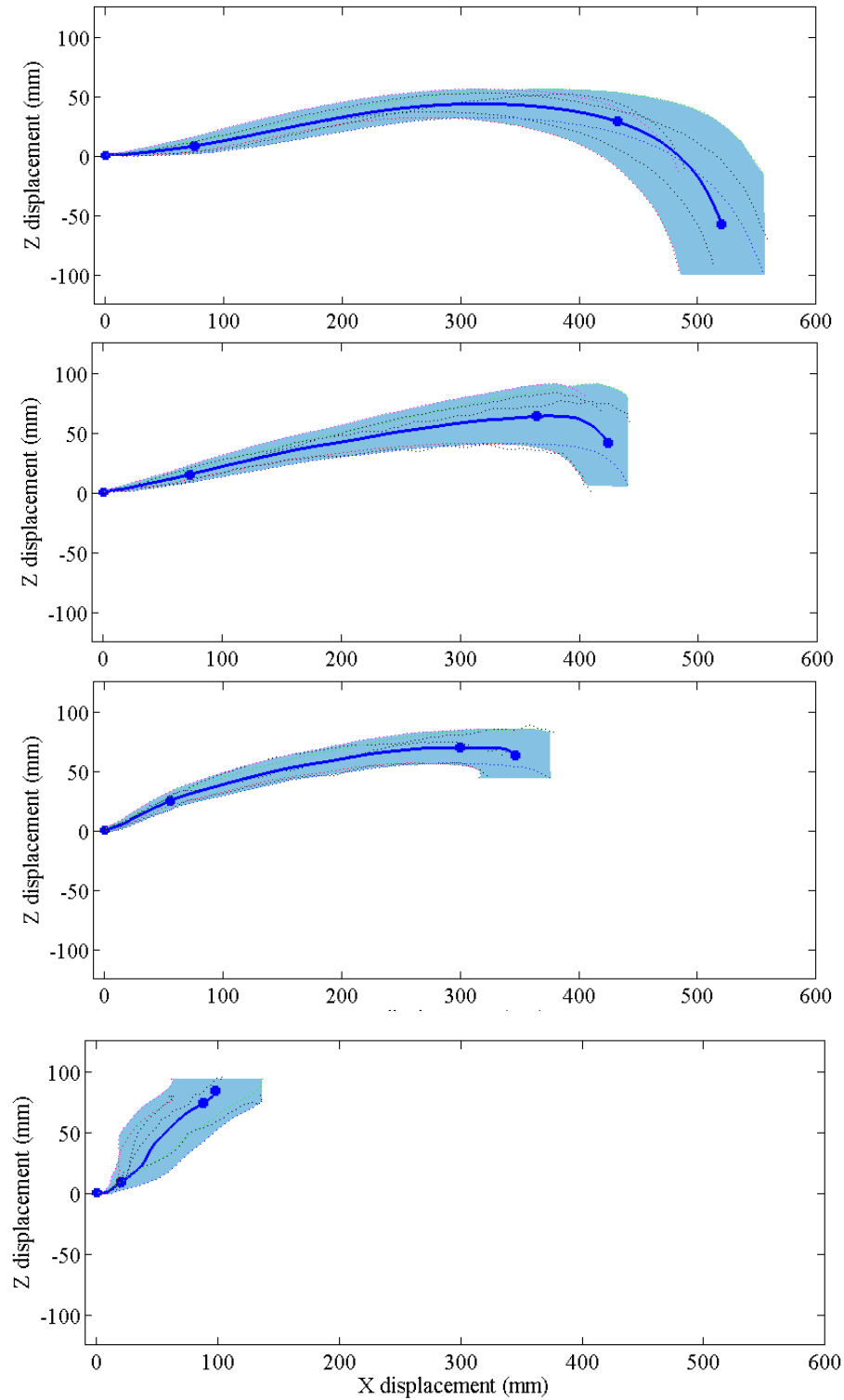


Figure 4.8 Normalized average displacements (solid blue line) and displacement corridors (shaded area) of the PMHS head, T1, T8 and pelvis at 40 km/h. Dots indicate the position of the relevant structure every 50 ms and at the maximum head excursion.

4.3.3 PMHS kinematics in the XY plane

The motion of the head and spinal segments of the PMHS was also analyzed in the XY plane of the BCS. Table 4.4 and Table 4.5 show the maximum Y displacement of the origin of the LCS, and the corresponding time. It was observed that the asymmetry of the shoulder belt loading induced the upper trunk to rotate about the left shoulder of the occupant, which acted as fulcrum. The lateral motion of the anatomical structures was greater in the 40 km/h tests.

Table 4.4 Peak lateral displacement of PMHS head, vertebrae and pelvis. 9 km/h. Y(mm), time (ms).

	PMHS1		PMHS2		PMHS3	
	Y	t	Y	t	Y	t
Head	59.3	233	41.2	239	72.3	291
T1	55.2	233	67.1	237	56.4	291
T8	41.1	233	47.6	239	30.7	250
L2	29.2	233	33.9	227	37.3	217
Pelvis	30.9	195	28.0	239	49.7	195

Table 4.5 Peak lateral displacement of PMHS head, vertebrae and pelvis. 40 km/h. Y(mm), time (ms).

	PMHS1		PMHS2		PMHS3	
	Y	t	Y	t	Y	t
Head	129.2	126	93.2	125	108.6	130
T1	51.6	126	55.7	125	80.6	130
T8	17.8	126	46.0	125	16.6	130
L2	20.2	120	61.1	125	28.4	121
Pelvis	29.21	126	78.7	125	44.7	127

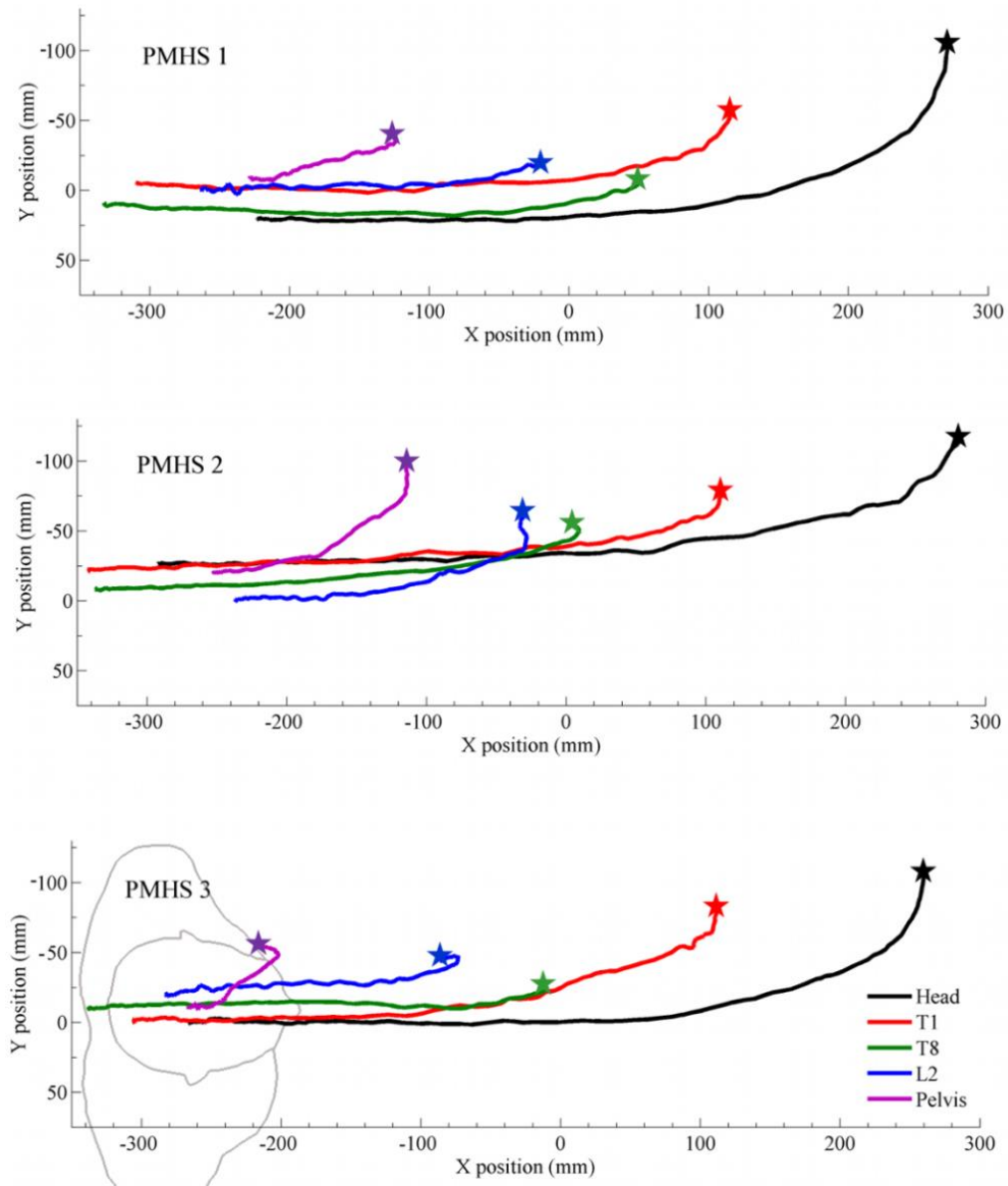


Figure 4.9 Trajectories of the PMHS head, spine and pelvis in the XY plane of the BCS at 40 km/h (* indicates the final position of the structure).

The trajectories of the LCS in the XY plane at 40 km/h are showed in Figure 4.9. The lateral component of the upper structures (head, T1) was, in general, greater than the one measured for the lower spinal segments. Despite the predominance of forward displacement, the ratio between lateral (Y) and anterior (X) peak motion at the T1 level varied between 12% and 19%, while the same ratio for the head varied between 16% and 26%.

4.3.4 Elongation

The elongation of the segments head-T1, T1-T8, T8-L2 and L2-pelvis was calculated according to Equation 4.2. Figure 4.10 shows the time history of the elongation of the sections between t_0 and t_{\max} .

At 9 km/h, only the elongation between the head and T1 and between L2 and the pelvis were noticeable. PMHS1 (test 1397) exhibited an elongation slightly greater than 10% between the head and T1, while the magnitude of the elongation of this section in PMHS2 (test 1401) was about 5%, being even smaller in the case of PMHS3 (test 1404). The elongation started to be different than zero at about $t=150$ ms for all three subjects. As for the L2 to pelvis segment, the value of the elongation reached 10% in the case of PMHS1 and PMHS3, starting to rise at $t=120$ ms. In all the low speed cases, whenever there was a relevant change in elongation, this change was always positive (i.e. the spinal section stretched).

The response found at 40 km/h demonstrated clear differences with respect to the one observed in the 9 km/h tests. First, the magnitude of the stretch was greater than 10% for all the four spinal segments in the three PMHS. Second, the upper portions (head-T1 and T1-T8) exhibited both positive and negative values of elongation: these segments did not only stretch, but also shortened during the event (likely induced by flexion of the spine). On the contrary, the lower portions (T8-L2 and L2-pelvis) only stretched during the deceleration. In the case of PMHS2 (test 1402), the L2-pelvis section shortened at the end of the test probably related to the femur fracture observed for this subject.

The magnitude of the shortening of the head to T1 and T1 to T8 segments reached a 5% value only in PMHS1 (Test 1398) and it happened early in the motion of the occupant (around $t=50$ ms). The magnitudes of the negative elongation in the head to T1 and T1 to T8 sections of PMHS2 and PMHS3 were smaller than 5%.

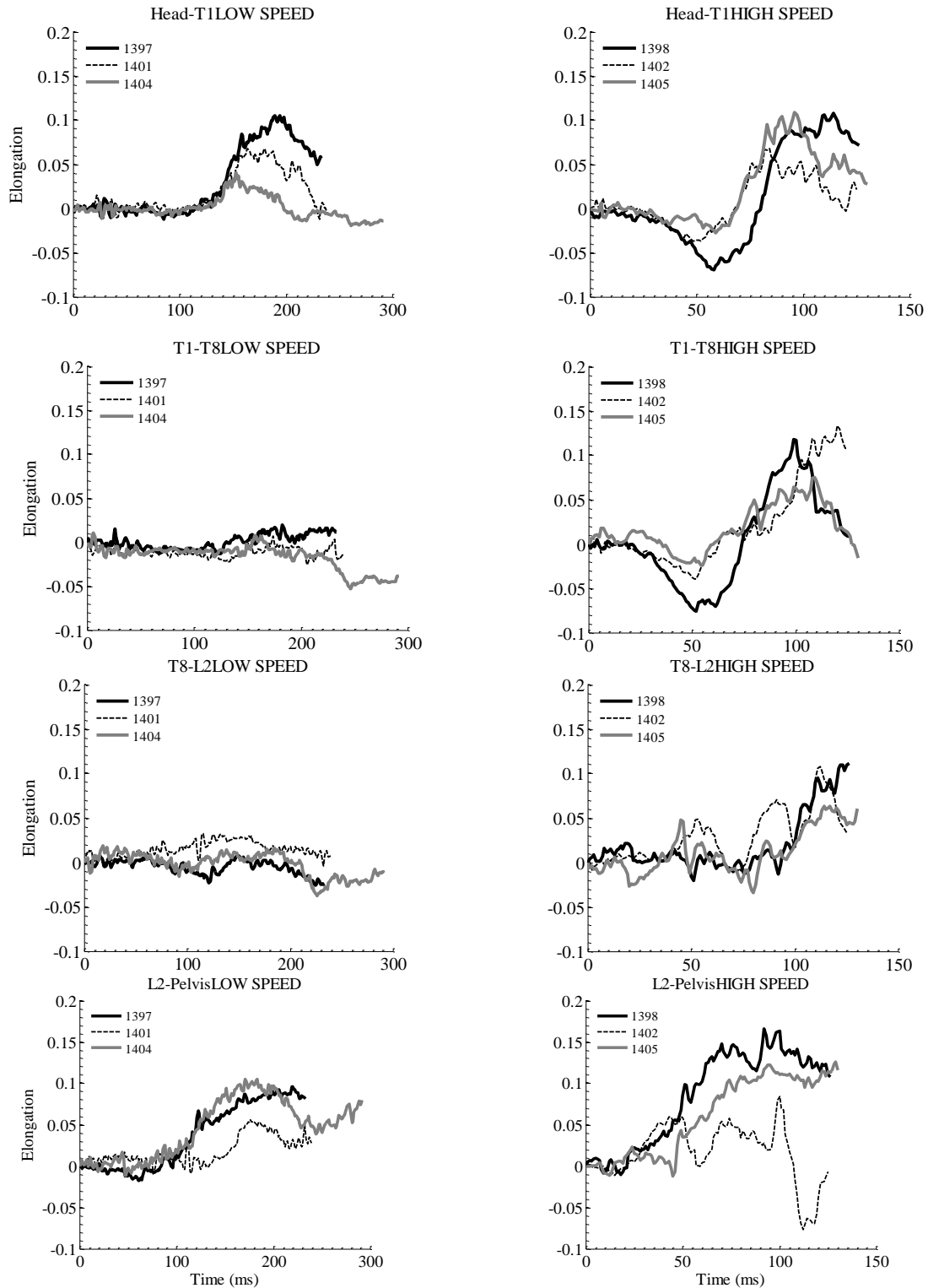


Figure 4.10. Elongation of spinal segments (head to T1, T1 to T8, T8 to L2 and L2 to pelvis) at 9 km/h (left column) and 40 km/h (right column)

As for the magnitude of the stretch, peak values of the head to T1 segment were around 10% for PMHS1 and PMHS3. Peak positive elongation of PMHS2 in this section was smaller. These magnitudes were not substantially different from the values found at 9 km/h. The main differences observed between the two speeds were the positive elongation in the intermediate segments (T1 to T8 and T8 to L2) found at 40 km/h. The magnitude of the stretch in these section was comparable to that observed between T1 and the head. Also the magnitude of the stretch in the lowest section was slightly greater than the one observed in the other spinal sections in the case of PMHS1 and PMHS3. Again the different elongation response of PMHS2 in this section was probably caused by the femur fracture experienced by the subject.

4.4 DISCUSSION

4.4.1 Influence of muscle activation

As shown in Chapter 2 of this dissertation, PMHS tests were used in the assessment of the methodologies developed to predict the kinematics of children in frontal impacts, as well as in the prediction itself. In the latter application, PMHS tests were used as a proxy for the response of adult volunteers at 40 km/h as described in Figure 2.3. Therefore, it is relevant for the focus of this dissertation to compare the response of the PMHS with the response of the adult volunteers. The comparison between the responses of the two types of surrogates was made possible due to the similar test environment used with the volunteers and the PMHS at 9 km/h.

There were two substantial differences between the trajectories of the volunteers and those of the PMHS: the first one was the differences in the magnitude of the peak displacement and the second one was the difference in the shape of the trajectory. Figure 4.11 shows the combined plots of the displacement and corridor of the average 50th PMHS and the average 50th adult volunteer.

As for the magnitude, the forward excursions of the head, T1 and T8 of the PMHS at 9 km/h were always greater than the ones observed in the adult volunteers. The difference was particularly important in the head, in which the magnitude of the PMHS excursion was twice the value of the head excursion of the volunteer (293.3 mm vs. 147.2 mm), and in T1 (206.4 mm vs. 121.9 mm).

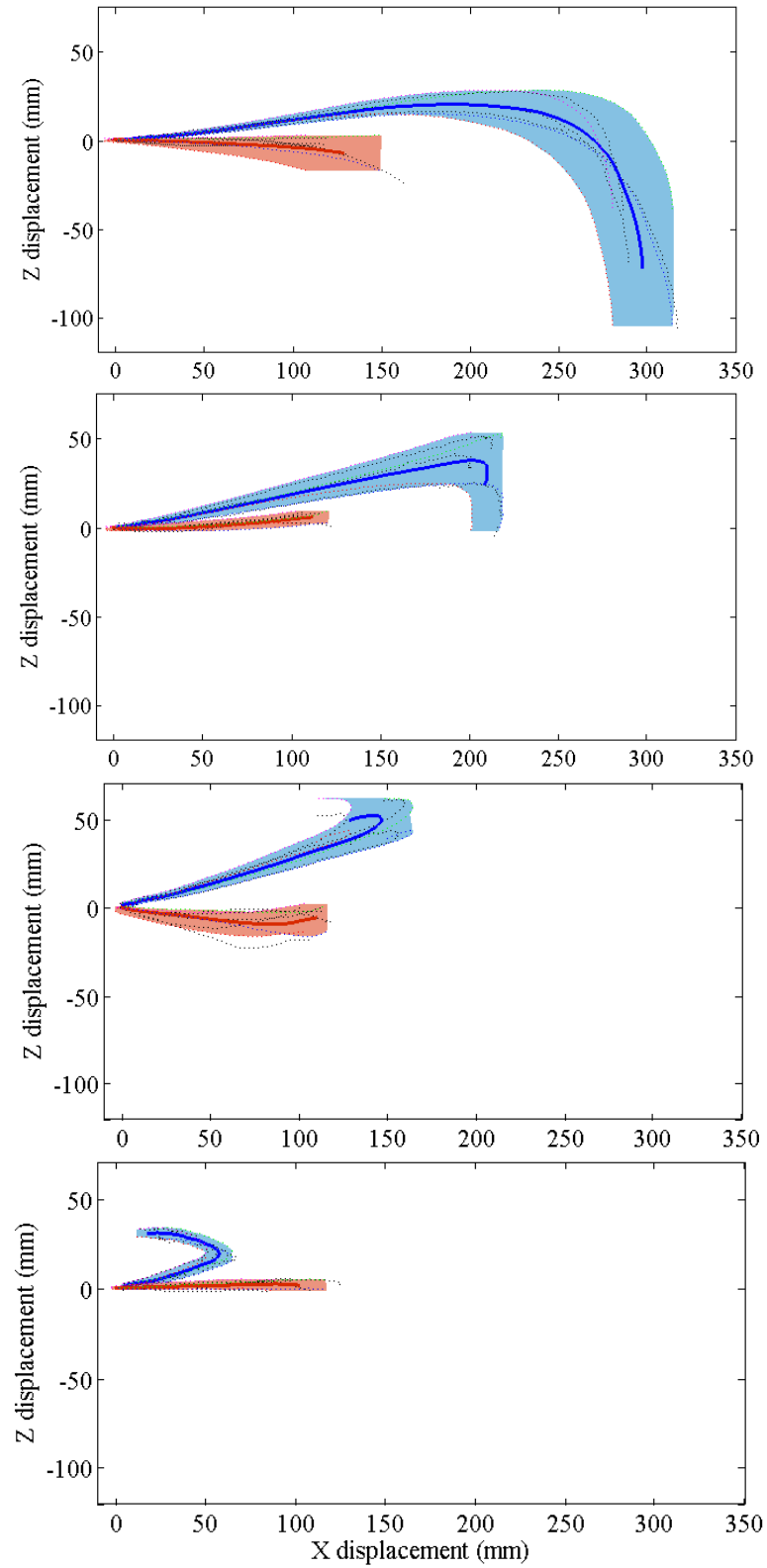


Figure 4.11 From top to bottom, comparison of the head, T1, T8 and pelvis sagittal trajectories between adult volunteers and PMHS at 9 km/h.

Although the displacement of T8 was also found to be greater in the average PMHS, the forward excursion of the volunteer pelvis (102.7 mm) was larger than the PMHS one (57.5 mm).

It was also remarkable that the displacements of the cadaveric structures were no longer parallel to the X axis, but there was a Z component that initially was positive and transitioned to negative in the case of the head and T1 when these structures were reaching their peak forward excursion. As for T8 and the pelvis, these structures were moving backwards (rebounding) from $t=150$ ms approximately, either maintaining its position in the Z axis (T8) or still moving upwards (pelvis). In the volunteer results, T8 and the pelvis were still moving forward in phase with the head and T1 motions. In summary, the average volunteer showed an in-phase motion of all the tracked structures while the PMHS head and T1 were still moving forward while the lower segments were already in the rebound phase.

These differences can be partially attributed to the lack of muscular activity in the PMHS. The muscle response of some of the volunteers in the Arbogast study was recorded using EMG electrodes. Mathews et al. (2012) analyzed some common patterns across subjects that can be used to understand the influence of muscle activity in the differences seen between adult volunteers and PMHS.

First, despite being asked to remain relaxed during the tests, all the volunteers showed contraction in several muscle groups. This was an involuntary response to resist the motion imposed by the firing of the sled. In particular, it was observed activation of the cervical paraspino (neck extensor), upper trapezius (which can act also as a neck extensor, if the scapulae are stable) and sternocleidomastoid (neck flexor, bilaterally), and also of the erector spinae (back extensor) and rectus femoris (hip flexor or knee extensor), although the activation levels were lower. This muscle contraction likely influenced the kinematics of the occupants and it is potentially one important factor in the different kinematics exhibited by the adult volunteers and adult PMHS, as shown in Figure 4.11. The contraction of the muscle groups controlling the motion of the head, neck and back could explain the great differences in magnitude in the forward excursion of the head and T1 between the PMHS and the volunteers. Most of the activated muscle groups are extensors of the neck and back, and therefore prevented the flexion of these structures. The contraction of these muscles can explain why flexion of the head and T1 was not observed in the volunteers up to the instant of maximum head excursion.

The rectus femoris is a hip flexor and since the position of the feet was fixed on the footrest, the contraction of this muscle can explain the increased forward displacement of the pelvis of the volunteers compared to the cadaveric one.

Mathews et al. (2012) did not find significant differences in the activation times across different age groups in the volunteers group. The latency period for all subjects (defined as the time between the beginning of the deceleration and the five percent normalized peak EMG amplitude) fell well within the time before the head reached its maximum forward excursion.

The question about the muscle activation time is of particular interest if the results from the low-speed volunteer tests are to be extrapolated to a high-speed impact. The results reported by Mathews et al. (2012) proved that should the same velocity of response of the muscles can be assumed at higher speeds, the action of these muscles groups would have influenced the kinematics of the occupants at 40 km/h. However, trying to estimate the level of activation of the muscle would be just a blind guess exercise, not based on any experimental known experimental data. It suffices to acknowledge that there is likely a difference in the behavior of PMHS and volunteers at higher speed caused by the contraction of the muscles.

4.4.2 Influence of the femur fracture observed in PMHS2 in the kinematics of the spine

Figure 4.6, Figure 4.9 y Figure 4.10 showed that PMHS2 exhibited some differences in the response of the pelvis and lower spine section at 40 km/h in comparison with the other two subjects. The post-test computer tomography scan and autopsy found that a fracture of the left femoral neck had occurred during the tests. The differences in the response of this cadaver were attributed to the fracture.

Although no substantial differences were observed in the overall displacement of the head and spine in the thoracic segments and head (Figure 4.8), the changes in the displacement of the pelvis likely propagated along the spine of the subject. Thus, whenever needed in the analyses done within this dissertation, results from PMHS2 at 40 km/h were considered only up to 40 ms or not considered at all.

4.5 CONCLUSION

Three PMHS were exposed to a low-speed frontal impact that matched the loading environment used with the adult volunteers. Subsequently to this impact, the same PMHS were exposed to a 40 km/h one.

The trajectories in the XZ and XY plane were calculated at both speeds, identifying the differences in the response of the anatomical structures analyzed in the study between the two impact speeds. There were also differences in the elongation of spinal segments: while the thoracic spine did not exhibit any substantial change in length at 9 km/h, the elongation was comparable to that of the cervical and lumbar regions at 40 km/h.

The instrumentation used in the tests allowed comparing the kinematics of the head and thoracic spine between the PMHS and the volunteers at 9 km/h. Important differences were found in the comparison between the two types of occupants and these differences were attributed to the muscle activity in the volunteer group. While acknowledging that this is a limitation in the comparison, in the absence of other experimental data at 40 km/h, PMHS will be chosen as a proxy for the living human response at high impact velocities when needed.

The data from these PMHS tests were used in the validation of the methodologies that were used to obtain the prediction of the pediatric trajectories at 40 km/h as well as in the predictions themselves. The results shown here are relevant to understand potential limitations of the referred methodologies.

5 THORACIC SPINE CHARACTERIZATION

5.1 INTRODUCTION

As explained in Chapter 2, the thoracic spine characterization tests were performed as auxiliary tests to assist in the development of the occupant model to be described in chapter 7. However, the characterization of the flexion behavior of the human thoracic spine constitutes an original contribution in itself and it was decided to dedicate its own chapter to the topic.

The results included here are the first known characterization of the *in vitro* mechanical behavior of the human thoracic spine in dynamic bending. An additional contribution to the existing body of literature was that this characterization was done both for adult and pediatric specimens. The chapter starts providing context to these experiments by reviewing previous literature on the mechanical behavior of the cervical pediatric spine (the only region of the human spine that had been characterized for pediatric specimens), on the mechanical response of the human thoracic spine (up to this moment, done in quasi-static conditions and for adult specimens) and on the scaling between the pediatric and adult cervical response.

After providing the review of the literature, the chapter describes the methods and provides the main results obtained from the experiments. The results that are included in the chapter are limited to the coefficients of the mathematical model used to describe the mechanical behavior of the thoracic spine and to those that were most directly related to the aims and objective of the dissertation. These results were used to investigate the following two hypotheses:

- a) That the instantaneous elastic response of different sections along the thoracic spine is the same within the same subject.
- b) That the instantaneous elastic response of a pediatric specimen is similar to that of an adult at the same thoracic level.

All other results and a detailed description of the methods are included in Appendix A1. The chapter finishes discussing the findings in light of the previous research reviewed in section 5.2.

5.2 REVIEW OF RELEVANT TESTS ON THE CHARACTERIZATION OF THE SPINE

5.2.1 Pediatric cervical spine

A handful of publications have addressed the biomechanics of the human pediatric cervical spine. The comparison between them is not always possible due to the differences in goals and methodologies and the reduced sample sizes. In occasions, some of the studies even report conflicting information that might be related to the relative low number of specimens tested. For instance, while Ouyang et al. (2005) could not find a relationship between the tensile failure of the cervical spine with age, Luck et al. (2008) found that the tensile tolerance of the upper cervical spine increased significantly with age. Table 5.1 summarizes the methodology and main outcomes of these papers.

The study by Ouyang et al. (2005) is of particular interest for this dissertation since it is the only one in which the pediatric neck was exposed to a bending moment in the sagittal plane. The study reported a mean bending stiffness of the whole pediatric neck of 0.041 ± 0.007 Nm/deg. The mean stiffness value was calculated independently for two different groups of age and no significant differences were found between them (2-4 years old vs. 5-12 years old). The range of moments applied to the specimens varied between 2.4 Nm (flexion) and -2.4 Nm (extension) to ensure that neither macro nor micro-damage was produced. The study also found that the range of motion of the lower cervical spine was larger than that of the upper cervical spine.

Even though the comparison between the tensile failure forces from the different studies has undeniable interest, the application to the purposes of this dissertation research is limited. Therefore, although the studies focusing on the tensile behavior of the pediatric cervical spine are included in Table 5.1 for reference, they will not be further discussed here.

Table 5.1 Summary of studies on the biomechanics of the pediatric cervical spine

Study	# spec	Age (years)*	Goal	Results	Other considerations
Duncan (1874)	5	0-2 weeks	Tensile failure force	Stillborn failure F=471±79 N 2-week failure F=654 N	Injuries distributed from C3-C7. Whole cadavers tested
McGowan et al. (1993)	1	8 hours	Quasi-static tensile test of cervical, thoracic and lumbar segments	Fixation failure in cervical and thoracic tests. Only failure of lumbar reported	NA
Ouyang et al. (2005)	10	2-12	Sagittal bending. Tensile tests (viscoelastic characterization and failure).	Bending stiffness: K _B =0.041Nm/deg Tensile failure F=726±121 N Displacement at failure d=20.2±3.2 mm	Injuries happened at the lower cervical spine, maybe due to artifactual fixation. Range of moments - 2.4 Nm (extension)– 2.4 Nm (flexion)
Luck et al. (2008)	11	20 weeks gestation – 14	Tensile tests. Viscoelastic characterization (tensile force vs. extension) and failure tensile force	Neonatal failure: C1-C3: F=213±52 N C4-C5: F=186±63 N C6-C7: F=162±35 N Older cohort: upper cervical spine significantly stronger than lower. Upper spine failure load increases with age (from 462 N to 2920 N)	Strength of upper cervical spine increases with age Sample size of the older cohort was very limited

* Unless otherwise specified.

Apart from the previous studies on the pediatric human cervical spine, there is a number of published papers using animal models to study the mechanical behavior of the immature spine. Two different species have been proposed as surrogates of the pediatric neck: caprine and baboon specimens. Most of these studies compared the mechanical response of immature specimens to mature ones, providing the bases for developing scaling factors between different stages of tissue development. Table 5.2 provides a summary of these studies.

Table 5.2 Summary of studies on the biomechanics of the immature cervical spine using animal models.

Study	# spec	Age (years) [*]	Animal model and goal of the study	Results	Other considerations
Pintar et al. (2000)	16	1-12, adult	Caprine model. Cervical spine dissected into functional spinal units. Flexion/extension, lateral bending, tensile failure.	Tensile failure load, tensile stiffness and bending stiffness scaling factors increase with age	
Ching et al. (2001)	17	2-26	Baboon. Cervical spine dissected into functional spinal units. Tensile loading.	Tensile stiffness and failure load increased significantly with age	
Hilker et al. (2002)	18	Adult (different sizes)	Caprine model. Cervical spine dissected into functional spinal units. Pure moment and axial loading (including failure).	Flexion bending stiffness (Nm/deg): KF=0.4 (small), KF=0.44 (mid), KF=0.42 (large) Extension bending stiffness (Nm/deg): KF=0.35 (small), KF=0.45 (mid), KF=0.45 (large)	Pediatric scaling factors from Pintar et al. (2000) were updated after the findings of this study. Some of the results from Pintar et al. (2000) were corrected in this study.
Nuckley et al. (2002)	22	1-30	Baboons. Cervical spine dissected into functional units. Dynamic compression (1.0 m/s)	Compressive failure load increased significantly with age.	
Nuckley and Ching, 2006)	18	1-26	Baboons. Cervical spine dissected into functional units (Oc-C2, C3-C4, ..., C7-T1). Non-destructive compression and tension and failure in tension.	Increasing stiffness and normalized stiffness with age both in tension and compression. Increasing failure tensile load and normalized failure load with age.	Previous literature supported the use of baboon spine as a good model for the human one.

^{*} human equivalent years.

Ching et al. (2001) used baboon specimens as models for the human developing spine. The specimens were loaded dynamically in tension (0.5 mm/s). The test subjects were divided into 4 groups (3-years old,

6-years old, 12-years old and adults) to study the relationship between failure tensile load and stiffness and spine development,. Both properties were significantly correlated with human equivalent age, regardless of the spinal level. The study also reported significant differences in both mechanical properties between the Oc-C2 level and all the other levels for the 3-years old, 6-years old and 12-years old groups.

The study by Hilker et al. (2002) is particularly interesting for this dissertation research since the caprine specimens were subjected to a pure bending moment ranging from 0.33 Nm to 2.0 Nm in both the sagittal (flexion-extension anatomical motions) and the frontal planes (lateral bending). However, other than the estimation of the bending stiffness showed in Table 5.2, no other test results were provided. The paper combined the responses of the three sizes of adult caprine specimens to update the scaling factors for immature specimens that had been previously reported by Pintar et al. (2000). The methodology used to update these scaling factors is not described in the paper and therefore, no further discussion on the differences between the results from both papers can be offered here. Interestingly, the paper includes an erratum to the data published in Pintar et al. (2000) without specifying why the update was needed. The data in Hilker et al. (2002) showed also an increase in tensile failure force, tensile stiffness, flexion stiffness, extension stiffness and lateral bending stiffness with age. The authors did not provide any assessment of the significance of this trend.

Nuckley et al. (2002) reported that the upper cervical spine of a baboon model exhibited the lowest tolerance to compression up to 8-human-equivalent years, while the lower spine had the smallest tolerance for ages over 8-human-equivalent years. These differences between levels were statistically significant ($p < 0.0001$), but not for the youngest specimens, in which the tolerances were similar. Compression failure loads increased significantly with increasing age regardless of the spine level (ANOVA, $p = 0.003$).

In a posterior study, Nuckley and Ching (2006) found differences both in the functional and failure experiments along the cervical spine. The C3-C4 functional spinal unit was the stiffest and the occiput Oc-C2 level was the most compliant in both compression and tension. The study also found statistically significant correlation between age and stiffness, normalized stiffness (normalization based on the cross sectional area of the intervertebral disc) in tension and compression, and tensile failure load. The ultimate failure load of the segment Oc-C2 was significantly higher than the one of all the other levels ($p < 0.006$).

5.2.2 Thoracic spine

Although there is no published study on the biomechanics of the pediatric thoracic spine, aspects of the mechanical behavior of the adult thoracic spine have been discussed in several publications. Most of them focus primarily on the response of the spine in physiological conditions or after surgical intervention, and therefore, the rates and amplitudes of the motion are hardly representative of those found in automotive crashes. The paragraphs below summarize the main findings from these studies.

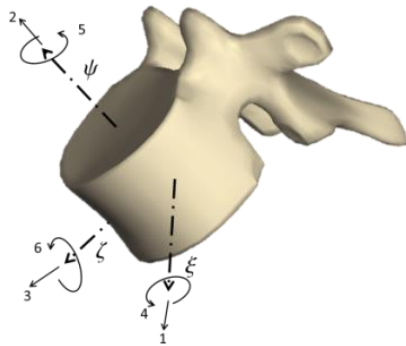


Figure 5.1 Local coordinate system in Panjabi et al. (1976)

$$K: \begin{pmatrix} 0.11 & 0. & 0. & 0. & 0.58 & 0.15 \\ 0. & 0.78 & 0.05 & 0.76 & 0. & 0. \\ 0. & 0.05 & 0.1 & 1.64 & 0. & 0. \\ 0. & 0.76 & 1.64 & 152. & 0. & 0. \\ 0.58 & 0. & 0. & 0. & 153. & 8.04 \\ 0.15 & 0. & 0. & 0. & 8.04 & 148. \end{pmatrix}$$

Equation 5.1 Average stiffness matrix (all vertebrae) of the human thoracic spine.

Panjabi et al. (1976) exposed 11 thoracic FSU harvested from five donors to a set of forces (magnitude: 100 N) and moments (magnitude: 5 Nm) in all three directions to obtain the flexibility matrix corresponding to each specimen. FSU consisted of two vertebrae with all the ligamentous tissue and the head and neck of the corresponding ribs. The stiffness matrix was obtained by inversion of the flexibility one. To our knowledge, this is the first study reporting on the 3D mechanical properties of the human thoracic spine. The authors demonstrated that there is little coupling between the spinal flexion/extension motion and the rotations in the other two anatomical axes. The average stiffness matrix (for all vertebrae) obtained when positive forces and moments were applied to the specimen (according to the coordinate system shown in Figure 5.1) is shown in Equation 5.1. According to Panjabis' nomenclature, the stiffness coefficient associated to flexion is the element k_{44} (152 Nm/rad) in the matrix (rotation in the ψ axis). The experiments performed by Panjabi et al. (1976) were done in quasistatic conditions.

Table 5.3 Summary of studies on the biomechanics of the adult thoracic spine

Study	# spec	Age (years)*	Goal	Results	Other considerations
Panjabi et al. (1976)	55	Not reported	Characterize the 3D flexibility and stiffness properties of all levels of the thoracic spine.	Average stiffness coefficient of the thoracic spine in flexion: 152 Nm/rad	FSU consisting of two vertebrae. Forces and moments applied to superior vertebra. Quasistatic
Oxland et al. (1992)	11	19-70	Characterize the 3D kinetics of T11-T12 and T12-L1 in flexion, lateral bending and axial rotation	Flexion-extension range of motion was 2.7 ± 1.3 deg and 2.4 ± 1.3 deg (T11-T12). Applied moments up to 7.5 Nm	Importance of the geometry of the facets in the kinematics of the FSU. Small coupling of other rotations with flexion/extension. Quasistatic
Willems et al. (1996)	60	18-24	To provide data on <i>in vivo</i> 3D spine kinematics	Flexion/extension physiological range of motion (SD): T1T4: 8.6(5.0)/ 8.1(7.2) deg T4T8: 10.7(3.8)/8.9 (5.3) deg T8T12: 12.7(3.4)/8.8(5.0) deg	<i>In vivo</i> study. Physiological range of motion. Coupling between lateral flexion and axial rotation
Sran et al. (2005)	8	70-93	To measure range of motion, neutral zone motion and 3D flexibility in T5-T8	Pure moments applied at 2 deg/s up to 4 Nm. Flexion/extension (deg) average range of motion (SD): T5T6: 0.69 (0.66)/ 0.80 (0.73) T6T7: 1.25 (0.87)/ 1.31 (0.81) T7T8: 0.83 (0.66)/0.99 (0.74)	Results skewed towards the elderly population. Research oriented to validate some spinal mobilization technique used clinically
Anderson et al. (2009)	6	62-99	To determine the effects of thoracic instrumentation anchor site preparation. Bending tests (3.2 deg) at 0.1 Hz.	All the interventions produced similar, small reductions of adjacent vertebrae stiffness.	Values for the healthy specimens (before performing any intervention) are not reported in the paper.
Wachowski et al. (2009)	3	66.6± 4.8	Characterize the 3D kinematics of several FSU: axial rotation, lateral bending, flexion/extension	Instantaneous helical axis (IHA) parallel to applied moment in flexion/extension and lateral bending. Migration of axis <4 mm	Range of motion of the FSU are not reliable since the preservation of the specimen affected the behavior of soft tissues.

Oxland et al. (1992) tested 11 thoracolumbar spinal specimens. FSU consisted of vertebrae T11 to L1 and the motion of each bony structure was measured by tracking markers that allowed the 3D reconstruction of

the rigid body motion. The results corresponding to the flexion-extension range of motion are shown in Table 5.3. The study calculated the so-called flexibility coefficient as the range of motion divided by the maximum moment applied to the specimen and related the obtained values to those already published in the literature at the moment, finding good agreement between the results (see Table 5.4). There were no important differences between T11-T12 and T12-L1 under flexion loading but, as Table 5.4 shows, the flexibility coefficient in extension was substantially higher at the T12-L1 level (indicating a more compliant behavior). The same pattern was also observed for the other loading modes (lateral bending and axial rotation). The authors hypothesized that the differences were caused by the change of the orientation of the facet joints along the spine. In particular, the authors proposed that while the only resistance to the flexion motion would be given by the tension of the joint capsules at both spinal levels, the thoracic facet geometry would provide additional constraint to the extension motion of T11-T12 compared to the T12-L1 segment.

Willems et al. (1996) conducted an *in vivo* study with 60 volunteers and showed that the rotation ranges increased in a cephalocaudal direction in the sagittal and coronal planes while axial rotation presented most mobility in the mid thoracic region. This work found again that flexion/extension were relatively pure motions although they were accompanied by slight axial rotation. There were no significant differences between the genders (the study enlisted 30 male and 30 female volunteers) in the range of motion in flexion/extension.

The stiffness and flexibility of the T5-T8 section of the human thoracic spine was evaluated by Sran et al. (2005). As shown in Table 5.3, the specimens were obtained from elderly subjects, which potentially influenced the observed results. Despite the differences in the test apparatus from that used in Oxland et al. (1992) and Panjabi et al. (1976), the test methodology was essentially similar and allowed the comparison between the studies (Table 5.4).

Anderson et al. (2009) exposed a total of 23 FSU (consisting of two vertebrae, the intervertebral disc and the ligaments) to a bending moment at 0.1 Hz. The goal of the study was to quantify the stiffness change that different posterior anchor site preparations induced in the thoracic spine. The authors showed that all

the interventions contributed to the reduction of the stiffness of the specimen. The stiffness values of the healthy specimens were not reported in the paper.

Wachowski et al. (2009) reported on the kinematics of several FSU using the position, alignment and migration of the instantaneous helical axis (IHA) to characterize the motion of the specimens. Unfortunately, only three thoracic FSU were tested (two T6/T7 specimens and one T7/T8). The specimens had been preserved which altered the stiffness properties of the ligamentous tissue. The study analyzed the kinematics of the FSU by measuring the range of motion under quasi-statically applied moments (axial rotation, lateral bending and flexion/extension). The magnitude of the applied moment was 7 Nm. In the transverse plane (axial rotation), the two segments T6-T7 differed considerably in range of motion, but showed common features of IHA displacement: the IHA was parallel to the applied moment initially and only declined ventrally by about 7 deg at maximum rotation. The IHA remained parallel to the applied moment in the cases of lateral bending and flexion/extension. While the IHA migrated dorsally and ventrally in response to an axial moment, the migration of the IHA was almost negligible (< 4 mm) in all three thoracic segments in the case of lateral bending and flexion/extension.

Table 5.4 Comparison of average intervertebral joint flexibility coefficients (inverse of stiffness coefficients) for several thoracic segments (deg/Nm).

	T11-T12 Oxland et al. (1992)	T12-L1 Oxland et al. (1992)	T11-T12 Panjabi et al. (1976)	T11-T12 Markolf, (1972)	T5-T8 Sran et al. (2005)
Flexion	0.36	0.39	0.35	0.5	0.27 (± 0.18)
Extension	0.32	0.52	0.25	0.33	0.31 (± 0.25)

5.2.3 Review of scaling between pediatric and adult cervical spinal responses

In addition to the studies that used animal surrogates to understand the developmental changes of the cervical spine, there are other two papers that adopted a different methodology to scale the response of the cervical spine of adult individuals.

Kumaresan et al. (2001) used data from individual spinal components and neck geometry to calculate scale factors under tension, compression, flexion and extension loading modes as a function of age. The process is based on the identification of active spinal components under each loading mode and the establishment of age-dependent relations between those components to obtain material-based scale factors. Then, dimensional analysis is used to propose the new scaling factors. This study accounted also for muscular activity and neck geometry during the developmental process. The second study by Yoganandan et al. (2000) follows the exact same approach and reports the same values (with the addition of the scale factor for a small female 5th percentile).

Table 5.5 Summary of scaling factors for the response of the cervical spine in tension.

Scale factor based on...	Hilker et al. (2001)		Ching et al. (2001)		Kumaresan et al (2001)	Pintar et al. (2000)		FMVSS 208
	Tensile Failure	K_F^+	Tensile Failure	K_F^+	Tensile load	Tensile Failure	K_F^+	Tensile Failure
1-year	0.10	0.13	--	--	0.25	0.12	0.17	0.24
3-year	0.16	0.18	0.33	0.54	0.30	0.20	0.23	0.34
6-year	0.30	0.38	0.55	0.71	0.37	0.38	0.54	0.45
12-year	0.62	0.66	0.66	0.76	--	0.78	0.85	--
15-year	--	--	--	--	--	--	--	--
Small adult	0.74	0.78	--	--	0.63	--	--	0.63
Mid-size adult	1	1	1	1	1	1	1	1
Large adult	1.13	1.10	--	--	--	--	--	1.21

⁺ K_F : tensile stiffness

Table 5.5 through Table 5.7 compare the scale factor values reported in the literature for three different loading modes: tensile load, compression load and bending in the sagittal plane (flexion/extension anatomical motion). Note that values from Yoganandan et al. (2000) and Kumaresan et al. (2001) are the same with the exception of the scaling factor for the small female, and they will be referred to as Kumaresan et al. (2001).

Table 5.5 shows a significant difference between the scaling factors obtained using dimensional analysis techniques (Kumaresan et al., 2001; Wang et al. 2009 and FMVSS 208) and the ones directly obtained

from testing animal models at different developmental stages (Ching et al. 2001; Hilker et al. 2002; Pintar et al. 2000). There are also substantial differences between the scaling factors obtained using the baboon model and the caprine model. These differences can be attributed to the inherent difficulty of relating an animal model to a specific human equivalent age. Of course, there also exist important anatomical differences between the cervical spine of baboons and goats that make challenging the comparison between the species.

Table 5.6 Summary of scaling factors for the response of the cervical spine in compression.

Study	Nuckley et al. (2002)	Kumaresan et al. (2001)
Scale factor based on...	Compression failure	Compression
1-year	0.27	0.24
3-year	0.32	0.30
6-year	0.40	0.36
12-year	0.55	--
15-year	0.62	--
Small adult	--	0.63
Mid-size adult	1	1
Large adult	--	--

Interestingly the differences in the scaling factors between the two methodologies (dimensional analysis, use of animal models) found in the tensile loading group are not significant when the loading mode is compression. Table 5.6 shows a reasonably good agreement between the values of the scaling factors from the baboon model used by Nuckley et al. (2002) and from the dimensional analysis approach by Kumaresan et al. (2001).

As for the scaling factors when the relevant loading mechanism is bending in the sagittal plane, there is a good agreement between the three published studies up to an age of 3 years old. Then, the scaling factors found in the animal model for the 6-year old (Hilker et al., 2002; Pintar et al., 2000) are almost twice the ones found using dimensional analysis (Kumaresan et al., 2001). Although the data from Hilker et al. updated the data from Pintar et al. both studies are kept in Table 5.7 since it was not clear to the author of this dissertation research how and why the data were updated.

Table 5.7 Summary of scaling factors for the response of the cervical spine in flexion/extension.

Study	Hilker et al. (2001)	Pintar et al. (2000)	Kumaresan et al. (2001)
Scale factor based on...	K_B^{++}	K_B	Flexion
1-year	0.13	0.11	0.14
3-year	0.19	0.15	0.18
6-year	0.42	0.57	0.24
12-year	0.76	0.62	--
15-year	--	--	--
Small adult	0.89	--	0.501
Mid-size adult	1	1	1
Large adult	1.03	--	--

⁺⁺ K_B : bending stiffness

5.3 METHODS

5.3.1 Test setup

A custom-made fixture specifically designed to induce a bending moment in a section of the spine was attached to a servohydraulic testing machine (INSTRON 8874 Axial-Torsion Fatigue Testing Systems, Norwood, MA, USA). The fixture was driven by the vertical motion of the piston of the machine, transforming the linear motion into a rotation of two cups through a mechanical linkage, which consisted of two aluminum arms joined by a low-friction rotational bearing. The vertical arm was attached to the crosshead of the testing machine by a low-friction linear bearing. The cups were supported by two cup-holders that could translate with negligible friction in the horizontal plane of the table of the test machine. A global coordinate system (GCS) rigidly attached to the table of the test machine was defined as shown in Figure 5.2.

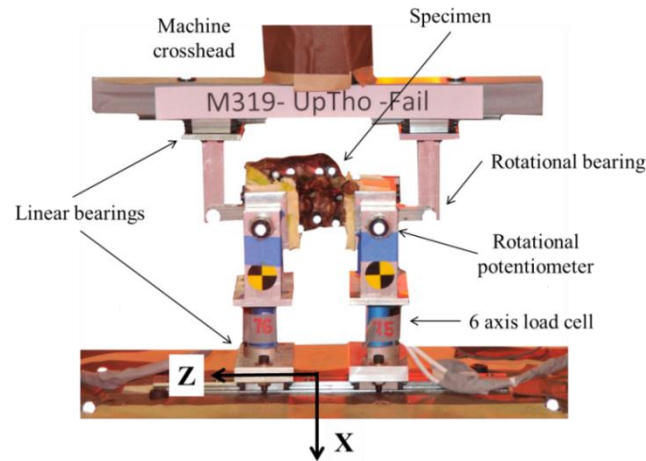


Figure 5.2 Schematic showing the test setup, instrumentation and positioning of the specimen

First, each specimen was exposed to a battery of 50 cycles at 1 Hz sinusoid with different amplitudes to precondition the tissue and achieve a steady-state behavior. Next, a series of five dynamic ramp and 60-second hold tests of varying amplitudes were applied to the specimens (D1-D5).

Table 5.8 Test matrix.

Specimen	Preconditioning		D1	D2	D3	D4	D5
	Freq (Hz)	# cycles/ Amplitude (deg)	Amplitude (deg)				
F470-T2T4	1	10/0.65, 10/1.35, 30/1.89	0.63	0.93	1.22	1.54	1.87
F470-T7T9	1	10/0.59, 10/1.17, 30/2.00	0.61	0.89	1.15	1.37	1.61
M485-T2T4	1	10/1.04, 10/2.27, 30/3.39	0.87	1.41	1.95	2.54	3.18
M485-T7T9	1	10/1.09, 10/2.33, 30/3.44	0.85	1.42	2.00	2.64	3.32
M319-T2T4	1	10/1.14, 10/2.25, 30/3.35	0.96	1.53	2.13	2.69	3.24
M319-T7T9	1	10/1.18, 10/2.43, 30/4.64	0.79	2.04	3.35	3.98	4.59
M320-T2T4	1	10/1.24, 10/2.36, 30/3.41	1.10	1.75	2.43	2.96	3.46
M320-T7T9	1	10/1.07, 10/2.01, 30/2.97	0.87	1.43	2.04	2.57	3.10

The amplitude of the ramps was chosen to avoid causing any damage to the tissue and the maximum amplitude reached during the dynamic tests was similar to that reached during the preconditioning of the tissue. The piston of the test machine moved upwards at a nominal rate of 100 mm/s. Table 5.8 summarizes the test matrix as well as the machine input values of each of the tests. The values of the

amplitudes presented in the table correspond to the rotation of the cups as measured by the rotational potentiometers.

5.3.2 Test specimens

For the purpose of this study, a Functional Spinal Unit (FSU) was defined as the specimen formed by three vertebral bodies, the corresponding two inter-vertebral discs and the ligaments connecting these structures. All the ligaments (supra-spinous (SSL), inter-spinous (ISL), flavum (LF), posterior longitudinal (PLL), anterior longitudinal (ALL)) were preserved during the preparation of the specimens with the exception of the inter-transverse ligaments. Two FSU were obtained from each thoracic spine: T2-T4 and T7-T9. A total of eight FSU were harvested from four donors (two pediatric, two adults). The anthropometry and general characteristics of the donors are shown in Table 5.9. The extraction, preparation and testing of the specimens were done in compliance with the Protocol for the Handling of Biological Material (Center for Applied Biomechanics, 2006) and approved by the University of Virginia – Center for Applied Biomechanics Oversight Committee.

Table 5.9 General characteristics of the PMHS.

Subject	Gender	Age	Stature (cm)	Weight (kg)
F470	Female	7	119	27
M485	Male	15	163	50
M319	Male	52	179	77
M320	Male	48	168	68

The proximal and distal vertebrae of each FSU were embedded into cement (Fast Cast, polyurethane isocyanate, Goldenwest Inc., CA, USA). A custom-made potting fixture was used to ensure that the two cement blocks were aligned without inducing any initial stress in the specimens. The center of the potted vertebral bodies was approximately positioned at the center of the cement block.

The specimens were kept frozen and thawed 24 hours prior to testing. To preserve the hydration of the ligamentous structure they were wrapped in gauze soaked in saline solution. The specimens were submerged in a temperature controlled bath set at 37.1 degrees Celsius for at least 30 minutes immediately prior to testing.

5.3.3 Instrumentation

5.3.3.1 Motion capture system.

The motion of the vertebrae was tracked using an 8-camera Vicon MX™ system operating at 1000 Hz. The system recorded the motion of retroreflective targets within the camera's collective viewing volume. Four targets were glued onto each vertebra to allow for the reconstruction of their 3D motion (Figure 5.3). A local coordinate system located at the center of the vertebral body was defined for each vertebra (Wu et al., 2005). Using geometric information from CT images, the position and attitude of the local coordinate system can be related to the position of the four retroreflective targets. A calibration procedure, performed prior to testing each specimen, estimated the optical characteristics of each camera and established its position and orientation in a reference coordinate system. With this information a photogrammetric algorithm within the Vicon Nexus software package reconstructed the 3D position of each target for each video sample increment from the multiple 2D camera images. Finally, following the method described in Kinzel et al. (1972), the motion of each vertebra can be determined with respect to an inertial global coordinate system (GCS) that coincides with the base of the test machine. Given the characteristics of the system, the motion analysis was restricted to the XZ plane as shown in Figure 5.2

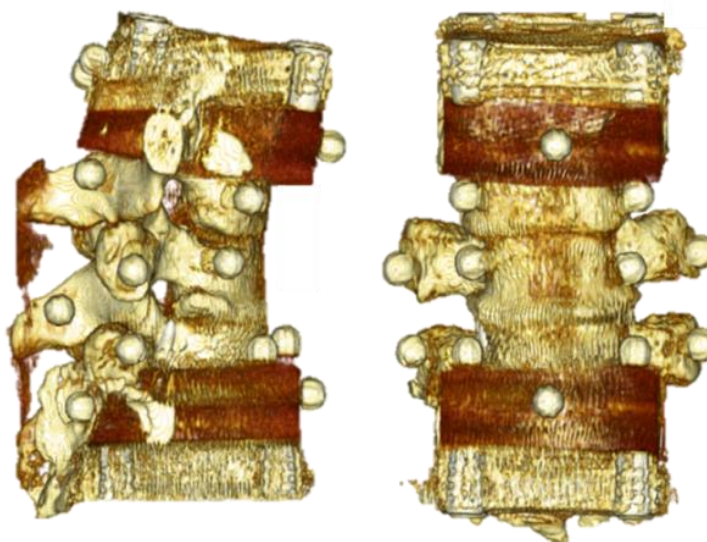


Figure 5.3 CT images showing the position of the marker on the FSU (specimen M320-T1T5).

The motion capture system permitted to measure the distances between the local coordinate system of each vertebra, needed to estimate the moments and forces experienced by the specimen according to the detailed methodology included in Appendix A1.

5.3.3.2 Other non-optical instrumentation.

Two load cells (Implantable Fibula, Model No. 5024J, Robert A. Denton, Inc. MI, USA) measured the reaction forces and moments in the three coordinate axes at the support of the cups. The longitudinal axis of the load cells intersected perpendicularly with the axis of rotation of the cups. The rotation of the cups was measured by two rotational potentiometers. Instrument data were collected at 10000 Hz using a DEWE-2600 (Dewetron Inc., Wakefield, RI, USA) data acquisition system. The data were filtered using 4-channel Butterworth low-pass CFC100 (rotational potentiometers) and CFC1000 filters (forces and moments).

The rotational potentiometers measured the rotation of the two distal vertebrae ($\theta_{superior}, \theta_{inferior}$), which allowed calculating the angle rotated by the specimen (α) that was defined as (Figure 5.4):

$$\alpha = \theta_{superior} + \theta_{inferior} \quad \text{Equation 5.2}$$

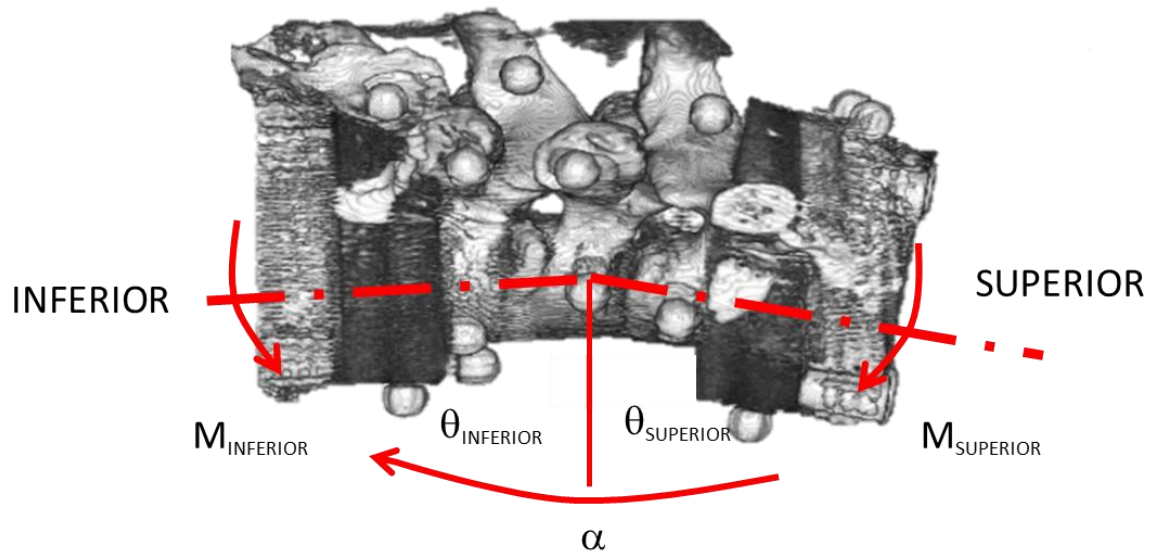


Figure 5.4 Schematic of the FSU showing the calculation of the relative angle between the two distal vertebrae.

5.3.4 Quasi-linear viscoelastic formulation

A quasi-linear viscoelastic model (QLV) was proposed to characterize the dynamic behavior of the thoracic FSU. The QLV formulation has been applied successfully to describe the transient non-linear behavior of biological tissues (Fung, 1993) as well as of structures as a whole (Funk et al., 2000; Kent et al., 2003; Kent et al., 2009b; Lucas et al., 2009; Salzar et al., 2009). The selected QLV formulation relates the calculated specimen angle to the generated bending moment, according to the following equation:

$$M[t] = \int_{-\infty}^t G[t - \tau](\partial M_e[\alpha]/\partial \alpha)(\partial \alpha[\tau]/\partial \tau) d\tau \quad \text{Equation 5.3}$$

where $M[t]$ is the moment generated, $\alpha[t]$ is the angle rotated and $M_e[\alpha]$ is the function describing the moment response to a step increase in rotation. The reduced relaxation function was described as the Prony series shown in Equation 5.4:

$$G[t] = \sum_{i=1}^3 G_i e^{-\beta_i t} + G_\infty \quad \text{Equation 5.4}$$

where β_i are time constants with associated weights G_i , and G_∞ the steady-state response. The maximum value of the reduced relaxation function occurs at time $t=0$ and is equal to unity:

$$\sum_{i=1}^3 G_i + G_\infty = 1 \quad \text{Equation 5.5}$$

A nonlinear equation was used to model the instantaneous elastic response (IER) $M_e[\alpha]$ as shown below:

$$M_e[\alpha] = A(e^{B\alpha} - 1) \quad \text{Equation 5.6}$$

A numerical convolution scheme was used to solve for the different parameters (A, B, G_i, β_i) that model the response of the FSU. The process showing the calculation of the coefficients of $G[t]$ and $M_e[\alpha]$ is detailed in Appendix A1. The parameters of the model were optimized simultaneously in the D3, D4 and D5 dynamic ramp-and-hold tests to minimize the sum of square errors between the model-predicted moment and the measured one. The results from the experiments D1 and D2 were not included to improve the fit of

the model to angle amplitudes relevant to the general objective of the dissertation. The optimization used a genetic algorithm scheme implemented in MATLAB that increased the likelihood of finding a global minimum of the problem. In the optimization problem, the earlier response of the specimens was assigned a greater weight than the long-time response to improve the prediction of the transient response.

5.3.5 Stiffness relationships in the human thoracic spine

As mentioned at the beginning of the chapter, these tests were designed to assist in the development of a multibody 2D model of the occupant. In the model, the spine was described as three rigid links (upper thoracic spine, lower thoracic spine and lumbar spine) connected by rotational joints. The flexural behavior of the spine was assumed to be described by incorporating stiffness and damping into the formulation of the joints.

The goal of the FSU tests was to provide a relationship between the stiffness of the joints connecting the thoracic links of the multibody model. It was assumed that the relationship between the model joint stiffness could be approximated by the relationship between the instantaneous elastic responses of the upper and middle FSU.

Thus, the following sections focus on obtaining and comparing the instantaneous elastic response between different sections of the thoracic spine or between different ages. For the comparison, the values of the instantaneous elastic response were obtained up to an angle value of 10 degrees, which corresponded to the amount of rotation observed during the sled tests presented in the previous chapters.

In the case of the variation of stiffness along the spine, a proportionality factor (κ) relating the upper and middle thoracic instantaneous elastic responses was calculated to minimize the distance between the elastic upper moment predicted $M_{e_{T2T4}}^*$ and the elastic upper moment observed $M_{e_{T2T4}}$ between 0 and 10 degrees.

The elastic moment predicted was calculated as:

$$M_{e_{T2T4}}^* = \kappa M_{e_{T7T9}} \quad \text{Equation 5.7}$$

5.4 RESULTS

5.4.1 QLV model of the human thoracic spine

For the sake of illustration of the results, Figure 5.5 and Figure 5.6 show the model fit to the experimental data of the upper and middle section of the pediatric specimen F470. Each of the plots shows time history of the predicted (red) and the measured (blue) moment at each of the selected test amplitudes (D3-D5).

Table 5.10 shows the estimated values of the QLV parameters that model the bending behavior of the different spine segments tested. Note that since the model fit to specimens M319-T2T4 and M320-T2T4 was less than satisfactory, no coefficients are shown for these specimens.

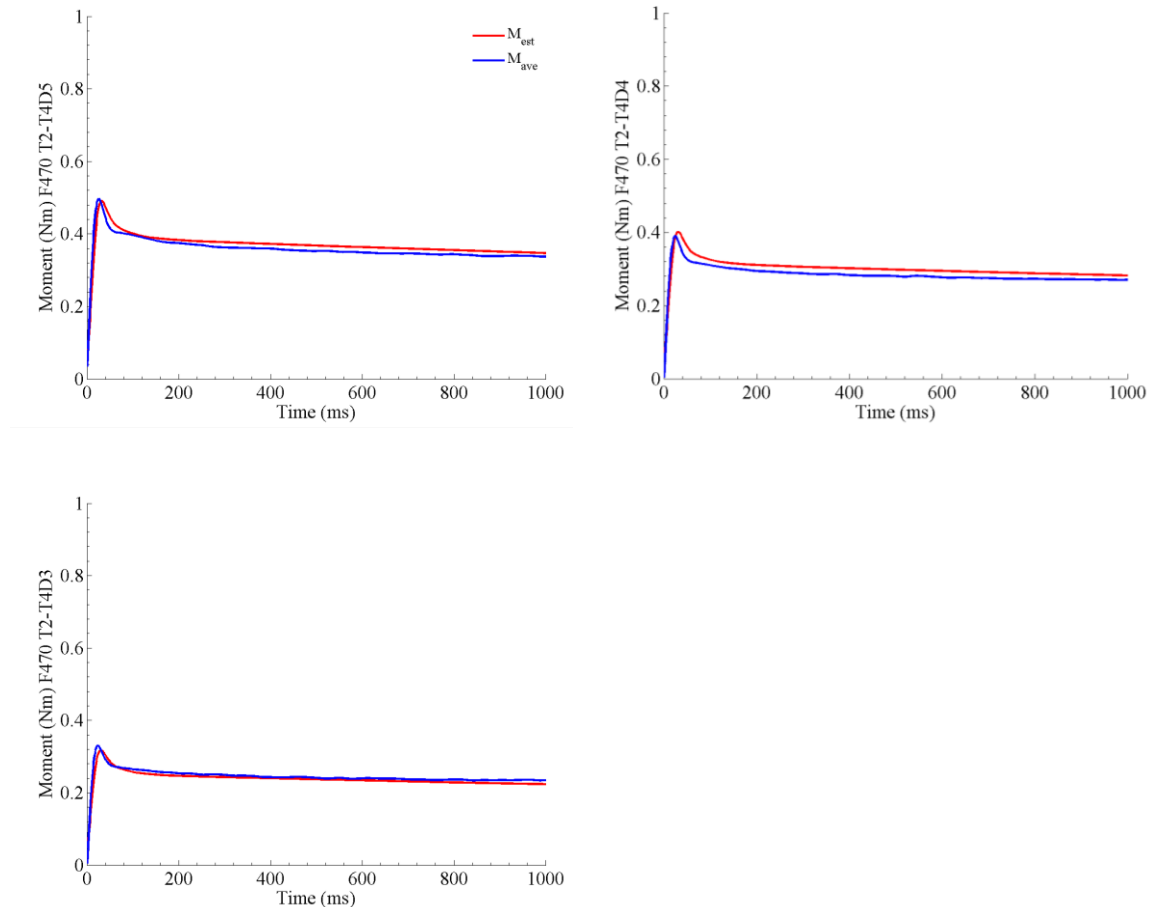


Figure 5.5 Comparison between the moment predicted (M_{est} , red) and the calculated average moment (M_{ave} , blue) of the upper thoracic section of pediatric specimen F470.

Table 5.10 Coefficient values of the QLV model of the human thoracic spine.

	β_1 (s)	β_2 (s)	β_3 (s)	G_1	G_2	G_3	A	B
F470-T2T4	0.0040	0.4107	26.0834	0.4057	0.2301	0.2607	2.9642	0.0428
F470-T7T9	0.0207	0.4275	46.1016	0.0625	0.2923	0.4054	1.1268	0.1398
M485-T2T4	0.7775	8.3484	198.5571	0.3350	0.0348	0.5988	10.8506	0.0826
M485-T7T9	0.3065	7.3973	205.5157	0.28203	0.0364	0.6310	17.9538	0.0690
M319-T2T4	NA	NA	NA	NA	NA	NA	NA	NA
M319-T7T9	3.0628	30.6941	999.3886	0.0752	0.0047	0.9081	3.0801	0.2968
M320-T2T4	NA	NA	NA	NA	NA	NA	NA	NA
M320-T7T9	3.3323	67.4706	894.5264	0.1268	0.0011	0.8583	10.3790	0.3474

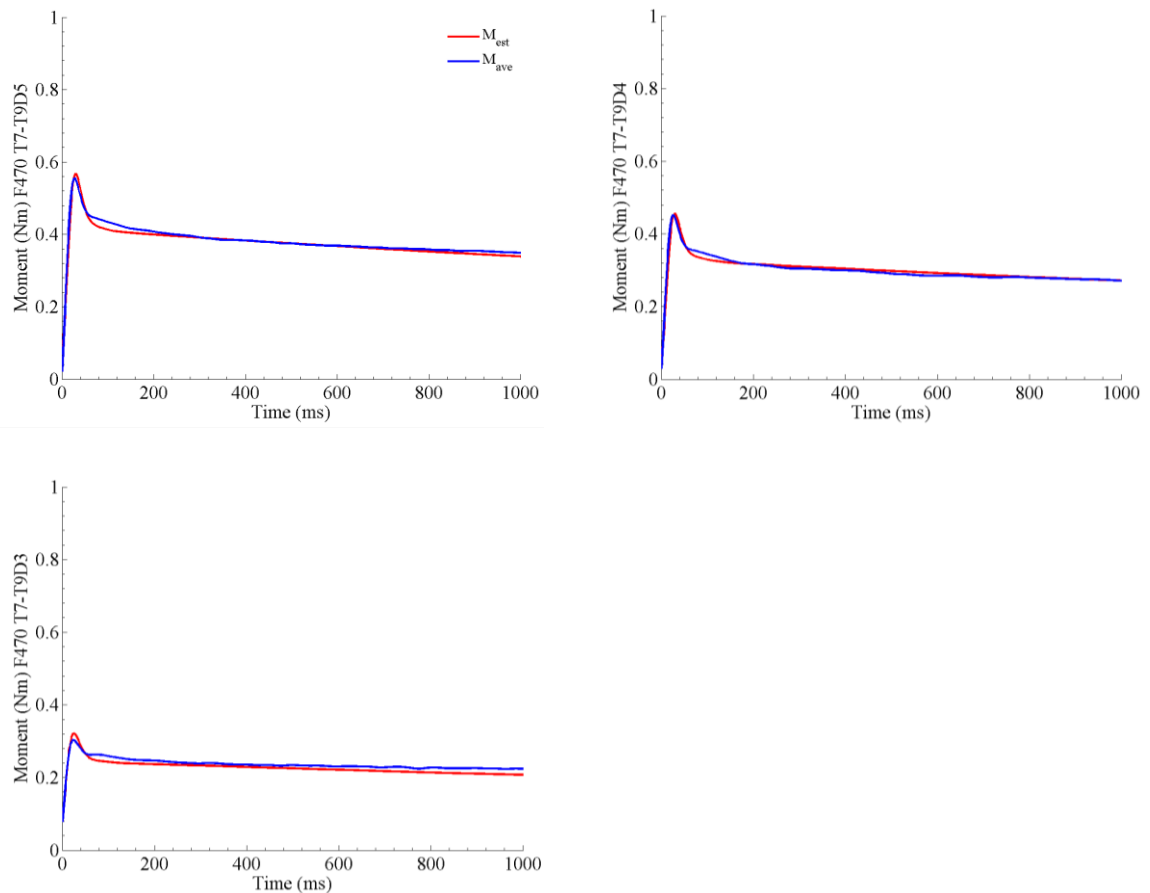


Figure 5.6 Comparison between the moment predicted (M_{est} , red) and the calculated average moment (M_{ave} , blue) of the middle thoracic section of pediatric specimen F470.

The results showing the fit of the model to each of the specimens are included in Appendix A1, and since they do not relate directly to the development of the model of the occupant are not further discussed here.

5.4.2 Comparison of the instantaneous elastic response of two thoracic FSU

This hypothesis was studied using only the results from the two younger subjects F470 and M485, due to the lack of data for the upper thoracic sections of M319 and M320. The instantaneous elastic response of the upper thoracic section of each specimen was plotted and compared to that of the middle thoracic section. The results of the comparison are shown in Figure 5.7. The stiffness of the middle thoracic section (T7T9) was consistently greater in the two analyzed subjects as shown in the plots. Table 5.11 shows the value obtained for a proportionality factor relating the instantaneous elastic responses of the upper and middle thoracic spinal sections as defined in Equation 5.6.

Table 5.11 Relationships between the instantaneous elastic responses of the tested FSU.

	F470	M485
$1/\tau_1$	0.52	0.77

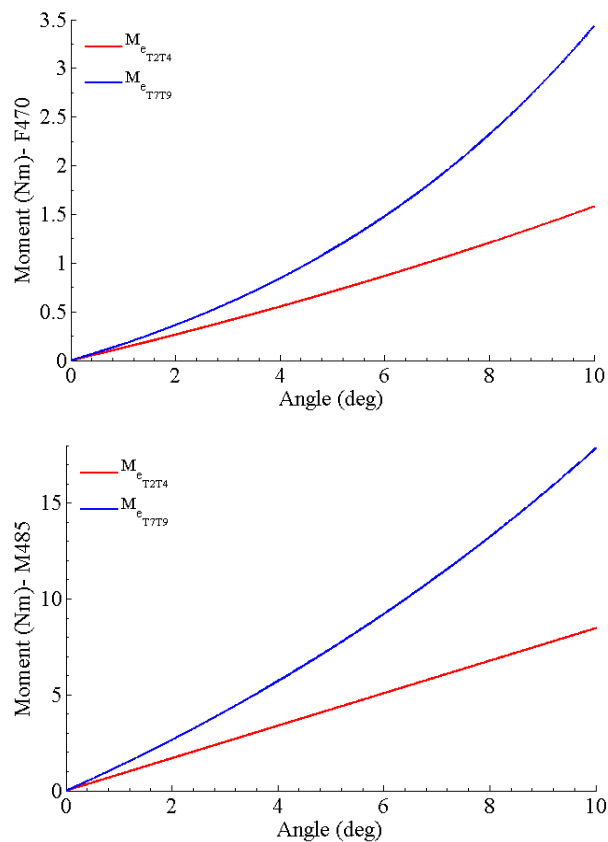


Figure 5.7 Comparison between the instantaneous elastic response between the T2T4 (red) and T7T9 (blue) thoracic sections for specimens F470 (7YO, top) and M485 (15YO, bottom).

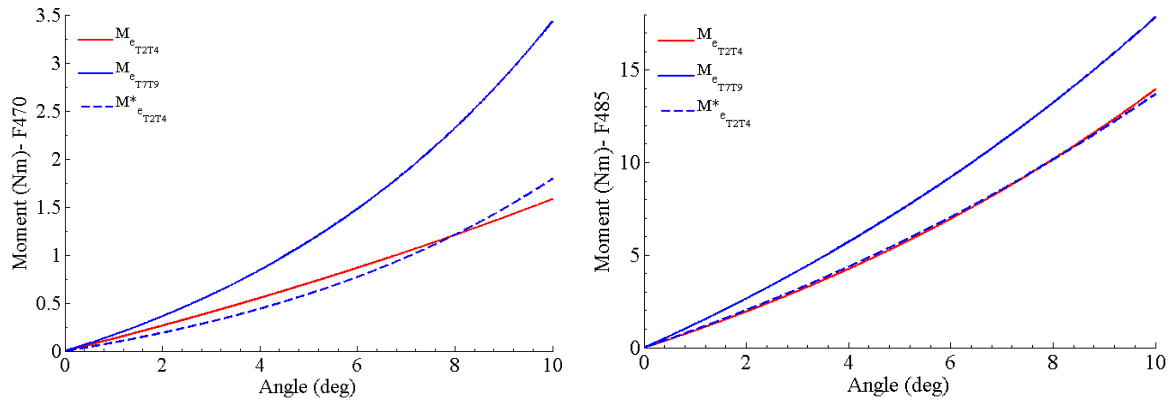


Figure 5.8 Prediction of the upper thoracic IER given by the calculated proportionality factor applied to the middle thoracic IER.

The prediction given by the proportionality factor produced a better estimation of the upper thoracic behavior in the case of specimen M485. The plots in Figure 5.8 illustrate the goodness of fit of the predictions up to 10 degrees.

5.4.3 Change of the instantaneous elastic response of the same thoracic FSU with age

In this case, the instantaneous elastic responses of the four specimens corresponding to the T7-T9 thoracic section were compared as shown in Figure 5.9.

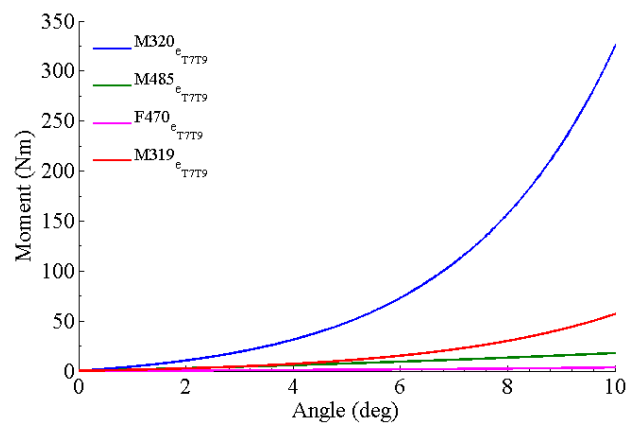


Figure 5.9 Comparison between the instantaneous elastic responses of the middle thoracic section across subjects.

It was found that the instantaneous elastic response of the older specimens demonstrated a stiffer behavior than the one exhibited by the younger specimens. Specimen M320-T7T9 demonstrated the stiffest behavior of all the specimens, followed by M319 and then M485 and F470.

5.5 DISCUSSION

These tests constitute the first *in vitro* dynamic bending tests on the human thoracic spine in the literature. Even if the number of specimen is too low to consider the question of the characterization of the flexion of the human thoracic spine completely solved, they provide the first published relationship between the mechanical behavior of different sections of the human thoracic spine in bending. Moreover, future attempts of testing sections of the human thoracic spine in dynamic bending conditions will also benefit from the results provided here to guide the experimental design.

The model proposed to describe the mechanical behavior of the thoracic spine in bending was based on the QLV formulation proposed by Fung (1993). This formulation was considered adequate to describe the bending behavior of the FSU under the loading conditions used in the experiments presented above. Figure 5.5 and Figure 5.6 (and all the other plots included in Appendix 1) show the goodness of fit of the model to the experimental results.

These tests were designed to assist in the development of the 2D model of the occupant that was introduced in chapter 2 and will be the focus of chapters 7 and 8. In particular, the motivation was to obtain a relationship between the moment/angle characteristic of the two thoracic sections (upper and middle) in dynamic conditions. This relationship was needed to reduce the number of unknown parameters in the development of the 2D occupant model and therefore to improve its accuracy. The value of the factor κ (defined in Equation 5.7) was shown in Table 5.11 for the case of the two pediatric subjects (6 YO and 15 YO). However, it was not possible to obtain similar values of κ for the two adult specimens. More details are given within Appendix A1, but the two upper thoracic spine adult specimens were likely damaged during preconditioning, and therefore it could not be found a relationship between the instantaneous elastic responses of the upper and middle thoracic sections in the case of adults.

The model obtained for the behavior of the middle thoracic spine allowed to assess the change in the instantaneous elastic response with age and it was shown that there was a substantial change in the middle section of the thoracic spine (Figure 5.9).

Two limitations must be acknowledged: the reduced number of specimens tested and whether these specimens were representative of their respective age groups. The first one precluded the use of statistics to check the hypothesis and thus a simple comparison between the specimens was done. In the absence of any other similar set of experimental data, it is not possible to assess the relevance of the second limitation. Further research must address this point by replicating these experiments and increasing the available experimental data.

It is also important to bear in mind that the response of the thoracic spine is influenced by the surrounding structures and therefore the mechanical behavior observed in the component test is not likely to be directly transferable to the case of the frontal deceleration of a whole occupant (Panjabi et al., 1976). However, modeling the structural behavior of specific thoracic segments helped to understand the differences in stiffness along the thoracic spine as well as the differences across ages. The assumption to be made in the development of the 2D occupant model is that the ratio between the stiffness of the different sections along the spine in the *in vitro* experiments holds also true in case of the frontal motion of the whole occupant.

5.6 CONCLUSION

This chapter presented the first model of the mechanical behavior of the dynamic bending of the human thoracic spine. A formulation based on QLV was used to model the structural behavior of the specimens by relating the rotation of the FSU to the moment generated. The model served to obtain a relationship between the instantaneous elastic response of subjects of different ages and between the instantaneous elastic response of different thoracic levels along the spine. It has been shown that, for the specimens tested here, stiffness increased with age and that the instantaneous elastic response of the middle thoracic section was more compliant than the one of the upper section. The factor κ relating the instantaneous elastic response of these two sections was calculated and it will be used as proxy of the relation between the joint stiffness of the thoracic spinal links of the multibody model that is presented in Chapter 7.

6 SCALING ADULT DATA TO PREDICT PEDIATRIC KINEMATICS

6.1 INTRODUCTION

The experimental data obtained by Arbogast et al. (2009) constitute a unique set of data that allowed comparing the kinematics of pediatric and adult volunteers in a low-speed frontal impact. In the case of this dissertation research, the data from the volunteer experiments were used to assess whether scaling methods that had been historically used in the field of impact biomechanics could provide a precise approximation of the sagittal trajectories of pediatric subjects in a low-speed frontal impact. The data also served to develop a new scaling method that considered not only the difference in size between the two types of subjects but also the differences in belt loading, although in a simplified manner.

This chapter focuses on scaling methods and uses the volunteer data to assess the predictions given by these methods. The predictions given by each scaling method are compared and the associated limitations are discussed. The different methods used in this chapter use the average responses of the pediatric and adult volunteers shown within Chapter 3.

6.2 METHODOLOGY

After obtaining the characteristic average displacement for each of the considered anatomical structures, three scaling methodologies were applied to the average response of the mid-size adult and compared to the average response and corridors of the average 6YO. These three scaling methodologies are described in the following paragraphs.

6.2.1 Mass scaling method

The method was first used in Eppinger et al. (1984) in the development of the characteristics and injury criteria of side impact dummies. It is completely based on dimensional analysis and therefore assumes that

there is geometrical and dynamic similarity between the two systems related by the scaling method. The three fundamental magnitudes that are used to scale all the other magnitudes in the system are length (L), mass density (ρ) and modulus of elasticity (E). The length scale factor is calculated as the cube root of the ratio of the mass (m) of a standard-sized subject to the actual subject, assuming that the densities are equal between the subjects. The length scale factor is assumed to be the same for all three coordinates (x,y,z) as this is required to keep the geometrical similarity between prototype and model. As an example, Table 6.1 shows the scaling factors (λ_i) to be applied to a 50th percentile to predict the corresponding magnitudes in a 6 YO. The time (t) scaling factor has been added just to illustrate the differences in the calculation of the scaling factors between the two scaling techniques.

Table 6.1 Scaling factors between a 50th percentile adult and a 50th percentile 6YO.

	λ_L	λ_ρ	λ_E	λ_m	λ_t
Mass scaling	$\lambda_x=\lambda_y=\lambda_z=0.70$	1.00	0.88	0.27	0.69
SAE scaling	$\lambda_z=0.70, \lambda_x=\lambda_y=0.62$	1.00	0.88	0.27	1.00

6.2.2 SAE scaling method

The SAE scaling method was originally applied to scale the response of the Hybrid III 50th percentile to the small female and large male ATD. The method involves the calculation of a length scale factor (given by the erect seated height of the subjects) and a mass scale factor (total body mass). The method assumes equal density between prototype and model and thus, the length scaling factors to be used in the other two directions (which coincide with the x and y directions according to the SAE coordinate system) are given by Equation 6.1:

$$\lambda_x = \lambda_y = \sqrt{\frac{\lambda_m}{\lambda_z}} \quad \text{Equation 6.1}$$

On top of the length and mass scale factors, the SAE scaling method uses the relationship between the modulus of elasticity of prototype and model (λ_E) to derive scaling factors for any other physical magnitude. The value of λ_E has been updated several times and the one shown in Table 6.1 corresponds to the last value proposed in Mertz et al. (2003).

6.2.3 Development of an energy-based scaling method

This scaling methodology is based on conservation of energy and simplifies to a large extent the problem of restraining the forward motion of the occupant during a frontal impact by considering that the occupant is a point mass and that the belt force is the only external force acting on it (and that it is a point force).

Then, the method is based on calculating the change in the kinetic energy of a moving point mass between the initial position (0) and the final position (max_s, maximum excursion) that equals the work done by the net force F acting upon the point mass from position 0 to position max_s as shown in Equation 6.2 (Goldstein, 1981):

$$\frac{1}{2}(V_F^2 - V_0^2)m = \int_0^{\max_s} F ds \quad \text{Equation 6.2}$$

where V_F is the final speed at position max_s, V_0 is the initial speed at position 0 and s is the path followed by the point mass.

6.2.3.1 Application to scaling between pediatric and adult occupants

Under the approach aforementioned, equation 6.2 can be used to estimate the work done by the restraint systems on the occupant to arrest its forward movement. Assuming that position 0 corresponds to the position at t=0, V_0 is the speed of the occupant at t=0. If position max_s is chosen as the position of maximum forward displacement of the occupant, then V_F is equal to zero. Thus, if the occupant is assumed to be a moving point mass under the action of a net force F arresting its forward motion, Equation 6.2 can be particularized for a pediatric (*ped*) and an adult (*ad*) occupant as follows:

$$\frac{1}{2}(V_F^2 - V_0^2)m_{ped} = \int_0^{\max_s_{ped}} F_{ped} ds_{ped} \quad \text{Equation 6.3}$$

$$\frac{1}{2}(V_F^2 - V_0^2)m_{ad} = \int_0^{\max_s_{ad}} F_{ad} ds_{ad} \quad \text{Equation 6.4}$$

In the sled tests, the term $V_F^2 - V_0^2$ is the same, and therefore Equation 6.3 and Equation 6.4 can be combined into a single equation:

$$\frac{m_{ped}}{m_{ad}} = \frac{\int_0^{\max_{s_{ped}}} F_{ped} ds_{ped}}{\int_0^{\max_{s_{ad}}} F_{ad} ds_{ad}} \Rightarrow \int_0^{\max_{s_{ped}}} F_{ped} ds_{ped} = \frac{m_{ped}}{m_{ad}} \int_0^{\max_{s_{ad}}} F_{ad} ds_{ad} \quad \text{Equation 6.5}$$

Finally, Equation 6.5 was further simplified approximating the value of the integrals as the product of the peak value of the forces restraining the occupant times the length of the path:

$$s_{ped} = \frac{m_{ped}}{m_{ad}} \frac{F_{ad_{peak}}}{F_{ped_{peak}}} s_{ad} \quad \text{Equation 6.6}$$

The last assumption was that the ratio between the two peak restraining forces could be approximated as the ratio of peak shoulder belt forces.

Thus, Equation 6.6 can be used to calculate the predicted value of the length of the pediatric path s_{ped} if the length of the adult one is known. Then the length of the path must be apportioned into the X and Z components. The same relationship between the X and Z components of the adult displacement was used to apportion the path s_{ped} into the components in the sagittal plane.

Figure 6.1 and Equation 6.7 show how the apportion was done at every time step between one point (x_1, y_1) and the following one (x_2, y_2) if the length of the arc at the time step (ds) and the angle were known (φ). In the case of the prediction of the pediatric displacement, the length of the arc was calculated using Equation 6.6 and the value of the angle was obtained from the adult results.

One important remark is that the trajectory paths to be used in the former expressions must be obtained with respect to an inertial reference frame, as mentioned above. All calculations were done with respect to a laboratory-fixed coordinate system (inertial reference system) with axes X' , Y' , Z' that were parallel to the axes of the buck coordinate system. The displacements were transformed back to the buck coordinate system for visualization.

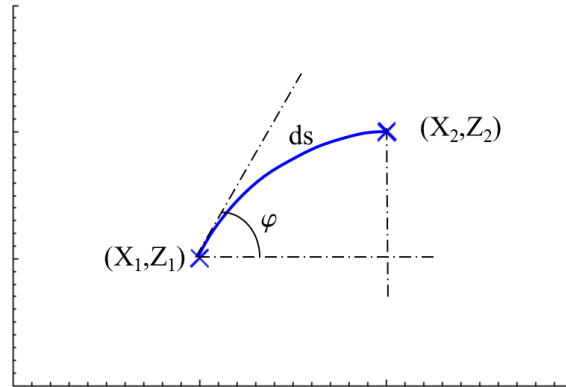


Figure 6.1 Schematic showing the parameters needed to apportion the length of the path at each time step (ds) between the X and Z axes if the preceding point and the angle formed by the tangent to the arc and the horizontal is known. See Equation 6.6.

$$\begin{aligned} X_2 &= X_1 + s_{ped} \cos \varphi \\ Z_2 &= Z_1 + s_{ped} \sin \varphi \end{aligned} \quad \text{Equation 6.7}$$

6.3 RESULTS

6.3.1 Assessment of conventional scaling methods

After obtaining the response and the associated corridor of the average subject within each age group, the corresponding scaling factors (as given in Table 6.1) were applied to the response of the average adult to predict the response of the average 6 YO.

The results obtained are shown in Figure 6.2. Both historic scaling methods predicted a shorter displacement (SAE scaling: 42.0%; Mass scaling: 48.6%) of the pediatric head. The predicted responses exhibited also a component in the negative direction of the Z axis that did not exist in the observed pediatric trajectory but was present in the adult trajectories. A similar result was observed for T1, and both methods fell short in the prediction of the forward displacement of the first thoracic vertebra (SAE scaling: 35.0%; Mass scaling: 42.4%). Also, the characteristic curvilinear trajectory exhibited by the pediatric T1 vertebra was not captured by either of the scaling methods. Table 6.2 shows the value for the peak forward displacement of each tracked anatomical structure and the predictions given by the two scaling methods together with the relative error.

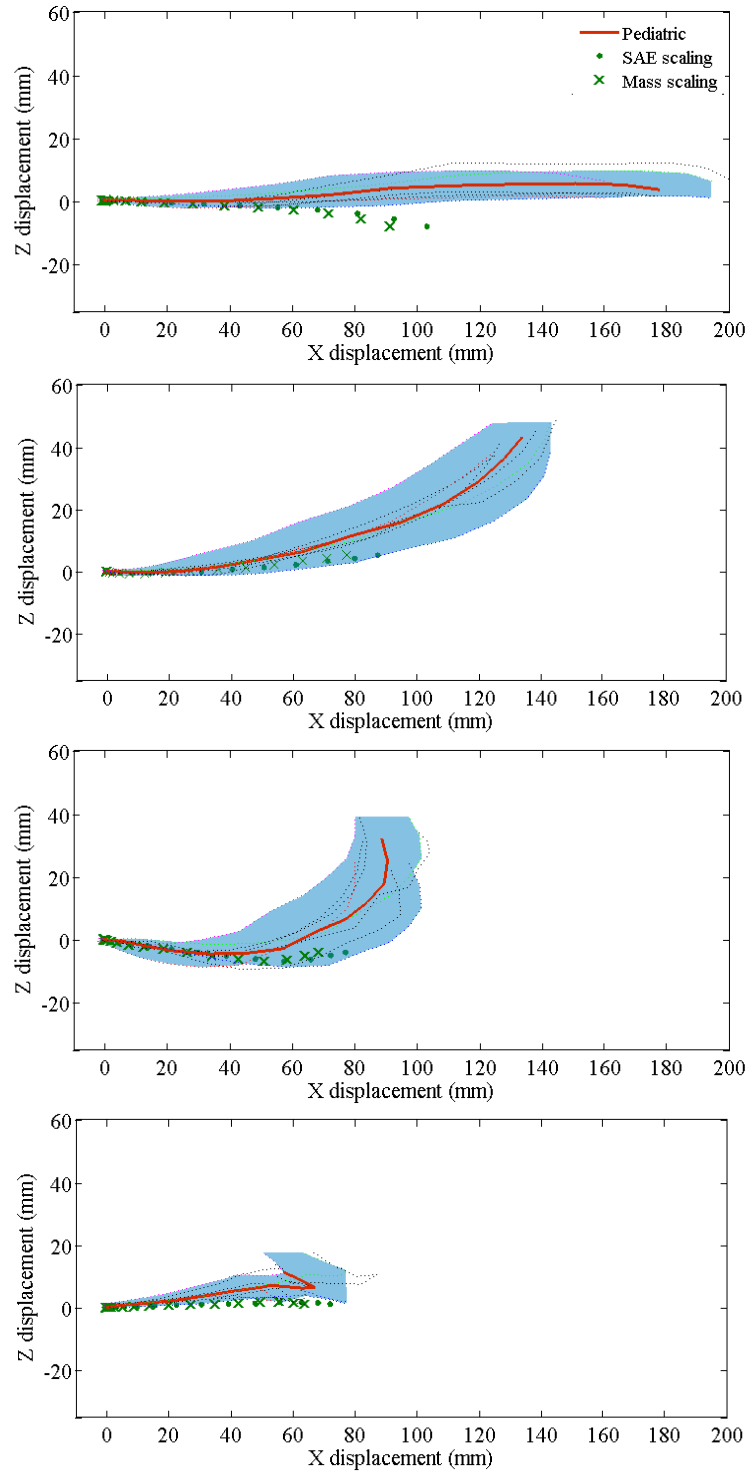


Figure 6.2 Comparison between the measured pediatric average displacements (solid red line) and corridors (blue shaded area) and the predicted pediatric response given by the SAE (green dotted line) and the mass scaling methods (green crossed line) at 9 km/h. From top to bottom: head, T1, T8 and pelvis.

Table 6.2 Summary of the forward peak displacement in the buck coordinate system (X) of the pediatric subjects and the predicted scaled displacements.

	Pediatric Average peak forward displacement	SAE predicted forward displacement (% error)	Mass scaling predicted forward displacement (% error)
Head	177.5	103 (-42.0%)	91.26 (-48.6%)
T1	134.1	87.2 (-35.0%)	77.2 (-42.4%)
T8	88.5	77.0 (-13.0%)	68.2 (-22.9%)
Pelvis	67.1	71.9 (+0.1%)	63.7 (-0.1%)

As for the next thoracic level, the observed trajectory of the pediatric T8 also exhibited a curvilinear characteristic that both scaling methodologies failed to predict. Both methods predicted again a shorter peak forward displacement (13% and 23% shorter), although the predictions were closer to the average X displacement measured for the pediatric volunteers in this case, as shown in Table 6.2.

Last, the pediatric pelvic peak horizontal displacement was predicted accurately (less than 0.5% error) by both scaling methods. In the experiments, the adult pelvis moved forward farther than the pediatric one, and therefore the scaled magnitude is closer to the actual pediatric displacement. Neither of the methods could capture the rebound observed in the pediatric trajectory since it was not present in the trajectories measured in the adult group.

6.3.2 Assessment of energy-based scaling method. Comparison with historic scaling methods

Similarly to Table 6.2, Table 6.3 summarizes the prediction given by the energy-based scaling method and compares the error obtained to the error of the two previously assessed scaling methods. As indicated above, the estimation of the pediatric displacements obtained with the energy-based method was transformed back to the buck coordinate system to allow the comparison with the SAE and mass scaling methods. This comparison is also shown in Figure 6.3, in which the predictions given by the two conventional methods are kept for comparison (represented as green dots and crosses).

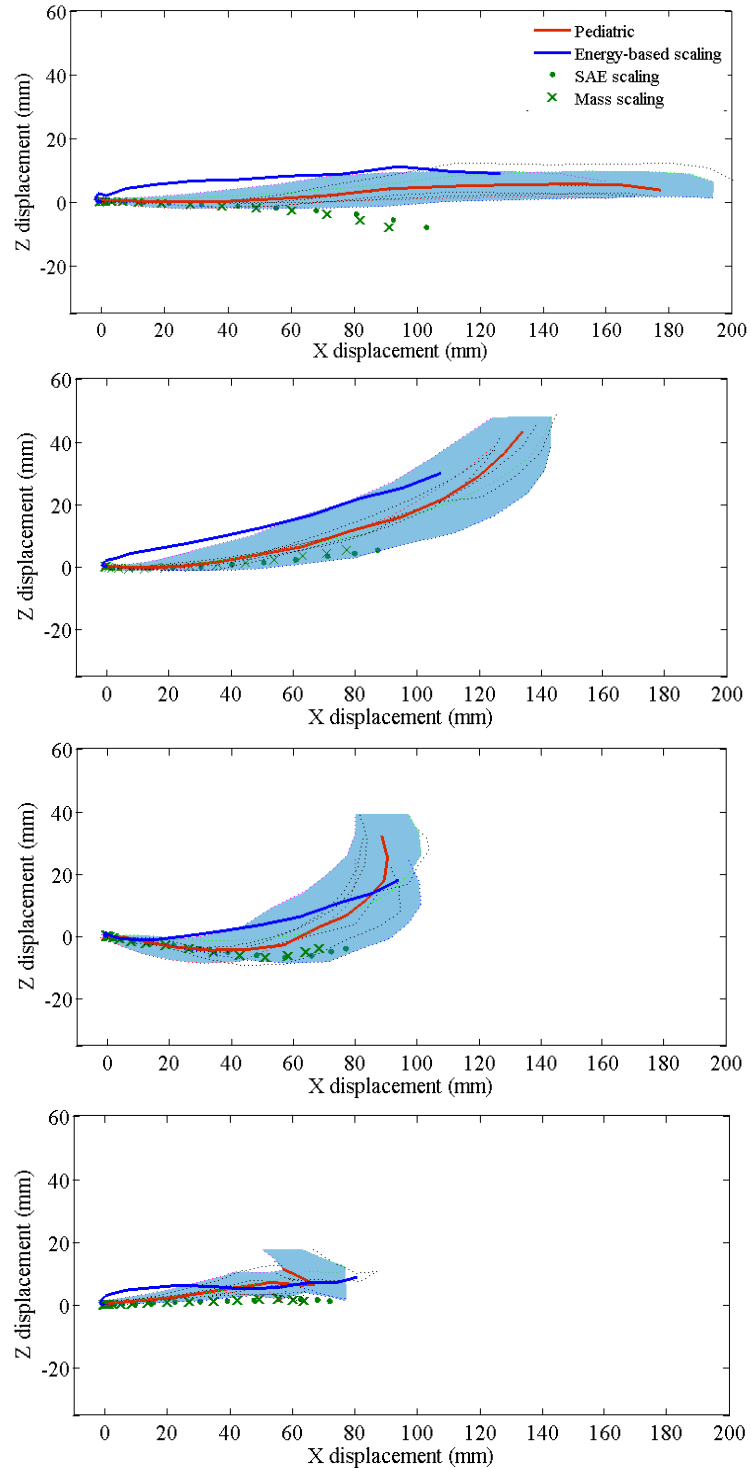


Figure 6.3 Comparison between the measured pediatric average displacements (solid red line) and corridors (blue shaded area), the conventional scaling methods (SAE and mass scaling) and the energy-based scaling method (blue solid line). Buck coordinate system. From top to bottom: head, T1, T8 and pelvis.

Table 6.3 Summary of the forward peak displacement in the buck coordinate system (X) of the pediatric subjects and the predicted scaled displacements (mm).

	Pediatric average peak forward displacement	Energy based scaling prediction (% error)	SAE (% error)	Mass scaling (% error)
Head	177.5	126.5 (-28.7%)	-42.0%	-48.6%
T1	134.1	107.6 (-19.8%)	-35.0%	-42.4%
T8	88.5	94.3 (+0.1%)	-13.0%	-22.9%
Pelvis	67.1	80.71 (+20%)	+0.1%	-0.1%

Although the method failed to predict the actual pediatric displacements as shown in Figure 6.2, it improved by almost 50% the predictions of the forward pediatric head excursion given by any of the two other scaling schemes. As with previous scaling methods, this technique did not capture the curvilinear trajectory of the pediatric thoracic vertebrae, albeit there is a more significant contribution of the vertical component to the trajectory of the relevant landmark than the one observed before.

6.4 DISCUSSION

6.4.1 Assessment of historic scaling methodologies: SAE and mass scaling

Neither methodology was developed to scale the mechanical response between human occupants of different age, but to scale between different sizes of anthropomorphic test devices. Therefore, they were never intended to be applied to scaling the trajectories between children and adults. However, in the absence of impact biomechanical data from children, pediatric ATD within the Hybrid III family and their associated IARV were developed using these techniques and pediatric ATD are currently used as surrogates for children in several testing programs. As expected, in a comparison of the kinematic and dynamic response of the Hybrid III 6YO to the same set of pediatric volunteer data discussed here, Seacrist et al. (2010) found that the ATD exhibited significant reductions in the head, cervical and upper thoracic (T1) spine X and Z excursions.

The direct application of dimensional analysis to the problem of scaling displacements between two different sizes makes use of the length scaling factor to relate the magnitude of the displacements. This scaling factor is, given its definition, always smaller than one. As shown in Figure 6.2, the SAE and mass

scaling methodologies predicted considerably shorter forward excursions of the head, T1 and T8. In addition to predicting always shorter displacements, and even if in the SAE method $\lambda_z \neq \lambda_x$, scaling did not capture the more curvilinear trajectory of the thoracic segments exhibited by the pediatric subjects.

While the Hybrid III 6YO can be considered a scaled replica of the Hybrid III 50th percentile and thus, they can be considered geometrically similar systems, it is not the case of a 6YO child and an adult. As discussed in Chapter 3, Arbogast's study reduced the effect of size in the trajectory plots by normalizing by occupant's size and yet, there were significant differences in the kinematics across ages. Arbogast's approach is therefore comparable to Eppinger's scaling method, and the comparison between the measured pediatric trajectories and the ones predicted by the scaling method manifested the inability of the mass scaling method to capture the differences between the children and adults.

The SAE scaling method, despite of being based on dimensional analysis, took a more empirical approach to the problem of scaling. Instead of using a single length scaling factor, the SAE scaling method proposed to use different length ratios in the X and Z directions, in an effort to capture the differences in the anthropometry of children and adults.

The results included in the previous section showed that both historic scaling methods failed to approximate the actual pediatric trajectories.

6.4.2 Assessment of energy-based scaling method

Neither of the two historic scaling methods included the forces acting on the occupants in the scaling relationships, but these were based solely on geometrical relationships between children and adults. The results obtained suggested that the requirements of geometrical and dynamic similarity were not satisfied. The development of the scaling method based on the conservation of energy attempted to achieve the required dynamic similarity by including a force term in the scaling relationship. The approach taken to develop this method is even more empirical than that adopted by Mertz in the development of the SAE method.

The new scaling method was also assessed using data from the volunteer tests and it was shown to improve substantially the prediction given by the SAE and mass scaling methods. However, the development of the method required to make the following assumptions:

- The occupant can be considered as a point mass and therefore the same scaling factor for the length of the path can be used for any anatomical structure.
- Equation 6.5 can be approximated by Equation 6.6.
- The apportioning of the predicted pediatric path into the X and Z components parallels that of the adult subjects (pediatric trajectory is a scaled model of the adult one).
- The peak belt force acting on the pediatric occupant is known or can be approximated (so that Equation 6.5 can be used to obtain s_{ped}).

6.4.2.1 Is it correct to assume the same ratio between the pediatric and adult path lengths for all the anatomical structures?

By modeling the occupant as a moving point mass, the energy-based scaling method assumed that the same ratio of the length of the paths between adult and pediatric occupants could be used for the head, the thoracic spine and the pelvis. This assumption can be evaluated using the data from Arbogast et al. (2009) that allow comparing the actual values between the two types of occupants. The comparison is shown in Table 6.4. Note that the values are given in the inertial coordinate system (laboratory-fixed coordinate system). In the volunteer test, the sled was pushed backwards (negative X direction) so that the occupant moved in the positive X direction with respect to the buck. The overall motion of the occupant was in the negative X' direction of the inertial coordinate system and that explains why the displacement of the head is smaller than the displacement of the pelvis in this coordinate system.

As it can be seen in Table 6.4, the ratios of the lengths of the path of the different anatomical structures were not the same at 9 km/h and therefore it is unlikely that this ratio would remain the same in the case of a higher speed impact.

Table 6.4 Comparison between the ratios of the lengths of the path of the selected anatomical structures.

	Length of path pediatric (mm)	Length of path adult (mm)	Ratio
Head	56.68	49.68	1.14
T1	108.98	73.98	1.47
T8	149.26	84.30	1.77
Pelvis	176.76	96.81	1.83

6.4.2.2 Equation 6.5 can be approximated by Equation 6.6

This approximation assumed that the ratio between the integrals providing the work done by the belt arresting the forward motion of the occupant could be estimated by the ratio between the peak shoulder belt force multiplied by the total length of the path described by the corresponding anatomical structure. Again the experimental data from Arbogast et al. (2009) was used to assess this approximation.

Thus, let π_1 and π_2 be defined as the following:

$$\pi_1 = \frac{\int_0^{\max_{s_{ped}}} F_{ped} ds_{ped}}{\int_0^{\max_{s_{ad}}} F_{ad} ds_{ad}} \quad \text{Equation 6.7}$$

$$\pi_2 = \frac{F_{ad_{peak}} S_{ad}}{F_{ped_{peak}} S_{ped}} \quad \text{Equation 6.8}$$

Table 6.5 shows the ratio π_1/π_2 calculated for the pediatric and adult subjects involved in the estimation of the pediatric corridors using the energy-based scaling method. The values in the table show that the error in approximating Equation 6.7 by Equation 6.8 was always around 25% at the most and it was around 10% for the majority of the subjects involved in the calculation. Therefore, the approximation to the ratio of the path integrals given by the product of the peak belt forces by the total length of the path was considered acceptable.

Table 6.5 Comparison between the ratios of the lengths of the path of the selected anatomical structures.

	AD1	AD2	AD3	AD4	AD5
PED1	1.02	1.03	1.03	1.22	1.09
PED2	1.03	1.04	1.04	1.24	1.10
PED4	1.06	1.08	1.07	1.28	1.13

6.4.2.3 Apportioning of the pediatric path into the X and Z components using the X and Z apportion exhibited by the adult subjects.

As described in the methods subsection, once the length of the path was scaled, the X and Z components of the pediatric displacements were approximated using the existing relation between the X and Z components of the adult subjects (Equation 6.6).

However, the plots showed in Figure 3.11 comparing the average response of the 6YO to that of the adult indicated that this assumption is probably not valid, especially in the case of the thoracic segments. The trajectory in the case of the thoracic spine showed substantial differences in the sagittal plane. These plots are reproduced in Figure 6.4 for illustration.

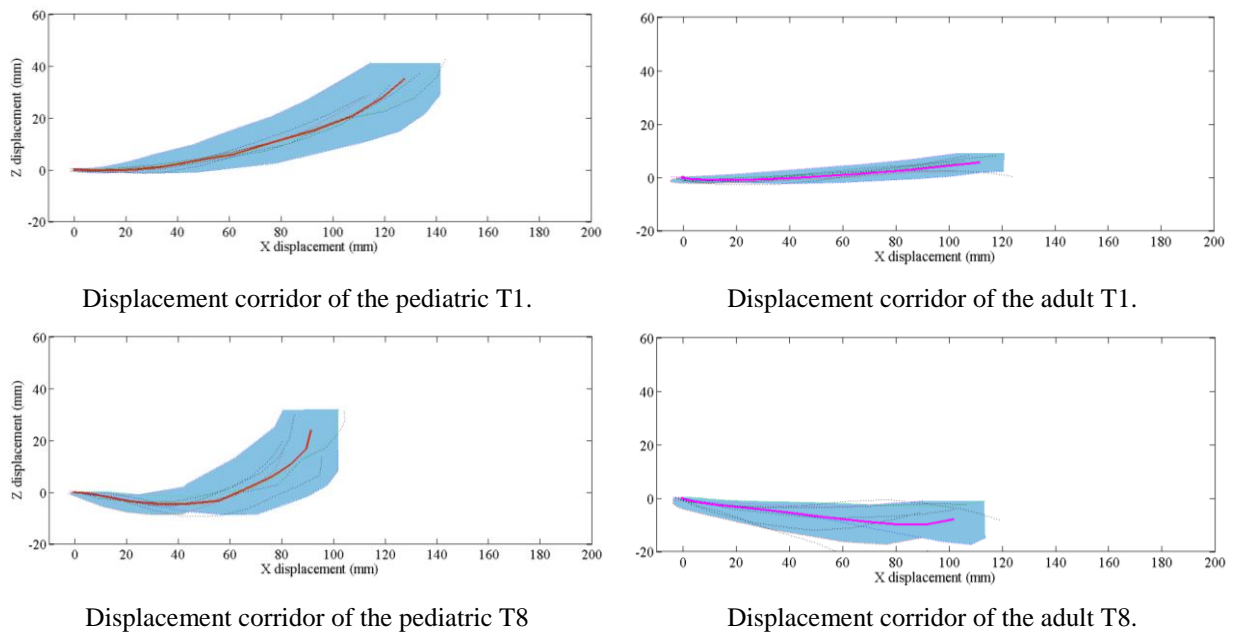


Figure 6.4 Comparison of the trajectories of T1 and T8 between pediatric and adult volunteers in the sagittal plane at 9 km/h. Reproduced from Figure 3.11.

6.4.2.4 *Calculation of the ratio between belt forces at 40 km/h*

The calculation of the predicted pediatric path length using Equation 6.6 required knowing the peak shoulder belt force of the average pediatric subject. This would not be normally the case and especially if the method was applied to predict the pediatric response at higher speeds (injurious tests). Therefore, if this method was to be applied to provide an approximation of the kinematics of children at higher speeds, it would require approximating the peak belt force acting on the children.

6.4.3 Developmental changes in the human spine

In recent years, a handful of papers have suggested that the changes occurring during the development of the subject might be responsible for the inaccuracies of scaling when it is used to predict the pediatric mechanical response using adult data.

Maltese et al. (2008) pointed out that the amount of time for bones in the rib cage to appear and fuse (bones of the sternum – manubrium, sternbrae and xyphoid process- , change of the position of the sternum with respect to the spine that causes the rib to angle downward when viewed laterally and calcification of costal cartilage). Maltese's study calculated the effective stiffness of the pediatric chest and compared it to the adult one using data obtained during cardiopulmonary resuscitation (CPR). The authors suggested that developmental changes may influence the impact response of children in ways that are not considered in scaling. A similar conclusion was reached by Kent et al. (2012) after studying the thoracoabdominal response under belt loading of three cadaveric PMHS and comparing it to the adult one in the same test setup. Both studies provided experimental data that should guide how adult data is used to predict the pediatric response.

Similarly to the changes occurring in the chest during development, there are a number of anatomical and physiological changes occurring in the development of the spine that are not considered in scaling and likely influence the impact response of children.

In fact, the vertebral column is one of the body structures that require more time to reach the complete adult developmental state. For instance, the ossification centers of the cervical spine may reach the complete

fusion state associated with adulthood after the age of 20 (Franklyn et al., 2007) and the ossification and fusion of the sacral vertebrae might not be completed until age 35 (Moore and Dalley, 2005).

Typically, vertebrae begin to ossify from cartilaginous tissue toward the end of the embryonic period (8th week) and continue during the fetal period. With the exception of C1, C2, C7 and the sacral vertebrae and the coccyx, there are three primary and five secondary ossification centers per vertebra. The three primary ossification centers give origin to the body of the vertebrae and to the neural arch. At birth, each vertebra consists of three bony parts joined by cartilaginous tissue with the exception of the inferior sacral vertebrae and the coccygeal vertebrae which are entirely cartilaginous and ossify during infancy. The upper neural arches begin fusing with the centra in the upper cervical region at age 3, but the process is not completed in the lower lumbar region until after the 6th year.

The five secondary ossification centers appear during puberty: one at the tip of the spinous process; one at the tip of each transverse process; and two annular epiphyses, one on the superior and one on the inferior edge of the vertebral body. The intervertebral discs are attached to them and are also referred to as epiphyseal growth plates. They form the zone from which the vertebral bodies grow in height. All secondary ossification centers have usually united with the vertebrae by age 25.

In case of the cervical spine, there are five ossification centers in C2 (axis) and three ossification (one at the anterior centrum and two in the posterior neural arches) centers in C1 (atlas) and all the other vertebrae (C3 - C7). The atypical morphology of C1 and C2 is also established during development. The centrum of C1 becomes fused to that of C2 and loses its connection to the remainder of C1, thus forming the dens and precluding the formation of the intervertebral disc between C1 and C2 (Moore and Dalley, 2005).

Between birth and age 5, the body of a lumbar vertebra may increase in height threefold (from 5 mm to 15 mm), and it may increase another 50% between ages 5 and 13. This growth continues during adolescence but at a slower rate. The process is completed at around age 25.

The intervertebral disks undergo also important developmental changes. The nucleus is large in the newborn with some loose annular fibers embedded in it, making unclear the distinction between the two components. Fiber formation occurs over time and it is possible to appreciate the annulus fibrosus at age 3

years. It is not until adolescence or adulthood that the nucleus pulposus reaches its skeletally mature level with a concomitant development of the annulus fibrosus (Nahum and Melvin, 2002). In the infant and child, the intervertebral disks grow at a different rate depending on the spinal level.

The differences in size between the anterior and posterior aspects of the vertebrae and intervertebral disks determine the curvature of the spine. The thoracic kyphosis (primary curvature) is the only curvature of the spine that is present in the newborn and it is caused by the different antero-posterior height of the thoracic vertebrae. The cervical lordosis develops when the infant is able to hold his head (3-4 months), while the lumbar one is associated with walking (between 12 and 18 months of age) (Franklyn et al., 2007). These two latter curvatures are associated to the differences between the anterior and posterior aspects of the intervertebral discs and are known as secondary curvatures.

The orientation of the facet joints changes also depending on the level of development of the spine. Younger specimens show a predominantly horizontal facet joint angle, while adult facet joints tend to be oriented more vertically. The joints in the upper spine are also less oblique than in the lower (C1-C2 angle in the newborn is 55° and increases up to 70° at maturity, at the lower cervical spine, facet angles are around 30° at birth increasing to 60° - 70° at maturity) (Green and Swiontkowski, 1998). During the developmental process, neck dimensions (e.g. breadth) and cross-sectional areas of the muscles increase, although flexors and extensors exhibit a different increase rate.

In summary, there exist developmental changes in the spine that are not limited to a simple change in size as the subject ages. These changes affect the material properties of the tissue (ossified vs. cartilaginous tissue), the geometrical orientation of the vertebrae with respect each other (different rate of growth for different regions of the spine) and the orientation of the articular surfaces (facet joints) between vertebrae. These developmental changes cannot be ignored in the process of scaling adult spinal trajectories to predict pediatric ones.

The large errors in magnitude and nature observed in the predicted pediatric trajectories were likely caused by the intrinsic differences between the two types of subjects. Due to the developmental changes, neither

geometrical nor dynamic similarity can be assumed to be satisfied between the adult and the developing states and therefore scaling cannot be used to predict the kinematics of children.

6.4.4 Aspects to be considered in the prediction of pediatric trajectories

It is unknown how the changes occurring during development affect the kinematics of the head and spine of children in frontal impacts. The experimental work by Arbogast et al. (2009) was crucial to understand the significant differences in magnitude and in nature between pediatric and adult occupants, but it cannot quantify the effect of tissue development on the kinematics. Such endeavor requires performing sled tests with pediatric occupants to measure the kinematics and having access to the anatomical structures to obtain the mechanical properties of the tissue and the morphology of the spine. It is not envisioned that such tests can be performed in a short term.

The scaling methods that were assessed within this chapter shared fundamental limitations in how they address the problem of predicting the kinematics of children from adult data. The summary of these limitations is that scaling cannot predict what is different in nature. The experimental data included in Chapter 3 showed that both the magnitude and the shape of the trajectories were essentially different between the two subject types. Then, the above paragraphs described several morphological changes occurring in the spine that are likely associated with the functional differences observed in the experiments. Thus, describing adequately the kinematics of children with focus on the head and spine requires to consider the changes occurring during development. These changes include, but are not limited to, the morphological developments detailed above.

In fact, the assessment of the last scaling method showed that a methodology that models the occupant as a point mass will fail to provide a good approximation of the true motion of the different sections of the body as it was illustrated in Table 6.4. The study by Kent et al. (2009) on the characterization of the pediatric torso under belt loading brought up a related subject: the differences in the apportionment of trunk volume between the thorax and abdomen in children and adults (Figure 6.5). Franklyn et al. (2007) indicated that the organs in the thoracic and abdominal cavities change in size and in position from the neonate state until

adolescence. The same study describes also the differences in the relative size of the head and the trunk between children and adults.

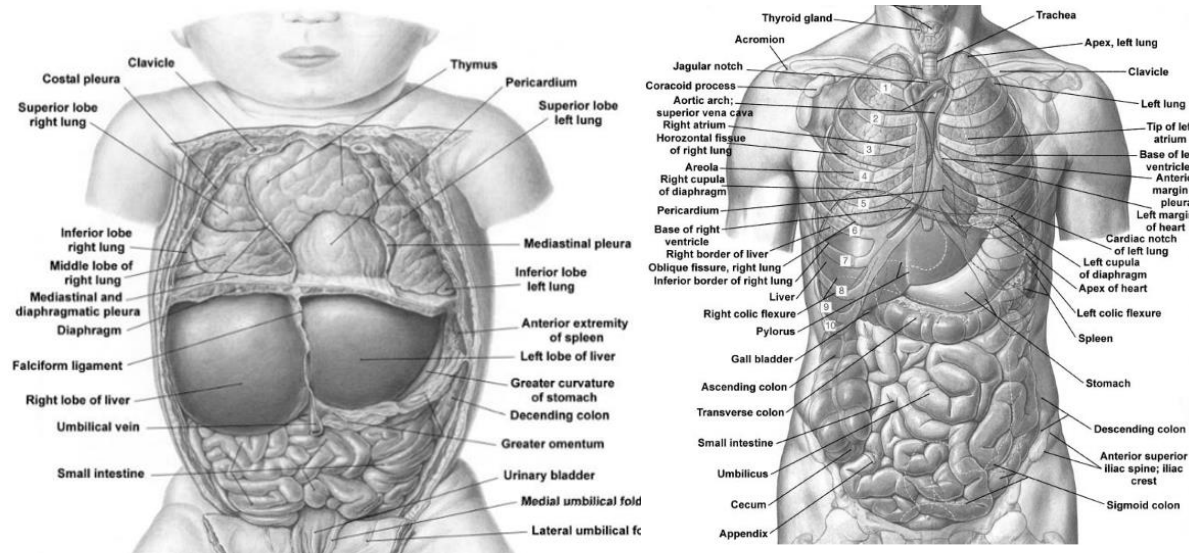


Figure 6.5 Torso anatomy of a newborn (left) and an adult (right). Note the changes in organ volume and the associated changes in mass distribution of the trunk between the two subjects (Kent et al., 2009).

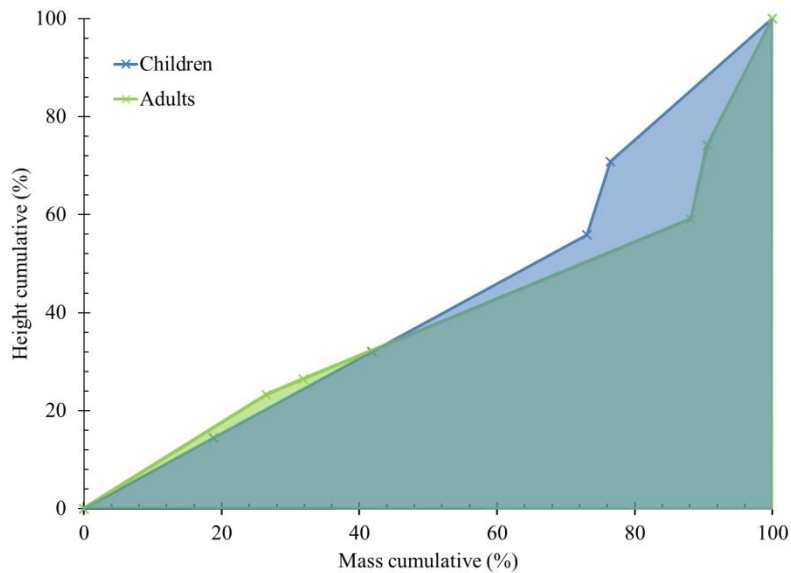


Figure 6.6 Relationship between percent of body weight and percent of body height in a 50th percentile adult and in a 6YO. Applicable only to the torso and head of the subjects.

To further explore these differences in mass distribution for the case of study of this dissertation, a number of studies providing the anthropometry of the 50th percentile 6YO and the 50th percentile adult were combined to compare the mass and height distribution of the head, thorax and abdomen (NASA, 1996; Irwin et al., 1997; Irwin et al., 2002). Figure 6.6 shows the comparison showing that over 35% of the height of the subject, the cumulative mass of a 6YO is always lower than that of the adult for the same cumulative height (indicating that upper portions of the pediatric trunk and head are relatively heavier than the corresponding portions of the adult).

These anatomy changes occur in a complex and non-linear way during development. The consequences of these changes are not fully understood in terms of the kinematics of occupants during the impact, but any attempt of identifying differences in the motion of different sections of the trunk between children and adults must consider them due to the changes in mass distribution and moment of inertia.

To partially include these developmental material and structural changes, the next chapter in this dissertation focuses on the development of a multibody model in which several rigid links representing different body regions are connected by revolute joints with constant stiffness and damping. Such model incorporates the effects of a distributed mass and those related to the development of joints, although in a simplified manner. Even if they are a rough approximation to a complex problem, multibody models have been successfully applied to describe the kinematics of car occupants in different loading conditions, from very simple models created in the early 1960s (McHenry, 1963) to complex ones such as MADYMO models that incorporate also finite elements to capture the deformation of the structures (TNO Madymo, 2005). In parallel, simpler models have been used to understand particular aspects of the kinematics of the occupant and its interaction with the restraints (Crandall et al., 2000; Habib, 2001; Huang, 1995; Katoh and Nakahama, 1982; Paulitz et al., 2006; Gordon and Hopkins, 1997).

6.5 CONCLUSION

Chapter 6 used the results by Arbogast et al. (2009) to assess the predictions to the kinematics of children given by three methods based on scaling. None of the methods provided an accurate approximation to the observed experimental data. The first two methods (SAE and mass scaling) are based on dimensional

analysis and they have been used historically in the field of impact biomechanics to scale the mechanical response within different sizes of dummies. The third one was developed within this dissertation and instead of including only geometrical considerations, it also included the force of the belt acting on the occupant (in an attempt to overcome the lack of dynamic similarity needed in dimensional analyses). All these three methods failed to approximate both the magnitude and the nature of the pediatric displacements. The chapter also examined anatomical changes occurring during development that can explain why the pediatric and adult kinematics were so different. Although the degree to which these changes affect the kinematics of pediatric subjects is unknown, the net effect was a substantial change in magnitude and nature that no scaling method can capture.

The next chapter develops a multibody model proposed as an alternative to describe the kinematics of pediatric and adult occupants.

7 USING A 2D MULTIBODY MODEL TO PREDICT PEDIATRIC KINEMATICS

7.1 INTRODUCTION

This chapter focuses on the development of a linear 2D multibody model of the occupant that incorporates the differences in mass distribution and joint properties between children and adults discussed in Chapter 6.

All the experimental data described in previous chapters and additional data from sled tests using animal surrogates were combined to develop and validate a tool to predict the kinematics of a pediatric occupant at 40 km/h. Instead of scaling between adult and pediatric subjects, this methodology related the kinematics of the same occupant between 9 km/h and 40 km/h.

The tool is based on the use of a linear multibody model of the occupant. A multibody model can incorporate the effects of different mass and moment of inertia by body regions that were suggested to play a major role in the nature of the kinematics of children and adults. The model can also include the joint stiffness differences observed in the thoracic FSU experiments described in Chapter 5. Given the limited amount of pediatric experimental data (only the volunteer sled tests from Arbogast et al. (2009) were considered), the model was set to be as simple as possible so that all the parameters needed to develop the model of a 6YO could be estimated as robustly as possible from the available experiments.

7.2 OVERVIEW OF THE DEVELOPMENT OF THE LINEAR TIME-INVARIANT 2D MODEL OF THE OCCUPANT

The development of a multibody model requires the following elements:

1. Definition of the number of rigid bodies and their relative position in space.
2. Definition of the mass and moment of inertia of each of the rigid bodies in the model.
3. Definition of the joints connecting the rigid bodies (number of degrees of freedom and stiffness and damping properties).

4. Definition of the external loads acting on the model.

Then, the governing equations of the system can be written in the most general form as:

$$\underline{\underline{M}} \cdot \underline{\underline{\ddot{q}}} + \underline{\underline{C}} \cdot \underline{\underline{\dot{q}}} + \underline{\underline{K}} \cdot \underline{\underline{q}} = \underline{\underline{Q}} \quad \text{Equation 7.1}$$

where $\underline{\underline{M}}$, $\underline{\underline{C}}$ and $\underline{\underline{K}}$ are square matrices with elements formed by combinations of the mass, length, moment of inertia of each link, and the joint stiffness and damping of each joint. Vectors $\underline{\underline{q}}$, $\underline{\underline{\dot{q}}}$ and $\underline{\underline{\ddot{q}}}$ are column vectors formed by the generalized coordinates and their time derivatives. Last, vector $\underline{\underline{Q}}$ is a column vector formed by the generalized forces resulting from the applied external loads that can be obtained according to the expression (Goldstein, 1981):

$$\sum_i \underline{F}_i \cdot \delta \underline{r}_i = \sum_{ij} \underline{F}_i \cdot \frac{\partial \underline{r}_i}{\partial q_j} \delta q_j = \sum_j Q_j \cdot \delta q_j \Rightarrow Q_j = \sum_i \underline{F}_i \frac{\partial \underline{r}_i}{\partial q_j} \quad \text{Equation 7.2}$$

where \underline{F}_i are each of the “i” external loads (either forces or moments) applied to the system, $\delta \underline{r}_i$ are the virtual displacements caused by the forces \underline{F}_i and therefore the term $\underline{F}_i \frac{\partial \underline{r}_i}{\partial q_j}$ expresses the virtual work done by forces \underline{F}_i in virtual displacements that are compatible with any of the “j” generalized coordinates.

Equation 7.1 establishes that if the $\underline{\underline{M}}$, $\underline{\underline{C}}$ and $\underline{\underline{K}}$ matrices of a mechanical system are known, for a given vector of generalized forces $\underline{\underline{Q}}$, the value of the corresponding generalized displacements $\underline{\underline{q}}$ (and therefore the corresponding time derivatives) can be calculated.

Thus, the objective of this chapter was to obtain the matrices $\underline{\underline{M}}$, $\underline{\underline{C}}$ and $\underline{\underline{K}}$ that characterize the mechanical response of a restrained 6YO occupant and to use Equation 7.1 to predict the displacement of the occupant.

Given the limited amount of available experimental data to guide the development of the multibody model, the following assumptions were made:

- The occupant can be modeled as a linear, time-invariant 2D system.

- Each of the body segments can be modeled as an ellipse of constant mass and dimensions.
- The deformation of the entire spine can be approximated by the flexion of three revolute joints at T1, T8 and L2.
- External forces can be modeled as point forces acting on selected anatomical landmarks. In particular, the distributed belt load can be approximated by a set of three point forces acting along the path of the belt.
- The motion of the occupant occurs primarily within the sagittal plane up to the time of peak forward head excursion.

The baseline model of the occupant consisted of seven rigid links (foot, leg, thigh, lumbar, lower thoracic, upper thoracic and cervical-head regions) connected by frictionless revolute joints at T1, T8, L2, hip, femoral epicondyle and lateral malleolus. The occupant can move with respect to the global coordinate system (GCS), which is a laboratory-fixed coordinate system, in the sagittal plane. The sled can move only in the horizontal direction with respect to the GCS. Positive X axis of the GCS pointed forward (opposite to the movement of the sled) and Z axis pointed upwards and was perpendicular to X. The Y axis was chosen to complete a right-hand coordinate system. This GCS is similar to the one used in the PMHS sled tests.

Seven generalized coordinates were required to define the position of the model within the GCS. These coordinates correspond to the motion of the sled with respect to the GCS (q_1) and the rotations of each link with respect to the global X axis (q_2, \dots, q_7). The model also considered six external loads acting on the occupant: upper shoulder belt force (FUSB), middle shoulder belt force (FMSB), lower shoulder belt force (FLSB), lap belt force (FLapB), seat reaction force (FS) and the knee bolster reaction force (FKB, which only existed in the case of PMHS at 40 km/h). The upper shoulder belt force was considered to be applied on T1, the middle shoulder belt force was applied on T8, the lower shoulder belt force was applied on L2, lap belt force and seat forces were applied on the pelvis and the knee bolster force was applied to the proximal tibia. The definition of the generalized coordinates and the point of application of the external

forces are shown in Figure 7.1. The corresponding system equations of motion were derived and included in Appendix A2.

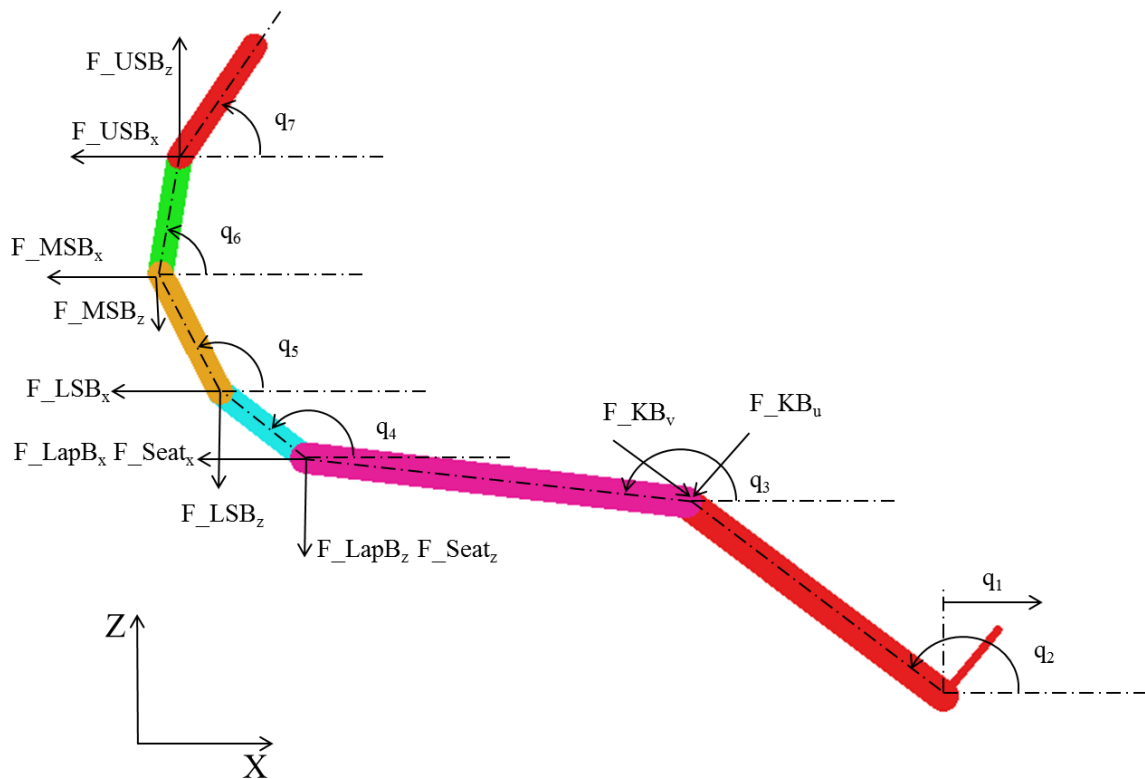


Figure 7.1 Definition of the generalized coordinates and points of application of external forces.

7.3 USING A LINEAR TIME-INVARIANT MODEL TO DESCRIBE THE KINEMATICS OF A RESTRAINED PEDIATRIC OCCUPANT

As mentioned above, the objective of this chapter was to obtain the \underline{M} , \underline{C} and \underline{K} matrices that characterize the mechanical behavior of a restrained pediatric occupant and use them to obtain the generalized displacements under the action of the corresponding generalized forces. In particular, these generalized forces will be the ones acting on a 6YO at 40 km/h.

Before applying the method to the prediction of the pediatric displacements and to assess its robustness, the following four hypotheses were investigated:

- 1- A linear, time-invariant multibody model of a restrained occupant can predict the sagittal displacement of the head and the thoracic spine at different impact speeds.
- 2- Such a model can predict the sagittal displacement of the head and the thoracic spine of a restrained 6YO occupant in a 9 km/h frontal deceleration.
- 3- The stiffness and damping characteristics of the joints are independent of the velocity of the impact.
- 4- The forces acting on a 6YO occupant can be approximated if the forces acting on an adult are known at the same impact speed.

The available experimental sources described earlier were combined in different ways in the analysis of the aforementioned hypotheses. The following sections within this chapter focus on the assessment of each of them. The evaluation of the first three hypotheses required obtaining the system matrices (M , C and K) of different types of occupant surrogates. Although the specific methodology is described specifically within the corresponding section, optimization was needed to solve for the unknown parameters involved in the formulation of the system matrices. Given the limited amount of experimental data available to be used in the optimization, the multibody model of the restrained occupant was, by design, kept as simple as possible to reduce the number of unknowns to be solved for. In parallel, it was required that the model could capture the inherent differences between subjects instead of just fitting an average occupant within each of the age groups and speed conditions.

Thus, section 7.4 focuses on describing the general framework used in the optimization and then section 7.5 through section 7.8 address each of the four hypotheses. Section 7.9 provides the estimated displacement corridors for the restrained 6YO at 40 km/h and section 7.10 discusses the approximations made in the method and their implications in the results obtained.

7.4 USING OPTIMIZATION TO SOLVE FOR UNKNOWN PARAMETERS IN THE SYSTEM MATRICES

7.4.1 Optimization

An optimization problem was set up to solve for the unknown parameters in the development of the multibody model of the occupant. The optimization was designed to minimize the sum of square errors (SSE) between the measured (experiments) and predicted (model) displacements of the head and thoracic spine every 10 milliseconds. A commercial multibody simulation package (ADAMS©) was used to solve the equations of motion at each iteration of the optimization problem and the package MATLAB© was used to solve the optimization problem. Specifically, MATLAB © Global Optimization Toolbox provides algorithms that search for global solutions to problems that contain multiple maxima or minima (Matlab, 2012). Two solvers were used to obtain the value of the global minimum (minimum value of SSE):

Global search solver. This solver uses gradient-based methods to obtain local and global minima. It starts a local solver (also implemented in MATLAB©) from multiple starting points. The starting points are generated using a scatter-search algorithm that filters the starting points based upon the values of the objective function and the constraints of the optimization problem. The global search solver runs a constrained nonlinear optimization solver to search for a local minimum for those starting points that are classified as promising starting points after passing the filtering process.

Genetic algorithm solver. The genetic algorithm solves optimization problems by using the principles of biological evolution, creating a population of starting points using principles based on gene combinations and natural selection. Thus, the algorithm chooses starting points in a way that is random in nature and uses them to produce the next generation of starting points. It has been shown that over successive generations, the population evolves toward an optimal solution. The genetic algorithm generates a population of points at each iteration in which the best point in the population approaches an optimal solution.

Regardless of the method chosen and depending on the size of the problem (i.e. how many subjects were included in the process of obtaining the optimized joint parameters), an Intel Core™ i7-2640M CPU @

2.80GHz and with 8GB RAM of installed memory took between 72 hours and 192 hours to provide the value of the unknown model parameters.

7.4.2 Assessment criteria for the acceptance of a model

A set of assessment criteria were used to evaluate the solutions obtained in the optimization problem. The criteria were based on comparing the displacement time history between the results predicted by the multibody model and the data measured in the actual experiments, with focus on the forward displacements of the head and thoracic vertebrae and especially on the peak forward displacement of the head.

Thus, the multibody model of the occupant was required to perform within the following criteria:

- a) The error between the model-predicted and the experiment-measured peak forward excursion of the head was less than 15%.
- b) The error between the model-predicted and the experiment-measured peak forward excursion of the thoracic vertebrae T1 and T8 was less than 25%.
- c) The motion of the occupant was human-like.
- d) The error between the model-predicted and the experiment-measured peak vertical excursion of the head, T1 and T8 was less than 25%.

Despite that the assessment of the models was primarily done considering the forward displacements of the relevant anatomical landmarks, the vertical displacement of the anatomical structures was also include in the calculation of the SSE in the optimization.

7.5 HYPOTHESIS 1: A LINEAR, TIME-INVARIANT MULTIBODY MODEL CAN PREDICT THE SAGITTAL DISPLACEMENT OF A RESTRAINED OCCUPANT AT DIFFERENT IMPACT SPEEDS.

The first hypothesis consisted of verifying that a linear, time-invariant model could be used to predict the sagittal displacement of the head and thoracic spine of a restrained occupant in frontal impacts at different speeds.

The experimental data used to verify this hypothesis were the data obtained from the PMHS tests at 9 km/h and at 40 km/h. As it was detailed in Chapter 4, the instrumentation used in these tests allowed measuring the 6-dof motion of the head, spine and pelvis of the occupants as well as the position of several other anatomical landmarks. Moreover, the load cells used in the experimental setup proportioned the needed data to model forces acting on the occupant during the deceleration. Thus, in this case, the known magnitudes were the generalized coordinates and forces and the unknown terms were the system matrices \underline{M} , \underline{C} and \underline{K} . Time-history plots of the generalized coordinates, velocities and accelerations, and of the generalized forces are included in Appendix A3 for illustrative purposes.

Table 7.1 summarizes the parameters involved in the development of the model, indicating the source (or sources, in some instances) from which the value of the parameter was obtained or calculated.

Table 7.1 Parameters included in the 2D model

Parameter	Symbol	Source
Generalized coordinates	q_i	Measured
Generalized velocities	\dot{q}_i	Measured
Generalized accelerations	\ddot{q}_i	Measured
Generalized forces	Q_i	Measured
Mass	m_j	Estimated combining literature and subject anthropometry
Length	l_j	Measured (subject anthropometry)
Moment of inertia	I_j	Calculated approximating the body regions as ellipses
Joint stiffness	k_j	Calculated using optimization
Joint damping	c_j	Calculated using optimization

Note: j = T1, T8, L2, pelvis, knee, ankle; i = 1... 7

7.5.1 Mass of the body regions

The mass of each body region was approximated using published anthropometric data from the 50th percentile American male (NASA, 1996). Although the definition of the body regions in the study differed slightly from the model body regions selected in this dissertation, it was considered a reasonable approximation as shown in Table 7.2

Table 7.2 Equivalence between the body regions used in the NASA study and the model body regions.

NASA (1996) body region	Model body region	NASA Mass (kg)
Head and neck	Head and neck (CH): Head to T1	5.5
Thorax (T1-T10)	Upper thoracic (UT): T1 to T8	26.1
Abdomen (T11-ASIS)	Lower Thoracic (LT): T8 to L2	2.5
Pelvis (ASIS-P.Symph)	Lumbar (L): L2 to H-point	12.3
Thigh	Thigh (UL): H-point to knee	20.7
Calf	Leg (LL): knee to ankle	8.1
TOTAL		82.2

The total mass of each PMHS was distributed across the model body regions according to the mass ratio of each body region as calculated from the NASA study. The resulting values are shown in Table 7.3.

Table 7.3 Body region mass of PMHS (kg).

Model body region	NASA mass ratio	PMHS1	PMHS2	PMHS3
CH	0.07	5.34	5.91	5.42
UT	0.32	25.35	28.08	25.73
LT	0.03	2.43	2.69	2.46
L	0.15	11.94	13.23	12.12
UL	0.25	20.08	22.24	20.38
LL	0.10	7.84	8.69	7.96
TOTAL	0.91	79.8	88.4	81.0

7.5.2 Length of the body regions

The length of the body regions was calculated using the data from the motion capture system. The regions were considered rigid and therefore, the length was assumed to be constant and equal to the length of the

segment at $t=0$ ms over the duration of the experiment. Table 7.4 shows the length of the body regions of the three subjects.

Table 7.4 Body region length of PMHS1 (m).

Model body region	PMHS1	PMHS2	PMHS3
CH	0.24	0.21	0.31
UT	0.14	0.21	0.18
LT	0.16	0.18	0.15
L	0.12	0.06	0.11
UL	0.44	0.47	0.51
LL	0.38	0.42	0.44

7.5.3 Moment of inertia of the body regions

The values of the moment of inertia of the body regions were calculated by assuming that the body regions were ellipses. The length of the minor (b) and major (a) axes of the ellipses were obtained from the anthropometry of the test subjects, and the moments of inertia were obtained from Equation 7.3:

$$I = \frac{1}{4}m \left(\left(\frac{a}{2}\right)^2 + \left(\frac{b}{2}\right)^2 \right) \quad \text{Equation 7.3}$$

where a and b are the magnitudes of the minor and major axes of the ellipse. The calculated values of the moment of inertia for each body region are shown in Table 7.5

Table 7.5 Body region moment of inertia of PMHS (kg m^2).

Model body region	PMHS1	PMHS2	PMHS3
CH	0.030	0.033	0.042
UT	0.098	0.162	0.107
LT	0.012	0.016	0.010
L	0.040	0.022	0.029
UL	0.282	0.340	0.370
LL	0.085	0.109	0.111

7.5.4 Joint stiffness

To ensure a common formulation to model the stiffness of the joints of the occupant but preserving the inherent inter-subject variability, joint stiffness was expressed as a function of other magnitudes that were subject-dependent, namely:

$$k_i = k_i(x_1, \dots, x_n) \quad \text{Equation 7.4}$$

where x_i can be either the same or a different property of the tissue or the subject (length, mass, Young's modulus, time, density...).

To the knowledge of the author, there was no published information about modeling joint stiffness using a formulation as the one shown in equation 7.4. The simple problem of a beam undergoing bending was analyzed to obtain a relationship between the effective stiffness of the beam and other beam parameters (Figure 7.2)



Figure 7.2 Schematic of a beam subjected to bending.

In particular, the moment ($M'(x) = P(x - L)$) acting on a section x of the beam and the angle rotated by the corresponding section ($\frac{dy}{dx}$) are related by Equation 7.5.

$$M'(x) = -EI \frac{d^2y}{dx^2} \quad \text{Equation 7.5}$$

where y is the deflection of the beam, E is the Young's Modulus and I is the moment of inertia of the cross section of the beam. Thus, the dimensions of the equivalent rotational stiffness of the beam can be obtained according to the following dimensional equation:

$$[k] = [E][I][L]^{-1} = [E][R_{cs}]^4[L]^{-1} \quad \text{Equation 7.6}$$

where R_{cs} is the radius of the cross sectional area (assuming a circular cross section).

Equation 7.6 proposes a relationship that is dimensionally correct between the effective stiffness of the beam and three other beam parameters: the Young's modulus, the radius of the cross sectional area and the length of the beam. This relationship was used to relate the stiffness of each of the joints of the multibody model to other subject-dependent (in fact subject and body-region dependent) characteristics.

While the values of the radius of the cross section and the length of the body regions were available from the anthropometry of the tests subjects, it was necessary to find an estimation of a parameter with the same dimensions of the Young's modulus that was subject-dependant. This parameter should be related to some known characteristic of the PMHS and it should include both the contribution of soft and hard tissue to the effective stiffness of the joints.

As for the soft tissue contribution, Iida et al. (2002) investigated the relationship between the ultimate load and elastic stiffness of lumbar spinous ligaments and age. A significant decreasing linear relationship was found between the ligamentous mechanical properties and the age of the donor ($p < 0.02$), as illustrated in Figure 7.3:

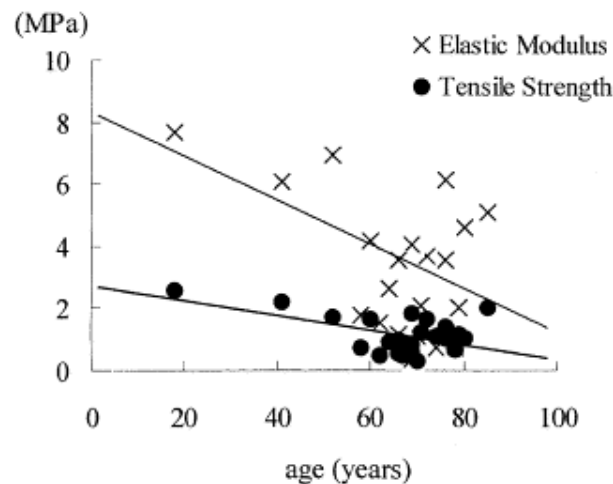


Figure 7.3 Correlation between age and elastic modulus of ligaments as provided by Iida et al. (2002).

Therefore, Iida et al. (2002) proposed a relationship between age and elastic modulus of the form:

$$E = -\gamma_1 \text{ age}$$

Equation 7.7

On the other hand, the contribution of the bone tissue to the stiffness joint can be modeled using the results from Diamant et al. (2005) showing a linear relationship between the modulus of elasticity of bone and the bone mineral density (BMD) (Figure 7.4).

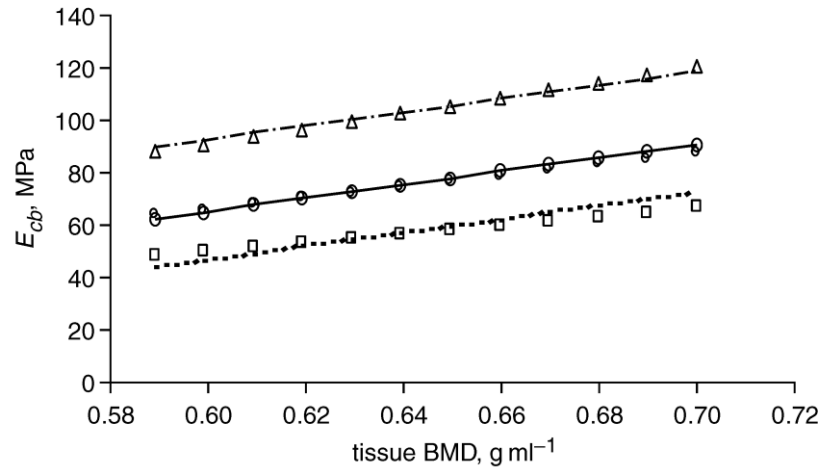


Figure 7.4 Linear relationship between the elasticity modulus and the bone mineral density of bone tissue as given by Diamant et al. (2005).

Thus, it can be concluded that:

$$E = \vartheta \text{BMD}$$

Equation 7.8

where ϑ is a proportionality constant. However, the bone mineral density for the subjects considered in this dissertation was also unknown. The problem of estimating the bone mineral density for different populations groups attending to age, life style, ethnicity and gender has been extensively addressed in the literature (Boot et al., 1997; Looker et al., 1997; Warming et al., 2002; Kalkwarf et al., 2007; Looker et al., 2009). This dissertation research made use of some of the published material to estimate the value for the BMD of the each of the test subjects.

In particular, Looker et al. (2009) provided a linear correlation showing that the BMD decreased linearly with age in a group of 13,091 American adults aged 20 years and older from different ethnic groups. Figure 7.5 shows these correlations for the non-Hispanic group to which the three PMHS belonged.

Therefore, Equation 7.8 can be written as follows:

$$E = \vartheta \text{ BMD} = \vartheta (-\gamma_1 \text{ age}) = -\gamma_2 \text{ age} \quad \text{Equation 7.9}$$

The estimated BMD values for the three PMHS are shown in Table 7.6.

Table 7.6 Estimated BMD for the PMHS considered in this dissertation.

	PMHS 1	PMHS 2	PMHS 3
BMD (kg/m ²)	10.42	11.75	11.82

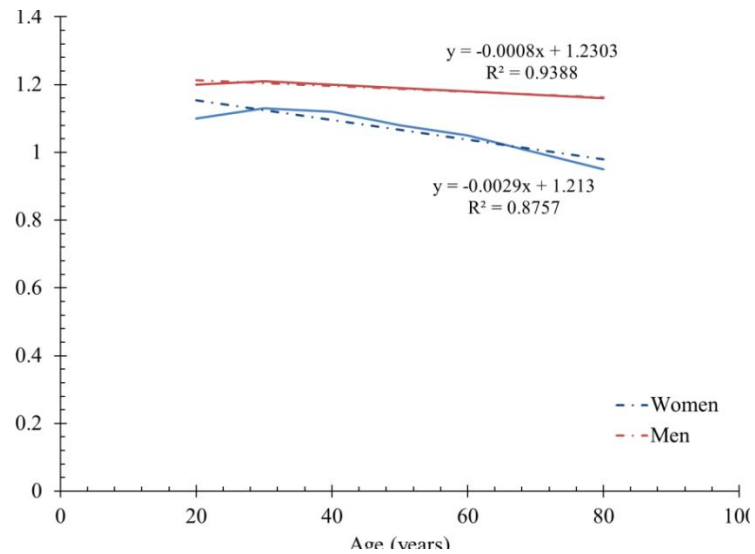


Figure 7.5 Mean total body BMD of adults aged 20 years and older by age, sex. Non-hispanic white people. Adapted from (Looker et al. (2009)).

After finding these relationships between BMD and the modulus of elasticity, the parameter representing the Young's modulus of the beam was chosen to be the product of an unknown constant ($\alpha_i, i = 1,2,3,4$) times the BMD corresponding to each PMHS. Thus, the expressions proposed to model the stiffness of the joints were:

$$k_{T1} = (\alpha_1 \text{ BMD}) l_{CH}^{-1} R_{CS_{T1}}^4 \quad \text{Equation 7.10}$$

$$k_{T8} = \tau_1 k_{T1} \quad \text{Equation 7.11}$$

$$k_{L2} = \tau_2 k_{T1} \quad \text{Equation 7.12}$$

$$k_P = (\alpha_2 BMD) l_L^{-1} R_{CS_P}^4 \quad \text{Equation 7.13}$$

$$k_K = (\alpha_3 BMD) l_{UL}^{-1} R_{CS_K}^4 \quad \text{Equation 7.14}$$

$$k_A = (\alpha_4 BMD) l_{LL}^{-1} R_{CS_A}^4 \quad \text{Equation 7.15}$$

As for the values of constant τ_1 , the relationship obtained for the adolescent specimen (M485) was used to approximate the relationship between the stiffness of the T8 and T1 joints, in the absence of information about the ratio between the stiffness of the joints in the adult FSU.

$$1/\tau_1 = 0.77 \quad \text{Equation 7.16}$$

The relationship between the lumbar and the lower thoracic joint was obtained from the quasistatic experiments reported in the literature and included in the review section within Chapter 5. These relationships and the studies in which they were based are shown in Table 7.7. Both Sran et al. (2005) and Oxland et al. (1992) reported values corresponding to the flexibility coefficients (f), which are the inverse of the stiffness coefficients (k). Table 7.7 also shows the value chosen for the constant τ_2 that relates the stiffness of the two joints.

Table 7.7 Relationships between the stiffness of different vertebral levels found in the literature.

	f_{T5-T8} Sran et al. (2005)	$f_{T11-T12}$ Oxland et al. (1992)	$f_{T11-T12} / f_{T5-T8}$ ($1/\tau_2$)	$k_{T11-T12} / k_{T5-T8}$ (τ_2)
Flexion	0.27	0.36	1.33	0.75

7.5.5 Joint damping

Similarly to the rationale done about the formulation of the stiffness, joint damping was derived as function of subject-specific properties as shown in Equation 7.17:

$$c_i = c_i(y_1, \dots, y_n) \quad \text{Equation 7.17}$$

In particular, it was chosen the following formulation to model the damping of the joints, based on the work by Lord Rayleigh to describe the viscous damping of a structure (Rayleigh, 1877):

$$c = \gamma_j m' + \delta_j k \quad \text{Equation 7.18}$$

where c is the joint damping, m' is the average mass of the two body regions connected by the joint, k is the stiffness of the joint, and γ_j and δ_j (j =spine, pelvis, knee and ankle) are two unknown dimensional magnitudes. Equation 7.18 is a standard formulation to model damping in mechanical systems (Caughey and O'Kelly, 1965). Appendix A4 provides background on the suitability of using such a model for the damping.

Coefficients γ_j and δ_j were assumed to have the same value throughout all the spinal joints (T1, T8 and L2), a second paired of γ_j and δ_j was used for the pelvic joint, and a last pair of γ_j and δ_j was used for the knee and ankle.

7.5.6 Generalized forces

Six external forces were considered to be acting on the occupant: upper shoulder belt force, middle shoulder belt force, lower shoulder belt force, lap belt force, seat reaction and the knee bolster force. As a result of hardware malfunction, not all the forces could be obtained for all the occupants. Table 7.8 summarizes the loads that were included in the model of each occupant type, indicating the malfunctioning of the sensor when relevant.

Table 7.8 Summary of the external forces applied to the occupant.

	Shoulder belt	Lap belt	Seatpan load	Knee bolster load
PMHS Low speed	CAD1 - CAD3	CAD1 - CAD3	CAD1 - CAD3	NA
PMHS High speed	CAD1 - CAD3	CAD1 - CAD3	CAD2, CAD3 ⁺	CAD1 - CAD3

⁺ Seat LC malfunctioned in CAD1 test. The average F_x and F_z seat forces of CAD2 and CAD3 were used instead.

The following paragraphs detail how these forces were calculated and combined to obtain the generalized forces applied to the model:

Lap belt forces (FLB). Lap belt tension was measured using tension gauges at both sides of the occupant. The belt force at each side ($LPforce_{left}$, $LPforce_{right}$) was apportioned into its X and Z components, after

calculating the angle formed by the lap belt with respect the positive global X axis. Equation 7.19 and Equation 7.20 shows how the forces were combined to obtain the two lap belt force components.

$$FLBx = F1x_{left} + F1x_{right} = -LPforce_{left} \cdot \cos(LPangle_{left}) - LPforce_{right} \cdot \sin(LPangle_{right})$$

Equation 7.19

$$FLBz = F1z_{left} + F1z_{right} = -LPforce_{left} \cdot \sin(LPangle_{left}) - LPforce_{right} \cdot \cos(LPangle_{right})$$

Equation 7.20

Upper shoulder belt force (FUSB), Middle shoulder belt force (FMSB) and Lower shoulder belt force (FLSB). The shoulder portion of the belt was considered to contribute to restraining the occupant by applying force on T1 (USforce), T8 (MSforce) and on L2 (LSforce). USforce was directly measured by a belt tension gage located on the shoulder belt, superiorly to the shoulder of the occupant. Since the tension was not measured at the lower shoulder belt location, LSforce was estimated from a series of PMHS tests performed in a similar test environment in which both the upper and lower shoulder belt tension were directly measured (Shaw et al., 2009). Data from eight PMHS tests were combined and the magnitude of the LSforce was plotted against the USforce. A linear relationship was found between the observed tension at each location ($R^2 = 0.99$), that allowed calculating LSforce from the value of USforce (see Figure 7.6 below).

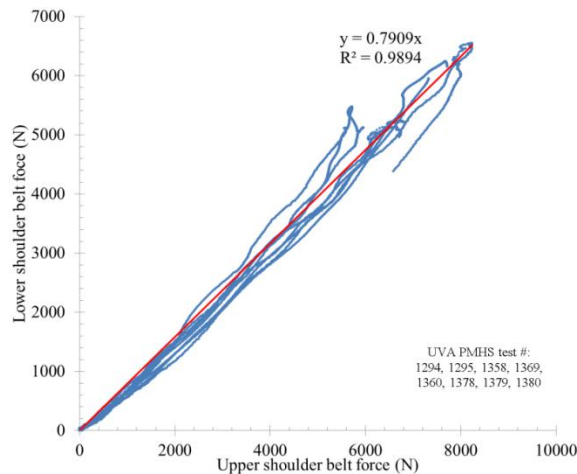


Figure 7.6 Relationship between the lower and upper shoulder belt forces obtained from the combination of data from 8 PMHS tests in a similar test setup.

Similarly to the lap belt tension, both forces were apportioned into their X and Z components after calculating the angle that the corresponding portion of the belt formed with the positive X axis. Finally, the MSforce was calculated by assuming that the shoulder belt force varied linearly from USforce to LSforce.

Equation 7.21 through Equation 7.24 shows the expressions to calculate the components of the shoulder belt forces in the global coordinate system.

$$FUSB_x = -USforce \cdot \cos(USangle) \quad \text{Equation 7.21}$$

$$FUSB_z = USforce \cdot \sin(USangle) \quad \text{Equation 7.22}$$

$$FLSB_x = -LSforce \cdot \cos(LSangle) \quad \text{Equation 7.23}$$

$$FLSB_z = -LSforce \cdot \sin(LSangle) \quad \text{Equation 7.24}$$

The middle shoulder belt force (FMSB) was considered to vary linearly between the upper shoulder belt location and the lower shoulder belt location.

Seat forces (FS_x, FS_z). Two seat reactions (Sforce_x, Sforce_z) acting on the subject were considered in the analysis. These were measured by a load cell located directly under the seat platform. The load cell measurement in the X direction was mass-compensated before being included in the model. The forces acting on the subject are then given by Equation 7.25 and Equation 7.26.

$$FS_x = Sforce_x \quad \text{Equation 7.25}$$

$$FS_z = Sforce_z \quad \text{Equation 7.26}$$

Knee bolster forces. A knee bolster initially in contact with the proximal tibia was included in the test setup in the high-speed PMHS test. The knee bolster was equipped with two load cells (one per each leg) that measured the loads in the sagittal plane of the subject. Measured loads were added and applied at the corresponding angle in the model of the PMHS exposed to a high-speed impact.

7.5.7 Constraints

Adequately constraining the unknown values in an optimization problem contributes to obtain a robust solution and helps the search algorithm to perform faster. Unless otherwise noted, and due to the absence of experimental data that could guide setting up more realistic upper and lower constraints for the unknowns of the problem, joint parameters were allowed to vary between 0 Nm/deg and 10000 Nm/deg (stiffness) and 0 Nms/deg and 10000 Nms/deg (damping).

The calculation of the SSE of the model was done by comparing the X and Z displacement of the head, the X displacement of T1 and the X displacement of T8 every 10 ms.

7.5.8 Model predictions of the forward displacements of the head and the thoracic spine

Table 7.9 and Table 7.10 include the comparison of the peak forward excursions of the head, T1 and T8 between the model and the experiments at 9 km/h and at 40 km/h. The experimental data from PMHS2 at 40 km/h were not used in the calculations to avoid that the femur neck fracture sustained by this subject could influence the estimation of the stiffness and damping of the joints.

Table 7.9 Comparison between the maximum X displacement measured in the tests and the predictions given by Model B2.1. Low speed tests. Results shown as: absolute displacement (relative error)

	PMHS1		PMHS2		PMHS3	
	Measured	Estimated	Measured	Estimated	Measured	Estimated
Head (mm)	283.8	215.3(-24%)	291.6	246.8(-15%)	319.7	279.3(-13%)
T1 (mm)	211.0	180.1(-14%)	203.7	192.2(-6%)	217.3	229.0(+5%)
T8 (mm)	161.4	121.0(-25%)	129.7	94.0(-28%)	157.7	143.4(-11%)

Table 7.10 Comparison between the maximum X displacement measured in the tests and the predictions given by Model B2.1. High-speed tests. Results shown as: absolute displacement (relative error)

	PMHS1		PMHS2		PMHS3	
	Measured	Estimated	Measured	Estimated	Measured	Estimated
Head (mm)	493.8	484.0 (-2%)	572.2		525.4	469.6 (-11%)
T1 (mm)	428.2	435.3 (+2%)	457.5		418.7	395.9(-5%)
T8 (mm)	385.7	339.5(-12%)	346.4		327.7	266.8 (-19%)

The average error between the model-estimated and the test-measured peak forward trajectories of the selected anatomical landmarks is shown in Table 7.11:

Table 7.11 Comparison between the average error in the prediction of the peak forward excursions of the head, T1 and T8.

	9 km/h average error (%)	40 km/h average error (%)
Head	-17.2%	-6.4%
T1	-4.9%	-1.2%
T8	-20.1%	-15%

7.5.9 Discussion

The goal of this section was to address the question of whether a linear time-invariant multibody model could predict the displacements of a restrained occupant at different impact speeds. The previous sections have described how the mass, stiffness and damping matrices of the multibody system were obtained and how the external loads acting on the occupant were combined to determine the generalized forces.

The predictions given by the model to the forward displacement of the selected anatomical landmarks were within the error proposed in the assessment criteria of the model, with the exception of the peak excursion of the head at 9 km/h in which the model underpredicted the measured displacement with an error of 17% (slightly over the assessment criterion for the head that was set to 15%).

In light of the general performance of the model, it was accepted that a linear time-invariant multibody model of the occupant developed as described in the paragraphs above captured the displacement of a restrained occupant in the sagittal plane at different impact speeds.

7.6 HYPOTHESIS 2: A LINEAR TIME-INVARIANT MULTIBODY MODEL CAN PREDICT THE SAGITTAL DISPLACEMENT OF A RESTRAINED 6YO IN A FRONTAL 9 KM/H IMPACT.

The goal of this section was to assess whether a model developed following the methodology detailed in the previous section could describe the sagittal displacements of the head and thoracic spine of a restrained 6YO in a frontal deceleration at 9 km/h. The development of the multibody model of the occupant parallels the one described above, but the model parameters were particularized to represent the pediatric volunteers as described in the paragraphs below.

7.6.1 Mass.

The distribution of mass over the different body segments was estimated using published studies on the anthropometry of the 6YO or adult 50th percentile. Two anthropometric studies were combined to find the distribution of the segment masses for a 6YO. First, Irwin and Mertz (1997) reported values of the mass and specific dimensions for some particular body regions of a 6YO. As in the case of the PMHS, the body regions in the Irwin and Mertz data did not coincide exactly with the ones chosen for this dissertation model. In particular, the study provided values for the upper and lower torso, and the thighs without specifying the exact limits of these regions. These data were then combined with the data in the NASA study (NASA, 1996) to obtain the mass distribution needed in the body regions considered in the model. Specifically, the mass of the three pediatric regions included in Irwin and Mertz (1997) was distributed according to the ratios calculated using the NASA data for the mass distribution of the thorax, abdomen, pelvis and upper leg in the 50th percentile. This was considered the best approximation possible to the real mass distribution of the 6YO.

Other studies reporting anthropometry of both adult and pediatric human subjects (Kumaresan et al., 2001) were also consulted in the effort of finding an approximation of the mass distribution of the occupants, but they were not as comprehensive as the two mentioned in the above paragraphs. A direct comparison between the studies cannot be done due to the differences in the definition of the body regions, but they are generally consistent with each other.

Table 7.12 shows the original values reported by Irwin and Mertz (1997) and the ratios used to apportion the mass in the model body regions. Table 7.13 shows the calculated body region mass for each of the pediatric volunteers (note that PED3 was dropped from this part of the study).

Table 7.12 Body region mass of a 6YO as reported by (Irwin and Mertz, 1997) and distribution of mass for the 6YO model (kg)

Model body region	Irwin and Mertz (1997)	Mass ratio (NASA, 1996)	Model mass distribution (6YO)
CH	4.27	0.22	4.27
UT	13.04	0.29	5.53
LT		0.03	0.53
L		0.14	2.60
UL		0.23	4.38
LL	1.98	0.10	1.98
TOTAL			19.29

Table 7.13 Body region mass of pediatric volunteers (kg).

Model body region	Mass ratio	PED1	PED2	PED4
CH	0.22	5.31	7.75	6.42
UT	0.29	6.88	10.03	8.31
LT	0.03	0.66	0.96	0.80
L	0.14	3.24	4.73	3.92
UL	0.23	5.45	7.94	6.58
LL	0.10	2.46	3.59	2.98
TOTAL	0.91	24	35	29

7.6.2 Length.

As in the PMHS group, the initial position of the occupants served to estimate the lengths of each of the body regions in the model, which were considered constant throughout the motion of the occupant. Table 7.14 shows the length of each of the model body regions of the pediatric occupants.

Table 7.14 Body region length of pediatric occupants (m).

Model body region	PED1	PED2	PED4
CH	0.27	0.33	0.28
UT	0.16	0.18	0.13
LT	0.05	0.05	0.09
L	0.11	0.15	0.13
UL	0.34	0.39	0.35
LL	0.27	0.33	0.29

7.6.3 Moment of inertia.

Pediatric body segments were also approximated by ellipses to calculate the corresponding moment of inertia according to Equation 7.3. The values of the moment of inertia obtained for each body region are shown in Table 7.15.

Table 7.15 Body region moment of inertia of pediatric occupants (kg m^2).

Model body region	PED1	PED2	PED4
CH	0.030	0.060	0.038
UT	0.020	0.038	0.024
LT	0.001	0.002	0.002
L	0.007	0.015	0.011
UL	0.044	0.084	0.057
LL	0.014	0.028	0.019

7.6.4 External forces.

The methodology used to calculate the external forces acting on the pediatric occupant was similar to the one used to model the loading environment in the PMHS tests. Table 7.16 summarizes all the sensor information used in the development of the pediatric models. Lap belt tension of PED3 was not measured

due to malfunctioning of the sensor, and thus, this subject was removed from the study. Also, force data from the seatpan load cell was recorded only for PED1 and PED4, but since PED2 was similar in anthropometry and age to PED4, the force time history of PED4 was used to estimate the seat forces of PED2, using a correcting factor given by the mass ratio of the corresponding subjects. Therefore, the multibody model was developed for subjects PED1, PED2 and PED4.

The knee bolster was not used with the pediatric volunteers.

Table 7.16 Summary of available sensor data within different subject groups.

	Shoulder belt	Lap belt	Seatpan load	Knee bolster load
Pediatric volunteers	1,2,4	1,2,4	1,4	NA

7.6.5 Position of vertebra L2 in the pediatric group

As mentioned in Chapter 3, the position of the pediatric L2 vertebra was not tracked due to interference with the seat assembly and the lack of space on the back of the volunteers. Thus, the position of L2 at each time step was inferred using a methodology based on a study of the seating posture of 101 volunteers.

Brouder and Reynolds (1995) provided an estimation of the position of the spinous process of each vertebrae along the spine if the position of T1 and the chest angle was known. The application of the method required fitting a spline through the available data points on the spine of the volunteers, assuming that the iliocristale was in the vicinity of the sacrum (since the iliocristale was the only landmark tracked in the pediatric subjects).

7.6.6 Joint stiffness and damping

A similar rationale to that described in the PMHS tests was applied to model the pediatric joint stiffness and damping. However, in the case of the pediatric occupants, the studies relating the magnitude of the modulus of elasticity to the age of the subject exhibited wide confidence intervals due to the reduced size of the sample (Kalkwarf et al, 2007) and therefore it was decided to solve directly for a subject-specific value of the parameter representing the modulus of elasticity in the stiffness equations.

Thus, the equations chosen to model the stiffness of the model joints were:

$$k_{T1} = \alpha_i l_{CH}^{-1} R_{CS_{T1}}^4 \quad \text{Equation 7.27}$$

$$k_{T8} = \tau_1 k_{T1} \quad \text{Equation 7.28}$$

$$k_{L2} = \alpha_4 k_{T1} \quad \text{Equation 7.29}$$

$$k_P = \alpha_2 \alpha_i l_L^{-1} R_{CS_P}^4 \quad \text{Equation 7.30}$$

$$k_K = \alpha_3 \alpha_i l_{UL}^{-1} R_{CS_K}^4 \quad \text{Equation 7.31}$$

$$k_A = \alpha_3 \alpha_i l_{LL}^{-1} R_{CS_A}^4 \quad \text{Equation 7.32}$$

where α_i (i =PED1, PED2, PED4) was a magnitude with same units as the modulus of elasticity that was representative of each of the pediatric occupants.

Table 7.17 Stiffness and damping coefficients of the joints of pediatric occupants in model B2.2.

PED1	T1	T8	L2	Pelvis	Knee	Ankle
k (Nm/deg)	11.8e-3	1.5e-6	1.7e-10	4.6	11.5e-3	2.1e-3
c (Nms/deg)	16.6	5.5e-1	5.2e-2	7.99e3	71.8	13.2
PED2	T1	T8	L2	Pelvis	Knee	Ankle
k (Nm/deg)	7.4e-3	9.5e-7	1.1e-10	2.8	7.7e-3	1.3e-3
c (Nms/deg)	10.8	7.9e-1	7.6e-2	4.8e3	48.1	8.3
PED4	T1	T8	L2	Pelvis	Knee	Ankle
k (Nm/deg)	5.6e-3	7.1e-7	7.8e-11	1.9	5.4e-3	9.6e-4
c (Nms/deg)	8.1	6.6e-1	6.3e-2	3.8e3	33.9	5.9

As for the stiffness relationship between the stiffness of the T1 and T8 joints, the value τ_1 found in the FSU tests for the 7 YO specimen was used ($1/\tau_1 = 0.52$). In the case of these occupants, no reference was found for a relationship between the stiffness of the L2 joint and the T1 one, so it was necessary to include an additional unknown in the model. Proportional damping was used to model the joint damping as in the PMHS case. Table 7.17 shows the stiffness and damping values of the joints of the pediatric subjects obtained in the optimization calculation using the experimental data at 9 km/h.

7.6.7 Refinement of the model

The joint stiffness and damping values shown in Table 7.17 were several orders of magnitude different between the different body regions and not comparable to any of the values reported in the literature for the quasi-static stiffness coefficients of the spine (Sran et al, 2005; Oxland et al, 1992; Panjabi et al, 1976; Markolf et al, 1972).

Following the reasoning that led this research to develop a multibody model of the occupant, the pediatric model was further improved by allowing the optimization process to apportion the mass of the three trunk body segments (upper thoracic, lower thoracic and lumbar) and the thigh segment. Subsection 7.6.1 had shown that while the total mass of these four body regions for a 6 YO could be obtained from the literature (Irwin and Mertz, 1997), the apportionment of the mass of each segment was done following the ratios obtained from the NASA study for adults (NASA, 1996). But these ratios were not necessarily representative of children. Therefore, the refined pediatric model calculated the distribution of mass of the trunk between the three torso regions and updated accordingly the mass moments of inertia of the corresponding segments. Although additional unknowns were introduced in the problem, these variables could be constrained by the corresponding total mass of the body regions, which was estimated for each pediatric subject according to Table 7.13.

Three additional modifications were introduced in the formulation of the optimization problem:

- The difference between the predicted and the observed vertical displacement of all segments was weighted, so that bigger errors in the vertical displacement were penalized.
- The difference between the predicted and the observed forward displacement of T8 was also penalized.
- The differences between the model and the experiments at two intermediate points (equally distributed during the duration of the motion of the occupant) were also weighted so that the trajectory predicted by the model resembled better the observed one.

Table 7.18 shows the values obtained for the stiffness and damping coefficients of the joints after these modifications were included. Table 7.19 shows the estimations of the masses of the body regions whose mass was considered unknown.

Table 7.18 Stiffness and damping coefficients of the joints of pediatric occupants in model B2.2.

PED1	T1	T8	L2	Pelvis	Knee	Ankle
k (Nm/deg)	8.94E+00	1.72E+01	1.72E-02	1.39E+02	5.64E+00	1.04E+00
c (Nms/deg)	3.92E+01	7.53E+01	7.53E-02	3.16E+04	1.22E+02	2.25E+01
PED2	T1	T8	L2	Pelvis	Knee	Ankle
k (Nm/deg)	1.14E+01	2.20E+01	2.20E-02	1.69E+02	7.71E+00	1.34E+00
c (Nms/deg)	5.02E+01	9.65E+01	9.65E-02	3.85E+04	1.67E+02	2.89E+01
PED4	T1	T8	L2	Pelvis	Knee	Ankle
k (Nm/deg)	9.26E+00	1.78E+01	1.78E-02	1.46E+02	4.72E+00	8.29E-01
c (Nms/deg)	4.06E+01	7.80E+01	7.80E-02	3.33E+04	1.02E+02	1.80E+01

Table 7.19 Mass of the body regions considered unknown in the modified model B2.2.

Mass body region (kg)	PED1	PED2	PED4
UT	1.50E+00	2.19E+00	1.81E+00
LT	7.50E-01	1.09E+00	9.07E-01
L	1.50E+00	2.19E+00	1.81E+00
UL	1.13E+01	1.64E+01	1.36E+01

7.6.8 Model predictions

The new values of the joint parameters and of the mass distribution of the torso and thigh of the pediatric subjects were incorporated into the multibody model. Then, the model was used to predict the sagittal displacements of the head and thoracic spine. Table 7.20 shows the comparison of the peak forward excursion of the head, T1 and T8 between the actual experiments and the predictions given by the multibody model.

Table 7.20 Comparison between the maximum X displacement measured in the tests and the predictions given by model B2.2. Results shown as: absolute displacement (relative error)

	PED1		PED2		PED4	
	Measured	Estimated	Measured	Estimated	Measured	Estimated
Head (mm)	206.6	178.3(-14%)	216.5	235.5(9%)	202.4	201.6(-0.4%)
T1 (mm)	152.1	145.0(-5%)	166.1	190.9(15%)	143.1	157.8(10%)
T8 (mm)	86.4	40.6(-53%)	99.8	52.33(-48%)	106.8	80.2(-25%)

Figure 7.7 shows the comparison between the predicted trajectories (blue solid line) and their associated corridor (purple shaded area) and the test measured displacements (red solid line) and the corresponding displacement corridor (blue shaded area). While the nature of the average predicted trajectories were different from the observed ones in all the three structures, the absolute differences between the magnitudes of the predicted and the observed average responses were small.

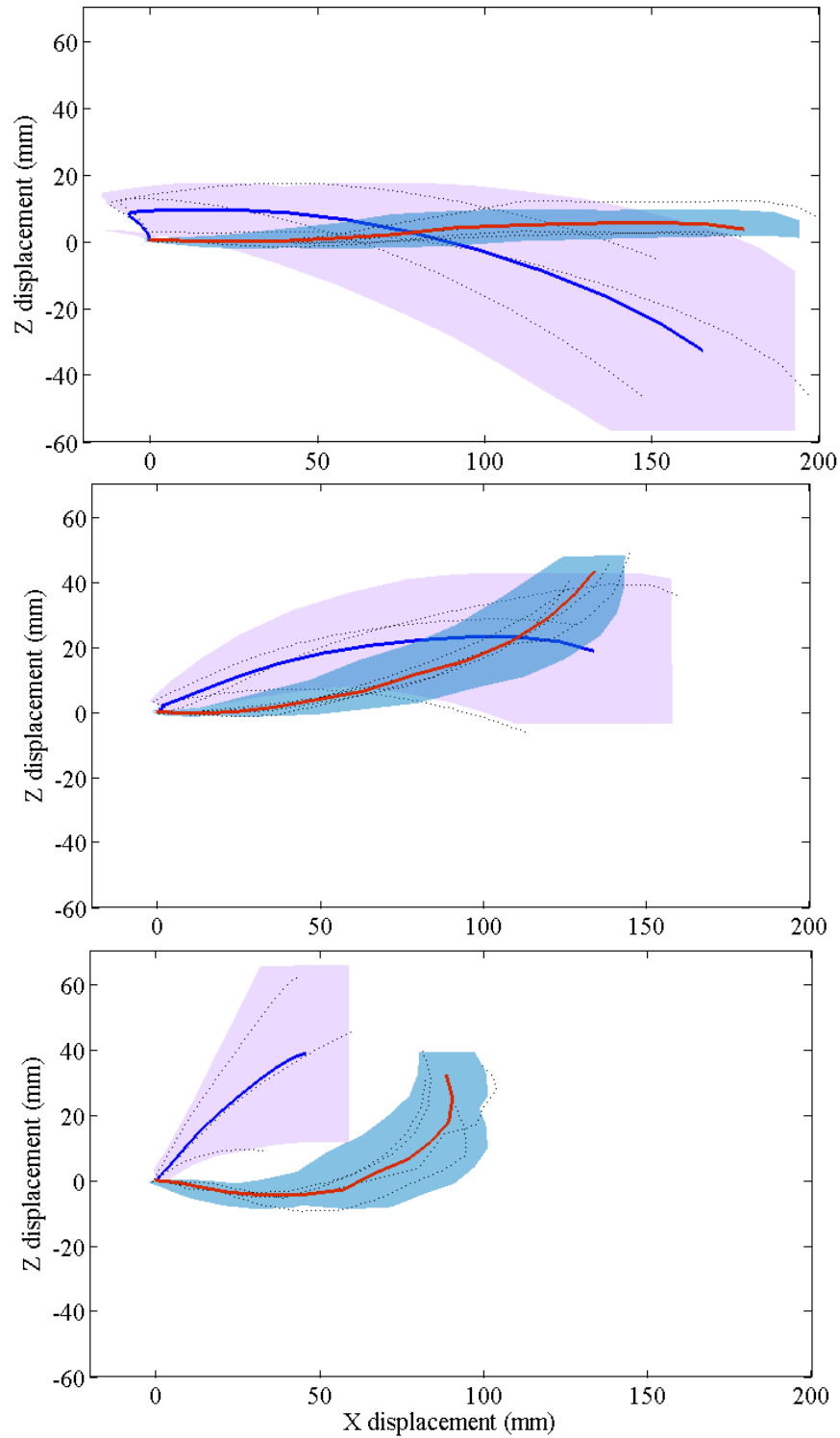


Figure 7.7 Predicted pediatric trajectory (blue solid line) and corridor (purple shaded area) as given by modified model B2.2 and comparison with observed experimental data from pediatric volunteers at 9 km/h (red solid line: average 6YO response; blue shaded area: corridor). (Top: head; Center: T1; Bottom: T8).

As shown in Figure 7.7, the magnitude of the forward excursions of both the head and T1 were captured correctly by the model. There were still differences between the trajectories, and the model could not describe the concave trajectory exhibited by the vertebrae, but predicted a convex one. In the case of T1, the predicted corridor overlapped with the observed one. As for the head, even if the model predicted again a negative vertical displacement not observed in the tests, the difference between the peak magnitudes of the model and the experiment was less than 30 mm. Finally, the model underpredicted by almost 50% (45.69 mm vs.88.53 mm) the forward excursion of the vertebra T8.

7.6.9 Discussion

The goal of this section was to assess whether a linear time-invariant multibody model could describe the sagittal kinematics of a restrained 6YO in a frontal 9 km/h impact.

The multibody model was developed paralleling the development of the one used to model the response of the PMHS, although modifications were included when needed. Although the model could not describe the nature of the observed motion of the head and the thoracic vertebrae, the comparison between the estimated and the observed peak forward displacements showed that the magnitude of the differences in the case of the head and T1 was within the proposed error. In case of the vertical displacement, the errors did not satisfy the assessment criteria, but the absolute magnitude of the error was less than 30 mm. The model did not describe correctly the motion of the lower thoracic vertebra (T8) and underestimated its peak forward displacement by 50% in the case of PED1 and PED2. Interestingly, the stiffness and damping coefficients of the L2 joint were two orders of magnitude smaller than the other spinal joints.

The estimated stiffness of the thoracic joints are either one or two orders of magnitude greater than the quasi-static stiffness found for the flexion of the pediatric cervical spine by Ouyang et al. (2005). It is reasonable to think that the thoracic spine is stiffer than the cervical one (at least in flexion), due to the stiffening effect of the rib cage and the internal organs (Panjabi et al, 1976). Also the differences in strain rate might have contributed to the increased stiffness obtained in the optimization.

Although there are not published data on the stiffness of the pediatric thoracic spine, a comparison with values reported for the quasi-static flexion of the adult thoracic spine shows that the stiffness coefficients obtained in the optimization are within the same order of magnitude of those reported in the literature. Sran et al. (2005) calculated that the stiffness coefficient of the T5-T8 section was nominally 3.7 Nm and the values obtained in the optimization are within the interval 1.72-2.2 Nm.

Another aspect to assess the values of joint stiffness obtained in the optimization is to relate these values to the FSU bending tests described in Chapter 5. Although the proportionality between the stiffness of T1 and T8 was built into the multibody model (not only in the pediatric multibody model, but also in the PMHS one), the finding about the increased stiffness of the adult spine was not used in the development of the multibody model. Table 7.21 compares the average stiffness of the T8 joint obtained in the optimization of the PMHS and the pediatric subjects, showing that the older occupants were stiffer than the pediatric ones as found in the QLV model of the thoracic spine.

Table 7.21 Comparison of the optimized stiffness value of the T8 joint between PMHS (adult) and pediatric occupants.

Subject	Age	k_{T8} (Nm/deg)
PMHS1	59	9.6 E+02
PMHS2	69	16.9 E+02
PMHS3	60	17.7 E+02
PED1	6	1.72 E+01
PED2	8	2.20 E+01
PED4	8	1.78 E+01
Average PMHS		14.7 E+02
Average PED		1.9 E+01

Despite the differences found in the nature of the observed and predicted displacement, the multibody model approximated correctly the forward peak displacements of the head and T1. The model exhibited problems approximating the displacement of T8. Partial assessments of the stiffness values obtained in the optimization show that the stiffness of the thoracic joints is within the same order of magnitude of the

quasi-static stiffness reported in the literature for the thoracic spine. The value of the stiffness of T8 also showed the same behavior with age found in the QLV experiments of the thoracic FSU tests described in Chapter 5.

Thus, it was accepted that the model could approximate the displacements of the upper segments of the restrained pediatric occupant (head and T1), while there were deficiencies in the behavior of the lower segments. These deficiencies might be related to the lower value of the stiffness and damping coefficients of the lumbar joint.

7.7 HYPOTHESIS 3: JOINT PARAMETERS ESTIMATED AT 9 KM/H CAN PREDICT THE SAGITTAL TRAJECTORIES OF THE HEAD AND THORACIC SPINE AT 40 KM/H.

The kangaroo sled tests were used to check that, under the corresponding loading environment, a model using joint stiffness and damping parameters obtained using only the experimental data obtained at 9 km/h would approximate correctly the experimental results observed at 40 km/h. The third hypothesis focused on assuring that if the mass, damping and stiffness matrices were known for the occupant at 9 km/h, these matrices still will represent the mechanical behavior of the occupant at 40 km/h.

The optimization problem was setup to minimize the SSE over the entire duration of the 9 km/h test, including the X and Z displacements of the head, T1, T8 and L2. The displacements of the head and the thoracic vertebrae as well as the final time steps were weighted to increase the accuracy of the prediction.

Table 7.22 shows the estimation of the joint parameter values obtained in the optimization process using only the data from the 9 km/h kangaroo sled test.

Table 7.22 Estimation of joint parameters for the kangaroo model.

	T1	T8	L2	Pelvis
k (Nm/deg)	1.35E-02	2.07E-01	5.00E+00	1.09E-01
c (Nms/deg)	3.45E-03	5.74E-02	3.82E-01	1.64E-01

As for the prediction of the trajectories in the sagittal plane, Figure 7.8 shows the comparison between the measured experimental trajectory (blue solid line) and the estimated one using the model (red solid line) at

9 km/h and at 40 km/h. As observed in the case of the pediatric occupants the greatest difference in the sagittal trajectories occurred in the case of the vertical displacement of thoracic vertebra T8. These results indicate that even if the forward excursions of the head and thoracic vertebrae are well approximated and the vertical displacements of the head and T1 are acceptable, the model can still predict a different vertical displacement of thoracic vertebra T8.

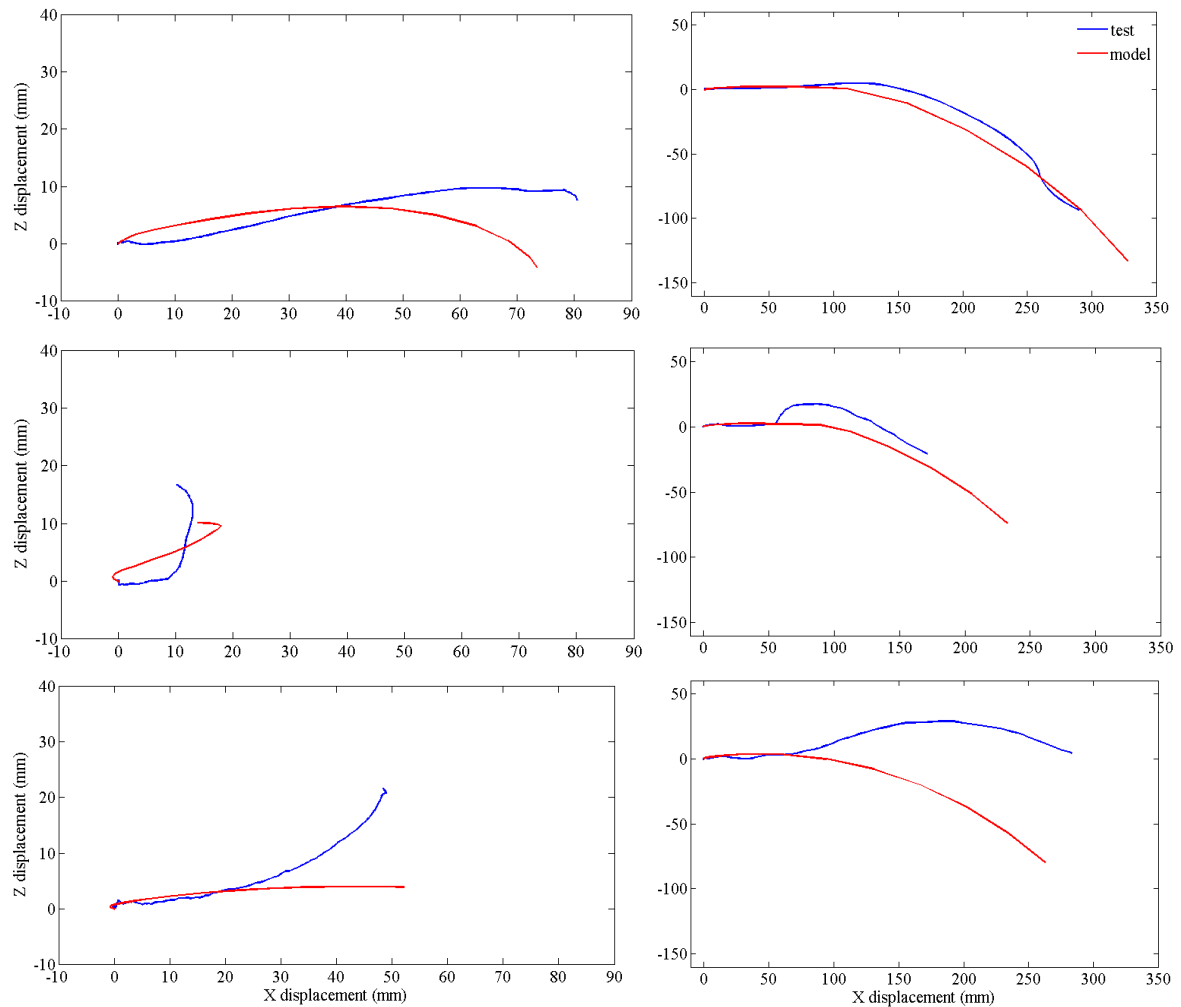


Figure 7.8 Kangaroo sagittal displacements. Comparison between the XZ trajectory predicted by the model (red) and the actual trajectory measured (blue) at 9 km/h (left) and at 40 km/h (right). Top: head; Center: T1; Bottom: T8. Note the change of scale in the axes between the two speeds.

The error observed in the model prediction at high speed was greater than the one obtained at low speed. This is reasonable since the joint parameters were obtained to minimize the low speed error. It is important to point out that the overall trajectories of the head and T1 both at 9 km/h and at 40 km/h were captured by

the model (although the model over-predicted the magnitude of the forward excursion of T1) even if the vertical displacement of T8 was not.

The relative errors between the predicted (as given by the model) and the measured peak forward displacement of the head and thoracic vertebrae at 9 km/h and 40 km/h are included in Table 7.23.

The model provided an estimation of the head and T8 forward displacements within 13% error regardless of the speed. The error in the T1 forward displacement prediction was up to 34% at 9 km/h and up to 36% at 40 km/h.

Table 7.23 Comparison of experimental-observed and model-estimated kangaroo peak forward displacements (X) at 9 km/h and at 40 km/h.

	9 km/h			40 km/h		
	Observed disp.(mm)	Estimated disp. (mm)	% error	Observed disp.(mm)	Estimated disp. (mm)	% error
Head	80.76	73.44	-9.06	289.5	327.30	13.06
T1	13.49	18.02	33.58	171.1	232.40	35.83
T8	49.60	52.22	5.28	283.5	262.82	-7.30

7.7.1 Discussion

The modeling approach used in this dissertation involved the extrapolation of joint properties obtained from low-speed test to high-speed ones. The validity of this extrapolation is fundamental to the validity of the methodology and it was assessed using experimental results from an animal surrogate.

Since testing a pediatric PMHS is currently unfeasible and pediatric ATD have been shown to lack the needed thoracic compliance to approximate the trajectory of the head and spine, an animal model was considered the only option. Juvenile animals have been used frequently as surrogates of pediatric occupants in the last thirty years (Backaitis et al., 1975; Ching et al., 2001; Kent et al., 2008; Nuckley et al., 2002). Some of these efforts have focused on the description of the interaction of the chest and the restraint system. In particular, animal surrogates that are anatomically similar to the human child (primates) have been primarily considered for testing with various belt geometries. However, primates are high on the

phylogenetic order, are difficult and not readily available to test, and their stature, mass, and age-size equivalence to humans would require both size and modulus scaling.

The search for an animal surrogate that would exhibit similar anatomical development of a 6 YO human as well as similar torso structure (including the presence of clavicles) led the researchers from the Center for Applied Biomechanics to explore the feasibility of the eastern grey kangaroo (*macropus giganteus*) as a biomechanical model of the pediatric human's chest. A detailed anatomical and developmental study of the grey kangaroo and its comparison with the 6 YO human can be found in Lau et al. (2008). Two main characteristics of the eastern gray kangaroo motivated its selection as surrogate of a pediatric occupant. First, the developmental state of the kangaroo was similar to that of a human 6YO when they had similar sizes. Second, kangaroos have clavicles, which permitted the shoulder belt to load the animal chest in a more human-like manner (Lau et al., 2008).

However, there were obvious differences between kangaroos and human occupants. Attending to the focus of this dissertation, the spine of the kangaroo was substantially larger than the human one in the cephalocaudal direction. Also, the shape of the pelvis made difficult the positioning of the subject in a realistic human seating position and prevented the use of a lap belt. Additionally, the kangaroo trunk was conical in shape, with a larger diameter in the abdomen and becoming narrower at the upper torso (see Figure A5.3 and Figure A5.4), and therefore, having a completely different mass distribution from that observed in the pediatric subjects. Even if these anatomical differences prevented drawing conclusions from the observed kinematics of the kangaroo surrogates that could be directly applicable to a pediatric occupant, they were considered advantageous to assess the robustness of the method discussed here.

The rationale for using a multibody model was to capture the effect of joint stiffness and mass distribution developmental changes on the kinematics of the subject. The kangaroo specimen was chosen to be in a similar developmental state to that of a 6YO but exhibited a completely different mass distribution. In particular, the point of the kangaroo assessment was to show that a multibody model in which the body regions and joint properties were tailored to a specific subject in a low-speed impact could be also applied to the same subject in case of a high-speed impact. The assessment of the method done using the adult PMHS had shown that the same joint properties and mass distribution could describe the kinematics of the

subject both at 9 km/h and at 40 km/h. In parallel, an animal model with a comparable developmental state of that of a 6YO but with a very different mass distribution allowed checking whether the joint parameters estimated using only low speed data could provide a valid estimation of the kinematics of the surrogate at a higher speed.

Using just one surrogate was a limitation of the assessment and including more kangaroos would have contributed to improve the robustness of the method. Adding more specimens would have provided an assessment of how sensitive the method was to inter-subject variability, and in particular, it would have allowed understanding the influence of mass distribution in the kinematics of a surrogate in a developmental state comparable to that of a human 6YO.

Interestingly, the multibody model of the kangaroo captured more precisely the nature of the motion of the upper segments (head and T1 vertebrae) rather than the motion of the T8 vertebrae, as it has been seen in the case of the model of the pediatric occupants. This can be attributable to the artifactually imposed motion of the pelvis in the model. As described in Appendix A5, a custom-made knee bolster was made to arrest the forward motion of the pelvis and thighs of the kangaroo, but the reaction forces between the knee bolster and the kangaroo were not measured. Thus, the multibody model of the kangaroo considered that there was no relative motion between the pelvis of the kangaroo and the test buck. Despite being a reasonable approximation in the absence of experimental data, the plot of the displacement of the kangaroo pelvis at 40 km/h shows that the kangaroo pelvis moved forward and upwards during the deceleration of the test vehicle. It is hypothesized that the deficient fit of the vertical component of the motion of the T8 vertebra was caused by this assumption of the model.

Despite the results observed for the displacement of the T8 vertebra, it was considered that the system matrices obtained from the low-speed tests could be used in the prediction of the displacements of the occupant at high-speed under the correct loading environment.

Precisely, the method followed to calculate the loading environment of the pediatric occupants at 40 km/h is the focus of the fourth hypothesis and is discussed in the following subsection

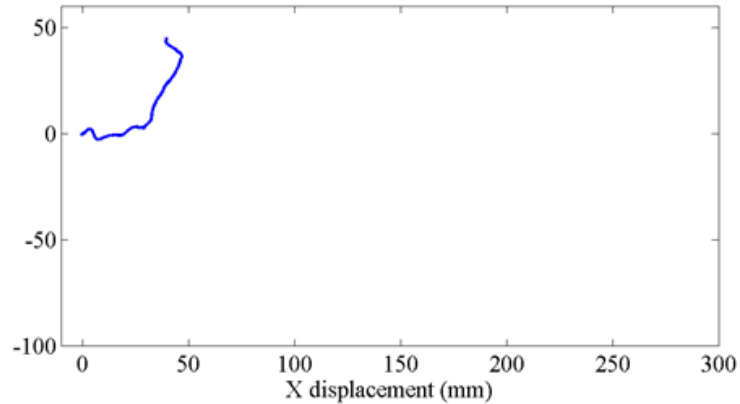


Figure 7.9 Displacement of the pelvis of the kangaroo in the sagittal plane at 40 km/h.

7.8 HYPOTHESIS 4: FORCES ACTING ON A PEDIATRIC SUBJECT AT 40 KM/H CAN BE ESTIMATED IF THE FORCES ACTING AT 9 KM/H ARE KNOWN

The last hypothesis that needed to be explored before using the multibody model of the pediatric occupant to predict the displacements of a restrained occupant at 40 km/h focused on how the forces acting on the pediatric subject could be estimated at that impact speed. The method for the prediction of these forces is developed using data from the adult and pediatric volunteer data. An additional set of data corresponding to sled tests done with dummies of different sizes and in a completely different loading environment was used to assess the robustness of the method. Last the methodology was applied to obtain the prediction of the loading environment of the restrained pediatric subject in a 40 km/h frontal impact. In this last prediction, the forces measured in the adult PMHS sled tests at 40 km/h were used to obtain the values of the predicted pediatric forces.

7.8.1 Development of the method. Volunteer test at 9 km/h.

The experimental data included in Arbogast et al. (2009) showed that that the time-history plots of the forces acting on the different age groups of volunteers differed mainly in the magnitude of the force, but that the duration of the action of the force and the evolution of the force in time were similar (Figure 7.10, Figure 7.11). This observation suggested to find a scaling relationship based on the ratio of the peak forces acting on them.

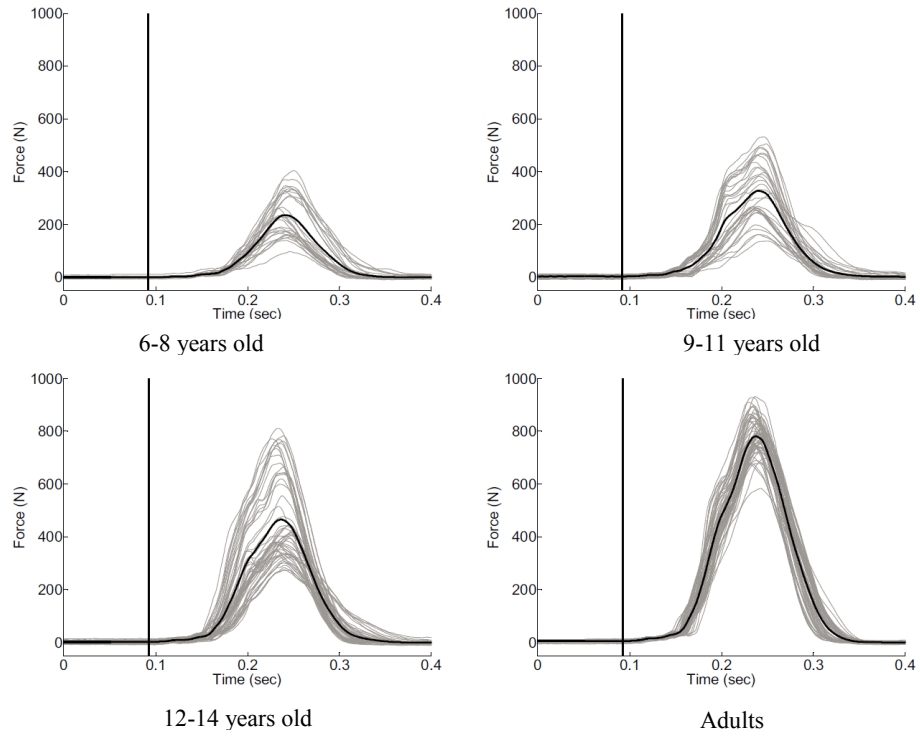


Figure 7.10 Shoulder belt forces per group age as reported by (Arbogast et al., 2009).

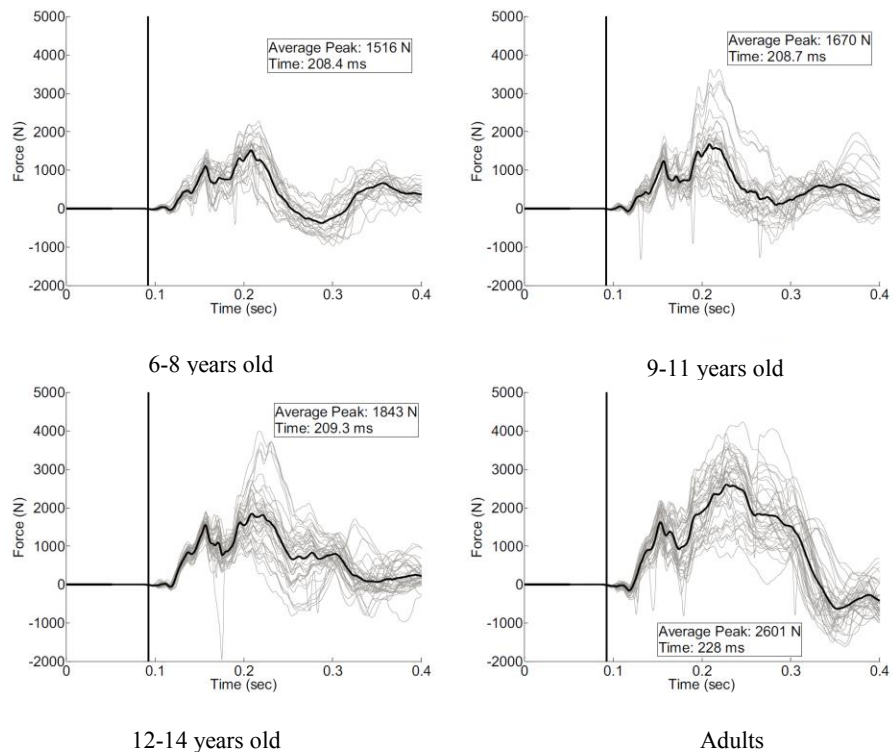


Figure 7.11 Seat normal forces per group age as reported by (Arbogast et al., 2009).

To illustrate numerically this observation, the relationship between the upper shoulder belt forces of the adult and pediatric volunteers is shown in Figure 7.12. The red solid lines correspond to the belt forces of the adult subjects, while the blue ones are the measured belt forces of the pediatric subjects. The solid dark green line is the average upper shoulder belt within the adult group, while the dashed dark green line is the scaled average force to the size of a 6YO. The factor relating these two forces was the ratio between the peak average forces. It can be seen that the scaled response (dashed dark green line) approximates both in magnitude and timing the calculated average response within the pediatric group (solid light green line).

Also, the variability between the force acting on each subject and the one acting on the average subject can be calculated using the relationship:

$$\text{Var} = \frac{\max(F_{ave}) - \max(F_i)}{\max(F_{ave})} \quad \text{Equation 7.33}$$

where F_{ave} is the actual average force within the group and F_i is the individual subject force.

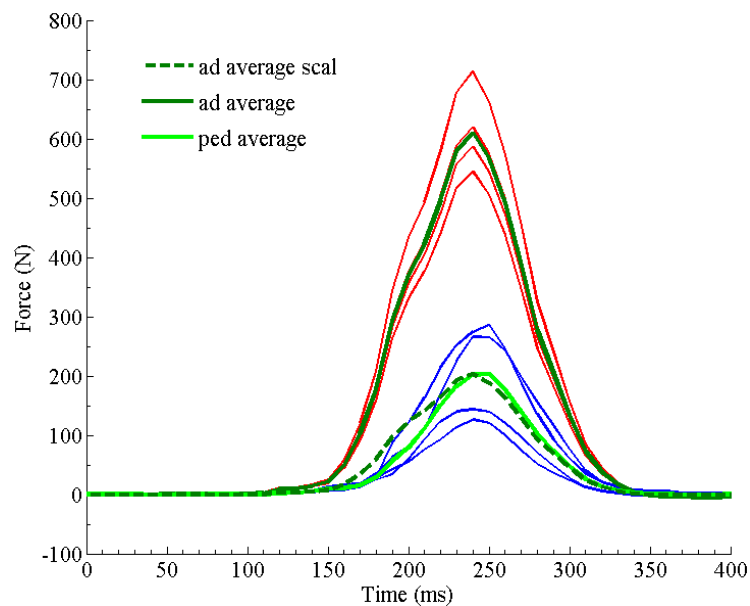


Figure 7.12 Volunteer shoulder belt forces. Comparison between the scaled adult average force (dashed dark green line) and the pediatric average force (solid light green line). Solid red lines are the adult individual belt forces and solid blue lines are the pediatric individual belt forces. Solid dark green line is the average adult belt force.

Thus, once the response of the average subject within a group was known, individual subjects' responses could be calculated using the variability given by Equation 7.33. Figure 7.13 and Figure 7.14 show the comparison between the predicted pediatric force after scaling the adult force (green) and the measured one (red) in case of the upper and lower shoulder belt force and the lap belt force.

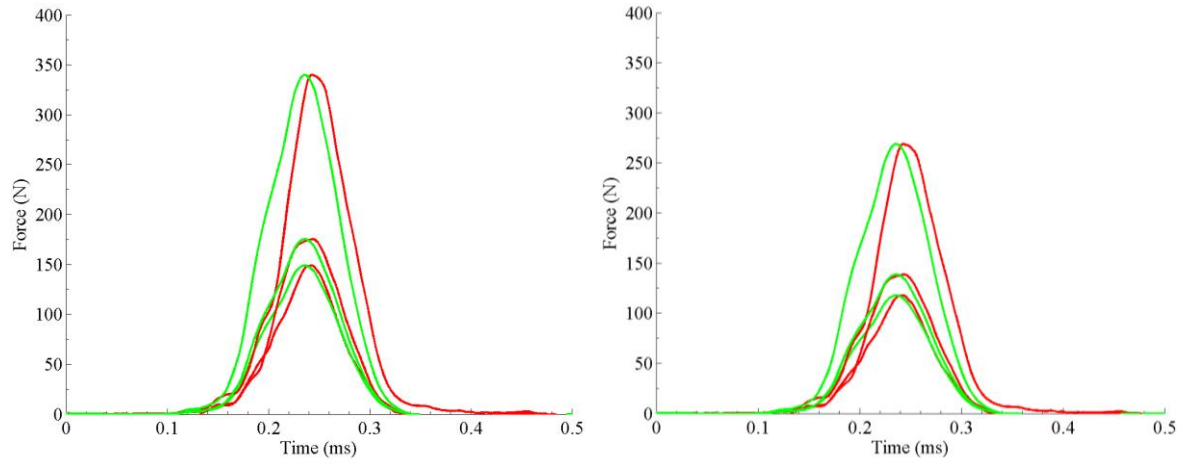


Figure 7.13 Comparison between predicted pediatric shoulder belt forces (green) and measured pediatric forces (red). Upper shoulder belt force (left), lower shoulder belt force (right).

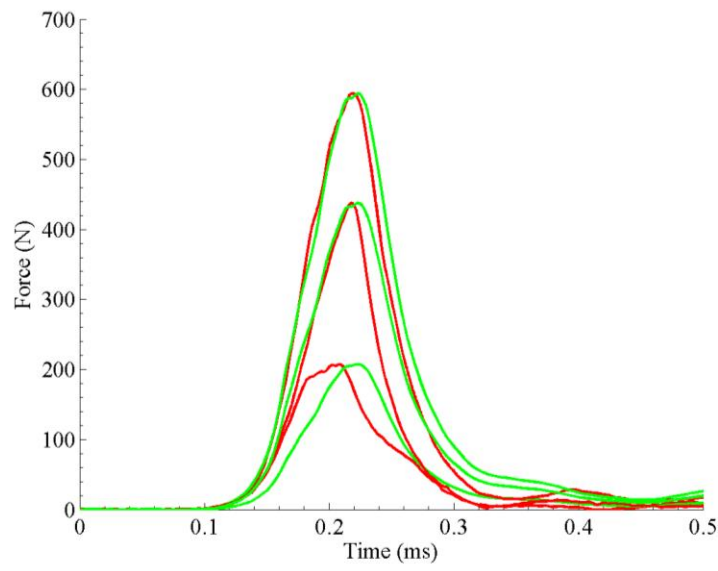


Figure 7.14 Comparison between predicted pediatric lap belt force (green) and measured pediatric force (red).

The variability observed between the average pediatric response and the individual peak force at low speed was calculated and assumed to remain constant between low and high speed. The values for these parameters are included in Table 7.24. When the variability for a sensor was not available, it was assumed the same variability exhibited by the shoulder belt force. It was also assumed that the scaling factor corresponding to the knee bolster forces was the same as the one of the seat forces.

Table 7.24 Scaling factors obtained at low speed. Subject variability for each of the forces applied to the occupant.

Force	Scaling factor average force	Var _{PED1}	Var _{PED2}	Var _{PED4}
Upper shoulder belt	0.3275	0.3996	-0.3703	0.2934
Lower shoulder belt	0.3275	0.3996	-0.3703	0.2934
Lap belt force	0.5203	0.5211	-0.3724	-0.0105
Seat force	0.5829	0.3996	-0.3703	0.2934
Knee bolster force	0.5829	0.3996	-0.3703	0.2934

7.8.2 Assessment of the method using a different set of data.

The assessment of whether the same scaling factor holds at a different impact speed was performed using the data from the tests reported in Forman et al. (2008), comparing the response of different dummy sizes in the rear seat of a mid-sized sedan at 29 km/h and 48 km/h. The method above was applied to scale between the Hybrid III 50th percentile and the AF 5th percentile (which has a size comparable to that of a 10 YO human). The measured shoulder belt forces for these two types of occupant at 29 km/h and at 48 km/h are shown in Figure 7.15. Then the scaling method was applied to the Hybrid III 50th percentile and Figure 7.16 shows the comparison between the scaled and measured forces at both speeds. The same ratio used to scaled the forces at 29 km/h was used at 48 km/h and the resultant scaled forces approximated accurately the response of the AF 5th percentile. Thus, it was concluded that the ratio found between the forces would remain constant across different impact speeds.

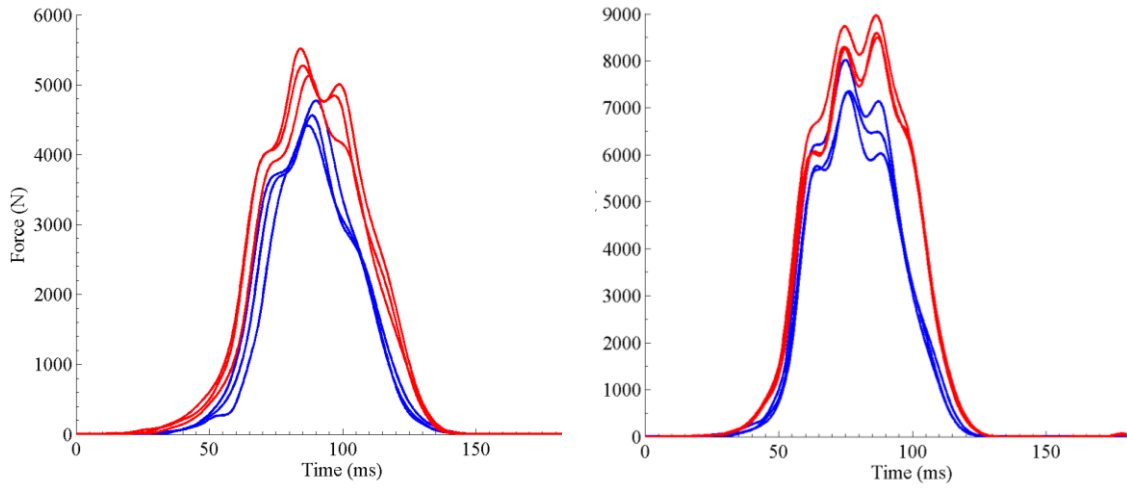


Figure 7.15 Upper shoulder force measured at 29 km/h (right) and at 48 km/h (left). H3 50th percentile (red) and AF 5th percentile (blue). Data taken from Forman et al. (2008).

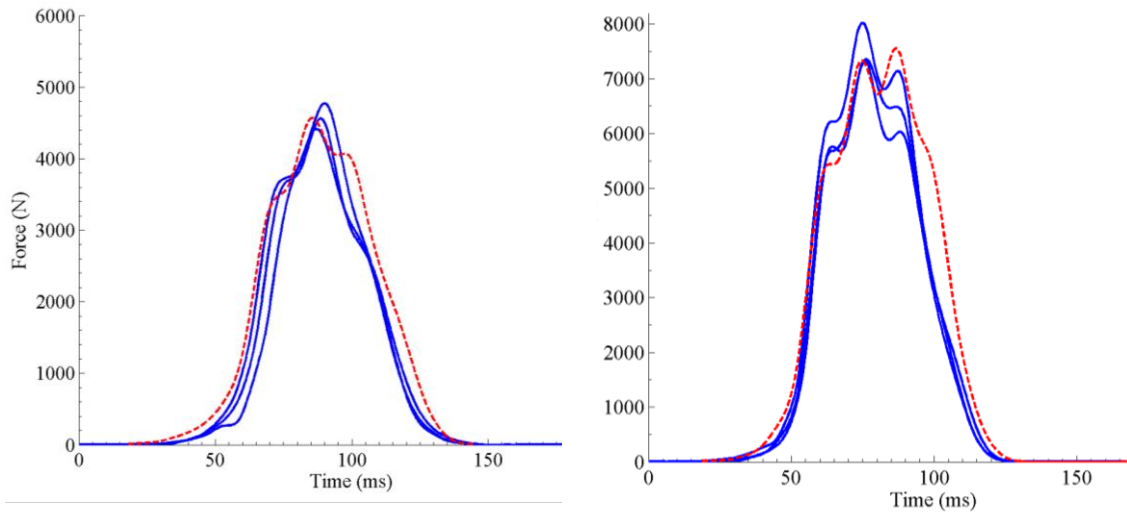


Figure 7.16 Comparison between the scaled upper shoulder force of the Hybrid III 50th (dashed-red line) and the upper shoulder belt force of the AM 5th (solid blue line). Left: 29 km/h; right: 48 km/h.

7.8.3 Prediction of the forces acting on a restrained 6YO occupant at 40 km/h

After assessing that the scaling factors between forces acting on different-size occupants remained approximately constant regardless the change in the speed of the impact (at least for the impact speed considered in this dissertation), the scaling factors obtained in the 9 km/h tests were applied to the average PMHS force measured at 40 km/h to obtain the corresponding predicted average force of a 6YO. The individual forces were then retrieved using the variability coefficients calculated from the measured forces at low speed. Figure 7.17 through Figure 7.22 show the time-history plots of the predicted pediatric forces

at 40 km/h. The solid red line corresponds to the average PMHS response. The predicted pediatric values are shown in green.

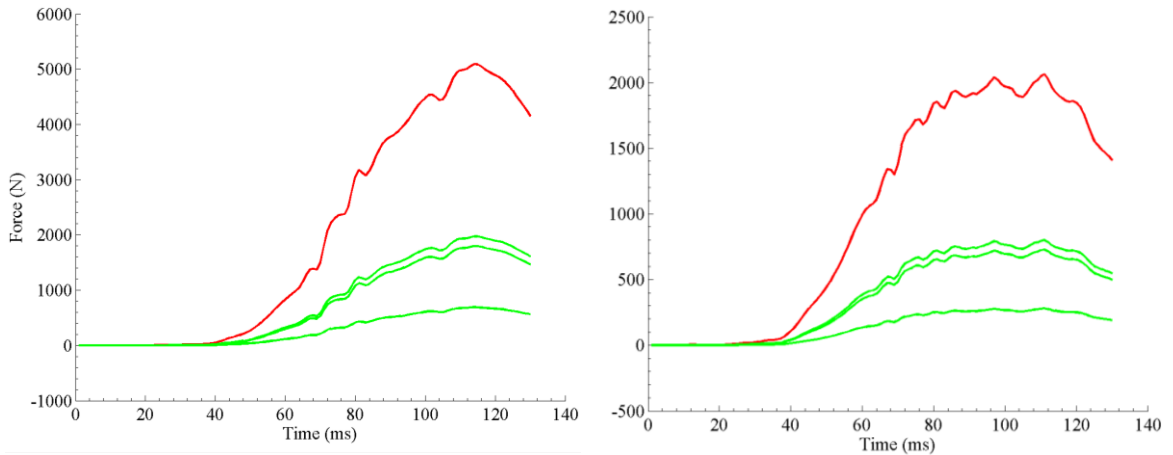


Figure 7.17 Prediction of pediatric upper shoulder belt force at 40 km/h: FUSBx (left) and FUSBy (right).

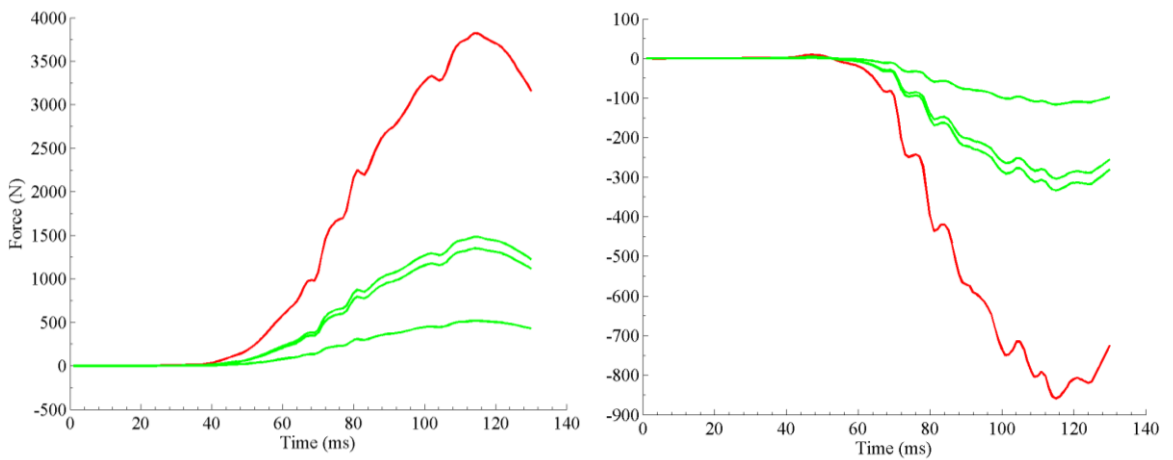


Figure 7.18 Prediction of pediatric middle shoulder belt force at 40 km/h: FMSBx (left) and FMSBy (right).

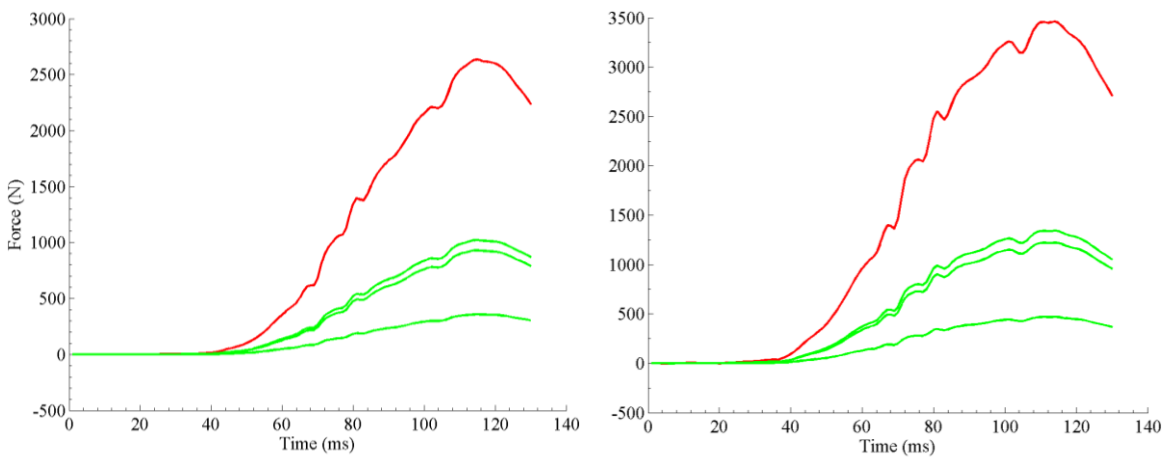


Figure 7.19 Prediction of pediatric lower shoulder belt force at 40 km/h: FLSBx (left) and FLSBy (right).

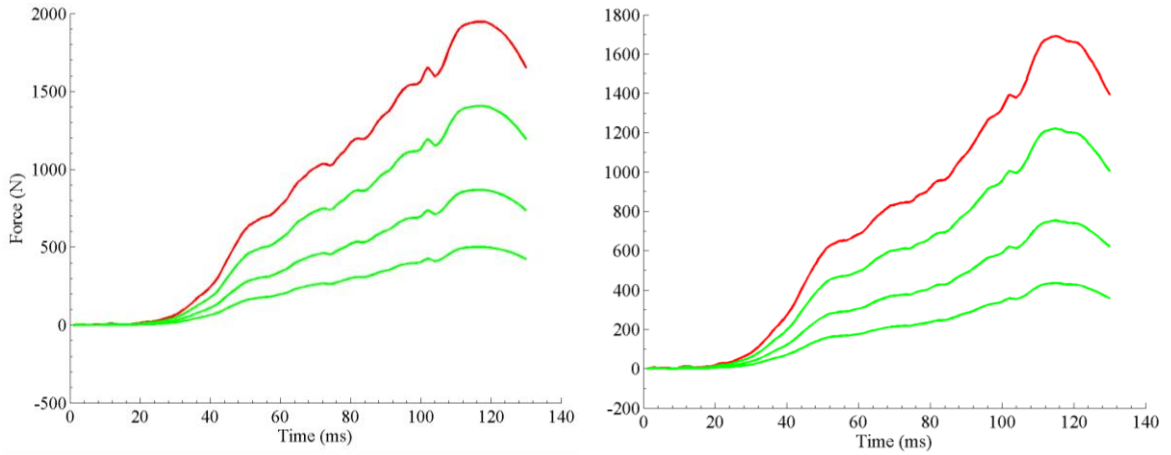


Figure 7.20 Prediction of pediatric lap belt force at 40 km/h: FLBx (left) and FLBy (right).

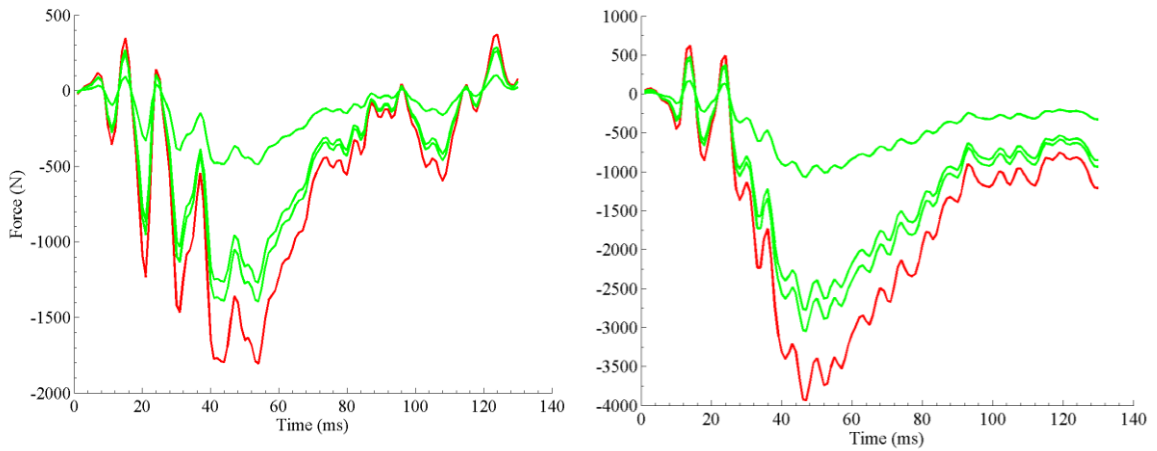


Figure 7.21 Prediction of pediatric seat force at 40 km/h: FSeatx (left) and FSeaty (right).

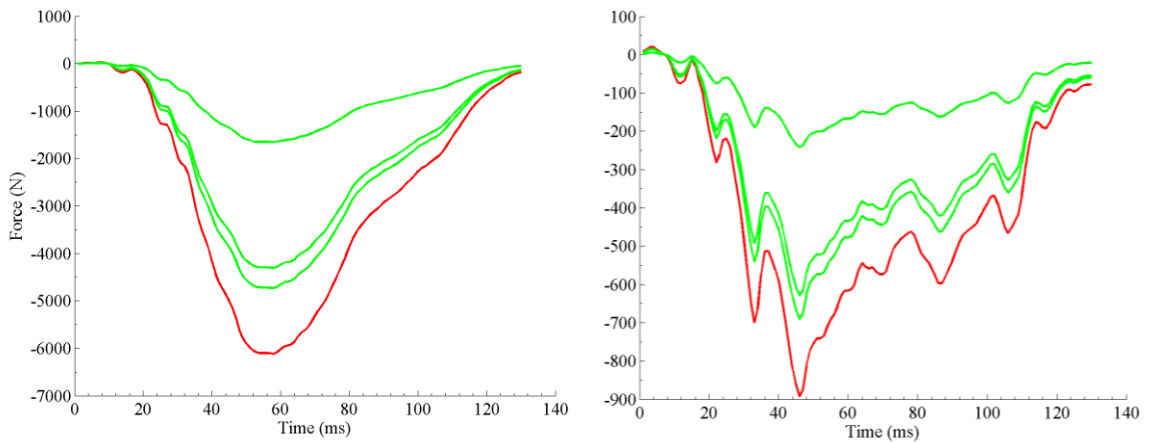


Figure 7.22 Prediction of pediatric knee bolster force at 40 km/h: FKBu (left) and FKbv (right).

7.8.4 Discussion

A method to scale between the forces acting on occupants of different anthropometry in a similar loading condition was developed to scale between pediatric and adult subjects at 9 km/h. It was assumed that similar scaling could be applied at 40 km/h. The validity of this assumption was assessed using data from dummy sled tests at 29 km/h and at 48 km/h.

Thus, it was concluded that the loading environment of the restrained pediatric occupant at 40 km/h could be approximated by scaling the time-history of the forces acting on the adult PMHS at 40 km/h.

7.9 KINEMATIC CORRIDORS OF PEDIATRIC OCCUPANTS AT 40 KM/H

In the most general case, the governing equations of the multibody system describing the motion of the restrained occupant during a deceleration had the form:

$$\underline{\underline{M}} \cdot \ddot{\underline{q}} + \underline{\underline{C}} \cdot \dot{\underline{q}} + \underline{\underline{K}} \cdot \underline{q} = \underline{Q} \quad \text{Equation 7.34}$$

where $\underline{\underline{M}}$, $\underline{\underline{C}}$ and $\underline{\underline{K}}$ are the matrices representing the mass distribution, damping and stiffness of the model.

The parameters involved in the formulation of these system matrices for a restrained pediatric occupant were found using optimization as shown in section 7.6. The previous section found the predicted time-history of the external forces that would act on a 6YO occupant, so that the generalized force vector in Equation 7.34 can be known.

Then, Equation 7.34 can be used to obtain the predicted pediatric displacements in the sagittal plane at 40 km/h. The plots in Figure 7.23 show the XZ displacement of the head, T1 and T8 of a restrained 6YO occupant in a 40 km/h. As in previous plots, the technique developed in Lessley et al. (2004) has been used to obtain the response of the average subject (solid blue line) and the corresponding corridor (shaded area).

It is important to remark that these predictions are dictated by the system matrices ($\underline{\underline{M}}$, $\underline{\underline{C}}$ and $\underline{\underline{K}}$) that are constant for a given subject and the set of external forces applied, that depend on the test environment. Thus, the predicted pediatric trajectories would be valid for a 6YO exposed to the forces described in the

previous section that are predicted to be the ones acting on the pediatric occupant in a test setup similar to the one described in Chapter 4.

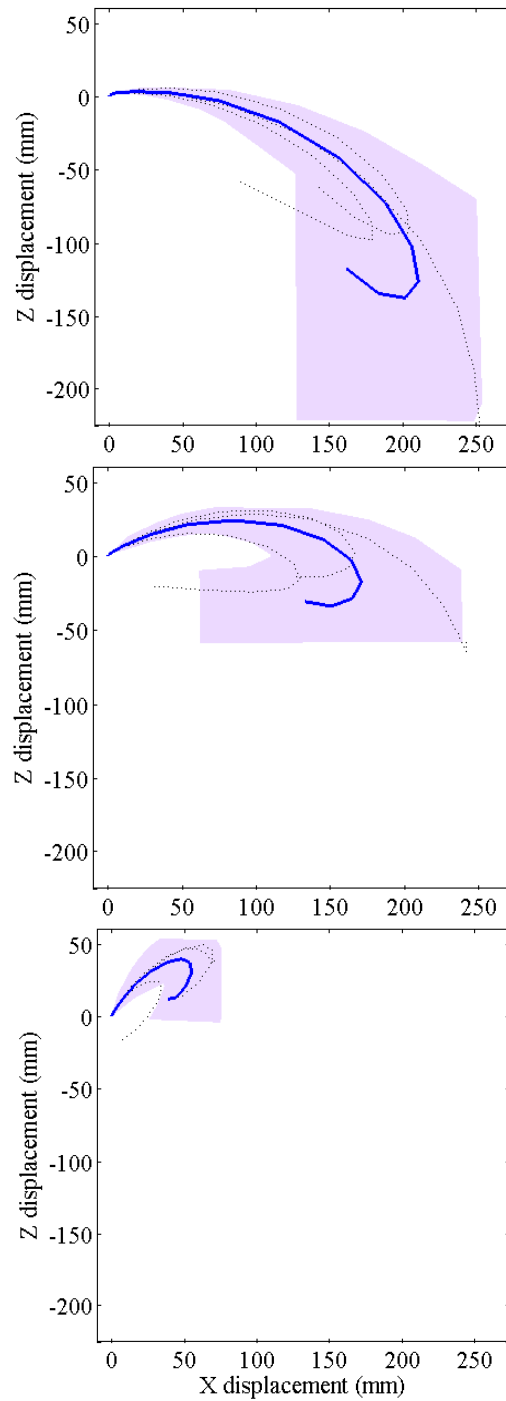


Figure 7.23 Prediction of the average sagittal trajectories (blue solid line) and corridors (purple shaded area) of the pediatric head, T1 and T8 at 40 km/h. Top to bottom: head, T1 and T8.

Table 7.25 shows the peak forward and vertical average excursions of the anatomical structures of a 6YO, when the three pediatric subjects are considered in the calculation. Also the boundary limits of the corridors are provided in the table, since these would be the limit displacement of the head and thoracic vertebrae. It is noticeable the width of the corridors especially in the vertical axis of the head prediction, due to the sparseness of the predicted results in this direction. The vertical spread of the results is not surprising since the fit in the Z axis had been shown to be marginal in the low speed validation (see Figure 7.7 and 7.8, specifically in the case of the thoracic vertebra).

Interestingly, while the head and T1 exhibited a concave trajectory towards the negative direction of the Z axis, T8 was predicted to move superiorly.

Table 7.25 Predicted peak excursions of a 6YO occupant at 40 km/h.

	Peak X excursion (mm)	X boundary limit (mm)	Peak Z excursion (mm)	Z boundary limit (mm)	Z boundary limit (mm)
Head	210.7	250.6	-137.8	-221.2	4.2
T1	170.8	239.5	-34.2	-58.6	31.9
T8	54.92	108.3	39.2	-4.7	52.6

7.10 DISCUSSION

7.10.1 Model assessment criteria

This dissertation was motivated by the high incidence of pediatric head injuries (that are potentially associated with head contacts) in the field (Arbogast et al, 2002; Adekoya et al, 2002; Thompson and Irby, 2003) despite that regulation FMVSS 213 controls the maximum excursion of the head.

Thus, matching the forward excursions of the head and the thoracic vertebrae was considered a priority in the development of the model. More specifically, the criterion requiring the measured head forward excursion to be matched by the model was considered the most important one and it was always selected in case of conflict with matching any of the other displacements. Therefore, whenever there was a tradeoff between matching the head forward excursion and any other displacement of the occupant, the decision made was to match the forward displacement of the head. This decision caused that the predicted

displacements in the vertical direction for the thoracic vertebrae of the pediatric volunteers were not as accurate as desired. In the current state of knowledge on pediatric kinematics and at the light of recent studies reporting on injury scenarios for restrained pediatric occupants, it was favored to focus on the forward displacement of the head.

According to this compromise, subsection 7.4.2 presented the criteria used to assess the solution given by the different types of multibody models that were developed to approximate the kinematics of the occupant. Although the complexity of these criteria increased as the model developed, the requirements focused initially on the comparison between the forward displacements of the head, T1 and T8 between model and actual test. It was only after this condition was satisfied that the model was considered acceptable and further developed.

7.10.2 Assumptions made in the development of the pediatric model and in its application to predict the kinematics at 40 km/h

The level of detail of the multibody model was directly linked to the amount of experimental data available. As already mentioned, it was necessary to keep the number of model unknowns low so that the optimization process would provide a realistic approximation to the actual value of the parameters. Thus, a number of assumptions were made in the development of the model that likely affected the accuracy of the results obtained. These assumptions are discussed in the following paragraphs.

7.10.2.1 Linear time-invariant model

Assuming a linear, time-invariant model to represent the behavior of the restrained occupant constituted an important simplification of the problem.

The multibody model was developed in the effort of capturing the different mass distribution of the body existing between children and adults, which had been one of the points of the critique to the use of scaling. The model can capture these differences, but it does not capture the changes of mass and moments of inertia occurring due to the motion of the internal organs in the trunk. The mass and moment of inertia of the body regions were assumed to remain constant throughout the impact.

Other factor influencing the accuracy of the results was the absence of arms in the model. Especially in the high-speed PMHS tests, it could be observed that the arms of the occupant swing around the shoulder joint affecting again the effective mass and moment of inertia distribution of the torso. It was decided not to include the arms in the model to avoid having to model the shoulder and elbow joints. The arm rotation was not important in the low speed tests and therefore it is expected that it became a source of error in the estimation of the pediatric trajectories at 40 km/h since the mass and moment of inertia distribution were optimized using data from the 9 km/h tests.

As for the joint stiffness and damping formulation, the characterization of the thoracic spine performed within this dissertation showed that the flexion of the human thoracic spine could be described using a quasi-linear viscoelastic model, which is intrinsically non-linear in the space component. Previous research on the flexion of the thoracic spine in animal surrogates has found a fully non-linear (both in space and time) behavior of the thoracic spine (Clarke et al., 2007). However, it was decided to use a linear model to describe the mechanical behavior of the joints. The multibody model showed a good agreement between the observed and predicted displacements of the head and the thoracic spine, especially in the case of the PMHS tests. Thus, it was considered that, for the range of impact speeds analyzed in this dissertation and with the goal of predicting the sagittal displacement of those selected anatomical landmarks, the joints could be described using a linear model. Other simple multibody models of a restrained occupant that focused on the interaction between the restraint system and the kinematics of the occupant had used successfully a similar formulation for modeling the rotational behavior of the spinal joints (Habib, 2001; Paulitz et al, 2006; Katoh and Nakahama, 1982; Wismans et al, 1987).

The proportional damping formulation chosen to model joint damping is a conventional method used commonly in the literature when the actual damping of the structure is not known (Liu and Gorman, 1995; Adhikari and Woodhouse, 2001; Adhikari, 2006). The hypothesis under which this approximation is valid is discussed in detail within Appendix 4. In general, it can be said that the model of proportional damping produces the same response of a linear viscoelastic generalized Maxwell model when the damping coefficient of the structure is smaller than 26%. Again, the good agreement between the model-predicted and experiment-measured displacements in the PMHS tests shows that such a model of damping is valid to

described the behavior of the joints at the rates explored in this dissertation and with the goal of predicting the sagittal displacements.

It is hypothesized that an improved description of the joint behavior (including its non-linear characteristic) can improve the accuracy of the prediction of the pediatric displacements, but this is something that can be assessed in further research on the topic.

7.10.2.2 Degrees of freedom of the model. Tensile and shear stresses in the spine in a frontal impact. Motion out of the sagittal plane

The multibody model of the occupant was developed to describe the motion within the sagittal plane (XZ). In the case of the human occupants, it was considered that the subject could move in the horizontal and vertical direction with respect to the test buck. The different body regions were connected by revolute joints that allowed a relative rotation between the contiguous regions while constraining any other motion.

This is again an approximation to the real behavior of the human spine. Research has shown that in a highly dynamic event such as the frontal impact at 40 km/h, tensile and shear stresses can be expected in the spine (Lopez-Valdes et al, 2010). Figure 4.10 showed that even at 9 km/h, tensile effects can be observed in the cervical and lower part of the lumbar spine. Additional degrees of freedom were considered at the T1 and pelvic joints to capture these observations, but the consequent increase of unknown joint parameters could not be solved by optimization. The solver failed to obtain a solution to the problem within the tolerance requested.

Also the model was constrained to move only within the sagittal plane, despite the trajectories in the transversal plane observed in the PMHS tests and shown in Figure 4.9. The out-of-plane motion was attributed to the asymmetry of the shoulder belt, causing the occupant to rotate. This phenomenon is worth of further study since the analysis of head impact contact points in Arbogast et al. (2012) pointed out that, even for properly restrained children in frontal collisions (principal direction of force 11 to 1 o'clock), there is an important lateral component to the motion of the head.

7.10.2.3 *The influence of muscle activity on the trajectories of the selected anatomical landmarks.*

Subsection 4.4.1 had pointed out the differences found in the nature and magnitude of the displacements between adult PMHS and volunteers. These differences were attributed to the influence of muscle contraction on the trajectories of the head and spine.

The process of obtaining the stiffness of the model joints was purely phenomenological, based on the optimization of the stiffness values to match the observed experimental results. Thus, muscle contraction is effectively included in the optimized stiffness values of the volunteer models but it is not present in the PMHS ones. In case of the model of the pediatric occupants, it was assumed that the same stiffness matrix that was calculated at 9 km/h was valid at 40 km/h. This assumption implies that the influence of the muscles on the kinematics at 9 km/h is similar to the influence of the muscles at 40 km/h. However this assumption can be questioned attending at the results reported in Wismans et al. (1987). This study compared the kinematics of the head and T1 between PMHS and adult volunteers exposed to the same deceleration at impact speeds up to 17 m/s, finding that the magnitude of the head center of gravity displacement relative to T1 was of the same order of magnitude in the PMHS and in the volunteers. The study also reported that the forward excursion of T1 with respect to the test buck was also similar between the two occupant types, but that the vertical excursion of T1 in the cadaver group was significantly greater than in the volunteer group. The main differences between the volunteers and the PMHS were found in the rotation of the head and T1. Should the findings in Wismans et al. (1987) be applicable to the setup analyzed in this dissertation, the multibody model of the pediatric occupant might be underpredicting the magnitude of the displacement of the head and the thoracic spine. It is unfortunate that there is no data from pediatric volunteers at higher impact velocities that would allow checking whether the influence of muscle on the magnitude of the displacements fades away as in the cases reported by Wismans.

Another potential influence of the muscles on the performance of the model relates to modifying the forces acting on the occupant. It has been assumed that the same relationship observed between pediatric and adult volunteers at 9 km/h would hold between pediatric volunteers and adult cadavers at 40 km/h. The assessment done of the force scaling method using ATD at two different speeds validated the method to scale between occupants of different sizes with no muscular activity. Unfortunately, it is not possible to

assess how much error is present in the estimation of the forces acting on the pediatric occupants at 40 km/h in the absence of experimental data.

7.10.3 Pelvis position and pelvic rotation

The multibody model of the pediatric occupants and the kangaroos exhibited a poor fit to the trajectories of the lower thoracic segment. Also, although the magnitudes of the forward and vertical displacements of the pediatric head and T1 was approximated within the errors set in the model assessment criteria, the nature of the model-predicted motion of the selected landmarks differed from that observed in the actual tests. These differences have been attributed to a deficient model of the motion of the pelvis of the occupants.

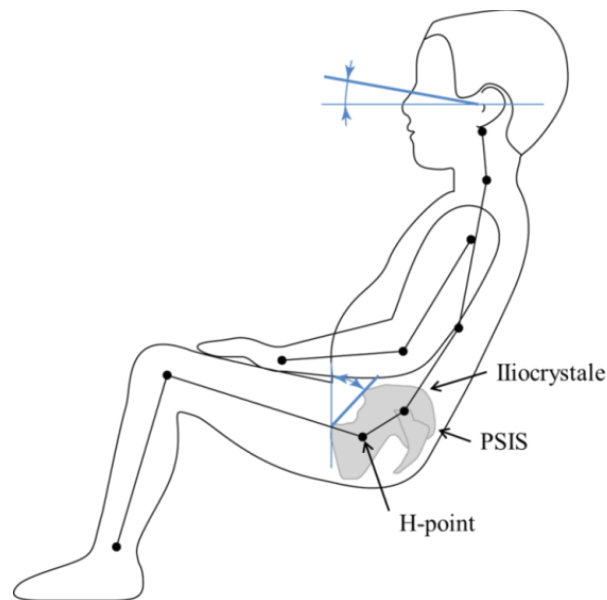


Figure 7.24 Schematic showing the typical seating position of a pediatric occupant and selected pelvic anatomical landmarks. Adapted from (Reed et al. (2006).

As described in Chapter 3, the position of the volunteer pelvis was tracked using a single marker that was placed nominally on the ilicrystale of the pelvis' subject. Only one marker could be fit due to the absence of physical space and the need of preserving the test subject clothed. Having just one marker attached to the subject's pelvis prevented measuring the rotation of the pelvis. Moreover, the position of that marker was used to place the joint connecting the thigh to the hip and the pelvis to the spine. In other words, the position of the marker at the ilicrystale was used to model the hip joint and the sacroiliac joint as if they

were a single point. In the case of the PMHS subjects a marker array was attached to the pelvis of the subjects. This array allowed reconstructing the 6-dof motion of the pelvis. A local coordinate system with origin on the mid-point between the two posterior superior iliac spines (PSIS) of the pelvis was defined.. Figure 7.24 depicts the position of the iliocrystale with respect to the PSIS and the H-point in a typical seating position of a pediatric occupant.

It should be noted that the analysis of the motion of the PMHS pelvis at 40 km/h showed a substantial rotation of the pelvis in the sagittal plane amounting up to 75 degrees, which is greater than the rotation measured in the thoracic vertebrae under the same test conditions (Lopez-Valdes et al, 2013).

Additionally, it was observed that depending on the pelvic point being tracked, the assumed motion of the pelvis would exhibit substantially different characteristics. The plot in Figure 7.25 compares the measured pelvic motion of the average adult volunteer (tracking the position of the iliocrystale) and the one corresponding to the average PMHS (tracking the position of the mid-point between the two posterior superior iliac spines of the pelvis). These two tests were conducted in the same loading environment and the comparison shows a completely different behavior both in magnitude and in nature.

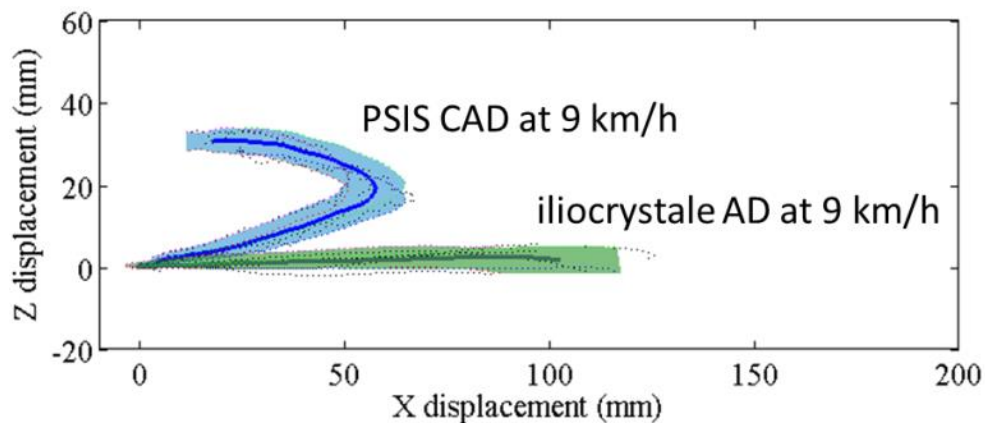


Figure 7.25 Comparison between the sagittal trajectory of the PSIS of the PMHS test (blue solid line) and its associated corridor with the one of the iliocrystale of the adult volunteers (green solid line) and its associated corridor.

It was hypothesized that a more realistic description of the motion of the pelvis would have influenced the outcome of the optimization process so that the nature of the predicted sagittal displacements of the head

and thoracic vertebrae of the restrained pediatric occupant would have resembled more biofidelically that observed in the sled tests.

Thus, a sensitivity study was designed to analyze the influence of the pelvic motion on the trajectories of the thoracic vertebrae and the head.

7.10.3.1 Sensitivity study of the influence of the motion of the pelvis on the sagittal trajectory of the head and thoracic vertebrae of a restrained 6YO occupant

To study the sensitivity of the model parameters to the motion of the pelvis of the occupant, the mass, damping and stiffness matrices of the pediatric volunteers were calculated again imposing a known displacement of the pelvis of the model.

The known displacement was taken from the measured displacement of the adult PMHS at 9 km/h. To explore the sensitivity of the predicted pediatric trajectories to the motion of the pelvis, the three different cases were analyzed:

- a) The pelvis of the pediatric occupant followed the same trajectory of the adult PMHS pelvis at 9 km/h.
- b) The pelvis of the pediatric occupant followed a trajectory with the same nature of that of the adult PMHS at 9 km/h, but with a magnitude of 30% of the full range of the measured PMHS displacement (in both X and Z axes)
- c) The pelvis of the pediatric occupant followed a trajectory with the same nature of that of the adult PMHS at 9 km/h, but with a magnitude of 60% of the full range of the measured PMHS displacement (in both X and Z axes).

The optimization problem was solved again for each of the previous cases and the sagittal trajectories of the head, T1 and T8 are shown in Figure 7.26 through Figure 7.28.

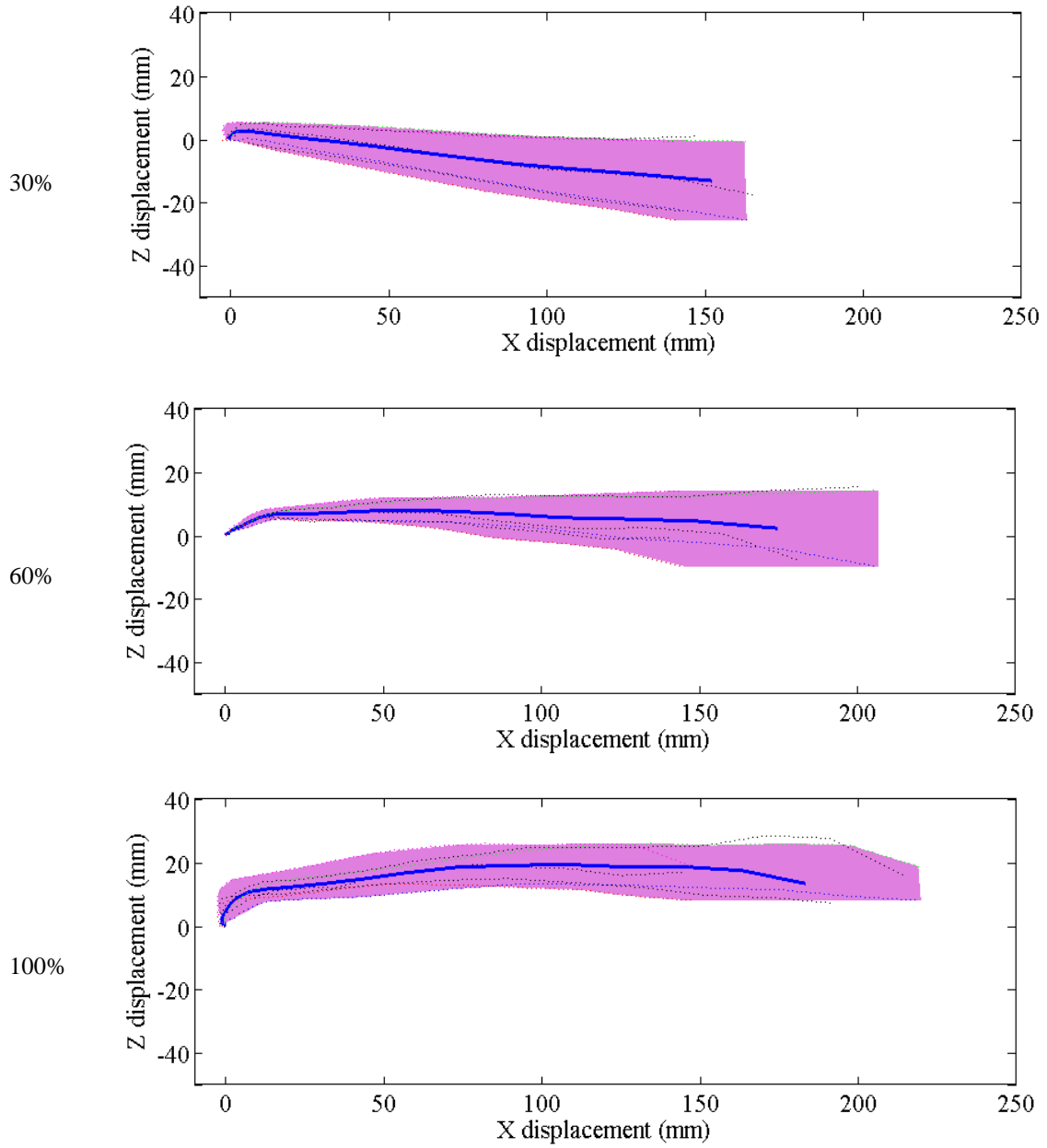


Figure 7.26 Comparison between the average sagittal trajectory (blue solid line) (and associated corridor, purple-shaded area) of the head of the 6YO at 9 km/h, when the pelvis is assumed to move 30%, 60% and 100% of the adult pelvic range of motion (top to bottom).

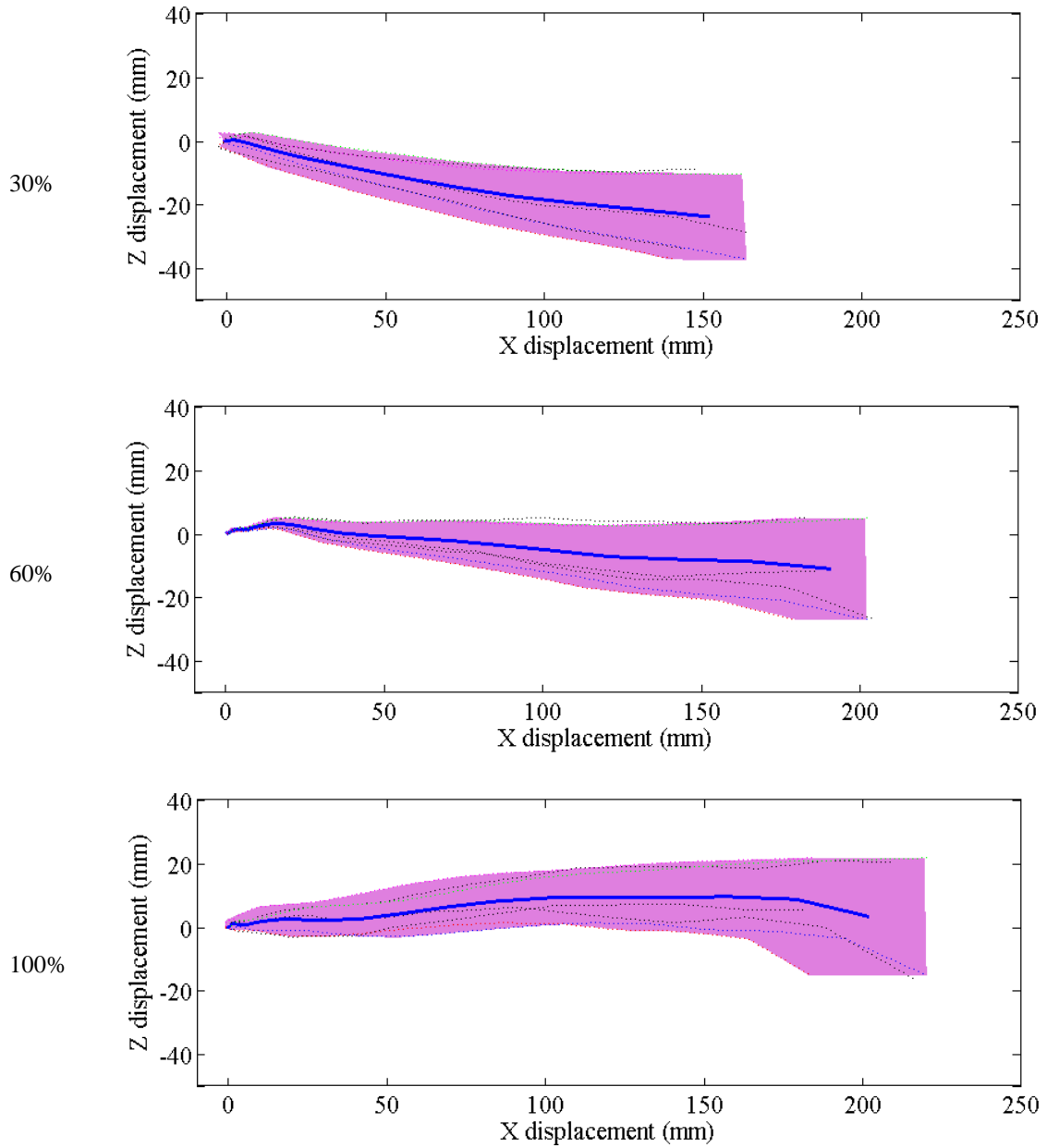


Figure 7.27 Comparison between the average sagittal trajectory (blue solid line) (and associated corridor, purple-shaded area) of the T1 vertebra of the 6YO at 9 km/h, when the pelvis is assumed to move 30%, 60% and 100% of the adult pelvic range of motion (top to bottom).

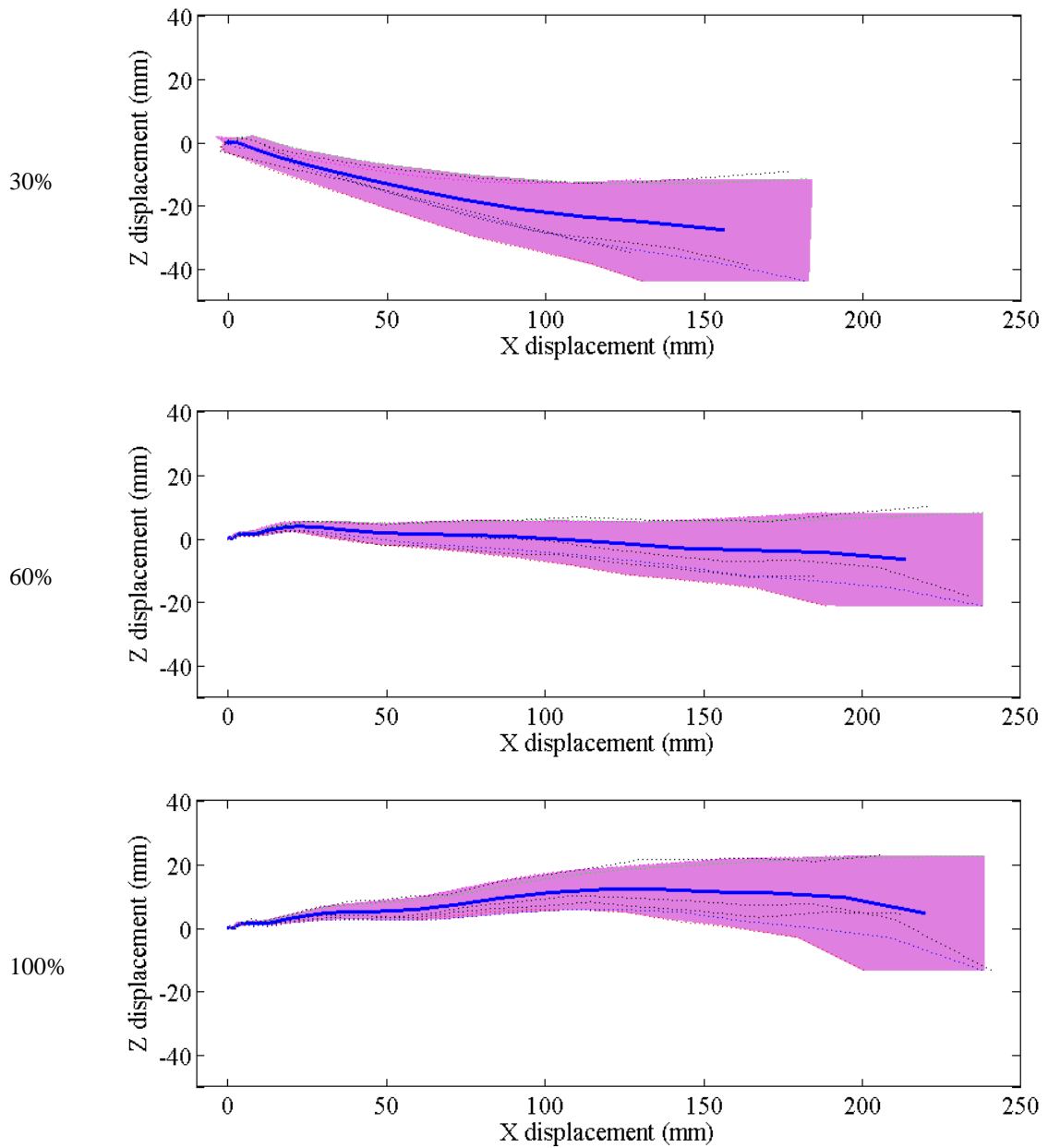


Figure 7.28 Comparison between the average sagittal trajectory (blue solid line) (and associated corridor, purple-shaded area) of the T8 of the 6YO at 9 km/h, when the pelvis is assumed to move 30%, 60% and 100% of the adult pelvic range of motion (top to bottom)

Regardless of the actual percentage of the range of adult pelvic motion imposed on the pediatric pelvis, the nature and the magnitude of the excursion of the three anatomical landmarks were influenced by the motion of the pelvis, as suggested previously. Interestingly, in the case of 30% and 60% of adult pelvic motion, the thoracic vertebrae exhibited a concave trajectory instead of the convex one predicted before. However, the

measured pediatric response showed that the vertebrae displaced superiorly while the plots obtained in this sensitivity study showed a caudal trajectory. As for the magnitudes, the models overpredicted the maximum forward excursion of the thoracic vertebrae and this overprediction was greater with increasing percentage of adult pelvic motion imposed on the pediatric pelvis.

Thus, it is strongly recommended to have at least two measurement points on the pelvis of each subject (if the model is focused on the sagittal plane, these landmarks should be in different locations within the sagittal plane, so that the rotation within this plane can be resolved). Knowing the rotation of the pelvis will allow modeling the pelvis as a separate body region resulting likely in a more biofidelic motion of the occupant. Also, it is suggested to locate carefully the subject anatomical landmarks in equivalent positions in the volunteers and the PMHS to facilitate the comparison between these two subject types.

8 PROPOSED RESPONSE TARGETS FOR THE DISPLACEMENT OF THE 6YO HEAD AND THORACIC SPINE

The first section within this chapter presents the displacement corridors that are proposed to be used to benchmark physical or computational models of a human 6YO in a high-speed frontal impact. Then section 8.2 compares the estimation of the pediatric head and thoracic spine trajectories of the different methodologies discussed in Chapter 6 and Chapter 7. Lastly, this chapter discusses how this model should be used, commenting on its limitations.

8.1 PROPOSED TARGETS FOR THE DISPLACEMENT OF THE HEAD AND FIRST THORACIC VERTEBRA OF A HUMAN 6YO IN A 40 KM/H FRONTAL IMPACT

The objective of the dissertation was to provide corridors for the sagittal displacement of the head and thoracic spine of a 6YO in a 40km/h frontal impact. After evaluating four approaches that involved scaling between adults and children and also the development of a multibody model of the occupant, the responses in Figure 8.1 should be targeted as benchmarks for 6YO models (either physical or computational). These corridors describe, as reliably as possible given the dearth of data available for their development, the trajectories that would be expected for the head and T1 of an average 6YO seated on a rigid seat, restrained by a conventional 3-point seatbelt with the anchorages positioned as described in Arbogast et al. (2009) and exposed to the set of external forces showed in Figure 7.17 to Figure 7.22.

Note that the prediction obtained for the displacement of T8 was not included here due to the error observed in the 9 km/h case (shown in Figure 7.18). The assessment of the method using the animal surrogate model showed that even if the prediction of the trajectory of T8 was marginal at both speeds, the multibody model can still approximate the trajectories of the head and T1 at 40 km/h. Thus it was decided

to discard the estimation obtained for T8, but to keep those obtained for the head and the first thoracic vertebrae.

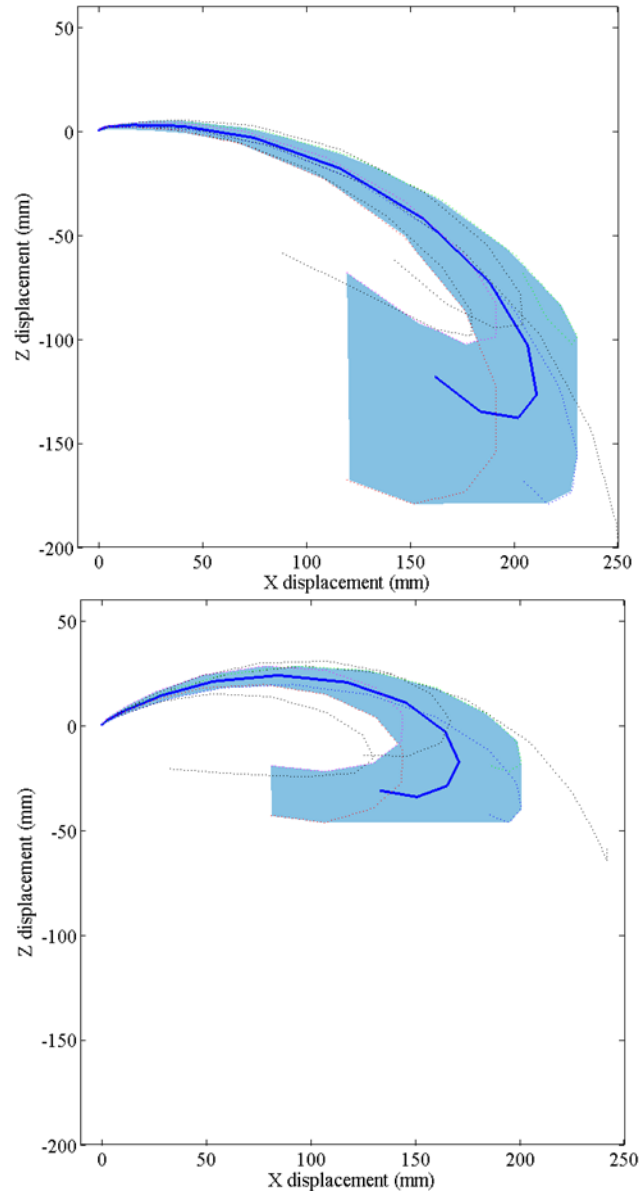


Figure 8.1 Proposed XZ average displacement (blue solid line) and associated corridors (blue-shaded area) for the head (top) and T1 vertebra (bottom) of a human 6YO in a 40 km/h frontal impact.

8.2 COMPARISON BETWEEN THE DIFFERENT METHODS PREDICTING THE KINEMATICS OF PEDIATRIC OCCUPANTS IN FRONTAL IMPACTS

The rationale for this dissertation research was the high incidence of pediatric head injuries in the field despite that the current regulation (FMVSS 213) limits the forward excursion of the dummy head in the assessment of child restraint systems (Arbogast et al, 2002; Adekoya et al, 2002; Thompson and Irby, 2003; Arbogast et al, 2012). This fact motivated that special attention was paid to the prediction provided by scaling technologies to the peak forward excursion of the head and thoracic vertebrae. Throughout the dissertation, these parameters became the discriminate criterion in the comparison between different methods.

Each of the methods used to predict the kinematics of pediatric occupants was first assessed using the observed experimental results from the pediatric volunteer tests as presented by Arbogast et al. (2009). Table 8.1 summarizes this assessment using the error in the prediction of peak forward excursion to compare between the different techniques (basic assessment level).

Table 8.1 Error in the prediction of the peak forward excursion of an average 6-year-old child's head and thoracic spine in a 9-km/h frontal impact using the four methods analyzed in this dissertation.

	Measured	SAE	Mass scaling	Conservation of energy	HIII 6YO Seacrist et al. (2010)	2D model (model B2.2)*
Head	177.5	-42.0%	-48.6%	-28.7%	-14%, -5%**	5%
T1	134.1	-35.0%	-42.4%	-19.8%	-27.8%	6%
T8	88.5	-13.0%	-22.9%	0.1%	NA	-27%

* Error calculated between average predicted response (blue solid line in Figure 7.7) and average measured response (red solid line in Figure 7.7)

* Error calculated for different points on the surface of the ATD head.

Table 8.1 shows that the amount of error found in the prediction of the forward displacement of the head and T1 using the multibody model was smaller than the one obtained with the methods based on scaling. The minimum error obtained with the scaling methods for the forward displacement of the head underestimated this displacement by 29% (Conservation of energy method), while the multibody model overestimated the displacement by 5%. A similar behavior can be found in the prediction of the peak

forward displacement of T1. Interestingly, the prediction given by the scaling methods to the forward peak excursion of T8 is better than the one obtained using the multibody model. It was pointed out in Chapter 7 that special attention would be given to the forward displacement of the head due to its relevance in contributing to injury causation. However, it was not the only reason that motivated the use of the multibody model to provide a prediction for the kinematics of children in high speed collisions.

As indicated in Chapter 6, the geometrical and dynamic similarity required by scaling cannot be assumed when scaling between children and adults. The results from Arbogast et al. (2009) proved that the kinematics of the pediatric volunteers were different in nature from those of the adults.

Also, the comparison between the 6-YO volunteer group and the Hybrid III 6YO done in Seacrist et al. (2010) found significant differences in all the measured reaction forces and in the measured forward displacement of the cranial markers and the C4 and T1 markers. To put the results obtained with the 2D model of the occupant into the right perspective, it should be noted that Seacrist et al. (2010) showed differences up to 14% in the prediction of the maximum forward head excursion (average displacement within the pediatric group: 199.5 mm; average displacement in the ATD tests: 171.7 mm) and up to 28% in the prediction of the peak forward excursion of T1 (average displacement within the pediatric group: 153.8 mm; average displacement in the ATD tests: 111.1 mm).

Thus, the method based on the development of a multibody model that could accommodate the differences in mass distribution and joint geometry and effective behavior occurring during development was the one chosen to provide an estimation of the kinematics of pediatric occupants at 40 km/h.

8.3 IMPLICATIONS. USE OF THE MULTIBODY MODEL TO PREDICT THE PEDIATRIC RESPONSE IN HIGH SPEED IMPACTS

8.3.1 Pediatric head injuries due to direct contact against the interior of the car

A recent study reviewing CIREN cases involving restrained forward facing pediatric occupants in frontal collisions (principal direction of force from 11 to 1 o'clock) showed that the head/face area was the most

severe injuries found and that injuries to other body regions were uncommon in pediatric occupants (Arbogast et al, 2012). The authors pointed out that even when the children were appropriately restrained, there was a substantial amount of head excursion that resulted in contact against the back seat of the front row or against the B-pillar (whenever there was also a lateral component to the collision). Another review of NASS CDS and CIREN cases including children restrained in frontal crashes who sustained AIS2+ head injuries, the head injuries were associated to the contact of the head with the seatback or the side interior of the car in approximately 60% of the cases (Bohman et al., 2011). The remaining of the cases showed no evidence of head contact and were characterized by a higher crash severity and accompanied by severe thoracic and spinal injuries. Unfortunately, any of the studies provided information about the distances between the pediatric occupant and the front seat back. Both studies analyzed recent data and therefore the interior of the cars and the child restraint used reflected contemporary solutions.

A more comprehensive review of the literature did not find any published study reporting on the initial distance between the head of the children and the contact point on the front seat back, so that the results reported here can be compared against real world data. The typical distance between the surface of the rear seat and the surface of the front seat back in the middle position is around 730 mm in a mid-size American sedan, which is approximately the maximum head forward excursion allowed in FMVSS 213. Although more information is necessary to understand the mechanics of the impacts of children's head against the interior of the car, field data show that they occur even when children were using correctly a certified child restraint system.

Thus, a more biofidelic tool that can predict realistically the excursion of the head of a 6YO can contribute to improve the requirements of current regulation, so that CRS regulatory tests reflect better what is being seen in the field.

8.3.2 Specificity of the results to a particular loading environment

The whole development of the multibody model of the pediatric occupant was based on the concept of characterizing the occupant by obtaining its mass, damping and stiffness matrices. Once the matrices are known, the displacements of the occupant can be obtained if the external forces are known.

The corridors presented in Section 8.1 are the particular solution of the governing equations of the multibody model when the forces acting on the occupant are the ones shown in Figure 7.17 through Figure 7.22. Nevertheless, the method developed here allows obtaining a prediction of the motion of the restrained 6YO for any particular set of known forces. The challenge is that the external forces acting on the pediatric occupant are not known beforehand and they have to be estimated following a procedure similar to the one presented in this dissertation.

8.3.3 Specificity of the 2D model to the experimental subjects. Extrapolation to other sizes within the same age group

Although the goal of the dissertation was to provide corridors for the trajectories of the head and the thoracic spine of the 6YO 50th percentile, all the modeling efforts were tailored to the specific subjects included in the experiments instead of trying to represent a mid-size occupant within each age group. A model that could explain the particularities of each subject was considered to be more robust than a model fitted to a generic subject within each age group.

This is particularly relevant in the models in which dimensional analysis was used to derive the expressions for the joint stiffness. As a first approach to modeling joint stiffness, BMD was used as a proxy for the modulus of elasticity of the joints. Since BMD was unknown, it was decided to use the existing relationship between BMD and age to estimate the BMD value for the subjects participating in the study. In the case of adult PMHS, the relationship proposed by Looker et al. (2009) was used. But the same study reported also on the variability observed in the sample, especially in the case of women. In the case of the pediatric volunteers, the data in Kalkwarf et al. (2007) shows even more variability due to the smaller sample size included in the analysis. While the displacements predicted by the model were acceptable in the case of the PMHS, it was considered that the error obtained in the case of the pediatric volunteers could be minimized further by including directly the modulus of elasticity as one of the unknowns in the optimization problem.

Thus, reducing the error implied reducing also the potential for generalization of the joint stiffness model to any other age (for example, a mid-size 6 YO). Instead, the corridors for the average 6YO were developed using the normalization technique introduced in Chapter 3 (Lessley et al., 2004), after simulating each

pediatric subject at high-speed. The reason for adopting this approach was that, while the loading environment for each specific subject could be approximated following the methodology detailed in Chapter 6, there was no information about the loading environment for an ideal mid-size 6YO at 9 km/h.

8.3.4 How is this model to be used in the field. Applicability of the results of this dissertation.

As stated at the beginning of this research, the main objective of the dissertation was to provide corridors for the sagittal trajectories of the head and thoracic spine of a 6YO in a 40 km/h frontal impact that could be used to benchmark future physical or computational models of a 6YO.

As discussed above, the requirement of a particular impact speed is imposed by the necessity of knowing the external forces acting on the occupant. Should these forces be estimated by any reliable method as the one developed within this dissertation, the predictions of the model can be trusted at least up to 40 km/h, which was the maximum impact speed used here.

The immediate application of the results included here is the benchmarking of computational models of pediatric occupants. In this case, the loads acting on the occupant can be completely defined with the information included in Chapter 7 and therefore the computational model performance can be compared against the corridors included in Section 8.1.

These corridors can be used to benchmark physical models (pediatric crash test dummies) too. In this case, the method requires the loading environment acting on the dummy to be equivalent to the one used in the simulation of the multibody model. If the loading environment is changed, then the multibody model of the occupant should be used to predict the displacements under the new loading conditions. Once again it is stressed the link between the outcome of the model and the test conditions under which the model is used.

9 CONCLUSIONS AND CONTRIBUTIONS

Predicting the kinematics of the pediatric head and spine in a high-speed frontal impact is a challenging endeavor and it is made even more difficult by the lack of any experimental data that can be used to assess the results obtained.

Field data shows that a vast majority of fatal pediatric injuries in crashes are head injuries (Adekoya et al., 2002; Arbogast et al., 2002). There is also evidence of the lack of biofidelity of the spine of the Hybrid III 6YO that causes a questionable prediction of the trajectory of the pediatric head and unreliable neck loads (Seacrist et al., 2012; Seacrist et al., 2010; Sherwood et al., 2003). These biofidelity issues have been attributed to the rigid thoracic spine of the ATD and it is envisioned that future models of pediatric occupants (either physical or computational) will consider some degree of deformation of the thoracic spine. Therefore, there is a need of providing biofidelic head and spine displacement targets that can guide future physical or computational pediatric models.

“The best instrument for measuring the tolerance of man to mechanical force is man”, states a line attributed to Col. Stapp. Thus, the ideal solution to the problem would be to measure the head and spine trajectories of a living child in a controlled crash environment at high speed. This is, of course, not possible. Computational modeling is an attractive alternative that allows to simulate a variety of impact environments and types of occupants. Unfortunately, the field is far from having a reliable computational model of a pediatric occupant, partially due to the lack of experimental data that can inform the modeling process. Despite of the lack of muscle activity, PMHS tests have been used extensively to improve the biofidelity of adult ATD and to produce injury criteria, and therefore contributing substantially to the continuous improvement of safety restraints performance. But again, pediatric PMHS data are scarce and the restraints and instrumentation used in the existing datasets are outdated. The last possible surrogates are animal models, but then the question of how to transfer the observations from the animal into a human being arises.

In response to the aforementioned limitations, this dissertation research combined several sources of data ranging from pediatric volunteers exposed to non-injurious tests to juvenile animals tested in realistic crash environments, to provide an estimation of the displacement of the head and thoracic spine of a restrained 6YO in a 40km/h frontal impact.

The two first aims proposed for this dissertation research have been achieved satisfactorily. Through the comparison of the normalized sagittal trajectories of the head and spine between pediatric and adult volunteers exposed to a 3.5 g deceleration frontal impact, this dissertation has shown that the scaling technique used in the development of the Hybrid III ATD family underpredicted the maximum forward excursion of the pediatric head by more than 40% of the actual displacement. Another commonly used scaling method (mass scaling) was found to produce a similar underestimation. Interestingly, these two scaling techniques were based on dimensional analysis and the scale factor used was derived as the ratio of some characteristic length of the subjects (in this case, seated height), since one of the assumptions of dimensional analysis is the dynamic similarity between the two systems. The observation of the poor results given by a pure geometrical scaling led the research towards considering other scaling methodologies that included the loading environment as well as the geometrical differences between the subjects in its formulation. This idea guided the research towards developing a scaling methodology based on conservation of energy, assuming that the kinetic energy of the occupant would be equal to the work done by the belt arresting the forward motion of the subject. A very simple model was then proposed in which only the belt force measured at the upper shoulder location was considered. The assessment of the method using the volunteer experiments at 9 km/h showed a substantial improvement, reducing the error in the prediction of the pediatric head peak forward displacement to less than 30%. However, none of these scaling techniques were able to capture the intrinsic differences observed between the trajectories of pediatric volunteers and adults in low speed frontal crashes. These differences were attributed to the developmental changes in the spine and in the whole body occurring during maturation. In effect, the morphological changes associated to human development invalidate the assumptions of geometric and dynamic similarity between pediatric and adult human subjects that are required so that dimensional analysis can be used (Arbogast et al., 2009; Kent et al., 2009a; Lopez-Valdes et al., 2011b).

Acknowledging the existing differences between children and adults led the research towards developing a model of the occupant that could recognize the existing differences in mass distribution, mechanical properties and loading environment between the two types of occupants. Thus, a multibody model tailored to the specific characteristics of each occupant type was developed.

The model never intended to describe without error the kinematics of the occupants, but to provide a simple tool that would allow approximating the kinematics of a 6YO in a high-speed frontal impact. The main simplification consisted of assuming that the motion of the occupant was circumscribed to the sagittal plane at least up to the time of head peak forward excursion, thus transforming the 3D motion of the occupant into a 2D problem. The second major simplification was to assume that the deflection of the spine could be described by a simplified lumped-mass model consisting on three rigid bodies connected by rotational joints. The selection of the number of joints and rigid bodies was dictated by the physical magnitudes measured in the experimental tests. After exploring different options, it was found that a linear, time-invariant model could describe the trajectories of the head and thoracic spine of the occupant with an error less than 20% both at 9 km/h and at 40 km/h, which was again a substantial improvement with respect to the previous model based on energy conservation. Last, this model was used to predict the kinematics of three pediatric volunteers at 40 km/h and their responses were normalized to the size of a mid-size 6YO, providing the average response and a corridor that included plus and minus one standard deviation in both the X and Z axes.

The process of developing such a model, including several intermediate assessments, required of the combination of experimental data from a variety of subjects that shared approximately the same loading environment. To the knowledge of the author, this is the first time that pediatric and adult volunteer tests are combined with adult PMHS tests at two different speeds to gain insight into the kinematics of the volunteers at higher speeds. The method required also testing a juvenile animal model to validate partially some of the assumptions.

Idealized springs with stiffness and damping were used to model the effective behavior of the joints connecting the model body segments. The values of stiffness and damping were obtained through optimization to minimize the X and Z distance between the head, T1 and T8 in the model and in the

experiments. To reduce the number of parameters to be solved for in the optimization, existing relationships between the stiffness of thoracic FSU were used. These relationships were either generated within this dissertation research or taken from existing literature.

All the available research previously done on the mechanical behavior of the human thoracic spine focused on its quasi-static behavior. This dissertation presented the first attempt of characterizing the bending behavior of two sections of the human thoracic spine under dynamic loading. A QLV model has been shown to describe appropriately the phenomenological relationship between the rotation applied and the angle generated observed in the test data. A comparison between the elastic responses across specimens has shown that there is an age effect in the elastic behavior of the analyzed FSU. There also exist differences in the instantaneous elastic responses of different FSU along the spine that correlated well with the quasi-static response reported in the literature, showing that the upper section of the thoracic spine was effectively more compliant than the middle one. The QLV model of the thoracic spine that has been developed within this dissertation is also novel in regards of reporting data on two pediatric specimens. In fact, the comparison between the instantaneous elastic responses of the two thoracic levels could be done only for the youngest subjects, since a good model fit could not be achieved due to the likely micro-failure of the tissue of the adult upper FSU during preconditioning. Thus, these experiments can also inform the design of the test matrix of future tests on the flexion behavior of the human thoracic spine.

In the absence of experimental data on the kinematics of pediatric occupants in high-speed crashes, modeling is the only alternative to approximate how children will move during the impact. Even if low-speed data are available as in this case, assumptions will have to be made to extrapolate the behavior observed at low speed to higher impact velocities. The methodology used in this dissertation, while not being able to provide a precise description of the kinematics of the subjects, proportionated a reasonable approximation that improved substantially the prediction given by any other method. Therefore, it is encouraged that the trajectories of the head and thoracic spine of future physical (ATD) or computational models are benchmarked against the corridors presented here. This is the immediate application of this dissertation.

Future efforts should focus on the development of models that incorporate a flexible spine with an improved description of joint parameters (including non-linearities) and including muscle activity. Since no pediatric PMHS sled test is envisioned in the near future, these models will have to be developed based on low-speed volunteer tests as the ones included here. While the robustness of the muscle model used cannot be assessed with experimental data at high speed, the appropriateness of the joint models can be evaluated using PMHS tests at different speeds as done within this dissertation.

The long term vision is the development of either physical or computational models of pediatric occupants that can predict accurately the kinematics of the head and several levels of the spine regardless of the speed of the impact. And that these models can be used to understand how the pediatric head moves under the action of different restraint systems and to prevent the high incidence of pediatric head injuries in the field. This dissertation attempted to pave the very first stages of this ambitious goal.

REFERENCES

- Adekoya, N., Thurman, D. J., White, D. D., Webb, K. W., 2002. Surveillance for traumatic brain injury deaths--United States, 1989-1998. *MMWR.Surveillance Summaries : Morbidity and Mortality Weekly Report.Surveillance Summaries / CDC* 51, 1-14.
- Alem, N. M., Bowman, B. M., Melvin, J. W., Benson, J. B., 1978. Whole-Body Human Surrogate Response to Three-Point Harness Restraint. Society of Automotive Engineers.
- Anderson, A. L., McIff, T. E., Asher M.A., Burton, D. C., Glattes, R. C., 2009. The effect of posterior thoracic spine anatomical structures on motion segment flexion stiffness. *Spine* 34, 441-446.
- Arbogast, K. B., Balasubramanian, S., Seacrist, T., Maltese, M. R., Garcia-Espana, J. F., Hopely, T., Constans, E., Lopez-Valdes, F. J., Kent, R. W., Tanji, H., Higuchi, K., 2009. Comparison of kinematic responses of the head and spine for children and adults in low-speed frontal sled tests. *Stapp Car Crash Journal* 53, 329-372.
- Arbogast, K. B., Cornejo, R. A., Kallan, M. J., Winston, F. K., Durbin, D. R., 2002. Injuries to children in forward facing child restraints. *Annual Proceedings of the Association for the Advancement of Automotive Medicine* 46, 213-230.
- Arbogast, K.B., Wozniak, S., Locey, C.M., Maltese, M.R., Zonfrillo, M.R. 2012. Head impact contact points for restrained child occupants. *Traffic Injury Prevention*, 13:2, 172-181.
- Ash, J., Sherwood, S., Abdelilah, Y., Crandall, J., Parent, D., Kallieris, D., 2009. Comparison of anthropomorphic test dummies with a pediatric cadaver restrained by a three-point belt in frontal sled tests. *Proc.21st Enhanced Safety of Vehicles (ESV) Conference*.
- Backaitis, S. H., Medlin, J. W., Radovich, V. G., Stalnaker, R. L., Shah, M. P., Shaffer, J. T., Letscher, R. M., 1975. Performance evaluation of child dummies and baboons in child restraint systems in a systematized crash environment. Society of Automotive Engineers.
- Backaitis, S. H., Mertz, H. J., 1994. Hybrid III: The First Human-Like Crash Test Dummy. Society of Automotive Engineers, Inc. ,
- Begeman, P. C., King, A. I., Prasad, P., 1973. Spinal Loads Resulting from -Gx Acceleration. Society of Automotive Engineers Paper No. 730977.
- Bohman, K., Arbogast, K.B., Bostrom, O., 2011. Head injury causation scenarios for belted rear-seated children in frontal impacts. *Traffic Injury Prevention*, 12: 62-70.
- Boot, A. M., de Ridder, M. A., Pols, H. A., Krenning, E. P., de Muinck Keizer-Schrama, S. M., 1997. Bone mineral density in children and adolescents: relation to puberty, calcium intake, and physical activity. *The Journal of Clinical Endocrinology and Metabolism* 82, 57-62.
- Brodeur, R. R., Reynolds, M., 1995. Modeling Spine Shape for the Seated Posture. ERL-TR-95-007.
- Brun-Casan, F., Page, M., Pincemaille, Y., Kallieris, D., Tarriere, C., 1993. Comparative study of restrained child dummies and cadavers in experimental crashes. Society of Automotive Engineers.

Caughey, T. K., O'Kelly, M. E. J., 1965. Classical Normal Modes in Damped Linear Dynamic Systems. *Journal of Applied Mechanics* 32, 583-588.

Center for Applied Biomechanics, 2006. Protocol for the Handling of Biological Material.

Ching, R. P., Nuckley, D. J., Hertsted, S. M., Eck, M. P., Mann, F. A., Sun, E. A., 2001. Tensile mechanics of the developing cervical spine. *Stapp Car Crash Journal* 45, 329-336.

Clarke, E. C., Appleyard, R. C., Bilston, L. E., 2007. Immature Sheep Spines Are More Flexible Than Mature Spines: An In Vitro Biomechanical Study. *Spine* 32, 2970-2979 10.1097/BRS.0b013e31815cde16.

Crandall, J.R., Bass, C.R., Pilkey, W.D., Miller, H.J., Sikorski, J., Wilkins, M., 1997. Thoracic response and injury with belt, driver side airbag and force limited belt restraint systems. *International Journal of Crashworthiness*, 2(1), 119-132.

Culver, C. C., Neathery, R. F., Mertz, H. J., 1994. Mechanical necks with humanlike responses. Society of Automotive Engineers, Warrendale, .

Dejeammes, M., Tarriere, C., Thomas, C., Kallieris, D., 1984. Exploration of biomechanical data towards a better evaluation of tolerance for children involved in automotive accidents. Society of Automotive Engineers.

Diamant, I., Shahar, R., Gefen, A., 2005. How to select the elastic modulus for cancellous bone in patient-specific continuum models of the spine. *Medical & Biological Engineering & Computing* 43, 465-472.

Duncan, J. M., 1874. Laboratory Note: On the Tensile Strength of the Fresh Adult Foetus. *British Medical Journal* 2, 763-764.

el-Khoury, G. Y., Whitten, C. G., 1993. Trauma to the upper thoracic spine: anatomy, biomechanics, and unique imaging features. *AJR American Journal of Roentgenology*. 160, 95-102.

Eppinger, R. H., Marcus, J. H., Morgan, R. M., 1984. Development of dummy and injury index for NHTSA's thoracic side impact protection research program. Society of Automotive Engineers.

Forman, J., Michaelson, J., Kent, R., Kuppa, S., Bostrom, O., 2008. Occupant restraint in the rear seat: ATD responses to standard and pre-tensioning, force-limiting belt restraints. *Annals of Advances in Automotive Medicine / Annual Scientific Conference ...Association for the Advancement of Automotive Medicine. Association for the Advancement of Automotive Medicine. Scientific Conference* 52, 141-154.

Foster, J. K., Kortge, J., Wolanin, M., 1977. Hybrid III - A biomechanically-based crash test dummy. *Proceedings of the 21st Stapp Car Crash Conference SAE paper No. 770938*.

Franklyn, M., Peiris, S., Huber, C., Yang, K., 2007. Pediatric material properties: a review of human child and animal surrogates. *Critical Reviews in Biomedical Engineering* 35, 197-342.

Fung, Y., 1993. *Biomechanics: Mechanical properties of living tissues*. Ed. Springer-Verlag.

Funk, J., Hall, G., Crandall, J., Pilkey, W., 2000. Linear and quasi-linear viscoelastic characterization of ankle ligaments. *J Biomech Eng* 122, 15-22.

Gennarelli, T. A., 1993. Mechanisms of brain injury. *The Journal of Emergency Medicine* 11 Suppl 1, 5-11.

- Goldstein, H., 1981. *Classical Mechanics*. Addison-Wesley Publishing Company, Inc, .
- Gordon, T.J. and Hopkins, R., 1997, Parametric identification of multibody models for crash victim simulation. *Multibody System Dynamics* 1, 85-112.
- Green, N. E., Swiontkowski, M. F., 1998. *Skeletal trauma in children- Vol III*. W.B. Saunders Company, Pennsylvania.
- Habib, M.S., 2001. Active control of vehicle occupant's motion in front- and rear-end collisions. In *Proceedings of the Automotive and Transportation Technology Congress and Exhibition*, 1-3 Oct, Barcelona, Spain. Paper No. 2001-01-3430 in *SAE Technical Papers*, 1-9.
- Hilker, C. E., Yoganandan, N., Pintar, F. A., 2002. Experimental determination of adult and pediatric neck scale factors. *Stapp Car Crash Journal* 46, 417-429.
- Huang, S.C., 1995. Biomechanic modeling and simulations of automobile crash victims. *Computers and structures* 57(3), 541-549.
- Hubbard, R. P., 1971. Flexure of Layered Cranial Bone. *Journal of Biomechanics* 13, 251-263.
- Iida, T., Abumi, K., Kotani, Y., Kaneda, K., 2002. Effects of aging and spinal degeneration on mechanical properties of lumbar supraspinous and interspinous ligaments. *The Spine Journal : Official Journal of the North American Spine Society* 2, 95-100.
- Irwin, A. L., Mertz, H. J., 1997. Biomechanical Basis for the CRABI and Hybrid III Child Dummies. *Proceedings of the 41st Stapp Car Crash Conference*, 1-12.
- Kalkwarf, H. J., Zemel, B. S., Gilsanz, V., Lappe, J. M., Horlick, M., Oberfield, S., Mahboubi, S., Fan, B., Frederick, M. M., Winer, K., Shepherd, J. A., 2007. The bone mineral density in childhood study: bone mineral content and density according to age, sex, and race. *The Journal of Clinical Endocrinology and Metabolism* 92, 2087-2099.
- Kallieris, D., Barz, J., Schmidt, G., Heess, G., Mattern, R., 1976. Comparison between child cadavers and child dummy by using child restraint systems in simulated collisions. *Proc.20th Stapp Car Crash Conference*, 511-542.
- Kallieris, D., Schmidt, G., Barz, J., Mattern, R., Schulz, F., 1978. Response and vulnerability of the human body at different impact velocities in simulated three-point belted cadaver tests. *Proceedings IRCOBI*,.
- Kent, R., Bass, C., Woods, W., Sherwood, C., Madeley, N., Salzar, R., Kitawaga, Y., 2003. Muscle tetanus and loading conditions effects on the elastic and viscous characteristics of the thorax. *Traffic Injury Prevention* 4, 297-314.
- Kent, R., Stacey, S., Kindig, M., Woods, W., Evans, J., Rouhana, S. W., Higuchi, K., Tanji, H., St Lawrence, S., Arbogast, K. B., 2008. Biomechanical response of the pediatric abdomen, Part 2: injuries and their correlation with engineering parameters. *Stapp Car Crash Journal* 52, 135-166.
- Kent, R., Stacey, S., Kindig, M., Woods, W., Evans, J., Rouhana, S. W., Higuchi, K., Tanji, H., St Lawrence, S., Arbogast, K. B., 2008. Biomechanical response of the pediatric abdomen, Part 2: injuries and their correlation with engineering parameters. *Stapp Car Crash Journal* 52, 135-166.
- Kent, R., Woods, W., Bass, C., Salzar, R., Damon, A., 2009. The transient relationship between pressure and volumen in the pediatric pulmonary system. *Journal of Biomechanics*.

- Kinzel, G. L., Hall Jr., A. S., Hillberry, B. M., 1972. Measurement of the total motion between two body segments—I. Analytical development. *Journal of Biomechanics* 5, 93-105.
- Klinich, K. D., Reed, M. P., Manary, M. A., Orton, N. R., 2010. Development and Testing of a More Realistic Pelvis for the Hybrid III 6-Year-Old ATD. *Traffic Injury Prevention* 11, 606-612.
- Kumaresan, S., Yoganandan, N., Pintar FA, 2001. Pediatric neck injury scale factors and tolerance. *Biomedical Sciences Instrumentation* 37, 435-440.
- Lau, S. H., Rafaels, K. A., Bass, C. R., Kent, R., 2008. An Assessment of Macropus Giganteus as a Biomechanical Model of the Pediatric Thorax. In *Proceedings of the 4th Injury Biomechanics Symposium at the Ohio State University*.
- Lessley, D., 2011. Medicion in-situ del movimiento del ocupante en colisiones de vehículos: análisis de la calidad de las mediciones e implicaciones en la predicción de lesiones. *Universidad de Navarra*.
- Lessley, D., Crandall, J., Shaw, G., Kent, R., 2004. A normalization technique for developing corridors from individual subject responses. *Society of Automotive Engineers*.
- Lessley, D., Shaw, G., Parent, D., Arregui-Dalmases, C., Kindig, M., Riley, P., Purtsezov, S., Sochor, M., Gochenour, T., Bolton, J., Subit, D., Crandall, J., Takayama, S., Ono, K., Kamiji, K., Yasuki, T., 2010. Whole-body response to pure lateral impact. *Stapp Car Crash Journal* 54, 289-336.
- Looker, A. C., Melton, L. J., 3rd, Harris, T., Borrud, L., Shepherd, J., McGowan, J., 2009. Age, gender, and race/ethnic differences in total body and subregional bone density. *Osteoporosis International : A Journal Established as Result of Cooperation between the European Foundation for Osteoporosis and the National Osteoporosis Foundation of the USA* 20, 1141-1149.
- Looker, A. C., Orwoll, E. S., Johnston, C. C., Jr, Lindsay, R. L., Wahner, H. W., Dunn, W. L., Calvo, M. S., Harris, T. B., Heyse, S. P., 1997. Prevalence of low femoral bone density in older U.S. adults from NHANES III. *Journal of Bone and Mineral Research : The Official Journal of the American Society for Bone and Mineral Research* 12, 1761-1768.
- Lopez-Valdes, F. J., Forman, J., Bostrom, O., Kent, R., 2010. The frontal-impact response of a booster-seated child-size PMHS. *Traffic Injury Prevention* 11, 320-327.
- Lopez-Valdes, F. J., Forman, J., Kent, R., Bostrom, O., Segui-Gomez, M., 2009. A comparison between a child-size PMHS and the Hybrid III 6 YO in a sled frontal impact. *Annual Proceedings / Association for the Advancement of Automotive Medicine. Association for the Advancement of Automotive Medicine* 53, 237-246.
- Lopez-Valdes, F. J., Lau, A., Lamp, J., Riley, P., Lessley, D. J., Damon, A., Kindig, M., Kent, R., Balasubramanian, S., Seacrist, T., Maltese, M. R., Arbogast, K. B., Higuchi, K., Tanji, H., 2010. Analysis of spinal motion and loads during frontal impacts. Comparison between PMHS and ATD. *Ann Adv Automot Med.* 54, 61-78.
- Lopez-Valdes, F. J., Seacrist, T., Balasubramanian, S., Maltese, M. R., Arbogast, K. B., Tanji, H., Higuchi, K., Kent, R., 2011. Comparing the kinematics of the head and spine between volunteers and PMHS: a methodology to estimate the kinematics of pediatric occupants in frontal impacts. In *Proceedings of the IRCOBI Conference. Krakow (Poland)*.

- Lopez-Valdes, F.J., Seacrist, T., Balasubramanian, S., Maltese, M. R., Arbogast, K. B., Tanji, H., Higuchi, K., Kent, R., 2012. A methodology to estimate the kinematics of pediatric occupants in frontal impacts. *Traffic Injury Prevention* 13(5), 393-401.
- Lopez-Valdes, F., Michaelson, J., Frampton, R., Kent, R., Segui-Gomez, M., 2008. Evaluating the appropriateness of the injury scaling method for pediatric motor vehicle injuries. In *Proceedings of the Conference of the Association for the Advancement of Automotive Medicine*.
- Lopez-Valdes FJ, Riley P, Lessley DJ, Arbogast K, Seacrist T, Balasubramanian S, Maltese M, Kent R. The six degree-of-freedom motion of the human head, spine and pelvis in a frontal impact. 2013. *Traffic Injury Prevention*. *Under review*.
- Lucas, S. R., Bass, C. R., Crandall, J. R., Kent, R. W., Shen, F. H., Salzar, R. S., 2009. Viscoelastic and failure properties of spine ligament collagen fascicles. *Biomechanics and Modeling in Mechanobiology*.
- Luck, J. F., Nightingale, R. W., Loyd, A. M., Prange, M. T., Dibb, A. T., Song, Y., Fronheiser, L., Myers, B. S., 2008. Tensile mechanical properties of the perinatal and pediatric PMHS osteoligamentous cervical spine. *Stapp Car Crash Journal* 52, 107-134.
- Malina, R. M., Hamill, P. V., Johnson, F. E., Lemeshow, S., 1973. Selected body measurements of children 6-11 years, United States.
- Markolf, K. L., 1972. Deformation of the thoracolumbar intervertebral joints in response to external loads: a biomechanical study using autopsy material. *The Journal of Bone and Joint Surgery.American* Volume 54, 511-533.
- Mathews, E. A., Balasubramanian, S., Seacrist, T., Maltese, M. R., Sterner, R., Arbogast, K. A., 2012. Electromyography responses of pediatric and young adult volunteers in low-speed frontal impacts. *Journal of Electromyography and Kinesiology*. *Under review*.
- Matlab. Global Optimization Toolbox. User's Guide. R2012b. Available at www.mathworks.com
- Mattern, R., Kallieris, D., Riedl, H., von Wiren, B., 2002. Reanalysis of two child PMHS-tests. Final Report.
- McGowan, J., Voo, L., Liu, Y., 1993. Distraction failure of immature spine. In *ASME Ad Bioeng. Colorado*.
- McHenry, R.R. 1963. Analysis of the dynamics of automobile passenger-restraint systems. 7th Stapp Car Crash conference.
- McPherson, G. K., Kriewall, T. J., 1979. The elastic modulus of fetal cranial bone: a first step towards an understanding of the biomechanics of fetal head molding. *J Biomech* 13, 9-16.
- Mertz H.J., Patrick, L. M., 1971. Strength and response of the human neck. *Proceedings of the 15th Stapp Car Cash Conference SAE paper No. 710855*, 207-255.
- Mertz, H. J., Irwin, A. L., Melvin, J. W., Stanaker, R. L., Beebe, M. S., 1989. Size, Weight and Biomechanical Impact Response Requirements for Adult Size Small Female and Large Male Dummies. *Society of Automotive Engineers, Inc*.
- Mertz, H. J., Jarrett, K., Moss, S., Salloum, M., Zhao, Y., 2001. The Hybrid III 10-Year-Old Dummy. *Stapp Car Crash Journal* 45, 319-328.

- Mertz, H. J., Prasad, P., Irwin, A. L., 2003. Biomechanical and scaling bases for frontal and side impact injury assessment reference values. *Stapp Car Crash Journal* 47, 155.
- Moore, K.L. and Dalley, A. F. *Clinically Oriented Anatomy*. 2005. 5th edition. Lippincott Williams and Wilkins.
- Nahum, A. M., Melvin, J. W., 2002. *Accidental Injury. Biomechanics and Prevention*. Springer.
- NASA, 1996. *Man-Systems integration standards*.
- Nuckley, D. J., Ching, R. P., 2006. Developmental biomechanics of the cervical spine: Tension and compression. *Journal of Biomechanics* 39, 3045-3054.
- Ouyang, J., Zhu, Q., Zhao, W., Xu, Y., Chen, W., Zhong, S., 2005. Biomechanical assessment of the pediatric cervical spine under bending and tensile loading. *Spine* 30, E716-23.
- Oxland, T. R., Lin, R. M., Panjabi, M. M., 1992. Three-dimensional mechanical properties of the thoracolumbar junction. *Journal of Orthopaedic Research : Official Publication of the Orthopaedic Research Society* 10, 573-580.
- Panjabi, M. M., Brand R.A., White A.A., 1976. Three-dimensional flexibility and stiffness properties of the human thoracic spine. *Journal of Biomechanics* 9, 185-192.
- Paulitz, T.J., Blacketter, D.M., Rink, K.K., 2006. Constant force restraints for frontal collisions. *Proceedings of the Institution of Mechanical Engineers, Part D: Journal of Automobile Engineering*, 220(9): 1177-1189.
- Peden, M., Oyegbite, K., Ozanne-Smith, J., Hyder, A., Branche, C., Rahman, F., Rivara, F., Bartolomeos, K., 2008.
World report on child injury prevention.
- Pintar, F. A., Mayer, R. G., Yoganandan, N., Sun, E., 2000. Child neck strength characteristics using an animal model. *Stapp Car Crash Journal* 44, 77-83.
- Reed, M. P., Ebert-Hamilton, S. M., Manary, M. A., Klinich, K. D., Schneider, L. W., 2006. Improved positioning procedures for 6YO and 10YO ATDs based on child occupant postures. *Stapp Car Crash Journal* 50, 337-388.
- Reed, M. P., Sochor, M. M., Rupp, J. D., Klinich, K. D., Manary, M. A., 2009. Anthropometric specification of child crash dummy pelves through statistical analysis of skeletal geometry. *Journal of Biomechanics* 42, 1143-1145.
- Salzar, R. S., Bass, C. R., Lessley, D., Crandall, J. R., Kent, R. W., Bolton, J. R., 2009. Viscoelastic response of the thorax under dynamic belt loading. *Traffic Injury Prevention* 10, 290-296.
- Seacrist, T., Balasubramanian, S., Garcia-Espana, J. F., Maltese, M. R., Arbogast, K. B., Lopez-Valdes, F. J., Kent, R. W., Tanji, H., Higuchi, K., 2010. Kinematic Comparison of Pediatric Human Volunteers and the Hybrid III 6-Year-Old Anthropomorphic Test Device. *Annals of Advances in Automotive Medicine / Annual Scientific Conference ...Association for the Advancement of Automotive Medicine. Association for the Advancement of Automotive Medicine. Scientific Conference* 54, 97-108.
- Seeman, M. R., Muzzy, W. H., Lustik, L. S., 1986. Comparison of Human and Hybrid III Head and Neck Dynamic Response. *Proceedings of the 30th Stapp Car Crash Conference SAE paper No. 86192*.

- Sethi, D., Towner, J., Vincent, J., Segui-Gomez, M., Racioppi, F., 2008. European report on child injury prevention.
- Shaw, G., Crandall, J., Butcher, J., 2000. Biofidelity Evaluation of the Thor Advanced Frontal Crash Test Dummy. In IRCOBI Conference on the Biomechanics of Impact.
- Shaw, G., Kent, R., Sieveka, E., Crandall, J., 2001. Spinal kinematics of restrained occupants in frontal impacts. In IRCOBI Conference on the Biomechanics of Impact, Isle of Man.
- Shaw, G., Parent, D., Purtsezov, S., Lessley, D., Crandall, J., Kent, R., Guillemot, H., Ridella, S. A., Takhounts, R., Martin, P., 2009. Impact Response of Restrained PMHS in Frontal Sled Tests: Skeletal Deformation Patterns Under Seat Belt Loading. *Stapp Car Crash Journal* 53, 1-48.
- Sherwood, C. P., Shaw, C. G., Van Rooij, L., Kent, R. W., Crandall, J. R., Orzechowski, K. M., Eichelberger, M. R., Kallieris, D., 2003. Prediction of Cervical Spine Injury Risk for the 6-Year-Old Child in Frontal Crashes. *Traffic Injury Prevention* 4, 206-213.
- Sran, M. M., Khan, K. M., Zhu, Q., Oxland, T. R., 2005. Posteroanterior stiffness predicts sagittal plane midthoracic range of motion and three-dimensional flexibility in cadaveric spine segments. *Clinical Biomechanics (Bristol, Avon)* 20, 806-812.
- Thompson, M. D., Irby, J. W., Jr, 2003. Recovery from mild head injury in pediatric populations. *Seminars in Pediatric Neurology* 10, 130-139.
- Wachowski, M. M., Mansour, M., Lee, C., Ackenhausen, A., Spiering, S., Fanghanel, J., Dumont, C., Kubein-Meesenburg, D., Nagerl, H., 2009. How do spinal segments move? *Journal of Biomechanics* 42, 2286-2293.
- Wang, M. C., Pintar, F., Yoganandan, N., Maiman, D. J., Wang, M. C., Pintar, F., Yoganandan, N., Maiman, D. J., 2009. The continued burden of spine fractures after motor vehicle crashes.[see comment]. *Journal of Neurosurgery Spine* 10, 86-92.
- Warming, L., Hassager, C., Christiansen, C., 2002. Changes in bone mineral density with age in men and women: a longitudinal study. *Osteoporosis International : A Journal Established as Result of Cooperation between the European Foundation for Osteoporosis and the National Osteoporosis Foundation of the USA* 13, 105-112.
- Willems, J. M., Jull, G. A., Ng, J. K., 1996. An in vivo study of the primary and coupled rotations of the thoracic spine. *Clinical Biomechanics* 11, 11-316.
- Wismans, J., Maltha, J., Melvin, J., Stalnaker, R., 1979. Child restraint evaluation by experimental and mathematical simulation. *Society of Automotive Engineers*.
- Wismans, J., Phillipens, M., van Oorschot E., Kallieris, D., Mattern, R. 1987. Comparison of human volunteer and cadaver head-neck response in frontal flexion. *Society of Automotive Engineers*. Paper no. 872194.
- Yoganandan, N., Sances, A. J., Pintar, F., 1989. Biomechanical Evaluation of the Human Cadaveric and Manikin Necks. *Journal of Biomedical Engineering* 111, 250-255.

A1-APPENDIX: CALCULATION OF BENDING MOMENT AND SHEAR FORCE AT THE ENDS OF THE FSU

This appendix details the methodology followed to fit a QLV model to the bending response observed in the FSU experiments. It also shows the results of the fit for the different specimens and discusses the difficulties found in modeling the mechanical response of two of the tested specimens.

A1.1 METHODOLOGY

As introduced in Chapter 5, the fixture used in the FSU experiments was designed to apply a controlled rotation to the distal and proximal ends of the specimens and measure the moments subsequently generated at both locations. The test fixture transformed the longitudinal translation of the piston of the axial machine into a rotation of the cups attached to the two ends of the specimens. Therefore, both the range of the applied angles as well as the angular rate depended on the size of the specimen.

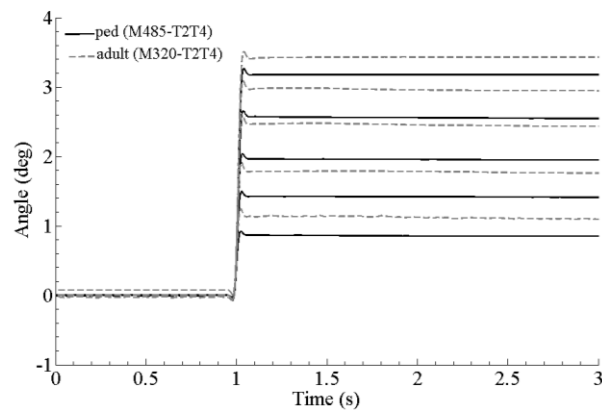


Figure A1.1 Angle vs. Time response comparison between one pediatric and one adult specimen showing the similar angular rate applied.

Given the rate-dependent nature of most biological tissues, it was important to assure that the angular rate among specimens was similar. Figure A1.1 compares the responses of one pediatric and one adult

specimen, showing almost no differences between the applied angular rates. Figure A1.2 and Figure A1.3 show the results obtained during the preconditioning of one pediatric and one adult FSU.

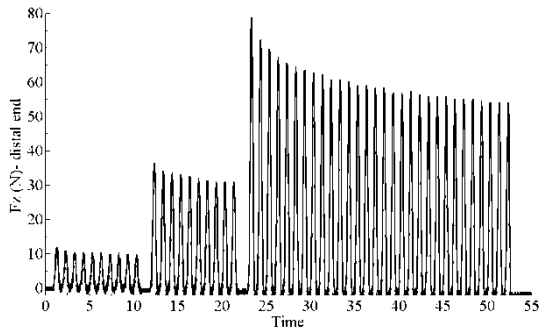


Figure A1.2 Preconditioning of pediatric specimen (F470 T7-T9).

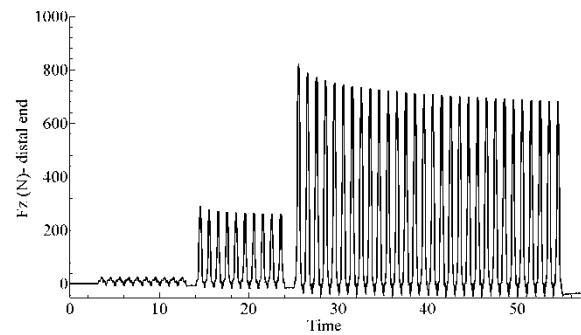


Figure A1.3 Preconditioning of adult specimen (M320 T7-T9).

The asymmetry of the specimens caused the moments at the two ends to be different, and therefore there was a variation of the moment along the length of the specimen. Given that the flexion moment of the distal and proximal vertebrae of each FSU was different, the bending behavior of each of the joints (between the distal and the central vertebra, and between the central and the proximal vertebra) was analyzed separately. The value of the bending moment at the joint was approximated as the average value of the moments calculated at the center of the vertebral body of each vertebra. The angle rotated by the joint was obtained subtracting the rotation of the two vertebrae. After this process, a relationship between the moment applied at the joint and the observed rotated angle was calculated.

Since a quasilinear viscoelastic model (QLV) had been applied successfully to describe the transient non-linear behavior of biological tissues (Fung, 1993) as well as of structures as a whole (Funk et al., 2000; Kent et al., 2003; Kent et al., 2009b; Lucas et al., 2009; Salzar et al., 2009), a QLV formulation was applied to characterize the dynamic behavior of these joints. As already mentioned in Chapter 5, the QLV model relating the angle rotated by the specimen (α) and the moment generated ($M[t]$) was derived according to Equation A1.1:

$$M[t] = \int_{-\infty}^t G[t - \tau] (\partial M_e[\alpha] / \partial \alpha) (\partial \alpha[\tau] / \partial \tau) d\tau \quad \text{Equation A1.1}$$

The expressions of the reduced relaxation function ($G[t]$) and of the instantaneous elastic response ($M_e[\alpha]$) were presented within Chapter 5. A numerical convolution scheme can be used to solve for the different parameters (A, B, G_i, β_i) that model the response of the FSU. The convolution can be developed by discretizing the time step and stepping forward in time to determine the steady state of the moment at each time step (M_∞):

$$M_\infty[t + dt] = M_\infty[t] + G_\infty(M_e[t + dt] - M_e[t]) \quad \text{Equation A1.2}$$

and the transient component of the moment at each time step (M_i):

$$M_i[t + dt] = \psi_i M_i[t] + (1 - \psi_i) \left(\frac{G_i}{\beta_i} \right) \left(\frac{M_e[t + dt] - M_e[t]}{dt} \right) \quad \text{Equation A1.3}$$

where:

$$\psi_i = e^{-\beta_i dt} \quad \text{Equation A1.4}$$

The total change in moment at each time point is then the sum of the two terms, as shown in Equation A1.5:

$$M[t] = M_\infty[t] + \sum_{i=1}^3 M_i[t] \quad \text{Equation A1.5}$$

The parameters of the model were optimized simultaneously in all the three dynamic ramp-and-hold tests with greater magnitude (D3, D4 and D5) to minimize the sum of square errors between the model-predicted moment and the measured one at each time step. Early values were given higher weight in the optimization so that the model would capture the initial peak shown in the experiments.

The following steps detail the process of obtaining all the relevant magnitudes involved in calculating the model parameters used in the QLV model fit:

- 1) Calculate the bending moment (M_S) and the shear force (V_S) at the distal and proximal ends of each FSU, for each dynamic tests.

The free body diagram of the fixture is shown in Figure A1.4

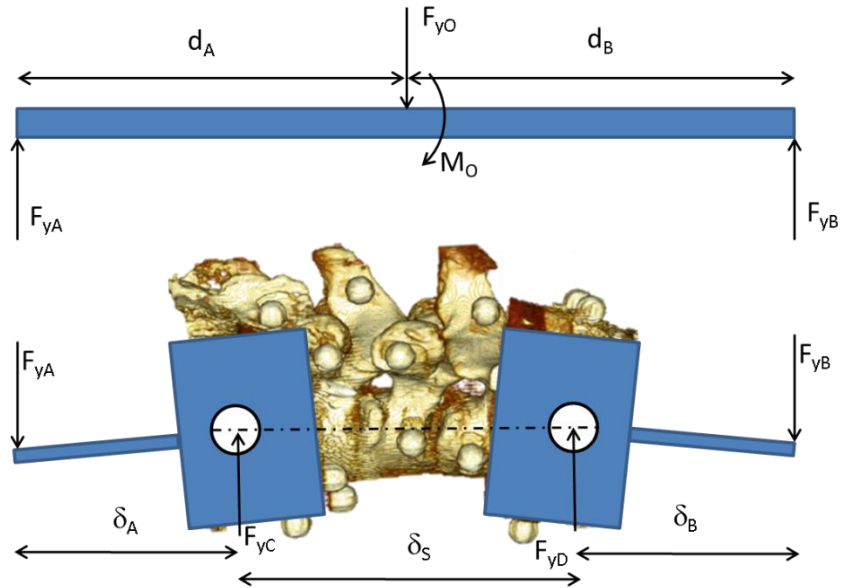


Figure A1.4 Free body diagram of the fixture with the specimen.

All the distances in Figure A1.4 were measured by the VICON system. The reactions F_{yA} and F_{yB} are the only forces that contribute to the moment generated at the pin joints C and D in the diagram above. The moment arms (δ_A and δ_B) were also measured during the tests. There is negligible horizontal force in the fixture due to the use of linear bearings connecting the fixture to the Instron crosshead and to the Instron table. F_{yC} and F_{yD} were measured directly by the two load cells. Therefore, the calculation to know the moment generated into the specimen relied only on obtaining the expression of F_{yA} and F_{yB} in terms of the known forces and distances. In the quasi-static case, these relationships can be easily obtained from the static equilibrium:

$$F_{yA} + F_{yB} = F_{yC} + F_{yD}$$

$$F_{yA} = \frac{F_{yD}\delta_B + F_{yC}(\delta_B + \delta_S)}{\delta_B + \delta_S + \delta_A}$$
Equation A1.6

However, the results presented in this manuscript correspond to dynamic tests and therefore Equation A1.6 might not be valid in this case. The following analysis shows that the contribution of the inertia to the calculation of the forces is so small that the equations derived for the quasi-static conditions can still be

used in the dynamic case. Figure A1.5 shows the free body diagram corresponding to one of the rotating cups, considering the reactions of the specimen on the cup.

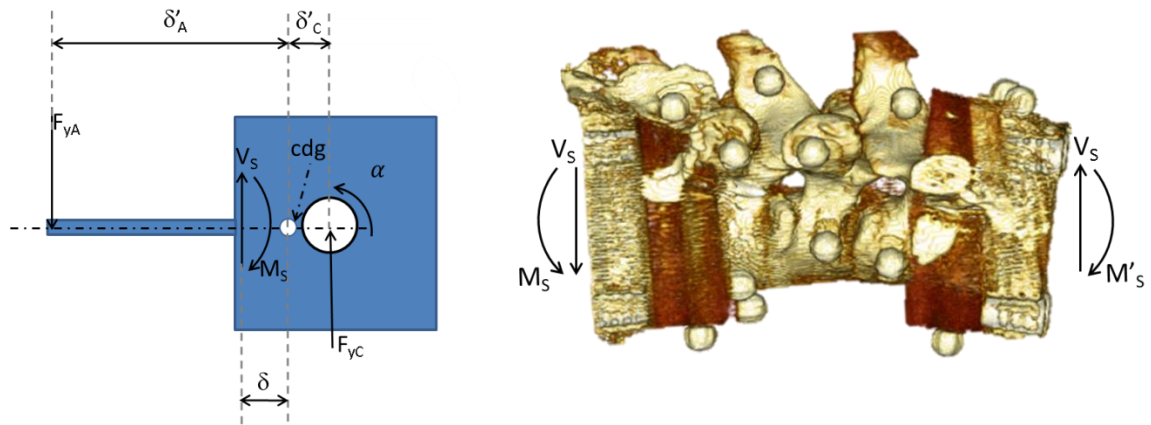


Figure A1.5 Free body diagram of the fixture with the specimen.

In the dynamic case, the equations of motion are given by Equation AA1.2, where V_s and M_s are the shear and moment reactions of the specimen on the cup:

$$\begin{aligned} F_{yA} - F_{yC} - V_s &= m\ddot{y}_{cdg} \\ -F_{yA}\delta'_A + V_s\delta + M_s - F_{yC}\delta'_C &= I_{cdg}\alpha \end{aligned} \quad \text{Equation A1.7}$$

The total mass of the cup and the lever is 0.114 kg and a representative value of the vertical acceleration of the center of gravity of the assembly is about 0.00525 m/s^2 (the distance between the pivot C and the center of gravity of the assembly is 3 mm). The magnitude of the inertial contribution to the force equation is several orders of magnitude smaller than the resolution of the load cell and can be neglected. A similar reasoning can be applied to the inertial term in the moments equation ($I_{cdg}=1.32\text{e-}4 \text{ kgm}^2$; $\alpha=67.7 \text{ rad/s}^2$) and again the inertia contribution to the moments equation is several orders of magnitude smaller than the contribution of the other moments. Thus, the inertial term can be neglected in both equations A1.7 and the expressions to calculate F_{yA} and F_{yB} given in Equation A1.6 are valid. These expressions allow calculating the moment generated in the specimen by the rotation of the cups.

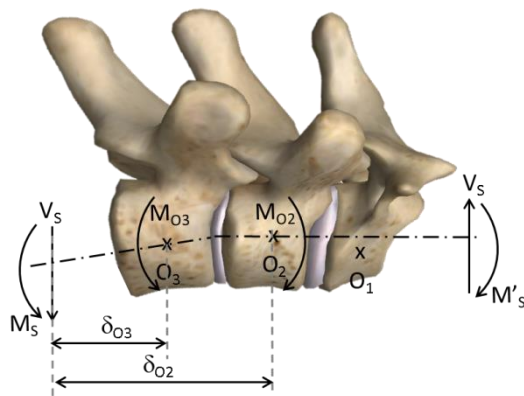
The asymmetrical nature of the specimen caused that specimens were subjected also to shear loads. However, Equations A1.7 can also help to estimate the magnitude of the shear applied to the specimen as

the difference between F_{yA} and F_{yC} , and the subsequent bending moment at each of the ends of the specimen:

$$V_s = F_{yA} - F_{yC} \quad \text{Equation A1.8}$$

$$M_s = F_{yA} \delta'_A - V_s \delta_s + F_{yC} \delta'_C$$

- 2) Calculate the bending moment at the center of each vertebra (M_{O_i}) using the distances measured by the Vicon system.



$$M_{O_3} = M_s + V_s \delta_{O_3}$$

Equation A1.9

$$M_{O_2} = M_s + V_s \delta_{O_2}$$

Figure A1.6 Schematic showing the bending moments M_{O_i} at the center of the vertebrae and the parameters involved in the calculations.

- 3) Average the bending moments calculated at the center of contiguous vertebrae to estimate the moment acting on the joint connecting the vertebrae.

$$M_{32} = \frac{1}{2} (M_{O_3} + M_{O_2}) \quad \text{Equation A1.10}$$

- 4) Calculate the relative rotation between contiguous vertebrae in the sagittal plane. After this step, there will be two values of the average moment and the relative angle per FSU, corresponding to the superior and inferior aspect of the specimen.
- 5) Input each of the previously obtained average moments (M_{32}) and relative angle pair into the deconvolution MATLAB script.

6) Obtain the value of the QLV model parameters that minimize the square standard error between the modeled moment and the average one (M_{32}). Only the tests with amplitudes D3, D4 and D5 were used in the calculation of the model. The optimization of the parameters was done using a genetic algorithm method and the results for the five different amplitudes were considered in a single optimization process. Thus, the obtained parameters are the ones that minimize the error between the predicted and the calculated moment. Before using this optimization method, it was found that the solutions provided by other solvers implemented in the package MATLAB were extremely dependent on the initial guess value for the solution and frequently the solution provided was a local minimum instead of a global one. The constraints used in the optimization were:

- a) All the parameters should be positive.
- b) $\sum_{i=1}^3 G_i < 1$
- c) The parameter values were contained within the intervals shown in Table A1.1:

Table A1.1 Bounds used in the optimization.

	Lower bound	Upper bound
β_1 (s)	0.0001	10
β_2 (s)	0.001	100
β_3 (s)	0.01	1000
G_1	0.000001	1
G_2	0.000001	1
G_3	0.000001	1
A	1	10000
B	0.0001	1

As mentioned in Chapter 5, the MATLAB genetic algorithm optimization was chosen to solve the unknown parameters of the model. The size of the population varied between 300 and 500 initial guesses depending on the specimens and the model was run up to 150 generations. In occasions, a local solver was used to refine the results (MATLAB *fmincon* solver). The tolerance for the evaluation of the objective function (error between calculated moment and estimated moment) was set to 1×10^{-10} .

A1.2 QLV MODEL RESULTS OF SPECIMENS

Although the table showing the values found for the parameters of the QLV model of the thoracic spine had been already shown in Chapter 5, they are again included here to provide context to the following paragraphs. Thus, Table A1.2 shows the estimated values of the coefficients that model the bending behavior of the different spine segments tested according to Equation A1.1.

Each of the subsections within section A1.2 examines the appropriateness of the model fit to the observed experimental results. As mentioned in Chapter 5, the experimental data from specimens M319-T2T4 and M320-T2T4 could not be satisfactorily fitted using a QLV formulation and the difficulties found in this process are also discussed within the corresponding subsections.

Table A1.2 Coefficient values of the QLV model of the human thoracic spine.

	β_1 (s)	β_2 (s)	β_3 (s)	G_1	G_2	G_3	A	B
F470-T2T4	0.0040	0.4107	26.0834	0.4057	0.2301	0.2607	2.9642	0.0428
F470-T7T9	0.0207	0.4275	46.1016	0.0625	0.2923	0.4054	1.1268	0.1398
M485-T2T4	0.7775	8.3484	198.5571	0.3350	0.0348	0.5988	10.8506	0.0826
M485-T7T9	0.3065	7.3973	205.5157	0.28203	0.0364	0.6310	17.9538	0.0690
M319-T2T4	NA	NA	NA	NA	NA	NA	NA	NA
M319-T7T9	3.0628	30.6941	999.3886	0.0752	0.0047	0.9081	3.0801	0.2968
M320-T2T4	NA	NA	NA	NA	NA	NA	NA	NA
M320-T7T9	3.3323	67.4706	894.5264	0.1268	0.0011	0.8583	10.3790	0.3474

A1.2.1 Specimen F470

The comparison between the predicted and observed moment in the different tests conducted on specimen F470 is shown in Figure A1.7 (for the upper thoracic section) and in Figure A1.8 (for the middle section). As it can be seen from the previous plots, the modeled moment described with precision the moment time history observed in the tests at all amplitudes. The slope of the initial ramp, the estimation of peak moment and the relaxation behavior of the specimens were predicted accurately by the QLV model proposed in this dissertation.

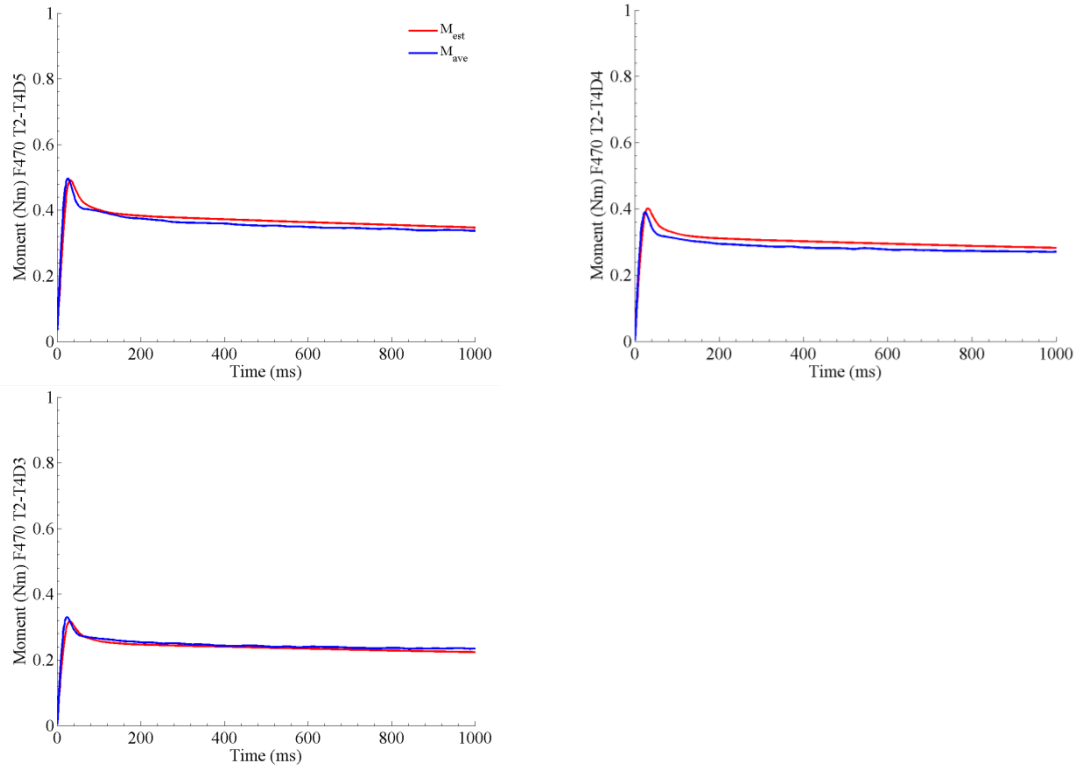


Figure A1.7 Comparison between the moment predicted (M_{est} , red) and the calculated average moment (M_{ave} , blue) of the upper thoracic section of pediatric specimen F470.

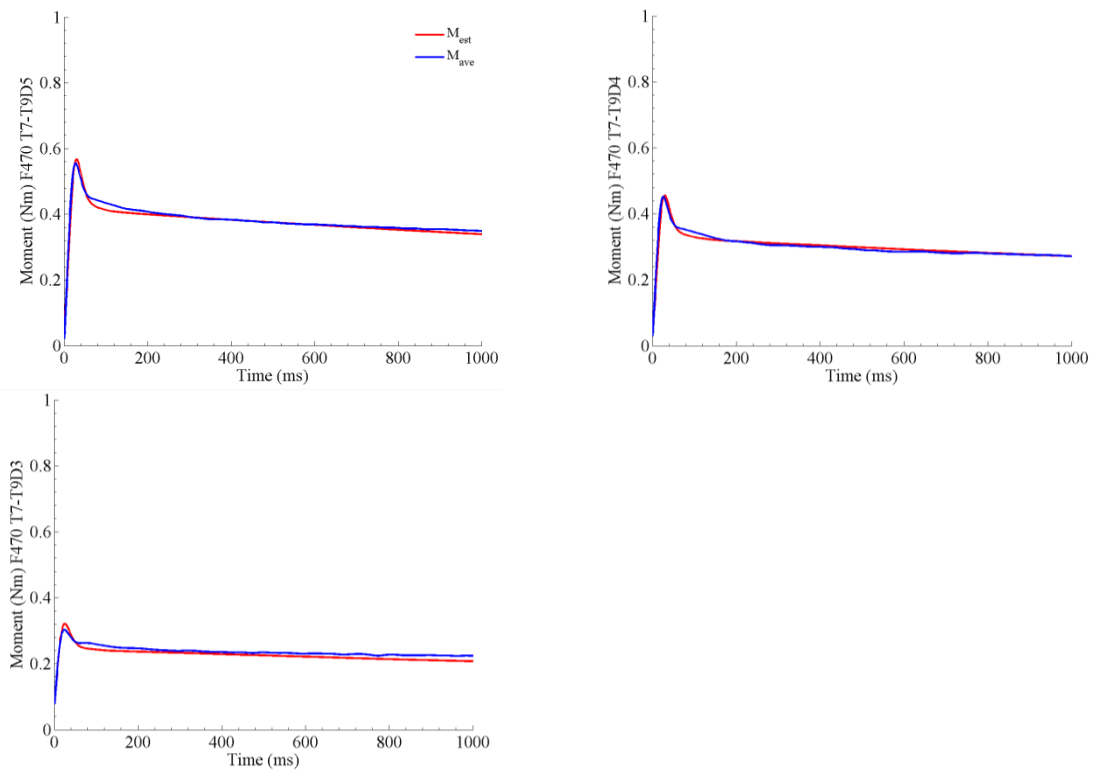


Figure A1.8 Comparison between the moment predicted (M_{est} , red) and the calculated average moment (M_{ave} , blue) of the middle thoracic section of pediatric specimen F470.

A1.2.2 Specimen M485

Figure A1.9 and Figure A1.10 show the results obtained in the model fit of the upper and middle sections of specimen M485.

In the case of the T2-T4 section, the model underpredicted the peak moment in the D5 amplitude test (3.69 Nm vs. 4.07 Nm) and in the D2 test (1.56 Nm vs. 1.79 Nm). The estimation of the peak moment was fairly accurate for the tests performed at the other two amplitudes. Despite these differences in peak prediction, the initial slope of the moment response of the specimen was conveniently described by the model. As for the relaxation part of the curve, the model response was parallel to that exhibited by the specimen.

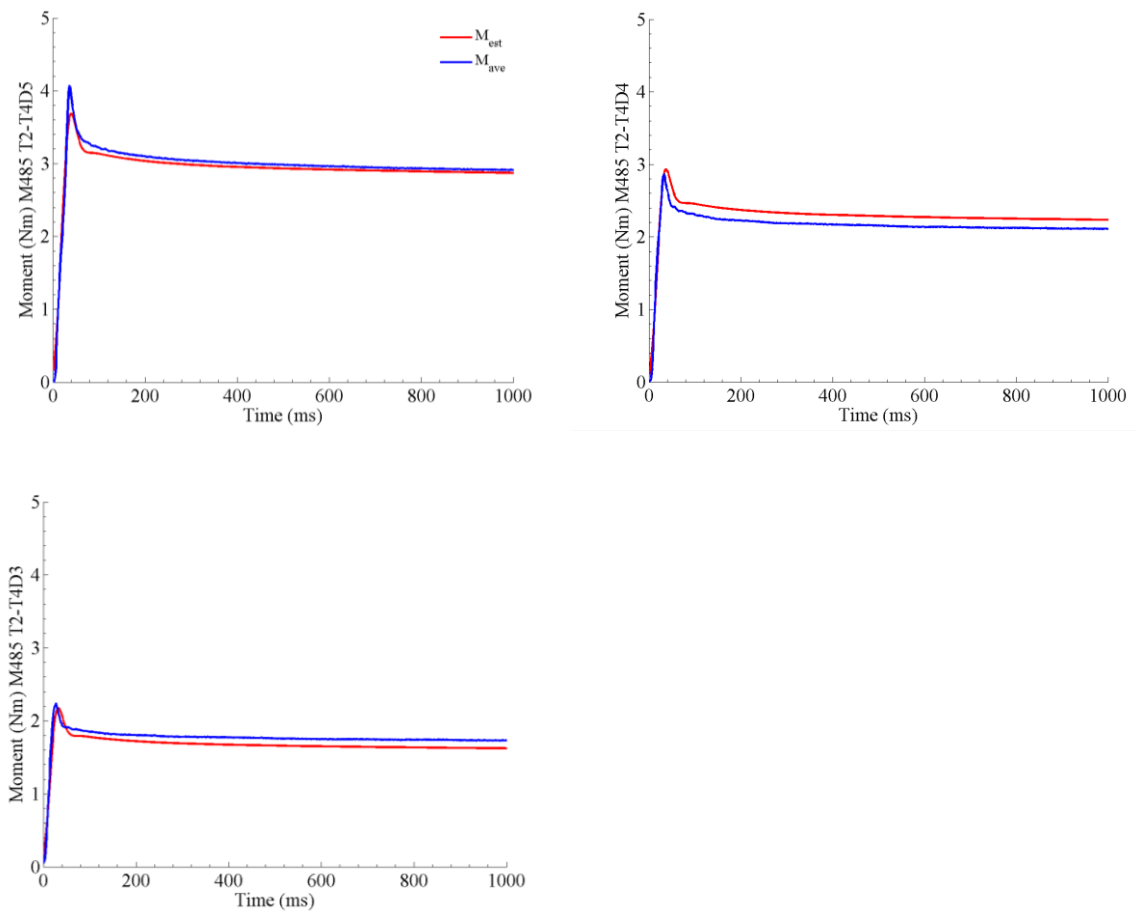


Figure A1.9 Comparison between the moment predicted (M_{est} , red) and the calculated average moment (M_{ave} , blue) of the upper thoracic section of pediatric specimen M485.

Similar results were observed for the middle thoracic section, with the model slightly underpredicting the peak moment at D5 (4.67 Nm vs. 5.05 Nm) and providing an accurate estimation of the peak value at D3 and D4. The model exhibited a slightly faster initial decay to evolve into a relaxation behavior matching the one observed during the experiments. As shown also at the upper section, the initial ramp slope was precisely captured by the model parameters.

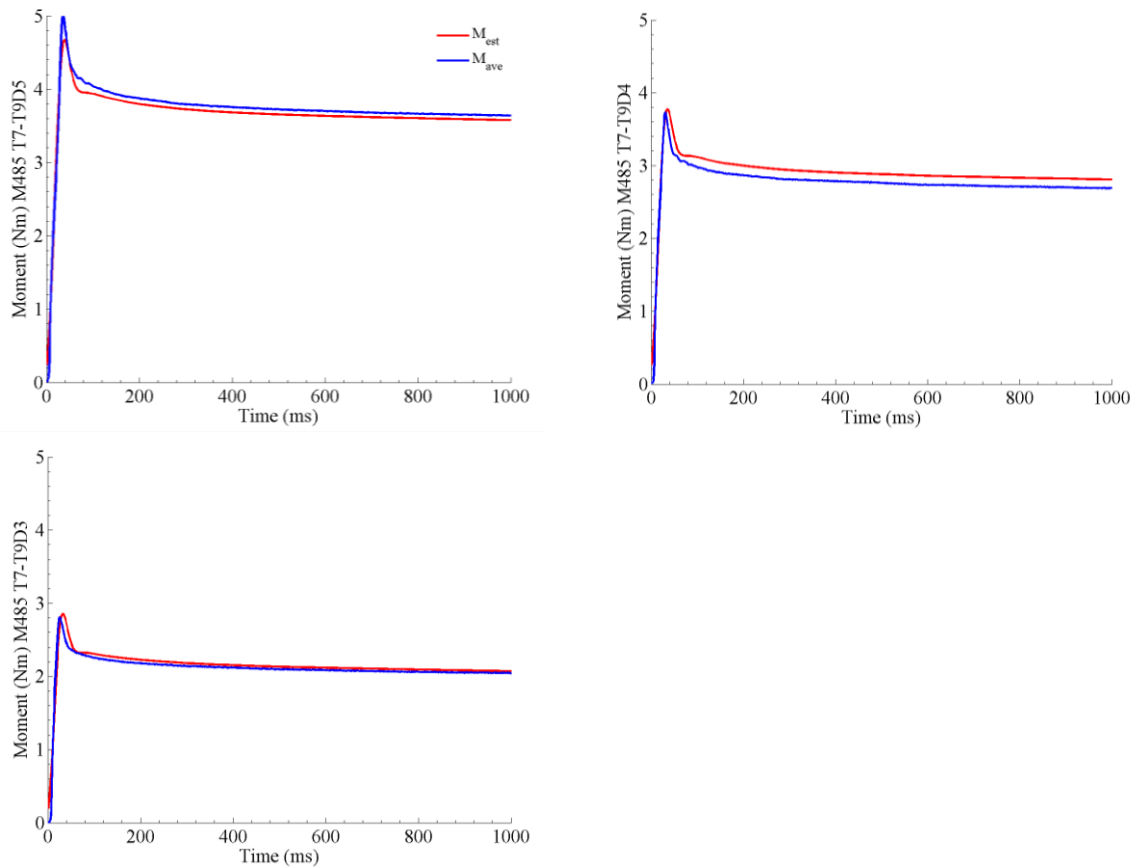


Figure A1.10 Comparison between the moment predicted (M_{est} , red) and the calculated average moment (M_{ave} , blue) of the middle thoracic section of pediatric specimen M485.

A1.2.3 Specimen M319

The fit of the model to specimen M319-T2T4 presented unexpected difficulties. A variety of methods were tried trying to obtain a good fit of the data, but it was observed that none of the results were able to describe the initial ramp and peak moment of several tests at the same time. Despite of reducing the tolerance or increasing the number of generations and the size of the population in the genetic algorithm optimization

scheme, no improvement was observed in the solution. A detailed analysis indicated that the form proposed for the instantaneous elastic response was not appropriate to describe the elastic behavior of the data. In particular, the data indicated that instead of an exponential function, the experiments suggested a logarithmic curve to describe the elastic behavior of the specimen. This kind of curve is not common in the description of the instantaneous elastic response of biological tissues and could suggest microscopic failure of the tissue. A closer look at the moment time history of the specimen showed that there was a drop in the moment value in all the tests with this specimen regardless of the amplitude as shown in Figure A1.11 at around $t=10$ ms.

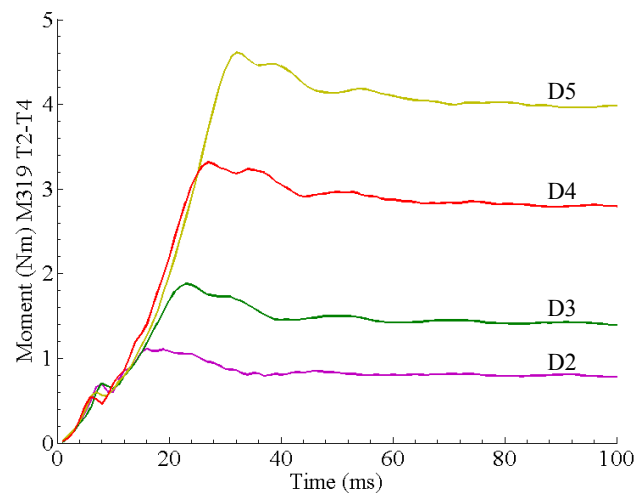


Figure A1.11 Time-history plot of the calculated average moment (M_{ave}) of the upper thoracic section of adult specimen M319.

Although the hypothesis of the failure of fibers of the tissue was not further explored since it was out of the scope of the dissertation, the reader is reminded that these experiments were the first dynamic bending experiments performed on human subjects. Therefore, the values for the non-failure experiment amplitudes were estimated using data published from quasi-static studies. There was also a trade-off between choosing amplitudes that could be measured by the VICON system and avoiding the damage of the tissue (Lopez-Valdes et al., 2011a). Since the preconditioning of the tissue was done before the ramp and hold tests, it is possible that the tissue was damaged during the preconditioning and therefore that microscopic damage would be manifested even in the smaller amplitude tests as shown in Figure A1.11. Another potential explanation for the responses shown in Figure A1.12 could be an experimental artifact that manifested only

with this specimen (a defective potting of the specimen in the cups, for instance), although no differences were noticed between this specimen and the others during the tests. As a result of these problems, the experimental values from M319-T2T4 were discarded and not considered further in this dissertation.

The model of specimen M319-T7T9 described adequately the observed experimental results. Figure A1.12 shows the comparison between the moment predicted (M_{est}) and the average calculated moment (M_{ave}) for the middle sections of specimen M319.

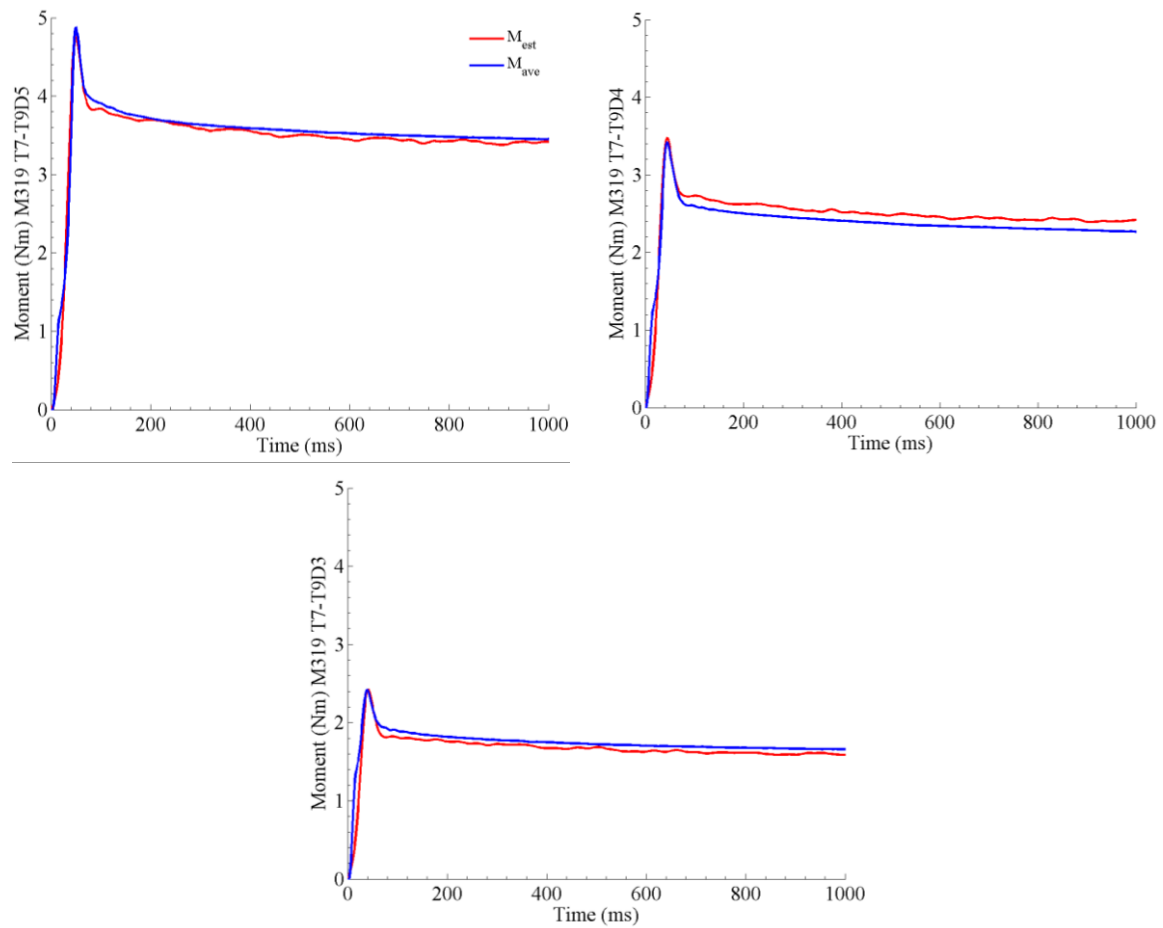


Figure A1.12 Comparison between the moment predicted by the QLV model and the calculated average moment (M_{ave}) of the middle thoracic section of adult specimen M319.

A1.2.4 Specimen M320

As for specimen M320, no QLV model was fitted to the upper thoracic section data from this specimen. The M320-T2T4 FSU exhibited a very significant difference between the value of the moments M_{O1} and

M_{O3} , regardless of the amplitude of the experiment. This difference was attributed to a pre-existing damage of the specimen. Figure A1.13 and Figure A1.14 show the measured vertical forces F_{yC} and F_{yD} during the preconditioning of M320-T2T4. Figure A1.13 shows that there was already a substantial difference in the magnitudes of the forces measured at the two ends, but zooming the plot into the first 10 seconds (corresponding to the cycles of smaller amplitude), it can be seen that time-history force did not correspond to a sequence of loading and unloading in bending, but that the specimen experienced some complex loading modes.

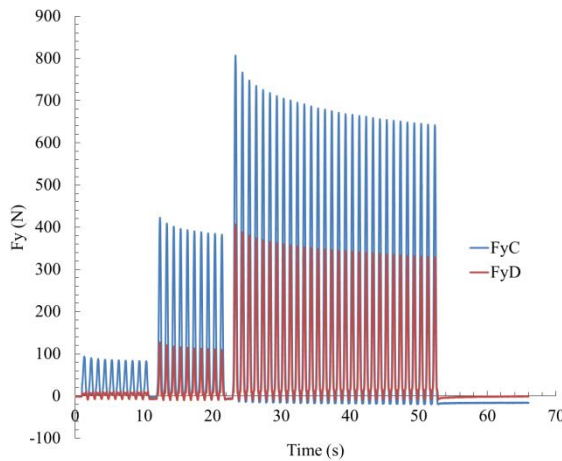


Figure A1.13 Time history of forces F_y measured during the preconditioning of M320-T2T4

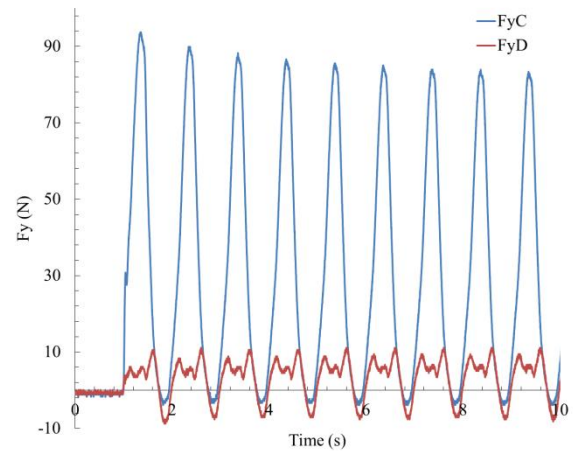


Figure A1.14 Detail of preconditioning forces F_y during the first 10 s. Specimen M320-T2T4

Figure A1.15 shows the comparison between the modeled moment and the calculated one in the case of specimen M320 T7-T9. The model described correctly the initial ramp of the tests at each of the amplitudes tested. The peak prediction was accurate in case of the maximum amplitude test (D5) and then it was slightly off in case of the other two amplitudes, overestimating the peak by less than 8% in the worst case (D3: 5.49 Nm vs. 5.092 Nm). With the exception of the D5 case, the predicted peak lagged the observed peak moment by a few milliseconds. The relaxation response of the estimated and observed responses were parallel almost at all times, with the modeled response showing a faster initial decay in the D5 test.

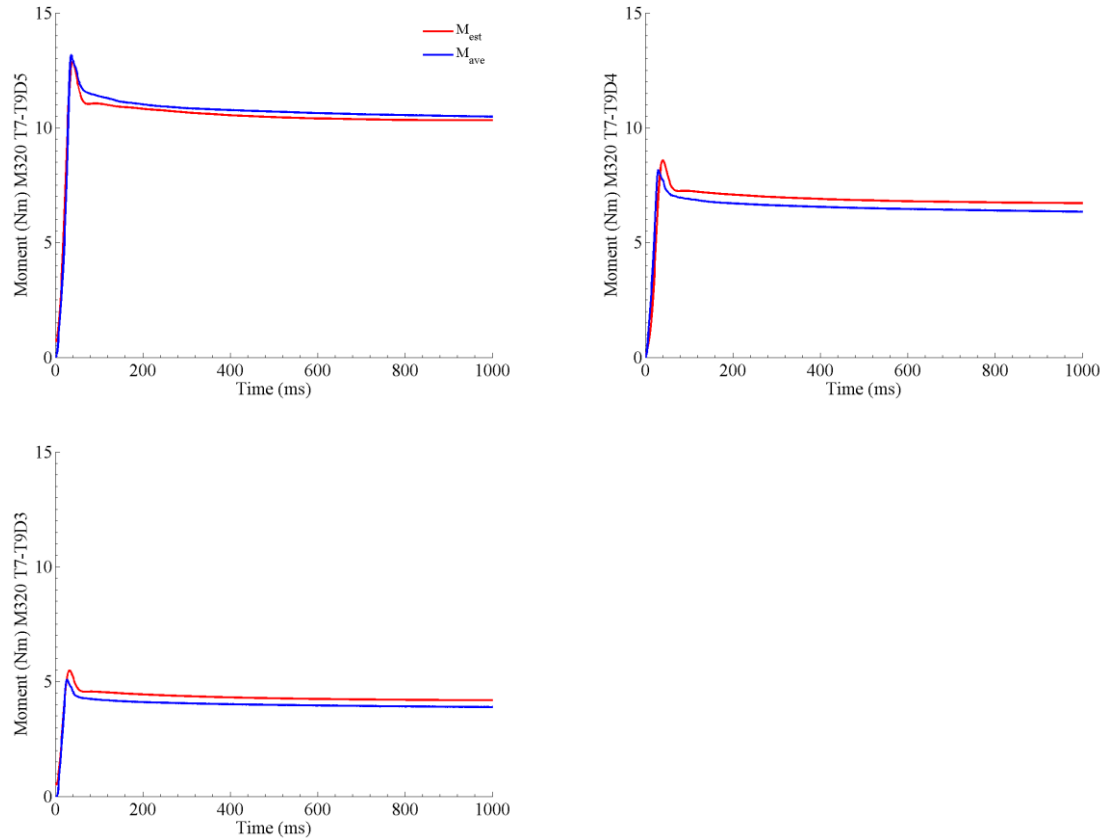


Figure A1.15 Comparison between the moment predicted by the QLV model and the calculated average moment (M_{ave}) of the middle thoracic section of adult specimen M320.

A1.3 CONSIDERATIONS ON THE SIZE OF THE SPECIMENS

Chapter 5 showed that the FSU from the T7T9 section and the older specimens exhibited a stiffer response. The formulation proposed to characterize the mechanical behavior of the FSU intended only to describe the structural response of the specimen without attempting to explain the underlying mechanics of the different tissues present in the FSU. Thus, a mere increase in size (a FSU with a cross section with greater inertia moment will exhibit a stiffer behavior) could have explained the observed stiffer behavior of some of the specimens.

The most relevant dimensions of each specimen were measured before potting the distal ends into the cast and these measurements are shown in Table A1.3 and Table A1.4.

Table A1.3 Dimensions (mm) of the proximal vertebra of each T7-T9 specimen as defined in Figure A1.16

	A	C	D	E
F470	9	17	24	44
M485	9	30	25	55
M319	7	27	34	65
M320	10	26	34	67

Table A1.4 Dimensions (mm) of the distal vertebra of each T7-T9 specimen as defined in Figure A1.16.

	A	C	D	E
F470	8	15	21	42
M485	8	22	23	57
M319	10	24	26	64
M320	9	19	26	69

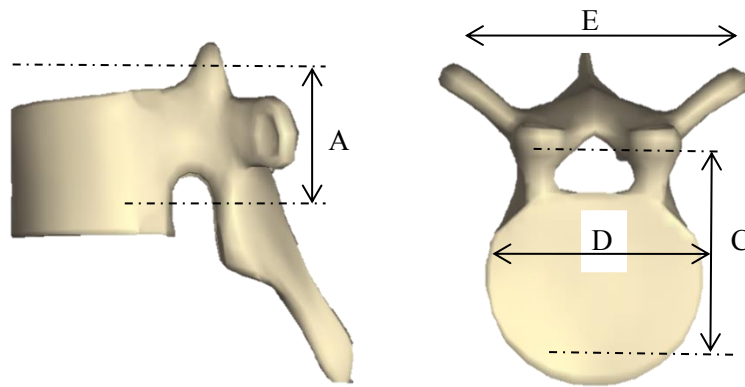


Figure A1.16 Schematic showing the dimensions measured at the distal and proximal vertebra of each specimen.

The dimensions of the proximal and distal vertebrae of the two adult specimens were similar, suggesting that the moment of inertia is not the only factor causing the observed changes in effective stiffness but that there is likely a change in the material properties across subjects or in other structural property that is not related to size. Also, although the dimensions of M485 are comparable to those of the adult subjects, this specimen exhibited a more compliant behavior than the older subjects.

Regardless of the factor causing the variation of stiffness (size vs. mechanical properties, or the combination of the two), it can be concluded that the effective bending behavior of the thoracic spine changed with the developmental state of the specimen, at least for the subjects tested.

A2-APPENDIX: DERIVATION OF EQUATIONS OF MOTION OF A LINEAR, TIME-INVARIANT 2D MODEL OF THE OCCUPANT

The governing equations for the motion of the occupant in the sagittal plane were developed using Lagrangian Dynamics. The following paragraphs detail the process of obtaining the expressions for the kinetic and potential energy of each of the links forming the model, as well as the partial results obtained in the derivations with respect the generalized coordinates.

A2.1 LAGRANGIAN OF THE SYSTEM

According to the Lagrangian Dynamics approach, the governing equations for a dynamic system as the one discussed within dissertation are given by the expression:

$$\frac{d}{dt} \left(\frac{\partial \mathcal{L}}{\partial \dot{q}} \right) + \frac{\partial \mathcal{L}}{\partial q} = Q$$

where \mathcal{L} is the lagrangian of the system as given by the expression:

$$\mathcal{L} = KE - PE$$

with KE and PE representing the kinetic energy and the potential energy of the system. Each of the terms within the Lagrangian of the system is calculated in the next section of this Appendix.

A2.2 CALCULATION OF KINETIC AND POTENTIAL ENERGY OF EACH BODY REGION

Lower Leg (LL): (henceforward, prime indicates a time derivative)

$$v_{LL} = \{0, 0, q_2'(t)\} \times \left\{ \frac{1}{2} l_{LL} \cos(q_2(t)), \frac{1}{2} l_{LL} \sin(q_2(t)), 0 \right\} + \{q_1'(t), 0, 0\}$$

$$KE_{LL} = \frac{1}{2} I_{LL} q_2'(t)^2 + \frac{1}{2} m_{LL} v_{LL} \cdot v_{LL}$$

$$PE_{LL} = \frac{1}{2} g m_{LL} (I_{LL} \sin(q_2(t))) + \frac{1}{2} k_m (q_2(t) - 0.873)^2$$

Upper Leg (UL):

$$v_K = \{0, 0, q_2'(t)\} \times \{I_{LL} \cos(q_2(t)), I_{LL} \sin(q_2(t)), 0\} + \{q_1'(t), 0, 0\}$$

$$v_{UL} = \{0, 0, q_3'(t)\} \times \left\{ \frac{1}{2} I_{UL} \cos(q_3(t)), \frac{1}{2} I_{UL} \sin(q_3(t)), 0 \right\} + v_K$$

$$KE_{UL} = \frac{1}{2} I_{UL} q_3'(t)^2 + \frac{1}{2} m_{UL} v_{UL} \cdot v_{UL}$$

$$PE_{UL} = g_{LL} m_{UL} \sin(q_2(t)) + \frac{1}{2} g_{UL} m_{UL} \sin(q_3(t)) + \frac{1}{2} k_k (q_3(t) - q_2(t))^2$$

Lumbar (L):

$$v_P = \{0, 0, q_3'(t)\} \times \{I_{UL} \cos(q_3(t)), I_{UL} \sin(q_3(t)), 0\} + v_K$$

$$v_L = \{0, 0, q_4'(t)\} \times \left\{ \frac{1}{2} I_L \cos(q_4(t)), \frac{1}{2} I_L \sin(q_4(t)), 0 \right\} + v_P$$

$$KE_L = \frac{1}{2} I_L q_4'(t)^2 + \frac{1}{2} m_L v_L \cdot v_L$$

$$PE_L = \frac{1}{2} g m_L (I_L \sin(q_4(t))) + g m_L (I_{LL} \sin(q_2(t)) + I_{UL} \sin(q_3(t))) + \frac{1}{2} k_p (q_4(t) - q_3(t))^2$$

Lower Thoracic (LT):

$$v_{L2} = \{0, 0, q_4'(t)\} \times \{I_L \cos(q_4(t)), I_L \sin(q_4(t)), 0\} + v_P$$

$$v_{LT} = \{0, 0, q_5'(t)\} \times \left\{ \frac{1}{2} I_{LT} \cos(q_5(t)), \frac{1}{2} I_{LT} \sin(q_5(t)), 0 \right\} + v_{L2}$$

$$KE_{LT} = \frac{1}{2} I_{LT} q_5'(t)^2 + \frac{1}{2} m_{LT} v_{LT} \cdot v_{LT}$$

$$PE_{LT} = g m_{LT} (I_L \sin(q_4(t)) + I_{LL} \sin(q_2(t)) + I_{UL} \sin(q_3(t))) + \frac{1}{2} g_{LT} m_{LT} \sin(q_5(t)) + \frac{1}{2} k_{L2} (q_5(t) - q_4(t))^2$$

Upper Thoracic (UT):

$$v_{T8} = \{0,0, q5'(t)\} \times \{lT\cos(q5(t)), lT\sin(q5(t)), 0\} + v_{L2}$$

$$v_{UT} = \{0,0, q6'(t)\} \times \left\{ \frac{1}{2}lUT\cos(q6(t)), \frac{1}{2}lUT\sin(q6(t)), 0 \right\} + v_{T8}$$

$$KE_{UT} = \frac{1}{2}lUTq6'(t)^2 + \frac{1}{2}mUTv_{UT} \cdot v_{UT}$$

$$PE_{UT} = gmUT \left(lL\sin(q4(t)) + lL\sin(q2(t)) + lT\sin(q5(t)) + lUL\sin(q3(t)) + \frac{1}{2}lUT\sin(q6(t)) \right) + \frac{1}{2}kT8(q6(t) - q5(t))^2$$

Cervical-head:

$$v_{T1} = \{0,0, q6'(t)\} \times \{lUT\cos(q6(t)), lUT\sin(q6(t)), 0\} + v_{T8}$$

$$v_{CH} = \{0,0, q7'(t)\} \times \left\{ \frac{1}{2}lCH\cos(q7(t)), \frac{1}{2}lCH\sin(q7(t)), 0 \right\} + v_{T1}$$

$$KE_{CH} = \frac{1}{2}mCHv_{CH} \cdot v_{CH} + \frac{1}{2}lCHq7'(t)^2$$

$$PE_{CH} = gmCH \left(\frac{1}{2}lCH\sin(q7(t)) + lL\sin(q4(t)) + lL\sin(q2(t)) + lT\sin(q5(t)) + lUL\sin(q3(t)) + lUT\sin(q6(t)) \right) + \frac{1}{2}kT1(q7(t) - q6(t))^2$$

Total kinetic and potential energy of the system

$$KTotal = KE_{CH} + KE_L + KE_{LL} + KE_{LT} + KE_{UL} + KE_{UT}$$

$$VTotal = PE_{CH} + PE_L + PE_{LL} + PE_{LT} + PE_{UL} + PE_{UT}$$

A2.3 PARTIAL DERIVATIVES OF THE LAGRANGIAN

$$\begin{aligned}
& \frac{d}{dt} \left(\frac{\partial \mathcal{L}}{\partial \dot{q}_i} \right) \\
&= \frac{1}{2} (-l_{CHmCH} q_7''(t) \sin(q_7(t)) - l_{CHmCH} q_7'(t)^2 \cos(q_7(t)) - 2l_{LmCH} q_4''(t) \sin(q_4(t)) \\
&- 2l_{LmCH} q_4'(t)^2 \cos(q_4(t)) - l_{LmL} q_4''(t) \sin(q_4(t)) - l_{LmL} q_4'(t)^2 \cos(q_4(t)) \\
&\quad - 2l_{LmLT} q_4''(t) \sin(q_4(t)) - 2l_{LmLT} q_4'(t)^2 \cos(q_4(t)) - 2l_{LmUT} q_4''(t) \sin(q_4(t)) \\
&\quad - 2l_{LmUT} q_4'(t)^2 \cos(q_4(t)) - l_{LL} q_2'(t)^2 \cos(q_2(t)) (2m_{CH} + 2m_L + m_{LL} + 2m_{LT} \\
&\quad + 2m_{UL} + 2m_{UT}) - 2l_{LLmCH} q_2''(t) \sin(q_2(t)) - 2l_{LLmL} q_2''(t) \sin(q_2(t)) \\
&\quad - l_{LLmLL} q_2''(t) \sin(q_2(t)) - 2l_{LLmLT} q_2''(t) \sin(q_2(t)) - 2l_{LLmUL} q_2''(t) \sin(q_2(t)) \\
&\quad - 2l_{LLmUT} q_2''(t) \sin(q_2(t)) - 2l_{LTmCH} q_5''(t) \sin(q_5(t)) \\
&\quad - 2l_{LTmCH} q_5'(t)^2 \cos(q_5(t)) - l_{LTmLT} q_5''(t) \sin(q_5(t)) \\
&\quad - l_{LTmLT} q_5'(t)^2 \cos(q_5(t)) - 2l_{LTmUT} q_5''(t) \sin(q_5(t)) \\
&\quad - 2l_{LTmUT} q_5'(t)^2 \cos(q_5(t)) - l_{UL} q_3'(t)^2 \cos(q_3(t)) (2m_{CH} + 2m_L + 2m_{LT} + m_{UL} \\
&\quad + 2m_{UT}) - 2l_{ULmCH} q_3''(t) \sin(q_3(t)) - 2l_{ULmL} q_3''(t) \sin(q_3(t)) \\
&\quad - 2l_{ULmLT} q_3''(t) \sin(q_3(t)) - l_{ULmUL} q_3''(t) \sin(q_3(t)) \\
&\quad - 2l_{ULmUT} q_3''(t) \sin(q_3(t)) - 2l_{UTmCH} q_6''(t) \sin(q_6(t)) \\
&\quad - 2l_{UTmCH} q_6'(t)^2 \cos(q_6(t)) - l_{UTmUT} q_6''(t) \sin(q_6(t)) \\
&\quad - l_{UTmUT} q_6'(t)^2 \cos(q_6(t)) + 2m_{CH} q_1''(t) + 2m_L q_1''(t) + 2m_{LL} q_1''(t) \\
&\quad + 2m_{LT} q_1''(t) + 2m_{UL} q_1''(t) + 2m_{UT} q_1''(t)
\end{aligned}$$

$$\begin{aligned}
\frac{d}{dt} \left(\frac{\partial \mathcal{L}}{\partial \dot{q}_2} \right) = & \frac{1}{4} (4m_{CH}q_2''(t)l_{LL}^2 + 4m_Lq_2''(t)l_{LL}^2 + m_{LL}q_2''(t)l_{LL}^2 + 4m_{LT}q_2''(t)l_{LL}^2 \\
& + 4m_{UL}q_2''(t)l_{LL}^2 + 4m_{UT}q_2''(t)l_{LL}^2 + 4l_{UL}m_{CH}\sin(q_2(t) - q_3(t))q_3'(t)^2l_{LL} \\
& + 4l_{UL}m_L\sin(q_2(t) - q_3(t))q_3'(t)^2l_{LL} + 4l_{UL}m_{LT}\sin(q_2(t) - q_3(t))q_3'(t)^2l_{LL} \\
& + 2l_{UL}m_{UL}\sin(q_2(t) - q_3(t))q_3'(t)^2l_{LL} + 4l_{UL}m_{UT}\sin(q_2(t) - q_3(t))q_3'(t)^2l_{LL} \\
& + 4l_{Lm}m_{CH}\sin(q_2(t) - q_4(t))q_4'(t)^2l_{LL} + 2l_{Lm}l_{Lm}\sin(q_2(t) - q_4(t))q_4'(t)^2l_{LL} \\
& + 4l_{Lm}m_{LT}\sin(q_2(t) - q_4(t))q_4'(t)^2l_{LL} + 4l_{Lm}m_{UT}\sin(q_2(t) - q_4(t))q_4'(t)^2l_{LL} \\
& + 4l_{LT}m_{CH}\sin(q_2(t) - q_5(t))q_5'(t)^2l_{LL} + 2l_{LT}m_{LT}\sin(q_2(t) - q_5(t))q_5'(t)^2l_{LL} \\
& + 4l_{LT}m_{UT}\sin(q_2(t) - q_5(t))q_5'(t)^2l_{LL} + 4l_{UT}m_{CH}\sin(q_2(t) - q_6(t))q_6'(t)^2l_{LL} \\
& + 2l_{UT}m_{UT}\sin(q_2(t) - q_6(t))q_6'(t)^2l_{LL} + 2l_{CH}m_{CH}\sin(q_2(t) - q_7(t))q_7'(t)^2l_{LL} \\
& - 2(2m_{CH} + 2m_L + m_{LL} + 2m_{LT} + 2m_{UL} + 2m_{UT})\cos(q_2(t))q_1'(t)q_2'(t)l_{LL} \\
& - 2q_2'(t)(l_{UL}(2m_{CH} + 2m_L + 2m_{LT} + m_{UL} + 2m_{UT})\sin(q_2(t) - q_3(t))q_3'(t) \\
& + l_L(2m_{CH} + m_L + 2(m_{LT} + m_{UT}))\sin(q_2(t) - q_4(t))q_4'(t) + 2l_{LT}m_{CH}\sin(q_2(t) \\
& - q_5(t))q_5'(t) + l_{LT}m_{LT}\sin(q_2(t) - q_5(t))q_5'(t) + 2l_{LT}m_{UT}\sin(q_2(t) \\
& - q_5(t))q_5'(t) + 2l_{UT}m_{CH}\sin(q_2(t) - q_6(t))q_6'(t) + l_{UT}m_{UT}\sin(q_2(t) \\
& - q_6(t))q_6'(t) + l_{CH}m_{CH}\sin(q_2(t) - q_7(t))q_7'(t))l_{LL} - 4m_{CH}\sin(q_2(t))q_1''(t)l_{LL} \\
& - 4m_L\sin(q_2(t))q_1''(t)l_{LL} - 2m_{LL}\sin(q_2(t))q_1''(t)l_{LL} - 4m_{LT}\sin(q_2(t))q_1''(t)l_{LL} \\
& - 4m_{UL}\sin(q_2(t))q_1''(t)l_{LL} - 4m_{UT}\sin(q_2(t))q_1''(t)l_{LL} + 4l_{UL}m_{CH}\cos(q_2(t) \\
& - q_3(t))q_3''(t)l_{LL} + 4l_{UL}m_L\cos(q_2(t) - q_3(t))q_3''(t)l_{LL} + 4l_{UL}m_{LT}\cos(q_2(t) \\
& - q_3(t))q_3''(t)l_{LL} + 2l_{UL}m_{UL}\cos(q_2(t) - q_3(t))q_3''(t)l_{LL} + 4l_{UL}m_{UT}\cos(q_2(t) \\
& - q_3(t))q_3''(t)l_{LL} + 4l_{Lm}m_{CH}\cos(q_2(t) - q_4(t))q_4''(t)l_{LL} + 2l_{Lm}l_{Lm}\cos(q_2(t) \\
& - q_4(t))q_4''(t)l_{LL} + 4l_{Lm}m_{LT}\cos(q_2(t) - q_4(t))q_4''(t)l_{LL} + 4l_{Lm}m_{UT}\cos(q_2(t) \\
& - q_4(t))q_4''(t)l_{LL} + 4l_{LT}m_{CH}\cos(q_2(t) - q_5(t))q_5''(t)l_{LL} + 2l_{LT}m_{LT}\cos(q_2(t) \\
& - q_5(t))q_5''(t)l_{LL} + 4l_{LT}m_{UT}\cos(q_2(t) - q_5(t))q_5''(t)l_{LL} + 4l_{UT}m_{CH}\cos(q_2(t) \\
& - q_6(t))q_6''(t)l_{LL} + 2l_{UT}m_{UT}\cos(q_2(t) - q_6(t))q_6''(t)l_{LL} + 2l_{CH}m_{CH}\cos(q_2(t) \\
& - q_7(t))q_7''(t)l_{LL} + 4l_{LL}q_2''(t))
\end{aligned}$$

$$\begin{aligned}
\frac{d}{dt} \left(\frac{\partial \mathcal{L}}{\partial \dot{q}_3} \right) &= \frac{1}{4} (4m_{CH}q_3''(t)I_{UL}^2 + 4m_Lq_3''(t)I_{UL}^2 + 4m_{LT}q_3''(t)I_{UL}^2 + m_{UL}q_3''(t)I_{UL}^2 \\
&+ 4m_{UT}q_3''(t)I_{UL}^2 - 2I_{LL}(2m_{CH} + 2m_L + 2m_{LT} + m_{UL} + 2m_{UT})\sin(q_2(t) \\
&- q_3(t))q_2'(t)^2I_{UL} + 4I_{LmCH}\sin(q_3(t) - q_4(t))q_4'(t)^2I_{UL} + 2I_{LmL}\sin(q_3(t) \\
&- q_4(t))q_4'(t)^2I_{UL} + 4I_{LmLT}\sin(q_3(t) - q_4(t))q_4'(t)^2I_{UL} + 4I_{LmUT}\sin(q_3(t) \\
&- q_4(t))q_4'(t)^2I_{UL} + 4I_{LTmCH}\sin(q_3(t) - q_5(t))q_5'(t)^2I_{UL} + 2I_{LTmLT}\sin(q_3(t) \\
&- q_5(t))q_5'(t)^2I_{UL} + 4I_{LTmUT}\sin(q_3(t) - q_5(t))q_5'(t)^2I_{UL} + 4I_{UTmCH}\sin(q_3(t) \\
&- q_6(t))q_6'(t)^2I_{UL} + 2I_{UTmUT}\sin(q_3(t) - q_6(t))q_6'(t)^2I_{UL} + 2I_{CHmCH}\sin(q_3(t) \\
&- q_7(t))q_7'(t)^2I_{UL} - 2(2m_{CH} + 2m_L + 2m_{LT} + m_{UL} \\
&+ 2m_{UT})\cos(q_3(t))q_1'(t)q_3'(t)I_{UL} + 2I_{LL}(2m_{CH} + 2m_L + 2m_{LT} + m_{UL} \\
&+ 2m_{UT})\sin(q_2(t) - q_3(t))q_2'(t)q_3'(t)I_{UL} - 4I_{LmCH}\sin(q_3(t) \\
&- q_4(t))q_3'(t)q_4'(t)I_{UL} - 2I_{LmL}\sin(q_3(t) - q_4(t))q_3'(t)q_4'(t)I_{UL} \\
&- 4I_{LmLT}\sin(q_3(t) - q_4(t))q_3'(t)q_4'(t)I_{UL} - 4I_{LmUT}\sin(q_3(t) \\
&- q_4(t))q_3'(t)q_4'(t)I_{UL} - 4I_{LTmCH}\sin(q_3(t) - q_5(t))q_3'(t)q_5'(t)I_{UL} \\
&- 2I_{LTmLT}\sin(q_3(t) - q_5(t))q_3'(t)q_5'(t)I_{UL} - 4I_{LTmUT}\sin(q_3(t) \\
&- q_5(t))q_3'(t)q_5'(t)I_{UL} - 4I_{UTmCH}\sin(q_3(t) - q_6(t))q_3'(t)q_6'(t)I_{UL} \\
&- 2I_{UTmUT}\sin(q_3(t) - q_6(t))q_3'(t)q_6'(t)I_{UL} - 2I_{CHmCH}\sin(q_3(t) \\
&- q_7(t))q_3'(t)q_7'(t)I_{UL} - 4m_{CH}\sin(q_3(t))q_1''(t)I_{UL} - 4m_L\sin(q_3(t))q_1''(t)I_{UL} \\
&- 4m_{LT}\sin(q_3(t))q_1''(t)I_{UL} - 2m_{UL}\sin(q_3(t))q_1''(t)I_{UL} \\
&- 4m_{UT}\sin(q_3(t))q_1''(t)I_{UL} + 4I_{LLmCH}\cos(q_2(t) - q_3(t))q_2''(t)I_{UL} \\
&+ 4I_{LLmL}\cos(q_2(t) - q_3(t))q_2''(t)I_{UL} + 4I_{LLmLT}\cos(q_2(t) - q_3(t))q_2''(t)I_{UL} \\
&+ 2I_{LLmUL}\cos(q_2(t) - q_3(t))q_2''(t)I_{UL} + 4I_{LLmUT}\cos(q_2(t) - q_3(t))q_2''(t)I_{UL} \\
&+ 4I_{LmCH}\cos(q_3(t) - q_4(t))q_4''(t)I_{UL} + 2I_{LmL}\cos(q_3(t) - q_4(t))q_4''(t)I_{UL} \\
&+ 4I_{LmLT}\cos(q_3(t) - q_4(t))q_4''(t)I_{UL} + 4I_{LmUT}\cos(q_3(t) - q_4(t))q_4''(t)I_{UL} \\
&+ 4I_{LTmCH}\cos(q_3(t) - q_5(t))q_5''(t)I_{UL} + 2I_{LTmLT}\cos(q_3(t) - q_5(t))q_5''(t)I_{UL} \\
&+ 4I_{LTmUT}\cos(q_3(t) - q_5(t))q_5''(t)I_{UL} + 4I_{UTmCH}\cos(q_3(t) - q_6(t))q_6''(t)I_{UL} \\
&+ 2I_{UTmUT}\cos(q_3(t) - q_6(t))q_6''(t)I_{UL} + 2I_{CHmCH}\cos(q_3(t) - q_7(t))q_7''(t)I_{UL} \\
&+ 4I_{UL}q_3''(t))
\end{aligned}$$

$$\begin{aligned}
\frac{d}{dt} \left(\frac{\partial \mathcal{L}}{\partial \dot{q}_4} \right) = & \frac{1}{4} (4lLq4''(t) - 2lCHlLmCHq4'(t)q7'(t)\sin(q4(t) - q7(t)) + 2lCHlLmCHq7''(t)\cos(q4(t) \\
& - q7(t)) + 2lCHlLmCHq7'(t)^2\sin(q4(t) - q7(t)) + 4lL^2mCHq4''(t) + lL^2mLq4''(t) \\
& + 4lL^2mLTq4''(t) + 4lL^2mUTq4''(t) + 2lLlLq2'(t)q4'(t)(2mCH + mL + 2(mLT \\
& + mUT))\sin(q2(t) - q4(t)) - 2lLlLq2'(t)^2(2mCH + mL + 2(mLT \\
& + mUT))\sin(q2(t) - q4(t)) + 4lLlLmCHq2''(t)\cos(q2(t) - q4(t)) \\
& + 2lLlLmLq2''(t)\cos(q2(t) - q4(t)) + 4lLlLmLTq2''(t)\cos(q2(t) - q4(t)) \\
& + 4lLlLmUTq2''(t)\cos(q2(t) - q4(t)) - 4lLlLTmCHq4'(t)q5'(t)\sin(q4(t) - q5(t)) \\
& + 4lLlLTmCHq5''(t)\cos(q4(t) - q5(t)) + 4lLlLTmCHq5'(t)^2\sin(q4(t) - q5(t)) \\
& - 2lLlLTmLTq4'(t)q5'(t)\sin(q4(t) - q5(t)) + 2lLlLTmLTq5''(t)\cos(q4(t) - q5(t)) \\
& + 2lLlLTmLTq5'(t)^2\sin(q4(t) - q5(t)) - 4lLlLTmUTq4'(t)q5'(t)\sin(q4(t) - q5(t)) \\
& + 4lLlLTmUTq5''(t)\cos(q4(t) - q5(t)) + 4lLlLTmUTq5'(t)^2\sin(q4(t) - q5(t)) \\
& + 2lLlULq3'(t)q4'(t)(2mCH + mL + 2(mLT + mUT))\sin(q3(t) - q4(t)) \\
& - 2lLlULq3'(t)^2(2mCH + mL + 2(mLT + mUT))\sin(q3(t) - q4(t)) \\
& + 4lLlULmCHq3''(t)\cos(q3(t) - q4(t)) + 2lLlULmLq3''(t)\cos(q3(t) - q4(t)) \\
& + 4lLlULmLTq3''(t)\cos(q3(t) - q4(t)) + 4lLlULmUTq3''(t)\cos(q3(t) - q4(t)) \\
& - 4lLlUTmCHq4'(t)q6'(t)\sin(q4(t) - q6(t)) + 4lLlUTmCHq6''(t)\cos(q4(t) - q6(t)) \\
& + 4lLlUTmCHq6'(t)^2\sin(q4(t) - q6(t)) - 2lLlUTmUTq4'(t)q6'(t)\sin(q4(t) - q6(t)) \\
& + 2lLlUTmUTq6''(t)\cos(q4(t) - q6(t)) + 2lLlUTmUTq6'(t)^2\sin(q4(t) - q6(t)) \\
& - 4lLmCHq1''(t)\sin(q4(t)) - 4lLmCHq1'(t)q4'(t)\cos(q4(t)) \\
& - 2lLmLq1''(t)\sin(q4(t)) - 2lLmLq1'(t)q4'(t)\cos(q4(t)) \\
& - 4lLmLTq1''(t)\sin(q4(t)) - 4lLmLTq1'(t)q4'(t)\cos(q4(t)) \\
& - 4lLmUTq1''(t)\sin(q4(t)) - 4lLmUTq1'(t)q4'(t)\cos(q4(t))
\end{aligned}$$

$$\begin{aligned}
\frac{d}{dt} \left(\frac{\partial \mathcal{L}}{\partial \dot{q}_5} \right) = & \frac{1}{4} (4\text{ILT}q5''(t) - 2\text{CHIL}Tm\text{CH}q5'(t)q7'(t)\sin(q5(t) - q7(t)) \\
& + 2\text{CHIL}Tm\text{CH}q7''(t)\cos(q5(t) - q7(t)) + 2\text{CHIL}Tm\text{CH}q7'(t)^2\sin(q5(t) - q7(t)) \\
& + 4\text{LIL}Tm\text{CH}q4''(t)\cos(q4(t) - q5(t)) + 4\text{LIL}Tm\text{CH}q4'(t)q5'(t)\sin(q4(t) \\
& - q5(t)) - 4\text{LIL}Tm\text{CH}q4'(t)^2\sin(q4(t) - q5(t)) + 2\text{LIL}Tm\text{LT}q4''(t)\cos(q4(t) \\
& - q5(t)) + 2\text{LIL}Tm\text{LT}q4'(t)q5'(t)\sin(q4(t) - q5(t)) - 2\text{LIL}Tm\text{LT}q4'(t)^2\sin(q4(t) \\
& - q5(t)) + 4\text{LIL}Tm\text{UT}q4''(t)\cos(q4(t) - q5(t)) \\
& + 4\text{LIL}Tm\text{UT}q4'(t)q5'(t)\sin(q4(t) - q5(t)) - 4\text{LIL}Tm\text{UT}q4'(t)^2\sin(q4(t) \\
& - q5(t)) + 2\text{LIL}T(2m\text{CH} + m\text{LT} + 2m\text{UT})q2'(t)q5'(t)\sin(q2(t) - q5(t)) \\
& - 2\text{LIL}T(2m\text{CH} + m\text{LT} + 2m\text{UT})q2'(t)^2\sin(q2(t) - q5(t)) \\
& + 4\text{LIL}Tm\text{CH}q2''(t)\cos(q2(t) - q5(t)) + 2\text{LIL}Tm\text{LT}q2''(t)\cos(q2(t) - q5(t)) \\
& + 4\text{LIL}Tm\text{UT}q2''(t)\cos(q2(t) - q5(t)) + 4\text{LT}^2m\text{CH}q5''(t) + \text{LT}^2m\text{LT}q5''(t) \\
& + 4\text{LT}^2m\text{UT}q5''(t) + 2\text{LTl}U\text{L}(2m\text{CH} + m\text{LT} + 2m\text{UT})q3'(t)q5'(t)\sin(q3(t) \\
& - q5(t)) - 2\text{LTl}U\text{L}(2m\text{CH} + m\text{LT} + 2m\text{UT})q3'(t)^2\sin(q3(t) - q5(t)) \\
& + 4\text{LTl}U\text{L}m\text{CH}q3''(t)\cos(q3(t) - q5(t)) + 2\text{LTl}U\text{L}m\text{LT}q3''(t)\cos(q3(t) - q5(t)) \\
& + 4\text{LTl}U\text{L}m\text{UT}q3''(t)\cos(q3(t) - q5(t)) - 4\text{LTl}U\text{L}m\text{CH}q5'(t)q6'(t)\sin(q5(t) \\
& - q6(t)) + 4\text{LTl}U\text{L}m\text{CH}q6''(t)\cos(q5(t) - q6(t)) + 4\text{LTl}U\text{L}m\text{CH}q6'(t)^2\sin(q5(t) \\
& - q6(t)) - 2\text{LTl}U\text{L}m\text{UT}q5'(t)q6'(t)\sin(q5(t) - q6(t)) \\
& + 2\text{LTl}U\text{L}m\text{UT}q6''(t)\cos(q5(t) - q6(t)) + 2\text{LTl}U\text{L}m\text{UT}q6'(t)^2\sin(q5(t) - q6(t)) \\
& - 4\text{LT}m\text{CH}q1''(t)\sin(q5(t)) - 4\text{LT}m\text{CH}q1'(t)q5'(t)\cos(q5(t)) \\
& - 2\text{LT}m\text{LT}q1''(t)\sin(q5(t)) - 2\text{LT}m\text{LT}q1'(t)q5'(t)\cos(q5(t)) \\
& - 4\text{LT}m\text{UT}q1''(t)\sin(q5(t)) - 4\text{LT}m\text{UT}q1'(t)q5'(t)\cos(q5(t)))
\end{aligned}$$

$$\begin{aligned}
\frac{d}{dt} \left(\frac{\partial \mathcal{L}}{\partial \dot{q}_6} \right) &= \frac{1}{4} (4IUTq6''(t) - 2lCHIUTmCHq6'(t)q7'(t)\sin(q6(t) - q7(t)) \\
&+ 2lCHIUTmCHq7''(t)\cos(q6(t) - q7(t)) + 2lCHIUTmCHq7'(t)^2\sin(q6(t) - q7(t)) \\
&+ 4lLIUTmCHq4''(t)\cos(q4(t) - q6(t)) + 4lLIUTmCHq4'(t)q6'(t)\sin(q4(t) \\
&- q6(t)) - 4lLIUTmCHq4'(t)^2\sin(q4(t) - q6(t)) + 2lLIUTmUTq4''(t)\cos(q4(t) \\
&- q6(t)) + 2lLIUTmUTq4'(t)q6'(t)\sin(q4(t) - q6(t)) \\
&- 2lLIUTmUTq4'(t)^2\sin(q4(t) - q6(t)) + 2lLLIUT(2mCH \\
&+ mUT)q2'(t)q6'(t)\sin(q2(t) - q6(t)) - 2lLLIUT(2mCH + mUT)q2'(t)^2\sin(q2(t) \\
&- q6(t)) + 4lLLIUTmCHq2''(t)\cos(q2(t) - q6(t)) + 2lLLIUTmUTq2''(t)\cos(q2(t) \\
&- q6(t)) + 4lLTIUTmCHq5''(t)\cos(q5(t) - q6(t)) \\
&+ 4lLTIUTmCHq5'(t)q6'(t)\sin(q5(t) - q6(t)) - 4lLTIUTmCHq5'(t)^2\sin(q5(t) \\
&- q6(t)) + 2lLTIUTmUTq5''(t)\cos(q5(t) - q6(t)) \\
&+ 2lLTIUTmUTq5'(t)q6'(t)\sin(q5(t) - q6(t)) - 2lLTIUTmUTq5'(t)^2\sin(q5(t) \\
&- q6(t)) + 2lULIUT(2mCH + mUT)q3'(t)q6'(t)\sin(q3(t) - q6(t)) \\
&- 2lULIUT(2mCH + mUT)q3'(t)^2\sin(q3(t) - q6(t)) \\
&+ 4lULIUTmCHq3''(t)\cos(q3(t) - q6(t)) + 2lULIUTmUTq3''(t)\cos(q3(t) - q6(t)) \\
&+ 4IUT^2mCHq6''(t) + lUT^2mUTq6''(t) - 4IUTmCHq1''(t)\sin(q6(t)) \\
&- 4IUTmCHq1'(t)q6'(t)\cos(q6(t)) - 2IUTmUTq1''(t)\sin(q6(t)) \\
&- 2IUTmUTq1'(t)q6'(t)\cos(q6(t)))
\end{aligned}$$

$$\begin{aligned}
\frac{d}{dt} \left(\frac{\partial \mathcal{L}}{\partial \dot{q}_7} \right) = & \frac{1}{4} (4lCHq7''(t) + lCH^2mCHq7''(t) + 2lCHlLmCHq4''(t) \cos(q4(t) - q7(t)) \\
& + 2lCHlLmCHq4'(t)q7'(t) \sin(q4(t) - q7(t)) \\
& - 2lCHlLmCHq4'(t)^2 \sin(q4(t) - q7(t)) + 2lCHlLmCHq2''(t) \cos(q2(t) - q7(t)) \\
& + 2lCHlLmCHq2'(t)q7'(t) \sin(q2(t) - q7(t)) \\
& - 2lCHlLmCHq2'(t)^2 \sin(q2(t) - q7(t)) \\
& + 2lCHlLTmCHq5''(t) \cos(q5(t) - q7(t)) \\
& + 2lCHlLTmCHq5'(t)q7'(t) \sin(q5(t) - q7(t)) \\
& - 2lCHlLTmCHq5'(t)^2 \sin(q5(t) - q7(t)) \\
& + 2lCHlULmCHq3''(t) \cos(q3(t) - q7(t)) \\
& + 2lCHlULmCHq3'(t)q7'(t) \sin(q3(t) - q7(t)) \\
& - 2lCHlULmCHq3'(t)^2 \sin(q3(t) - q7(t)) \\
& + 2lCHlUTmCHq6''(t) \cos(q6(t) - q7(t)) \\
& + 2lCHlUTmCHq6'(t)q7'(t) \sin(q6(t) - q7(t)) \\
& - 2lCHlUTmCHq6'(t)^2 \sin(q6(t) - q7(t)) - 2lCHmCHq1''(t) \sin(q7(t)) \\
& - 2lCHmCHq1'(t)q7'(t) \cos(q7(t)))
\end{aligned}$$

$$\left(\frac{\partial \mathcal{L}}{\partial q_1} \right) = 0$$

$$\begin{aligned}
\frac{\partial \mathcal{L}}{\partial q_2} = & -\frac{1}{2} l L q_2'(t) (l C H m C H q_7'(t) \sin(q_2(t) - q_7(t)) + 2 l L m C H q_4'(t) \sin(q_2(t) - q_4(t)) \\
& + l L m L q_4'(t) \sin(q_2(t) - q_4(t)) + 2 l L m L T q_4'(t) \sin(q_2(t) - q_4(t)) \\
& + 2 l L m U T q_4'(t) \sin(q_2(t) - q_4(t)) + 2 l L T m C H q_5'(t) \sin(q_2(t) - q_5(t)) \\
& + l L T m L T q_5'(t) \sin(q_2(t) - q_5(t)) + 2 l L T m U T q_5'(t) \sin(q_2(t) - q_5(t)) \\
& + l U L q_3'(t) \sin(q_2(t) - q_3(t)) (2 m C H + 2 m L + 2 m L T + m U L + 2 m U T) \\
& + 2 l U T m C H q_6'(t) \sin(q_2(t) - q_6(t)) + l U T m U T q_6'(t) \sin(q_2(t) - q_6(t)) \\
& + q_1'(t) \cos(q_2(t)) (2 m C H + 2 m L + m L L + 2 m L T + 2 m U L + 2 m U T)) \\
& + g l L L m C H \cos(q_2(t)) + g l L L m L \cos(q_2(t)) + \frac{1}{2} g l L L m L L \cos(q_2(t)) \\
& + g l L L m L T \cos(q_2(t)) + g l L L m U L \cos(q_2(t)) + g l L L m U T \cos(q_2(t)) - k k(q_3(t) \\
& - q_2(t)) + k m(q_2(t) - 0.873)
\end{aligned}$$

$$\begin{aligned}
\frac{\partial \mathcal{L}}{\partial q_3} = & -\frac{1}{2} l U L q_3'(t) (l C H m C H q_7'(t) \sin(q_3(t) - q_7(t)) + 2 l L m C H q_4'(t) \sin(q_3(t) - q_4(t)) \\
& + l L m L q_4'(t) \sin(q_3(t) - q_4(t)) + 2 l L m L T q_4'(t) \sin(q_3(t) - q_4(t)) \\
& + 2 l L m U T q_4'(t) \sin(q_3(t) - q_4(t)) \\
& - l L L q_2'(t) \sin(q_2(t) - q_3(t)) (2 m C H + 2 m L + 2 m L T + m U L + 2 m U T) \\
& + 2 l L T m C H q_5'(t) \sin(q_3(t) - q_5(t)) + l L T m L T q_5'(t) \sin(q_3(t) - q_5(t)) \\
& + 2 l L T m U T q_5'(t) \sin(q_3(t) - q_5(t)) + 2 l U T m C H q_6'(t) \sin(q_3(t) - q_6(t)) \\
& + l U T m U T q_6'(t) \sin(q_3(t) - q_6(t)) \\
& + q_1'(t) \cos(q_3(t)) (2 m C H + 2 m L + 2 m L T + m U L + 2 m U T)) \\
& + g l U L m C H \cos(q_3(t)) + g l U L m L \cos(q_3(t)) + g l U L m L T \cos(q_3(t)) \\
& + \frac{1}{2} g l U L m U L \cos(q_3(t)) + g l U L m U T \cos(q_3(t)) + k k(q_3(t) - q_2(t)) \\
& - k p(q_4(t) - q_3(t))
\end{aligned}$$

$$\begin{aligned}
\frac{\partial \mathcal{L}}{\partial q_4} = & -\frac{1}{2} lLq4'(t) \left(lCHmCHq7'(t) \sin(q4(t) - q7(t)) \right. \\
& - lLq2'(t) (2mCH + mL + 2(mLT + mUT)) \sin(q2(t) - q4(t)) \\
& + 2lLTmCHq5'(t) \sin(q4(t) - q5(t)) + lLTmLTq5'(t) \sin(q4(t) - q5(t)) \\
& + 2lLTmUTq5'(t) \sin(q4(t) - q5(t)) - 2lULmCHq3'(t) \sin(q3(t) - q4(t)) \\
& - lULmLq3'(t) \sin(q3(t) - q4(t)) - 2lULmLTq3'(t) \sin(q3(t) - q4(t)) \\
& - 2lULmUTq3'(t) \sin(q3(t) - q4(t)) + 2lUTmCHq6'(t) \sin(q4(t) - q6(t)) \\
& + lUTmUTq6'(t) \sin(q4(t) - q6(t)) \\
& \left. + q1'(t) \cos(q4(t)) (2mCH + mL + 2(mLT + mUT)) \right) + glLmCH \cos(q4(t)) \\
& + \frac{1}{2} glLmL \cos(q4(t)) + glLmLT \cos(q4(t)) + glLmUT \cos(q4(t)) - kL2(q5(t) \\
& - q4(t)) + kp(q4(t) - q3(t))
\end{aligned}$$

$$\begin{aligned}
\frac{\partial \mathcal{L}}{\partial q_5} = & -\frac{1}{2} lLTq5'(t) (lCHmCHq7'(t) \sin(q5(t) - q7(t)) - 2lLmCHq4'(t) \sin(q4(t) - q5(t)) \\
& - lLmLTq4'(t) \sin(q4(t) - q5(t)) - 2lLmUTq4'(t) \sin(q4(t) - q5(t)) \\
& - lLL(2mCH + mL + 2mUT)q2'(t) \sin(q2(t) - q5(t)) \\
& - 2lULmCHq3'(t) \sin(q3(t) - q5(t)) - lULmLTq3'(t) \sin(q3(t) - q5(t)) \\
& - 2lULmUTq3'(t) \sin(q3(t) - q5(t)) + 2lUTmCHq6'(t) \sin(q5(t) - q6(t)) \\
& + lUTmUTq6'(t) \sin(q5(t) - q6(t)) + (2mCH + mL + 2mUT)q1'(t) \cos(q5(t))) \\
& + glLTmCH \cos(q5(t)) + \frac{1}{2} glLTmLT \cos(q5(t)) + glLTmUT \cos(q5(t)) \\
& + kL2(q5(t) - q4(t)) - kT8(q6(t) - q5(t))
\end{aligned}$$

$$\begin{aligned}
\frac{\partial \mathcal{L}}{\partial q_6} = & -\frac{1}{2} lUTq6'(t)(lCHmCHq7'(t)\sin(q6(t) - q7(t)) - 2lLmCHq4'(t)\sin(q4(t) - q6(t)) \\
& - lLmUTq4'(t)\sin(q4(t) - q6(t)) - lLL(2mCH + mUT)q2'(t)\sin(q2(t) - q6(t)) \\
& - 2lLTmCHq5'(t)\sin(q5(t) - q6(t)) - lLTmUTq5'(t)\sin(q5(t) - q6(t)) \\
& - 2lULmCHq3'(t)\sin(q3(t) - q6(t)) - lULmUTq3'(t)\sin(q3(t) - q6(t)) + (2mCH \\
& + mUT)q1'(t)\cos(q6(t))) \\
& + glUTmCH\cos(q6(t)) + \frac{1}{2} glUTmUT\cos(q6(t)) - kT1(q7(t) - q6(t)) + kT8(q6(t) - q5(t))
\end{aligned}$$

$$\begin{aligned}
\frac{\partial \mathcal{L}}{\partial q_7} = & -\frac{1}{2} lCHmCHq7'(t)(-lLq4'(t)\sin(q4(t) - q7(t)) - lLLq2'(t)\sin(q2(t) - q7(t)) \\
& - lLTq5'(t)\sin(q5(t) - q7(t)) - lULq3'(t)\sin(q3(t) - q7(t)) \\
& - lUTq6'(t)\sin(q6(t) - q7(t)) + q1'(t)\cos(q7(t))) + \frac{1}{2} glCHmCH\cos(q7(t)) \\
& + kT1(q7(t) - q6(t))
\end{aligned}$$

A3-APPENDIX: GENERALIZED COORDINATES TIME HISTORY PLOTS

The time history plots of the generalized coordinates, velocities and accelerations for one subject within each group (pediatric, PMHS low speed and PMHS high speed) are shown in the following figures

A3.1 PEDIATRIC OCCUPANT

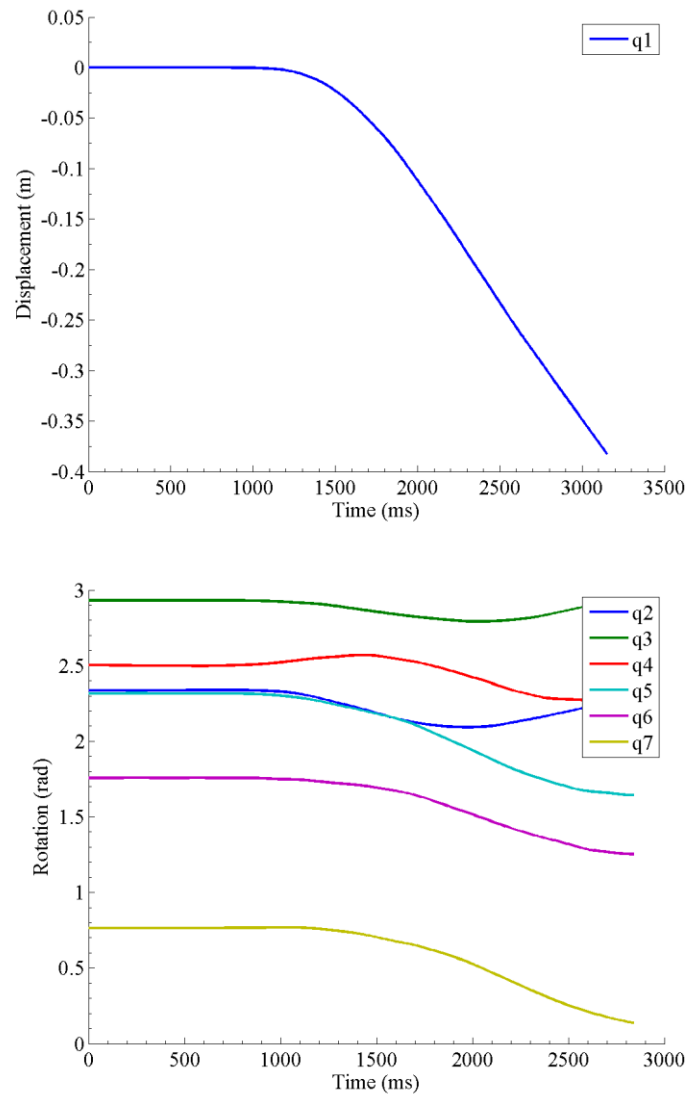


Figure A3.1 PED2 time history of generalized coordinates.

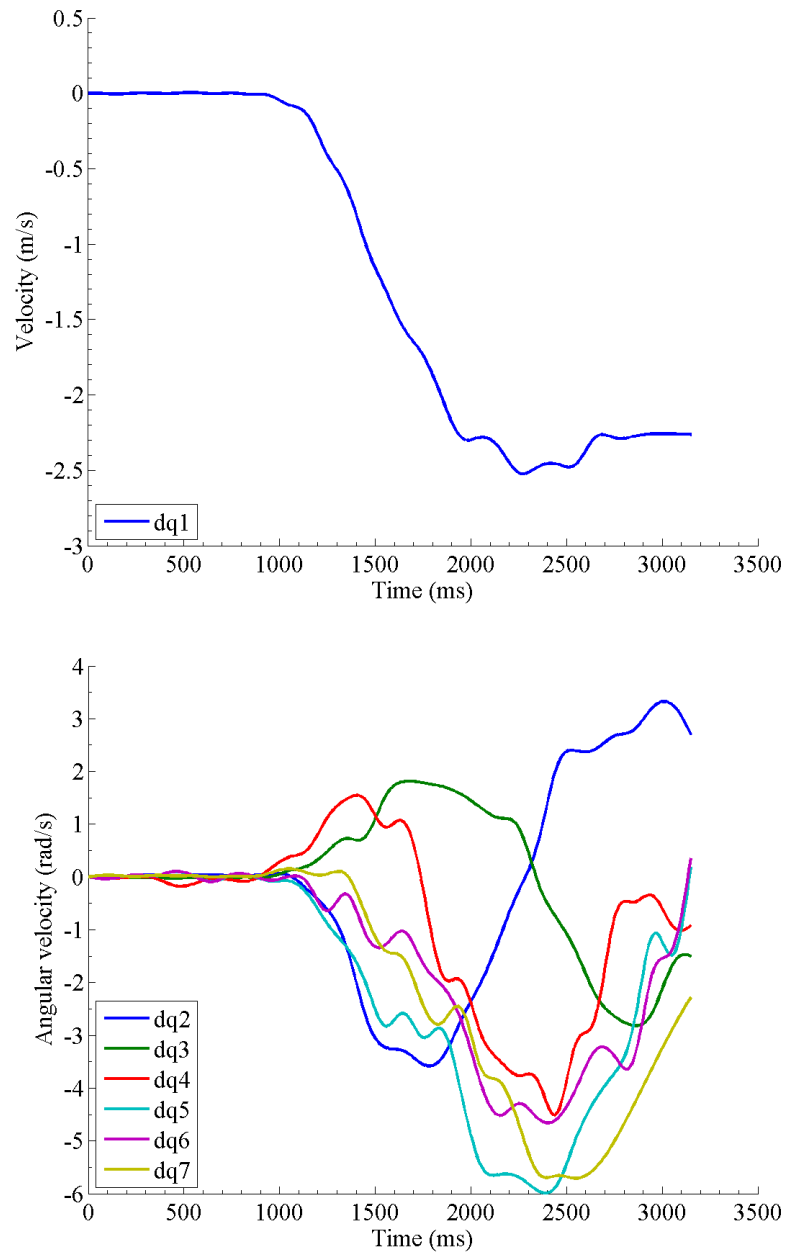


Figure A3.2 PED2 time history of generalized velocities.

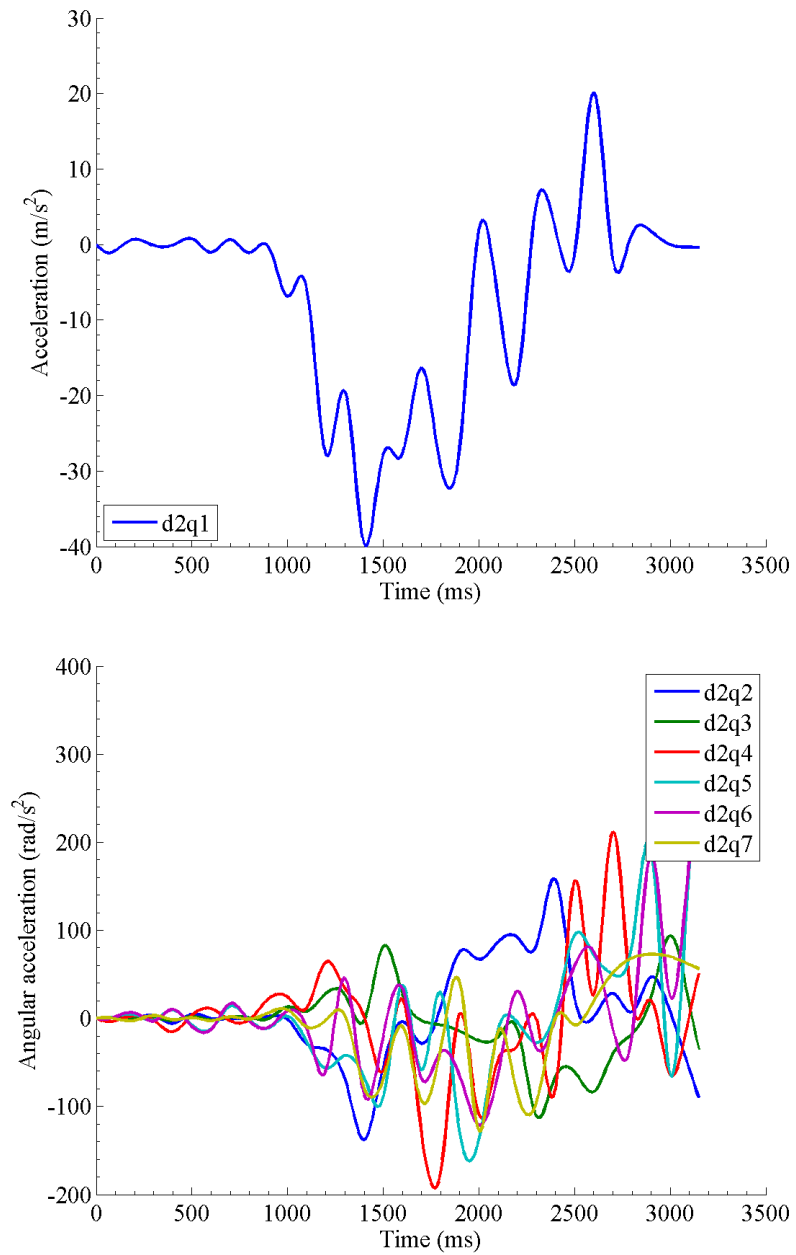


Figure A3.3 PED2 time history of generalized accelerations.

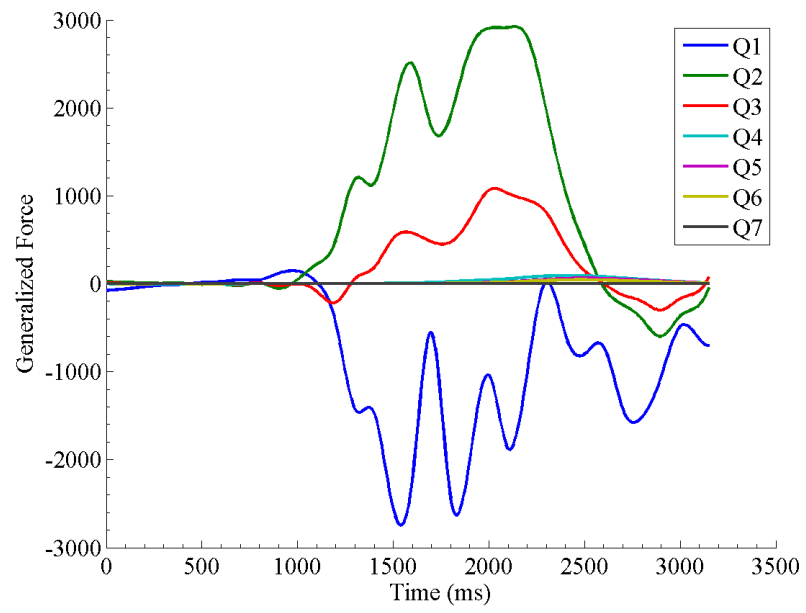


Figure A3.4 PED2 time history of generalized forces.

A3.2 PMHS OCCUPANT AT LOW SPEED

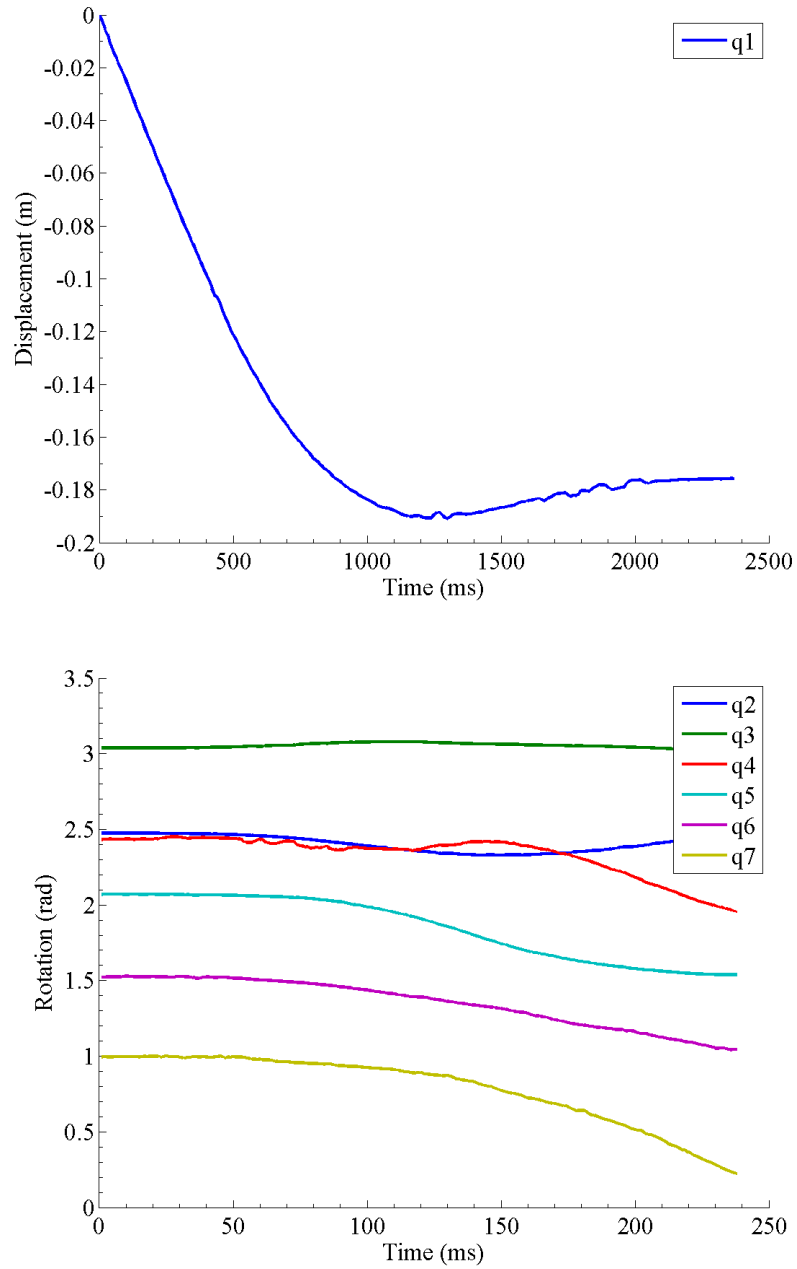


Figure A3.5 Time history of generalized coordinates calculated for a PMHS at low speed.

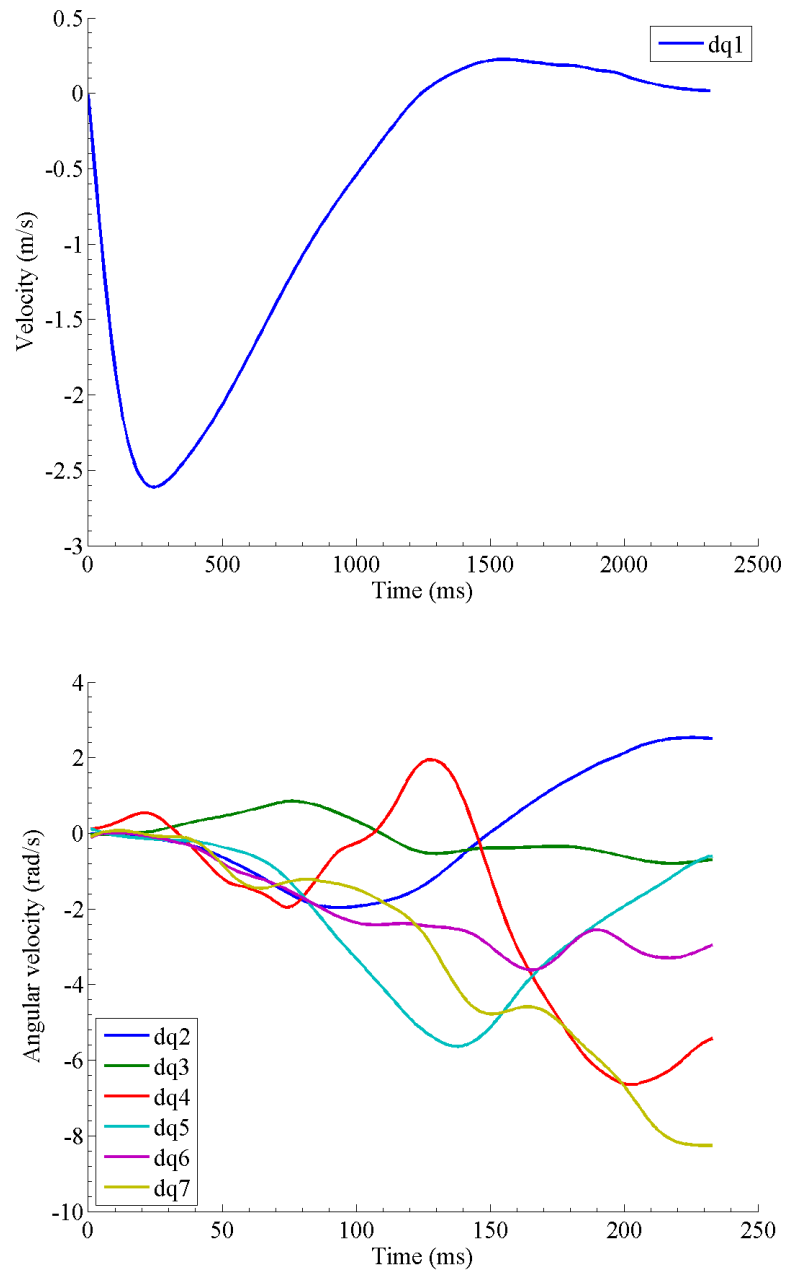


Figure A3.6 Time history of generalized velocities calculated for a PMHS at low speed.

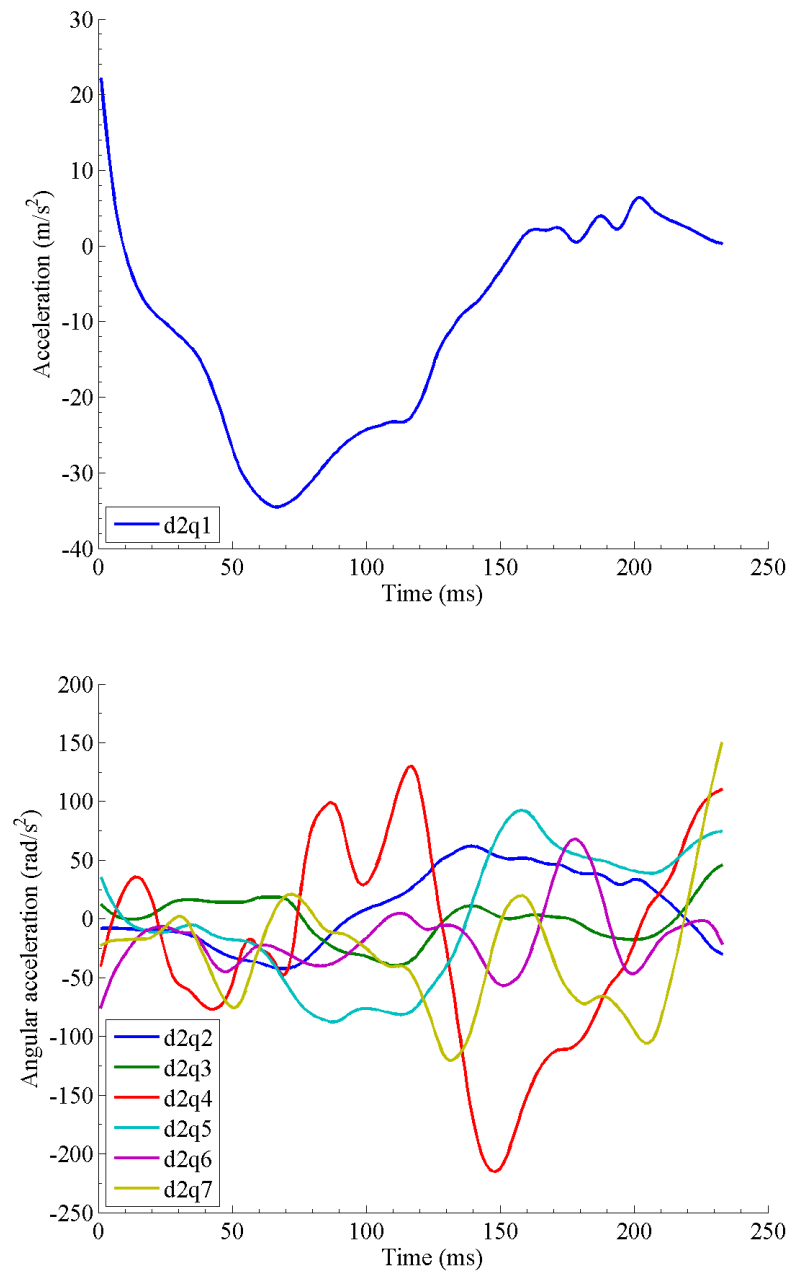


Figure A3.7 Time history of generalized accelerations calculated for a PMHS at low speed.

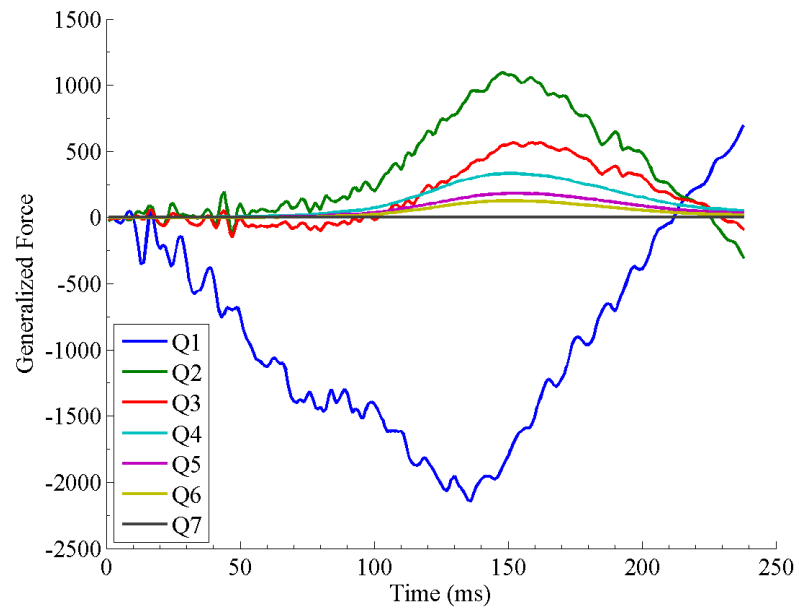


Figure A3.8 Time history of generalized coordinates calculated for a PMHS at low speed.

A3.3 PMHS OCCUPANT AT HIGH SPEED

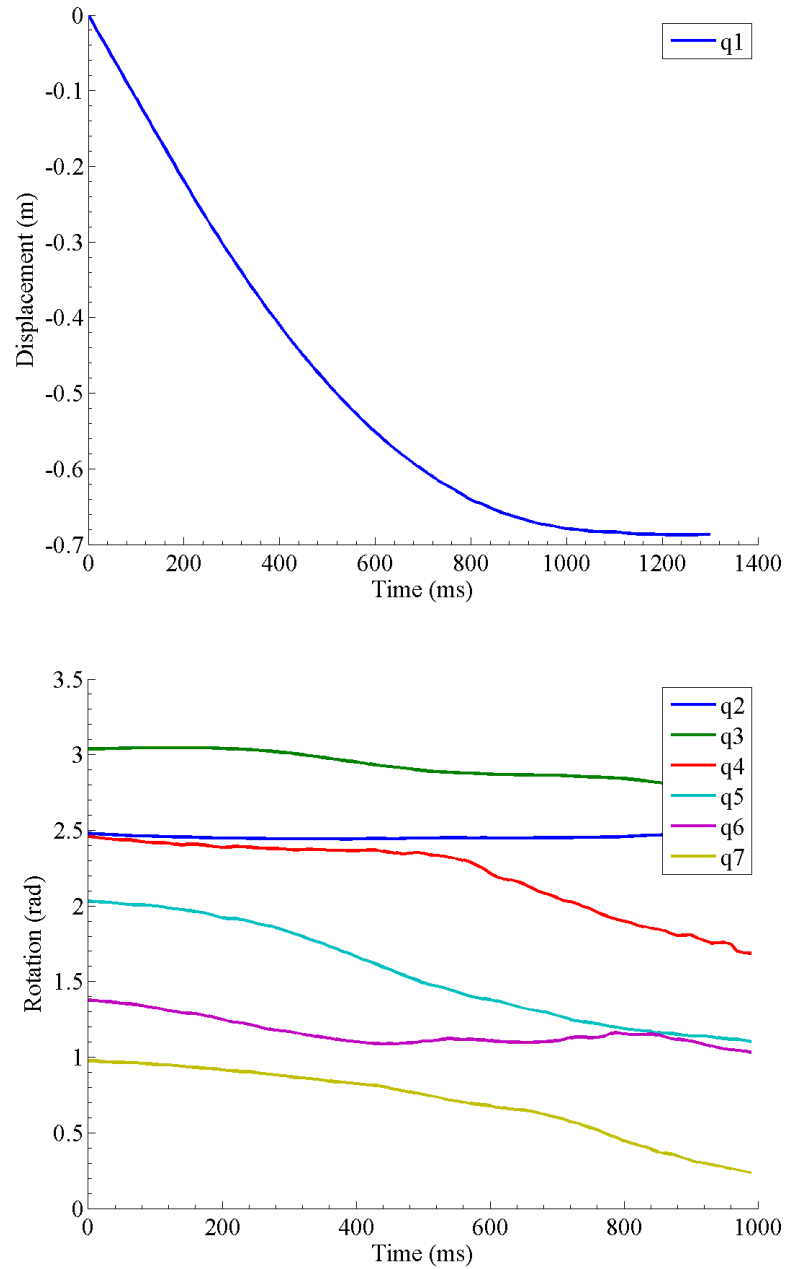


Figure A3.9 Time history of generalized coordinates calculated for a PMHS at high speed.

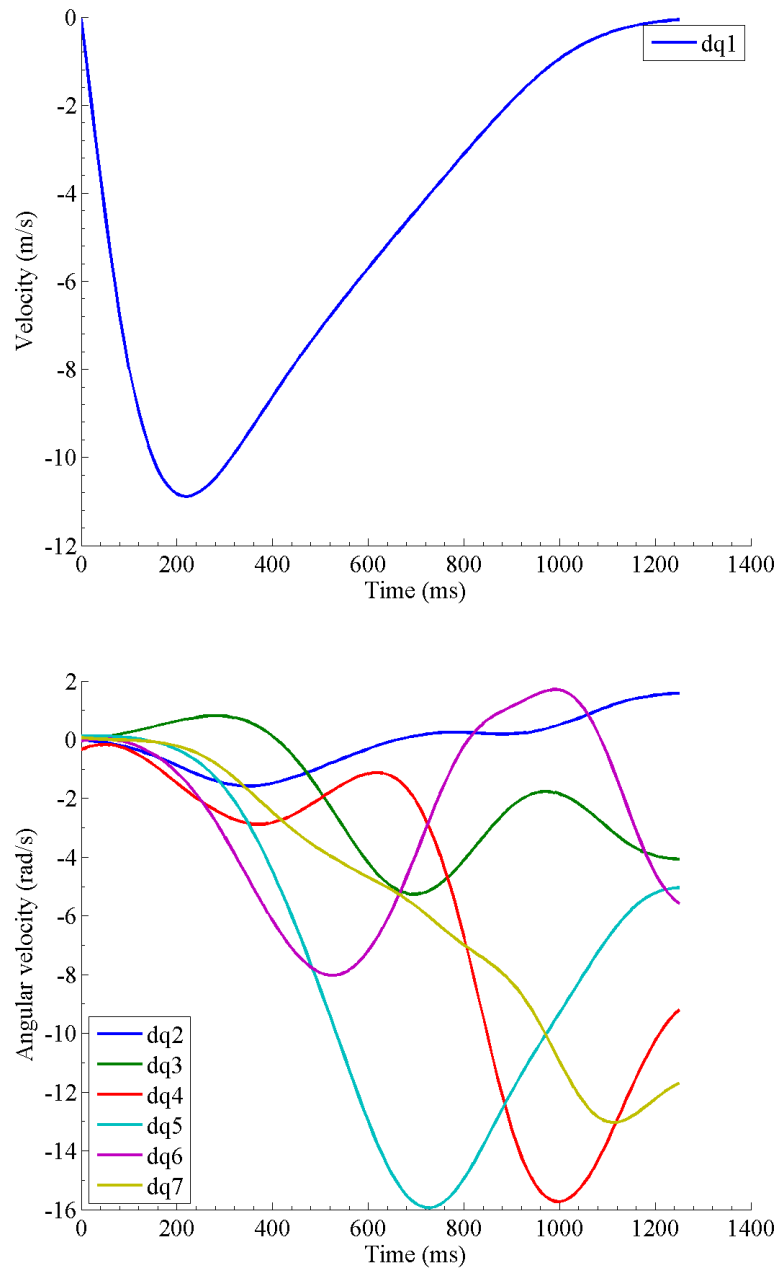


Figure A3.10 Time history of generalized velocities calculated for a PMHS at high speed.

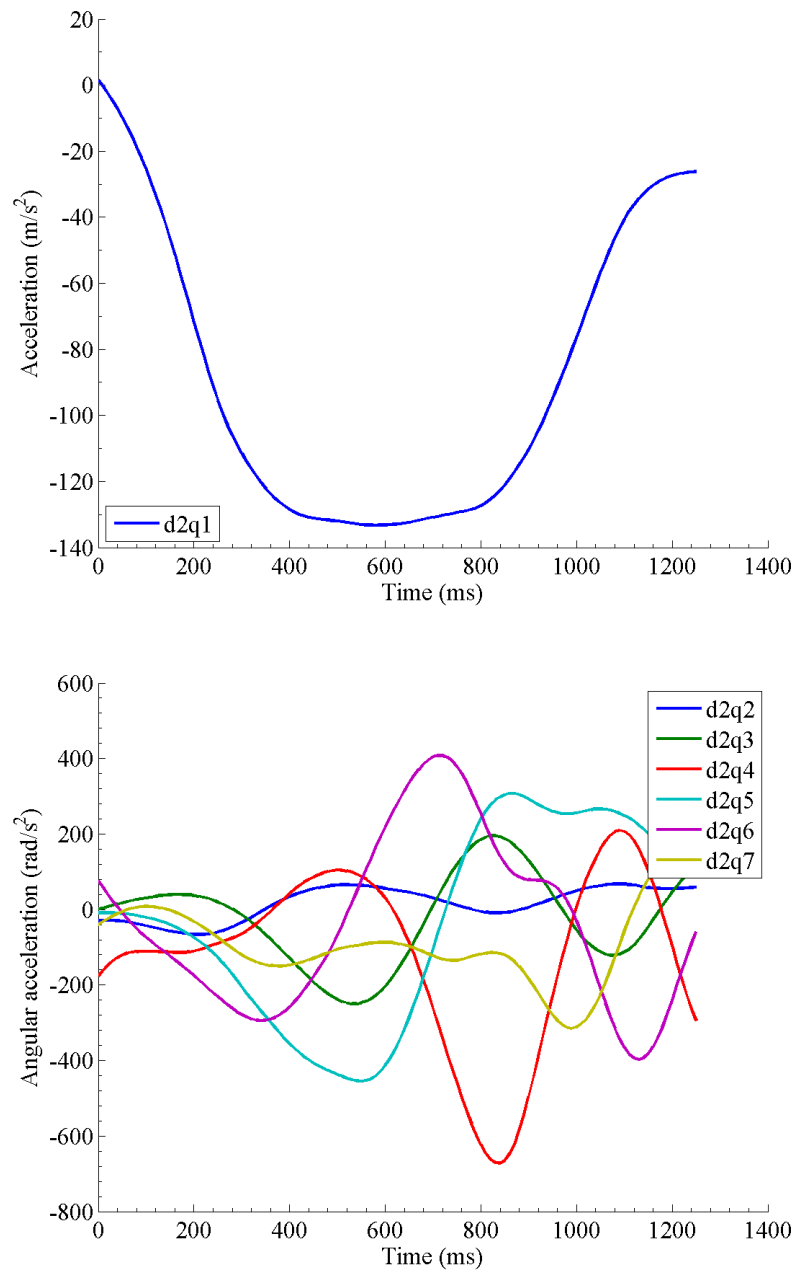


Figure A3.11 Time history of generalized accelerations calculated for a PMHS at high speed.

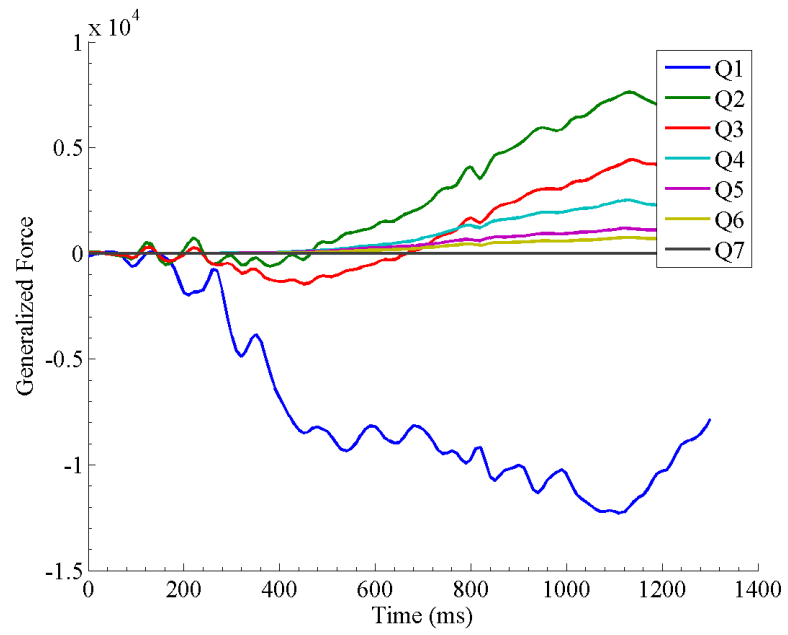


Figure A3.12 Time history of generalized forces calculated for a PMHS at high speed.

A4-APPENDIX: PROPORTIONAL DAMPING APPROXIMATION

The understanding of damping forces in mechanical systems is not well developed despite of a substantial amount of research. The most common approach to model the damping acting on a structure is to use viscous damping. Under this approach, the only relevant variables that affect damping forces are the instantaneous generalized velocities. Although this is not the only damping mechanism that dissipates energy in a mechanical system, it constitutes a valid starting model when the actual structural damping mechanism is unknown (Liu and Gorman, 1995; Adhikari and Woodhouse, 2001; Adhikari, 2006). Even if the validity of the viscous damping model is accepted, a new difficulty arises at the time of finding an expression for the damping of the structure. Lord Rayleigh proposed a convenient model of viscous damping that allowed to generalize the modal analysis of undamped system to damped systems (Rayleigh, 1877). This model is known as proportional damping and expresses the damping matrix as a linear combination of the mass and stiffness matrices, that is:

$$\underline{\underline{C}} = \alpha_1 \underline{\underline{M}} + \alpha_2 \underline{\underline{K}} \quad \text{Equation A4.1}$$

where α_1 and α_2 are real scalars. The advantage of this formulation is that it preserves all the characteristics of the real normal modes of the undamped system. Thus, the equations of motion of the system can be uncoupled using the real matrix given by the normal modes and, therefore, they can be solved analytically. Moreover the numerical solution of such a system is much simpler and less computational expensive than in the case of a coupled system.

Given all the advantages provided by the proportional damping model, research on structural behavior has identified the conditions under which damped systems can be modeled as proportionally damped systems. The original work establishing these conditions for both discrete and continuous system was published by Caughey and O'Kelly in 1965 (Caughey and O'Kelly, 1965). The authors provide a mathematical justification of the validity of using proportional damping, finding that this approach is valid if and only if the system matrices satisfy the relationship:

$$\underline{\underline{K}} \underline{\underline{M}}^{-1} \underline{\underline{C}} = \underline{\underline{C}} \underline{\underline{M}}^{-1} \underline{\underline{K}} \quad \text{Equation A4.2}$$

However, the assumption of proportional damping was used within this dissertation to solve for the stiffness terms and therefore is built-in in the model. Despite being a commonly accepted premise when there is no more information about the damping of the system, this Appendix provides a rheological interpretation of Rayleigh damping based on the work by J.F. Semblat (Semblat, 1997).

Assuming that Rayleigh damping describes correctly the energy dissipation behavior of a system, the loss factor (η) can be written as:

$$\eta = 2\xi = \frac{\alpha_1}{\omega} + \alpha_2\omega \quad \text{Equation A4.3}$$

where ξ is the damping ratio given by the expression:

$$\xi = \frac{c}{c_0} = \frac{c}{2\sqrt{km}} \quad \text{Equation A4.4}$$

Semblat investigated if there was a rheological model that would exhibit the same loss factor vs. frequency behavior as the one shown by the Rayleigh damped system. The author proposed a particular type of the generalized Maxwell model to describe a similar response to that of the Rayleigh model. The generalized Maxwell model is represented in Figure A4.1

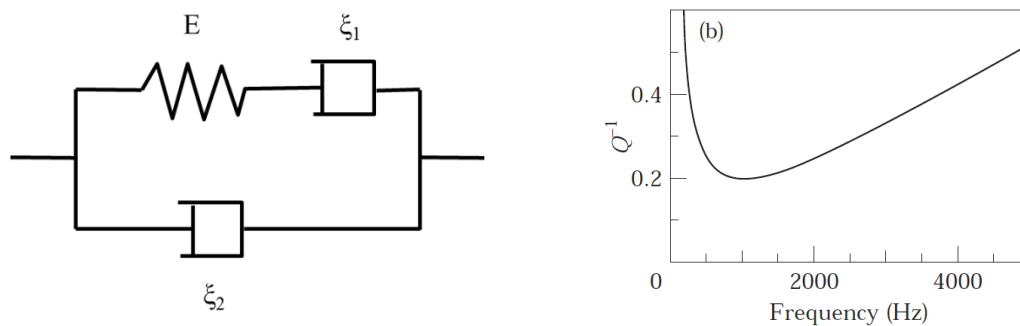


Figure A4.1 Generalized Maxwell model proposed by (Semblat, 1997) and corresponding attenuation curve.

The plot on the left of Figure A4.1 shows the attenuation curve of the generalized Maxwell model using the inverse of the quality factor (Q), that is defined as the ratio between the real and the imaginary part of the complex modulus of the Maxwell element:

$$Q = \frac{E_R}{E_I} \quad \text{Equation A4.5}$$

And for moderate damping, the quality factor can be related to the damping ratio by the following expression:

$$Q^{-1} = 2\xi \quad \text{Equation A4.6}$$

Obtaining the complex modulus of the Maxwell element represented in Figure A4.1, the inverse of the quality factor is derived and given by Equation A4.7:

$$Q^{-1} = \frac{E(\xi_1 + \xi_2)}{\xi_1^2} \frac{1}{\omega} + \frac{\xi_2}{E} \omega \quad \text{Equation A4.7}$$

Thus, using Equation A4.3 and Equation A4.7, a direct relationship between the constants in the Rayleigh damping model and the model parameters of the generalized Maxwell can be established as follows:

$$\begin{aligned} \alpha_1 &= \frac{E(\xi_1 + \xi_2)}{\xi_1^2} \\ \alpha_2 &= \frac{\xi_2}{E} \end{aligned} \quad \text{Equation A4.8}$$

Semblat (1997) showed that for values of damping ratio up to 26% (Figure A4.2), the Rayleigh model gives an adequate description of the amplitude reduction and phase delays exhibited by the generalized Maxwell model. In other terms, the Rayleigh damping model would be equivalent to a linear viscoelastic generalized Maxwell model.

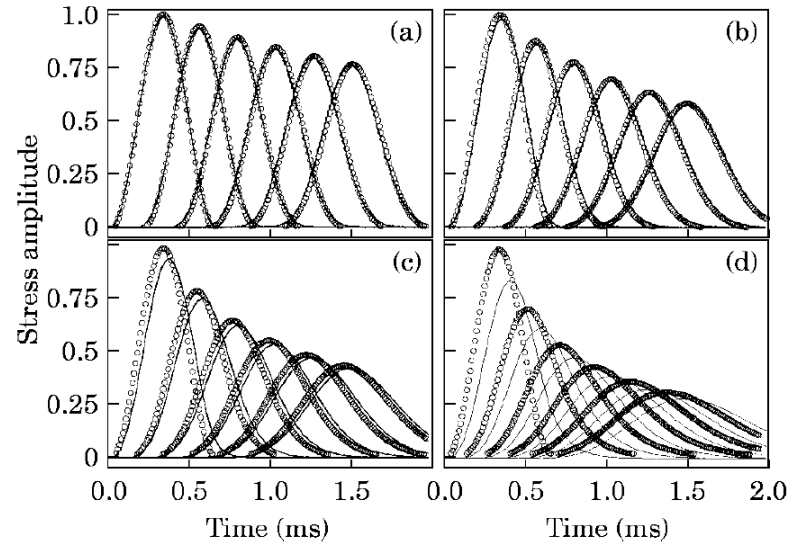


Figure A4.2 Comparison between the Rayleigh damping model (circles) and the generalized Maxwell model (solid line) in a one-dimensional wave propagation model for different values of the damping coefficient ((a) $\xi=5\%$; (b) $\xi=13\%$; (c) $\xi=26\%$; (d) $\xi=52\%$).

This formulation was considered acceptable for the purpose of this dissertation.

A5-APPENDIX: KANGAROO SLED TESTS

A5.1 INTRODUCTION

As described in Chapter 6, eastern grey kangaroos were used as surrogates of human 6YO in sled tests. The setup of the tests paralleled closely that used in the volunteer and PMHS experiments. The following sections describe the main characteristics of the test setup, the observed experimental results and the parameters needed to develop the 2D ADAMS© model of the kangaroo that was used in the assessment of the scaling methodology between 9 km/h and 40 km/h (Subsection 6.2.3.5).

A5.2 METHODS

A5.2.1 Test Setup

The test buck was essentially the same used in the PMHS tests, although a number of hardware modifications were required to adapt the buck to the kangaroo. In particular, the anchor point of the shoulder belt was displaced towards the center line of the buck to improve the fit of the belt on the torso of the kangaroo, which was narrower than the adult human torso. Also a custom-made leg restraint was attached to the seat to prevent anterior translation of the pelvis. No lap belt was used in these tests since the leg restraint was assumed to provide enough restraint to the pelvis and the geometry of the kangaroo pelvis would have prevented that the lap belt loaded the iliac spines of the specimens. The dorsal aspect of the torso of the animal surrogate was supported by an adjustable matrix of wires and cables as in the PMHS case.

The kangaroo was exposed to a low-speed deceleration pulse ($\Delta v=9\pm 0.75$ m/s) followed by a high-speed one ($\Delta v=39.2\pm 0.76$ m/s). The deceleration pulses were chosen to match those of the PMHS tests. Figure A5.1 and Figure A5.2 show the time history of the deceleration of the test buck.

The shoulder belt was constructed from restraint webbing. The belt was notched in a dog bone shape to facilitate its accommodation on the narrow shoulder of the kangaroo. A custom-made force-limiting device consisting of two scored aluminum plates of predetermined thickness was used to allow for increased torso

rotation of the test surrogates. This force-limiting device had been already used successfully at the Center for Applied Biomechanics to control the belt force during the crash (Forman et al., 2005).

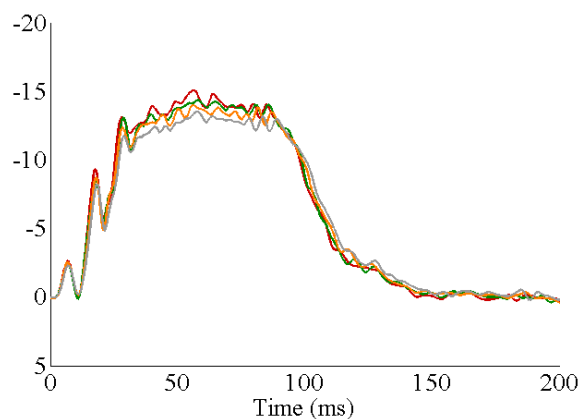
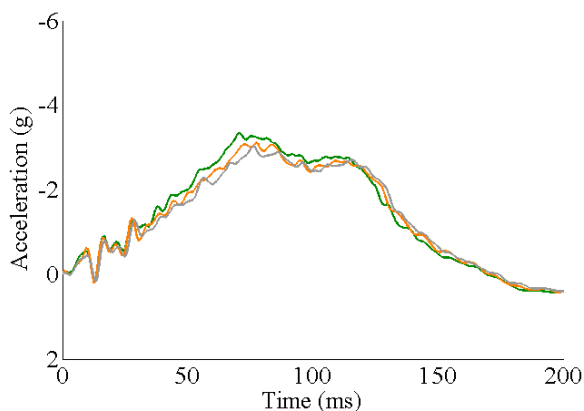


Figure A5.1 Kangaroo deceleration at low speed.

Figure A5.2 Kangaroo deceleration at high speed.

The test matrix is shown in Table A5.1. Figure A5.3 shows the position of the kangaroo in the test buck.

Table A5.1 Kangaroo test matrix.

	Low speed (~9 km/h)	High speed (~40 km/h)
Test number	1440	1441

A5.2.2 Test specimen

An eastern grey kangaroo carcass was used in these tests. The legs were amputated at the mid tibia and the majority of caudal vertebrae were removed to allow a sitting posture. The animal was frozen shortly after death and computer tomography (CT) scans were performed on each to assure the integrity of the thorax and no pre-existing fractures. Blood tests to check for Q-fever were also performed and the surrogate tested negative. The procurement of the test surrogate was reviewed and approved by the Australian Department of Environment, the U.S Food and Drug Administration, the University of Virginia Animal

Care and Use Committee and the University of Adelaide Ethics Committee. Table A5.2 summarizes some of the characteristics of the kangaroo test surrogate.

Table A5.2 Kangaroo characteristics.

	K05M
Test number	1440, 1441
Significant anomalies	None
Gender	Male
Cause of death	Head shot
Seated height (cm)	82
Seated surface to acromion (cm)	69
Weight (kg)	24

The initial position of the animal surrogate on the seating buck was documented carefully. In this case, the obvious anatomical differences between the animal model and the human subjects precluded any effort of matching initial positions between the two types of occupants.

A5.2.3 Instrumentation

Optical instrumentation. Orthogonal arrays of VICON markers were rigidly attached into selected vertebrae (T1, T4, T8 and L2) as well as in the pelvis and on the head. According to the methodology described in Chapter 4, these arrays allowed the 3D reconstruction of the trajectories of the corresponding anatomical structures. The installation of all VICON marker arrays paralleled completely that of the PMHS experiments described in Shaw et al. (2009). These arrays on the spine are shown in Figure A5.4. Other individual markers were attached to selected body landmarks to measure the deformation of the thorax during the loading of the belt as well as other trajectories of interest.

Kinematic data were obtained at 1000 Hz by a 16-camera VICON system and processed as described in the PMHS tests section in Chapter 4.



Figure A5.3 General setup of the kangaroo sled tests.



Figure A5.4 Marker plates along the spine and the pelvis of the kangaroo.

The origin of the pelvic local coordinate system was defined as the mid-point of the segment joining the two posterior-superior iliac spines of the kangaroo pelvis. It must be noted that the morphological differences between the kangaroo and human pelvis made impossible to establish a direct comparison between these two local anatomical reference systems despite of sharing the same definition. To avoid that the geometry of the pelvis and its interaction with the seat surface influenced the kinematics of the spine, the motion of the pelvis was arrested by a custom-designed knee bolster (shown in Figure A5.3). The goal of the joint action of the knee bolster and the seat pelvic block was to prevent the translation of the pelvis during the tests and therefore to minimize its influence on the motion of the kangaroo spine.

Other instrumentation. Similarly to the PMHS tests, triaxial accelerometers (Endevco model 7264B), were mounted on the head plate, and on T1, T4, T8, L2 and the pelvis. Angular rate sensors (DTS model, ARS-12k) were also mounted on the head plate and T1. Data were collected at 10000 Hz by an onboard data acquisition system (DTS Inc.). Channels were hardware-filtered to 3000Hz, debiased, and filtered again using SAEJ-211 CFC filters.

A5.3 RESULTS

Figure A5.5 and Figure A5.6 show the displacements of the anatomical landmarks described above in the case of a low-speed frontal impact (Test 1450) and of a high-speed impact (Test 1451).

The differences in the trajectories of the anatomical landmarks between humans and kangaroos are noticeable, regardless of the speed. Both the magnitude and the shape of the trajectories are different as shown in Figure A5.5 and Figure A5.6. The peak forward displacements of all the anatomical structures analyzed were smaller than the ones observed in the pediatric volunteer tests at 9 km/h. Also the pattern of increasing forward displacement moving from the caudal to the cranial region in the humans, was not exhibited by the kangaroos at either impact speed.

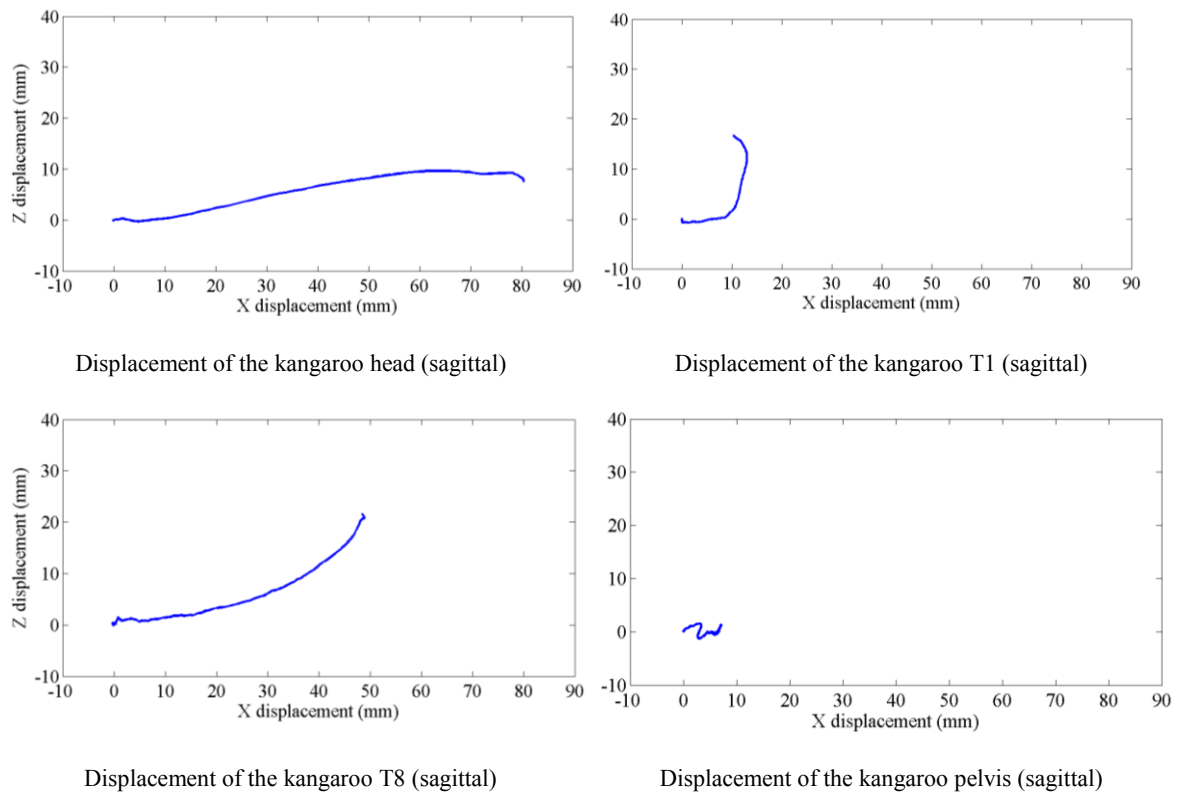


Figure A5.5 Displacements of the kangaroo at 9 km/h.

The differences in mass distribution of the torso and head, as well as the differences in the way the belt loaded the chest of the specimens, caused the spine of the kangaroo to exhibit a more lordotic curvature throughout the duration of the deceleration at both speeds. Not only the majority of the mass of the

kangaroo is concentrated in the pelvic/lumbar region, but also the seatbelt loaded primarily the most superior part of the kangaroo chest. Also, the relative weight of the kangaroo head with respect to the torso weight is significantly smaller than in the case of humans. The combination of all these factors caused that the forward motion of the lower part of the torso (which was essentially unrestrained) pulled from the lower segments of the spine inducing a significant lordotic curvature not observed in the PMHS test.

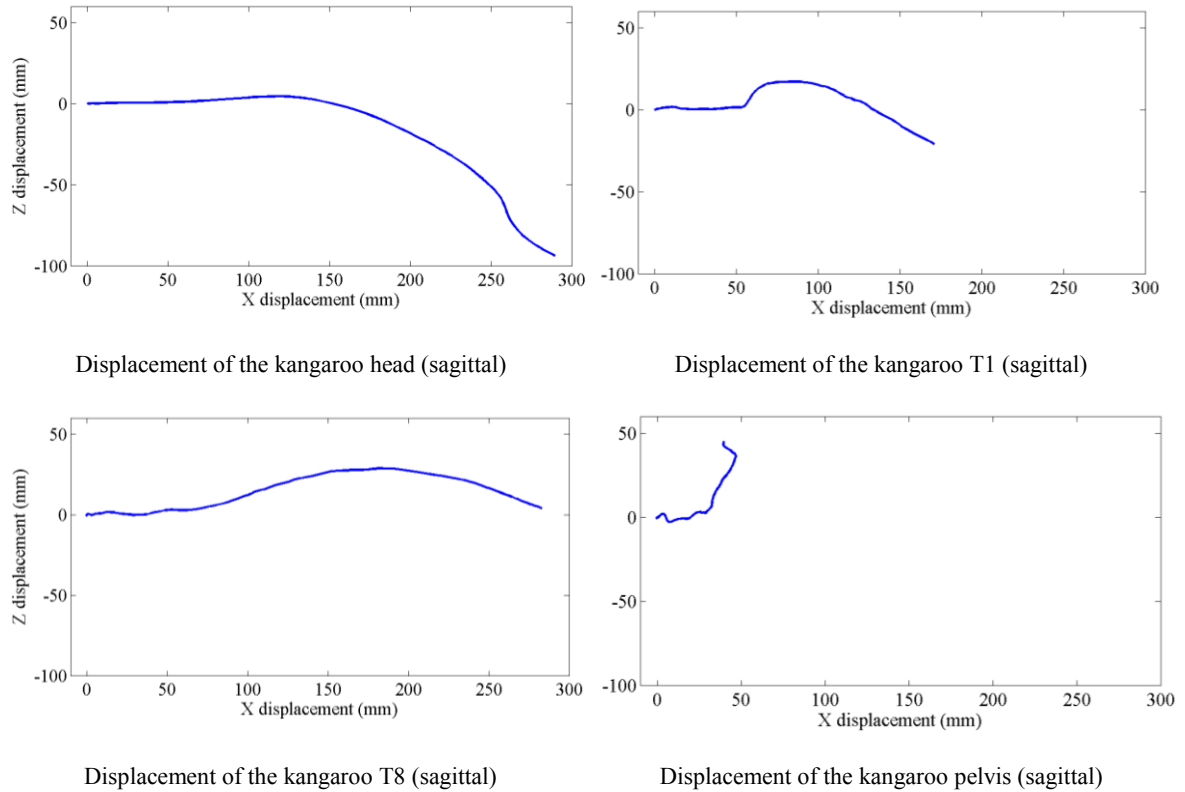


Figure A5.6 Displacements of the kangaroo at 40 km/h.

The above differences between the kangaroo and the human subjects can be qualitatively seen in Figure A5.7 and Figure A5.8 which show three snapshots of the PMHS and kangaroo tests at each of the speeds.

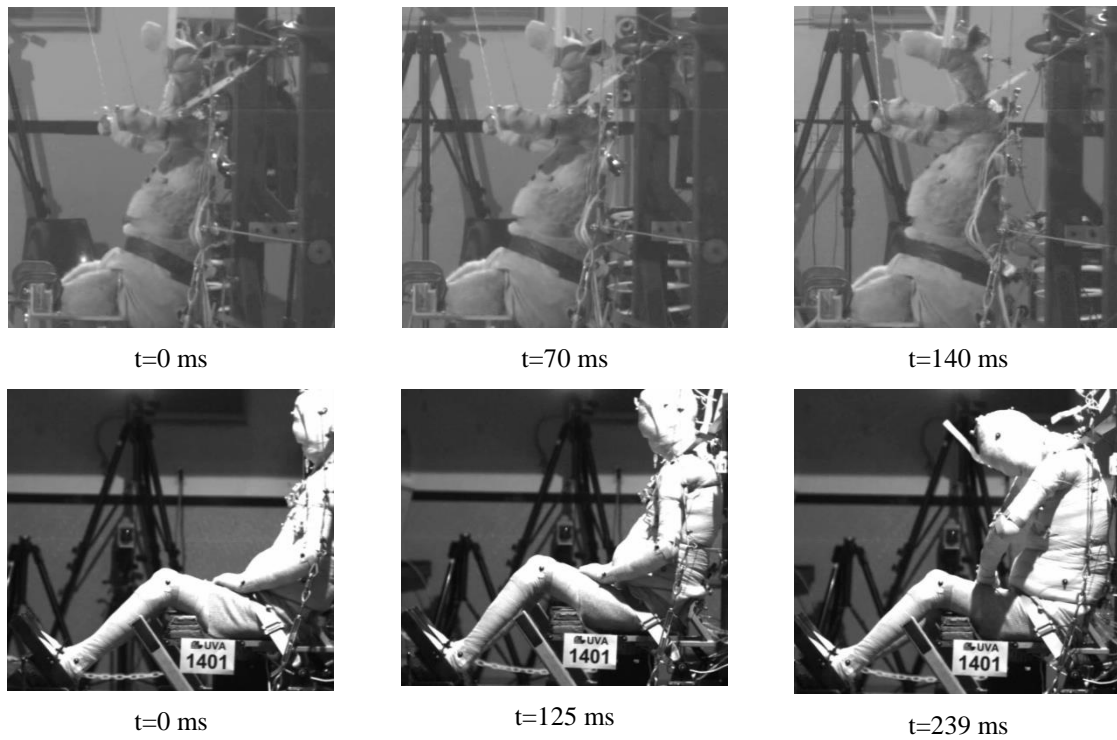


Figure A5.7 Comparison between PMHS and kangaroo at the start, intermediate position and final position of the 9km/s impact.

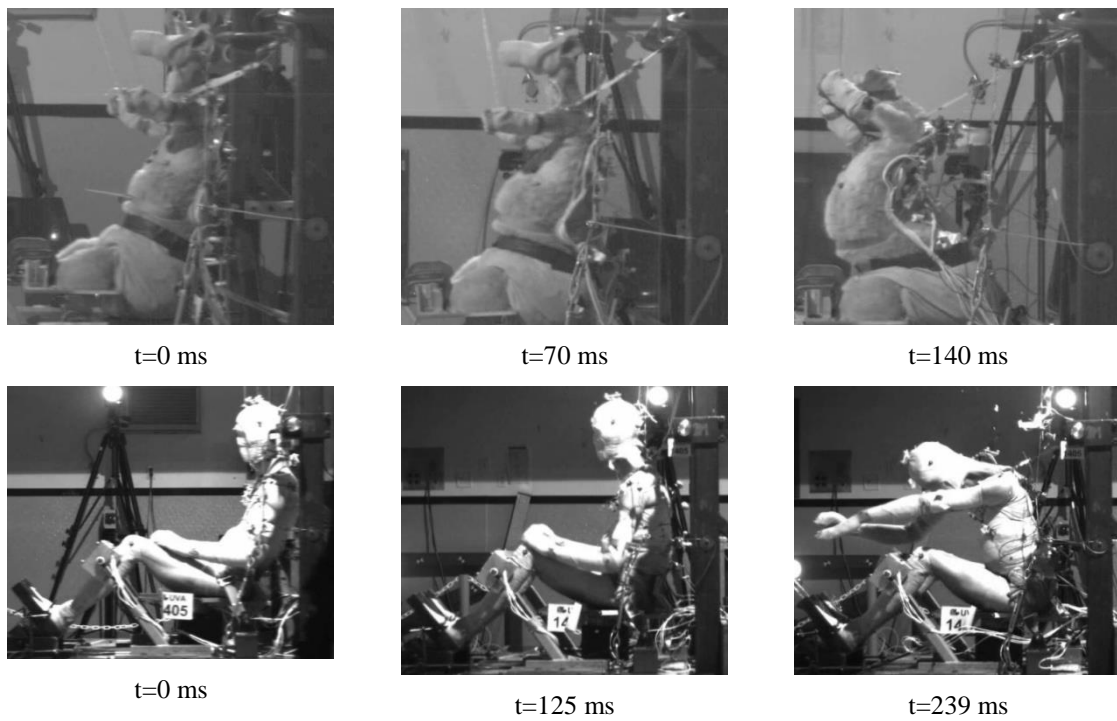


Figure A5.8 Comparison between PMHS and kangaroo at the start, intermediate position and final position of the 40 km/s impact.

A5.4 DEVELOPMENT OF 2D ADAMS© MODEL OF THE KANGAROO SURROGATE

Table A5.3 through Table A5.5 show the needed parameters to build a model in ADAMS© of the kangaroo surrogate. The process of building the model paralleled completely that explained in Section 6.2.2 of this dissertation.

The kangaroo was decapitated after test and the head weight was obtained by direct measurement. The trunk mass was distributed over the three torso regions according to their relative volume.

Table A5.3 Body region mass of kangaroo (kg).

Model body region	Volume (m ³)	Mass
CH		0.8
UT	4.5e-4	1.76
LT	8.8e-4	3.41
L	4.6e-3	18.03
TOTAL		24

Table A5.4 Body region length of kangaroo (m).

Model body region	Length (m)
CH	0.12
UT	0.15
LT	0.15
L	0.40

Table A5.5 Body region moment of inertia of kangaroo (kg m²).

Model body region	Moment of inertia (m)
CH	0.002
UT	0.004
LT	0.012
L	0.231

